AB INITIO DENSITY MATRIX RENORMALIZATION GROUP METHODOLOGY AND COMPUTATIONAL TRANSITION METAL CHEMISTRY

A Dissertation

Presented to the Faculty of the Graduate School

of Cornell University

in Partial Fulfillment of the Requirements for the Degree of

Doctor of Philosophy

by

Johannes Hachmann

February 2010

AB INITIO DENSITY MATRIX RENORMALIZATION GROUP METHODOLOGY AND COMPUTATIONAL TRANSITION METAL CHEMISTRY

Johannes Hachmann, Ph.D.

Cornell University 2010

This thesis is concerned with two topics from the field of computational electronic structure theory.

In the first part we will describe our contributions to the *ab initio* density matrix renormalization group (DMRG) methodology in quantum chemistry, in particular our quadratically scaling local algorithm. We will present applications aimed towards new insights into the physics of conjugated π-electron systems as found, e.g., in organic electronic materials.

The second part of this thesis covers our computational study of 3d-M(smif)$_2$ complexes synthesized and characterized in the Wolczanski Group. These compounds exhibit unusual electronic structure phenomena which we address from a theoretical perspective.

BIOGRAPHICAL SKETCH

Johannes Hachmann was born on 11 December 1978 in Ibbenbüren, Westfalia, Germany and grew up in the nearby town of Tecklenburg.

After graduating from the Graf-Adolf-Gymnasium Tecklenburg in 1998 and 13 months of Civilian Service in the field of environmental protection and education, he began his undergraduate studies of chemistry at the Friedrich-Schiller-Universität Jena in Thuringia, Germany. He specialized in theoretical and physical chemistry and was mentored by PD Dr. H.-G. Fritsche. From 2000 until 2004 he held a scholarship from the Studienstiftung des Deutschen Volkes (German National Academic Foundation).

From October 2003 until July 2004 he joined Prof. N. C. Handy FRS at the Cambridge University Centre for Computational Chemistry (CUC^3), University of Cambridge, UK, for the preparation of his diploma-thesis in theoretical chemistry. He worked on 'Nodal hypersurfaces and sign domains in many-electron wavefunctions', and was supported by an additional study-abroad scholarship by the Studienstiftung. Johannes received his Dipl.-Chem. degree from the FSU Jena with honours.

Following his stay in Cambridge he began his graduate studies at Cornell University to work with Prof. G. K.-L. Chan. This thesis is the outcome of this enterprise. Between 2005 and 2007 Johannes held a Kekulé Fellowship of the Fonds der Chemischen Industrie (Fund of the German Chemical Industry), and in 2007 he received an M.Sc. degree from Cornell University.

After completion of his Ph.D. he will begin post-doctoral research with Prof. A. Aspuru-Guzik at Harvard University.

Johannes is married to Anna-Barbara Hachmann, enjoys bicycle road racing, geneology, and is a bibliophile.

This thesis is dedicated to my parents

Torsten and Christa Hachmann

for their constant support and encouragement,

and

to my wife Anna.

She is my love and rock, and truly my better half.

Without her, I could not be where I am today.

ACKNOWLEDGEMENTS

Je größer die abstrakte Schönheit einer Theorie, desto größer ist auch ihr Wahrheitsgehalt. Die innere Harmonie in der Struktur der Materie zu erkennen, d.h. für uns Menschen im Gewande mathematischer Schönheit zu erfassen, ist wohl die Hauptantriebskraft, sich mit soviel Mühe auf diesen schweren Weg der Erkenntnis zu begeben.

The greater the abstract beauty of a theory, the greater is also its degree of truth. To recognize the inner harmony in the structure of matter, i.e., for us human beings to apprehend it in its mathematical beauty, appears to be the central motive to set out with so much effort on this hard way of cognition.

Günther Ludwig[1]

I am deeply grateful to my advisor and mentor, Prof. Garnet Kin-Lic Chan. It was a privilege to work with someone of his creativity and intellect. I would also like to thank Prof. Gregory S. Ezra and Prof. Roald Hoffmann for serving on my committee, and being the source of sound advice and support. Both have inspired me as great teachers and communicators of science.

In the course of my graduate studies and research I was fortunate to work with a number of remarkable colleagues and friends: Dr. Wim Cardoen, Jonathan J. Dorando, Debashree Ghosh, and Prof. Takeshi Yanai.

My thanks also go to the rest of the Chan Group, in particular Dr. Dominika Zgid and Eric Neuscamman, as well as the honorary members Showey Yazdanian and Alex Fishman.

Robert and Nancy Nead have become our American family and they made Anna and me feel at home in the US.

They all made my time in Ithaca cheerful and rewarding.

[1]From the preamble of *Die Grundlagen der Quantenmechanik*, Springer, Heidelberg, **1954**.

TABLE OF CONTENTS

LIST OF TABLES

LIST OF FIGURES

CHAPTER 1

INTRODUCTION I: *AB INITIO* DMRG IN QUANTUM CHEMISTRY

In the following chapter we will introduce the electron correlation problem (Sec. 1.1), which is at the center of interest of modern electronic structure theory and of this work in particular. We will stress the notion of certain regimes and its value for the design and application of quantum chemical methods. The special case of electron correlation phenomena in quasi-one-dimensional problems will be discussed in Sec. 1.1.8 in connection with a brief review of organic electronic materials, whose conjugated π-electron systems were the focus of our application studies. Sec. 1.2 gives an overview of general renormalization group (RG) ideas and the density matrix renormalization group (DMRG), with an emphasis on the *ab initio* DMRG approach to quantum chemistry. We will discuss both the original algorithmic and the more recent wavefunction perspective of DMRG.

Sec. 1.2 uses passages of our paper 'J. Hachmann, W. Cardoen, G. K.-L. Chan, *J. Chem. Phys.* 125 (**2006**), 144101' [1]. In addition, our introduction follows lines of argument from the literature, in particular Refs. [2, 3, 4].

1.1 The electron correlation problem

1.1.1 The quantum many-body problem in chemistry

The quantum many-body problem lies at the heart of chemistry: Chemical compounds are comprised of nuclei and electrons, which are rearranged in the course of chemical reactions, and whose interactions are governed by the laws of quantum mechanics. P.A.M. Dirac summarized this fundamental relation 80

years ago in his iconic quote:

'The underlying physical laws necessary for the mathematical theory of a large part of physics and the whole of chemistry are thus completely known, and the difficulty is only that the exact application of these laws leads to equations much too complicated to be soluble.' [5]

The central expression in molecular quantum mechanics [6] is arguably the nonrelativistic, time-independent Schrödinger equation [7]

$$\hat{H}\,|\Psi\rangle = E\,|\Psi\rangle \tag{1.1}$$

with the Hamiltonian

$$\begin{aligned}\hat{H}(\mathbf{r},\mathbf{R}) &= \hat{T}_e(\mathbf{r}) + \hat{V}_{ee}(\mathbf{r}) + \hat{V}_{eN}(\mathbf{r},\mathbf{R}) + \hat{T}_N(\mathbf{R}) + \hat{V}_{NN}(\mathbf{R}) \\ &= \sum_a^n -\frac{1}{2}\nabla_a^2 + \sum_{a<b}^n \frac{1}{r_{ab}} + \sum_{a,A}^{n,N} -\frac{Z_A}{r_{aA}} + \sum_A^N -\frac{1}{2M_A}\nabla_A^2 + \sum_{A<B}^N \frac{Z_A Z_B}{R_{AB}}\end{aligned} \tag{1.2}$$

(in atomic units [8][1]), with $\hat{T}_e$ the kinetic energy operator for the electrons, $\hat{T}_N$ the kinetic energy operator for the nuclei, $\hat{V}_{ee}$ the repulsive electron-electron Coulomb potential energy operator, $\hat{V}_{NN}$ the repulsive nuclear-nuclear Coulomb potential energy operator, and $\hat{V}_{eN}$ the attractive electron-nuclear Coulomb potential energy operator (see Fig. 1.1).

In the 'clamped nuclei' version of the Born-Oppenheimer (BO) approximation [9], this complex Hamiltonian is simplified to

$$\hat{H}_{BO}(\mathbf{r};\mathbf{R}) = \hat{T}_e(\mathbf{r}) + \hat{V}_{ee}(\mathbf{r}) + \hat{V}_{eN}(\mathbf{r};\mathbf{R}) + V_{NN}(\mathbf{R}), \tag{1.3}$$

[1] With $\mathbf{r}$ we denote all electronic and with $\mathbf{R}$ all nuclear coordinates, r_{ab} is the interelectronic distance between electrons a and b, r_{aA} the distance between electron a and nucleus A, and R_{AB} the internuclear distance between nuclei A and B. Z_A stands for the charge of nucleus A and M_A is the ratio of its mass to the mass of an electron.

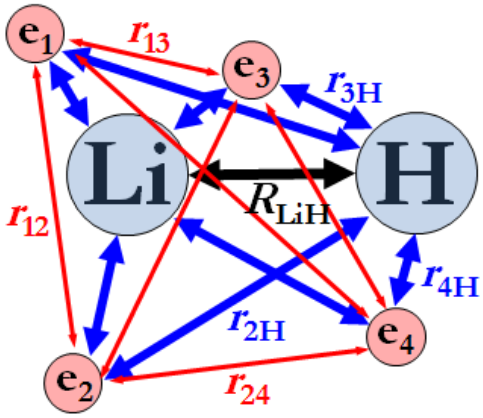

Figure 1.1: Interactions for the example of a simple lithiumhydride molecule with 2 nuclei and 4 electrons. Black arrows refer to the internuclear distance R_{AB}, associated with $\hat{V}_{NN}$, blue arrows to the nuclear-electron distance r_{aA}, associated with $\hat{V}_{eN}$, and red arrows to the interelectronic distance r_{ab}, associated with the complicated $\hat{V}_{ee}$ term.

by setting $\hat{T}_N = 0$ and $\hat{V}_{NN} = V_{NN} = const.$ (since the nuclei are – due to their larger mass – essentially stationary on the time scale of the electronic motion[2]). The electronic and nuclear dynamics are decoupled and the total wavefunction ($|\Psi\rangle$) factorizes into an electronic ($|\Psi_e\rangle$) and a nuclear ($|\Psi_N\rangle$) part

$$\Psi(\mathbf{r}, \mathbf{R}) \longrightarrow \Psi_e(\mathbf{r}; \mathbf{R}) \otimes \Psi_N(\mathbf{R}). \tag{1.4}$$

We now solve for the electronic wavefunction, which is parametrized by (i.e., only implicitly dependent on) the nuclear positions

$$\hat{H}_{BO} |\Psi_e\rangle = (E_e + V_{NN}) |\Psi_e\rangle \tag{1.5}$$

(instead of solving for the full eqn. (1.1)). The electrons are moving in the field of the nuclear charges, which leads to the concept of a potential energy surface

[2]For a detailed introduction of the BO-approximation, as well as a discussion of its limitations and possible corrections, see Refs. [10, 11].

(PES).[3]

The electronic wavefunction is still a highly complicated object, as it is a function in a $4n$ dimensional space (three spatial ($\mathbf{x}_a$) and one (binary) spin coordinate ($\sigma_a = \alpha, \beta$) per electron, i.e., $\mathbf{r}_a = \mathbf{x}_a\sigma_a \in \left\{\mathbf{x}_a^\alpha, \mathbf{x}_a^\beta\right\}$), which has to fulfill numerous conditions and constraints due to the singularities in the Hamiltonian. In addition, $|\Psi_e\rangle$ has to account for the fermionic nature of electrons, i.e., the Pauli principle and the resulting antisymmetry relation [12]

$$\Psi_e(\mathbf{r}_1, ..., \mathbf{r}_i, \mathbf{r}_j, ...\mathbf{r}_n) = -\Psi_e(\mathbf{r}_1, ..., \mathbf{r}_j, \mathbf{r}_i, ...\mathbf{r}_n). \tag{1.6}$$

In fact, there is no closed analytic solution for the partial differential equation (1.5) for general two- (or more) electron problems.

However, within a given basis of one-electron functions $\{\phi_i\}$ (e.g., atomic or molecular orbitals (AOs, MOs) [13]) of size k, which in principle can be made complete, we can construct a complete basis of many-electron functions $\{\Phi_I\}$ in terms of their (normalized) antisymmetrized products, e.g.,

$$\begin{aligned}
\Phi_{p,q,...,t}(\mathbf{r}_a) &= \mathcal{N}\hat{A}_a \prod_{i=p}^{t} \phi_i(\mathbf{r}_a) \\
&= \frac{1}{\sqrt{n!}} \det\left[\phi_p(\mathbf{r}_1)\phi_q(\mathbf{r}_2)...\phi_t(\mathbf{r}_n)\right] \\
&\equiv \left|\phi_p\phi_q...\phi_t\right|. \qquad (1.7)
\end{aligned}$$

This determinant based wavefunction ansatz [14, 15] naturally incorporates the correct antisymmetry with respect to exchange of like spin electron pairs in eqn. (1.6). The set of all possible Slater determinants $\{\Phi_I\}$ built from n elements of $\{\phi_i\}$ spans the complete space of n-electron functions. The exact solution of the

[3] On the PES, we can solve for $|\Psi_N\rangle$. In this thesis, we will only be concerned with the solution of eqn. (1.5), and will for simplicity drop indices, i.e., we will write $\hat{H}$ instead of $\hat{H}_{BO}$ and $|\Psi\rangle$ for $|\Psi_e\rangle$.

Schrödinger equation in the basis of all Slater determinants is called the *full configuration interaction* ansatz (FCI; in the physics literature often called '*exact diagonalization*' [16]) with

$$|\Psi\rangle = \sum_I C^I |\Phi_I\rangle \,. \tag{1.8}$$

However, the Hilbert space $\mathcal{H}$ of this ansatz grows factorially as

$$\begin{aligned} \dim(\mathcal{H}) &= \dim\left(\{\Phi_I\}\right) \\ &= \binom{k_\alpha}{n_\alpha}\binom{k_\beta}{n_\beta} \\ &= \frac{k_\alpha! k_\beta!}{n_\alpha! n_\beta! \left(k_\alpha - n_\alpha\right)! \left(k_\beta - n_\beta\right)!} \end{aligned} \tag{1.9}$$

(neglecting symmetry), with k_α and k_β the number of α and β one-particle basis functions, respectively, and n_α and n_β the number of α and β electrons (commonly, $k \sim const \times n$). The FCI coefficient tensor C^I is consequently a very high dimensional object. This unfavorable scaling renders the FCI approach fundamentally unfeasible for all but the simplest few-particle systems in small basis sets without hope for notable progress, e.g., by larger computational setups [17]. The current technical limit is reached for systems with about 16 electrons in 16 orbitals, or a maximum Hilbert space of about 10^9 Slater determinants [18, 19] (also called '*(electron) configurations*' or '*references*'[4]). Beyond this point, the FCI expansion cannot be stored and its eigenvalue problem cannot be solved on a (classical) computer any more [22].

[4] We omit a discussion of 'configuration state functions' [20, 21].

1.1.2 General motives of quantum chemistry

Quantum chemistry is concerned with the search for approximations to this hard quantum many-body problem [23, 24, 25, 26, 27] in order to make it tractable while at the same time preserving a good description of its inherent physics. The goal is to simplify the wavefunction of a system without losing the important information it carries. General themes in this effort are the reduction of the Hilbert space $\{\Phi_I\}$ by truncation[5] (e.g., within an excitation order hierarchy), or the approximation of C^I (or parts of it; e.g., within a (resummed) perturbative approach [29]) without its explicit representation[6]. While this may not be possible in the most general cases, in which the complexity of a system cannot be overcome, quantum chemistry has made great progress for many other situations, as chemistry often happens in more special domains. The key for progress is the exploitation of structure in the many-body problem and the resulting wavefunction. The first step in this direction is the identification of different regimes[7], which we will review in the following paragraphs (both from a physical and mathematical perspective).

[5] Ideally, we would like to have a wavefunction expansion, which contains all important basis states (in terms of their coefficient-magnitude and energy contribution), and in which only 'unimportant' configurations are truncated. This selected FCI idea requires in principle an *a priori* knowledge of the FCI solution. In practice, this is bypassed by a perturbative selection [28], which however turns out to be numerically unfavorable.

The renormalization group framework discussed below however can be seen as a well defined path to obtaining such a truncation scheme.

[6] We point out, that by approximating certain parts of C^I or restricting them to zero, all other coefficients are modified.

[7] The '*principle of the conservation of complexity*' [30] is often stated, when it comes to the solution of problems by means of different quantum chemical methods. We wish to point out, that this principle is only valid for the *intrinsic complexity* of a problem, which is not equal to the complexity of its description. Otherwise, every approach to quantum chemistry would have the same accuracy/cost-ratio and there could be no methodological progress. A complicated problem will need an adequately complicated representation, however such a representation will be wasteful for a simple problem.

1.1.3 Noninteracting electron systems and the Hartree-Fock approach

Noninteracting electron systems can be described exactly by a single Slater determinant, which is constructed of n occupied molecular orbitals. This simple wavefunction ansatz is at the heart of Hartree-Fock (HF) theory [23, 24, 25], and the starting point for the single-reference post-Hartree-Fock methods described below. The MOs are optimized with respect to minimizing the energy of the single-determinent wavefunction [31, 32]. This particular set of orbitals parametrizes the HF ansatz

$$\begin{aligned} \left|\Psi^{HF}\right\rangle &= \left|\varphi_1\varphi_2...\varphi_n\right| \\ &\equiv |\Phi_0\rangle\,, \end{aligned} \tag{1.10}$$

and defines the HF reference function $|\Phi_0\rangle$. Note, that $\{\varphi_i\}$ is the canonical representation of the one-electron basis $\{\phi_i\}$, and only one element of the FCI tensor C^I is nonzero in this independent particle model. The HF ansatz divides the one-electron space into an occupied and unoccupied subspace $\{\{\varphi_{occ}\}\,;\{\varphi_{unocc}\}\} = \{\{\varphi_1,...,\varphi_n\}\,;\{\varphi_{n+1},...\varphi_k\}\}$, separated by the Fermi level. The canonical representation $\{\varphi_i\}$ is not unique, since the HF energy is invariant with respect to unitary rotations $\mathbf{T}$ *within* the occupied and unoccupied subspaces, i.e., (in matrix form)

$$\boldsymbol{\chi}_{occ} = \mathbf{T}^{\dagger}_{occ}\boldsymbol{\varphi}_{occ} \tag{1.11}$$

and

$$\boldsymbol{\chi}_{unocc} = \mathbf{T}^{\dagger}_{unocc}\boldsymbol{\varphi}_{unocc}, \tag{1.12}$$

leading to $\{\{\chi_1,...,\chi_n\}\,;\{\chi_{n+1},...\chi_k\}\}$. (The relevance of this property will become clear in Sec. 2.2.) The Hartree-Fock ansatz is thus actually parametrized by the

division of the total one-particle space $\{\phi_i\}$, which is equivalent to the definition of the occupied space spanned by $\{\varphi_1, ..., \varphi_n\}$ (irregardless of any particular representation; see Fig. 1.2).

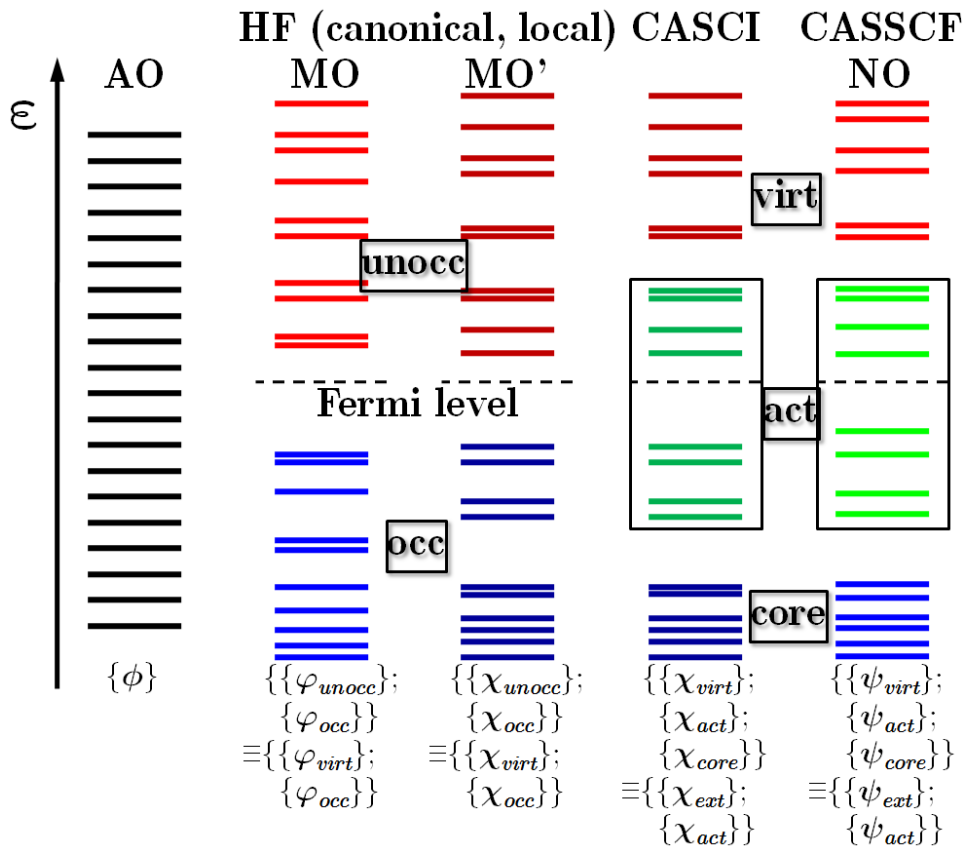

Figure 1.2: Scheme of the different one-electron spaces (from left to right): Total atomic orbital (AO) space $\{\phi\}$; molecular orbital (MO) space from HF-SCF with the occupied and unoccupied subspace division, e.g., in canonical $\{\{\varphi_{occ}\}; \{\varphi_{unocc}\}\}$ or other representation $\{\{\chi_{occ}\}; \{\chi_{unocc}\}\}$ (e.g., localized MOs); separation of the MO space into $\{\{\chi_{core}\}; \{\chi_{act}\}; \{\chi_{virt}\}\}$ ≡ $\{\{\chi_{act}\}; \{\chi_{ext}\}\}$ for CAS methods (e.g., CASCI); reoptimized orbitals $\{\{\psi_{core}\}; \{\psi_{act}\}; \{\psi_{virt}\}\}$ from a CASSCF ansatz.

As each electron 'occupies' an orbital, it moves in the self-consistent, average field of all other electrons without explicit reference to their positions,

and the electronic motions are hence uncorrelated. Mathematically, this can be seen from the underlying product structure of the wavefunction – the *n*-electron function is expressed as a product of *n* one-electron functions – which leads to uncorrelated properties in a probabilistic sense, i.e.,

$$P(\mathbf{r}_i, \mathbf{r}_j) = P(\mathbf{r}_i)P(\mathbf{r}_j). \tag{1.13}$$

Only antisymmetry (sometimes called *Fermi*, *Pauli* or *exchange correlation*) is enforced by the determinantal ansatz: The spatial distribution function for each pair of *like spin* electrons reflects the Pauli principle (eqn. (1.6)) and shows a *Fermi-hole* (see Fig. 1.3) around $r_{ij} = 0$, where

$$\Psi^{HF}(\mathbf{r}_1, ..., \mathbf{r}_i, \mathbf{r}_i, ...\mathbf{r}_n) = 0. \tag{1.14}$$

Note, that generally

$$\Psi^{HF}(\mathbf{r}_1, ..., \mathbf{x}_i^{\alpha}, \mathbf{x}_i^{\beta}, ...\mathbf{r}_n) \neq 0. \tag{1.15}$$

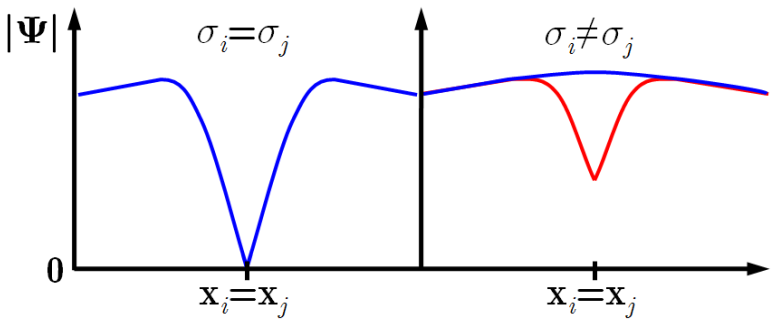

Figure 1.3: Features of $\Psi(\mathbf{r}_1, ...\mathbf{r}_i, \mathbf{r}_j, ..., \mathbf{r}_n)$ for $\mathbf{x}_i = \mathbf{x}_j$: left: parallel spin ($\sigma_i = \sigma_j$) leads to the Fermi hole; right: in case of antiparallel spin ($\sigma_i \neq \sigma_j$), a mean-field wavefunction (blue) shows no particular structure, while a correlated wavefunction (red) displays a Coulomb cusp.

Coulomb correlation due to the singularity in the interelectronic potential $\hat{V}_{ee}$ is not accounted for (however, this is of no concern in noninteracting systems). The Hamiltonian (eqn. 1.3) in HF theory simplifies to

$$\hat{H}^{HF}(\mathbf{r};\mathbf{R}) = \hat{T}_e(\mathbf{r}) + \hat{v}_{ee}^{eff}(\mathbf{r}) + \hat{V}_{eN}(\mathbf{r};\mathbf{R}) + V_{NN}(\mathbf{R}), \tag{1.16}$$

where the effective, averaged interaction potential $\hat{v}_{ee}^{eff}$ replaces the explicit $\hat{V}_{ee}$. The n-electron problem is reduced to a one-electron problem in a mean-field sense. The cost of Hartree-Fock theory scales as $O(k^4)$ which comes from the evaluation of the two-electron Hamiltonian integrals, and can be reduced to $O(k^3)$ or less in large systems using direct techniques and density matrix formulations [24].

1.1.4 Definition of correlation energy

In interacting electron systems, the motions of all particles are correlated, i.e.,

$$\begin{aligned} P(\mathbf{r}_i,\mathbf{r}_j) &= P(\mathbf{r}_i)P(\mathbf{r}_j) + \Gamma(\mathbf{r}_i,\mathbf{r}_j) \\ &\neq P(\mathbf{r}_i)P(\mathbf{r}_j). \end{aligned} \tag{1.17}$$

Löwdin [33] introduced the following definition for the (Coulomb) *correlation energy* E_{corr}, associated with the shortcoming of the independent particle model when applied to interacting systems:

$$E_{corr} = E_{exact} - E^{HF}. \tag{1.18}$$

Note, that the Hartree-Fock energy E^{HF} strictly refers to the Hartree-Fock limit, i.e., the situation in the complete basis set (CBS) limit. However, eqn. 1.18 is also used within incomplete one-particle spaces, and we identify $E_{exact} = E^{FCI}$

(again, E_{exact} refers to the exact, nonrelativistic energy in the BO approximation, eqn. (1.5); see Fig. 1.4).

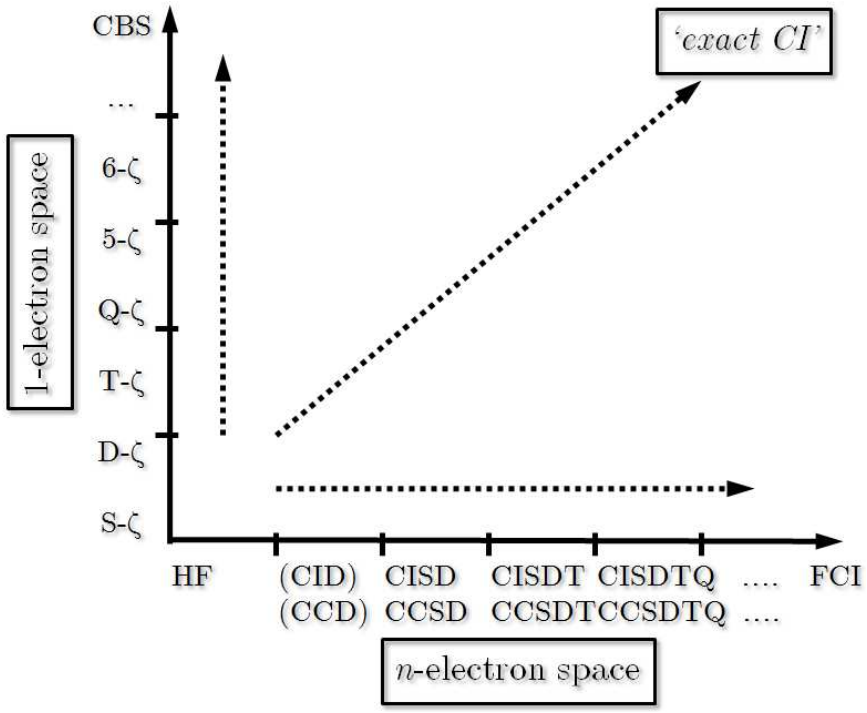

Figure 1.4: The hierarchy in the 1- and *n*-electron spaces, their convergence to the CBS and FCI limit, and their combined approach to the 'exact CI' solution (cf. [24]). Note, that the rate of convergence is generally not linear, but faster (e.g., CCSDT usually accounts for > 99% of the correlation energy).

The mean-field HF approximation typically accounts for more than 99% of the total energy. However, since we are usually interested in energy differences (e.g., comparing different species, alternative structures of the same species, or fragments along a reaction coordinate), the remaining fraction due to electron correlation is actually often decisive.

1.1.5 Weakly interacting systems, dynamic correlation, and single-reference post-HF methods

In weakly interacting systems the instantaneous, short-ranged repulsions of two electrons coming close together introduce a cusp in their spatial distribution[8] (see Fig. 1.3), which cannot be reproduced by a single Slater determinant. As the electrons do not avoid each other in the HF approach, the HF energy shows a penalty for this behavior – the correlation energy[9]. On other length scales, the HF wavefunction gives a reasonable representation of the true wavefunction. This *dynamic correlation* can be accounted for by correcting the predominant electron configuration with small contributions of (usually many) other configurations (see Fig. 1.5), typically associated with excitations from valence degrees of freedom into the many non-bonding orbitals[10]. The multiple weak excitations are responsible for establishing the detailed, quantitative structure of the electronic wavefunction.

Since these fluctuations with respect to the a mean-field reference $|\Phi_0\rangle$ require only a quantitative correction of the HF zeroth-order wavefunction, they can efficiently be described by methods such as restricted configuration in-

[8]The Coulomb cusp is foremost relevant for electron pairs with antiparallel spin, since the mean-field distribution function has no particular structure in this place (cf. eqn. (1.15)). While electron pairs with parallel spin already show the Fermi hole (cf. eqn. (1.14)), Coulomb correlation can still introduce an additional modification of its shape as both effects overlap.

[9]To be precise, the penalty is the correlation energy with opposite sign.

[10]Note, that the convergence of the dynamic correlation energy with basis set size is very poor, since the representation of the electron cusp in terms of excited determinants is very inefficient. The use of large basis sets increases the cost of correlation methods dramatically. Schemes for the extrapolation towards the complete basis set limit have been devised, however they already require an expensive set of calculations with successively increased basis set size.

A more modern approach is the use of an explicit correlation function, like Jastrow factors [34] in Quantum Monte Carlo (QMC) [35] methods or R12/F12 techniques in more conventional methods. We omit a detailed discussion of this important development and refer to the excellent reviews in Ref. [36].

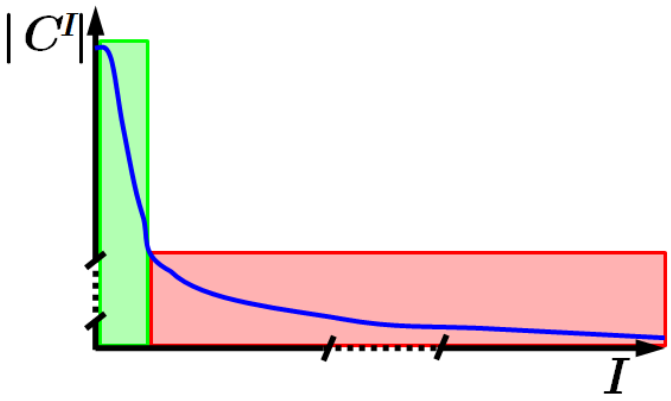

Figure 1.5: Sketch of the sorted configurations $|\Phi_I\rangle$ and their weights C^I of a wavefunctions expansion. The green box represents the static correlation problem with a moderate number of determinants of large weight, and the red box covers the large number of remaining determinants with small coefficient, which are responsible for the dynamic correlation.

teraction theory (CI), coupled cluster theory (CC) [37], or perturbation theory (associated with the acronyms PT, RSPT, MBPT, MP) [38] which are constructed accordingly. The cornerstone of these single-reference post-Hartree-Fock methods is the excitation hierarchy paradigm: the FCI space $\{\Phi_I\}$ can be structured in terms of successive substitution order with respect to $|\Phi_0\rangle$, i.e., $\{\Phi_0; \Phi_a^p, \Phi_a^q, ...; \Phi_{ab}^{pq}, \Phi_{ab}^{pr}, ...; \Phi_{abc}^{pqr}, \Phi_{abc}^{pqs}, ...; \Phi_{abcd}^{pqrs}, ...\}$[11], with Φ_a^p corresponding to all single (S) substitutions/excitations from the occupied orbitals a into the unoccupied orbitals p, Φ_{ab}^{pq} corresponding to all doubly (D) excited determinants, Φ_{abc}^{pqr} to triple (T) substitutions, and so forth (see Fig. 1.6). In weakly interacting systems, the importance of multiple substituted determinants should decay quickly. A truncation after a certain excitation order in this hierarchy is introduced and systematic improvement is possible by successive inclusion of higher orders. With each considered excitation order, the covered fraction of the Hilbert

[11] From this point on we will use second quantization notation for convenience [24, 25, 26, 37].

space $\{\Phi_I\}$ grows dramatically – as does the associated cost.

In configuration interaction theory, we employ the ansatz

$$\left|\Psi^{CI}\right\rangle = (1 + \hat{C})\,|\Phi_0\rangle \tag{1.19}$$

with

$$\begin{aligned}
\hat{C} &= \hat{C}^S + \hat{C}^D + \hat{C}^T + \hat{C}^Q + ..., && (1.20)\\
\hat{C}^S &= \sum_{a,p} c_a^p \hat{a}_p^\dagger \hat{a}_a, && (1.21)\\
\hat{C}^D &= \sum_{a>b,p>q} c_{ab}^{pq} \hat{a}_p^\dagger \hat{a}_q^\dagger \hat{a}_b \hat{a}_a, && (1.22)
\end{aligned}$$

etc., and arrive, e.g., at the CISD level

$$\begin{aligned}
\left|\Psi^{CISD}\right\rangle &= (1 + \hat{C}^S + \hat{C}^D)\,|\Phi_0\rangle \\
&= |\Phi_0\rangle + c_a^p \left|\Phi_a^p\right\rangle + c_a^q \left|\Phi_a^q\right\rangle + ... + c_{ab}^{pq} \left|\Phi_{ab}^{pq}\right\rangle + c_{ab}^{pr} \left|\Phi_{ab}^{pr}\right\rangle + ... \qquad (1.23)
\end{aligned}$$

We diagonalize the Hamiltonian from eqn. (1.3), written in second quantization as

$$\hat{H} = \sum_{i,j} t_{ij}^\dagger \hat{a}_j \hat{a}_j + \sum_{i,j,k,l} v_{ijkl} \hat{a}_i^\dagger \hat{a}_j^\dagger \hat{a}_k \hat{a}_l, \tag{1.24}$$

in the n-body space spanned by the CISD wavefunction and obtain the coefficients $c_a^p, c_a^q, ..., c_{ab}^{pq}, c_{ab}^{pr}, ...$ of the considered subset of C^I, all other coefficients are set to zero by construction.

In coupled cluster theory, we use the ansatz

$$\left|\Psi^{CC}\right\rangle = \exp\left[\hat{T}\right]|\Phi_0\rangle \tag{1.25}$$

with

$$\begin{aligned}
\hat{T} &= \hat{T}^S + \hat{T}^D + \hat{T}^T + \hat{T}^Q + ..., && (1.26)\\
\hat{T}^S &= \sum_{a,p} t_a^p \hat{a}_p^\dagger \hat{a}_a, && (1.27)\\
\hat{T}^D &= \sum_{a>b,p>q} t_{ab}^{pq} \hat{a}_p^\dagger \hat{a}_q^\dagger \hat{a}_b \hat{a}_a, && (1.28)
\end{aligned}$$

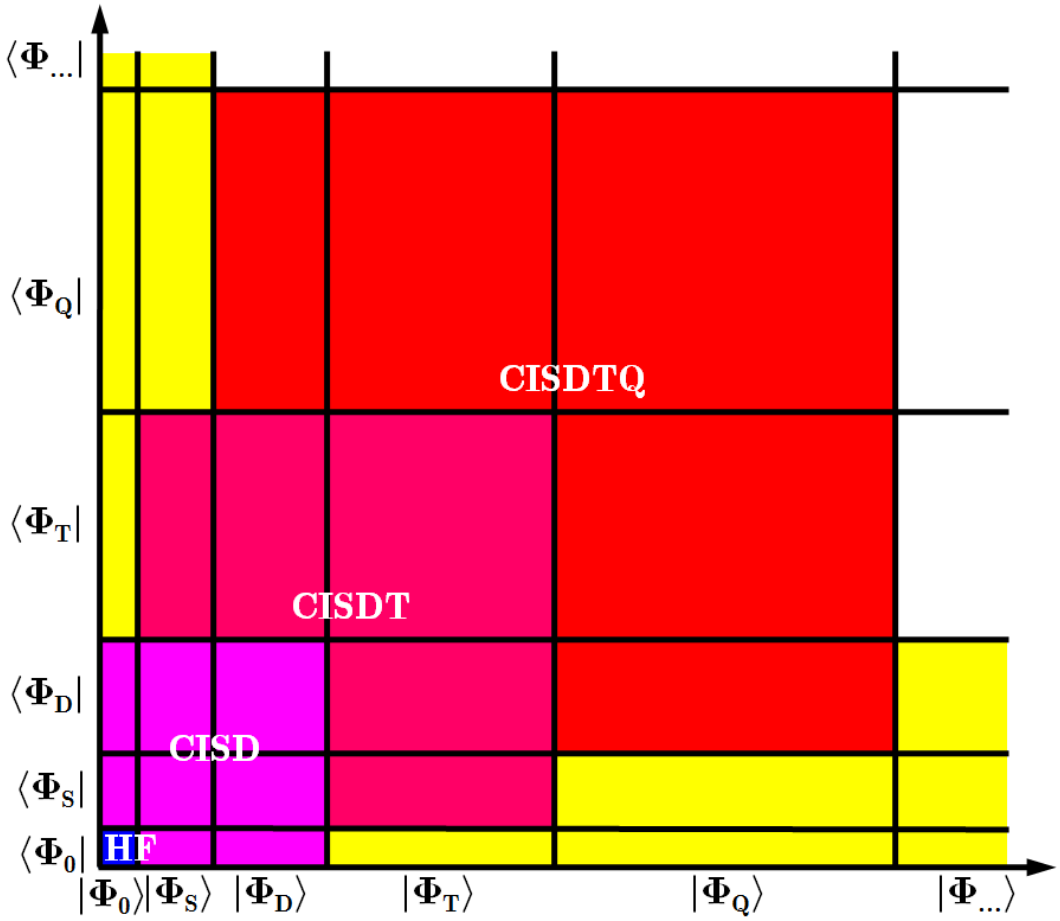

Figure 1.6: Hierarchy of the CI expansion reference space with single,double, triple, quadruple,... excited determinants and the corresponding Hamiltonian blocks. Yellow areas are zero, since $\hat{H}$ cannot connect determinants, which differ by more than two substitutions (Slater-Condon rules [15, 39]). CIS (i.e., a configuration interaction ansatz with only the HF reference and singly substituted determinants) does not constitute a ground state method, since the single-excitations are the linear terms of an orbital rotation, but as the MOs of $|\Phi_0\rangle$ are already optimal, they do not lead to an improvement (Brillouin's theorem). CIS is however a classic excited states ansatz.

etc., and arrive, e.g., at the CCSD level

$$\begin{aligned}
\left|\Psi^{CCSD}\right\rangle &= \exp\left[\hat{T}^S + \hat{T}^D\right]|\Phi_0\rangle \\
&= (1 + \hat{T}^S + \frac{1}{2!}(\hat{T}^S)^2 + \frac{1}{3!}(\hat{T}^S)^3 + ... + \hat{T}^D + \frac{1}{2!}(\hat{T}^D)^2 + ... \\
&\quad + \hat{T}^S\hat{T}^D + \frac{1}{2!}(\hat{T}^S)^2\hat{T}^D + ...)|\Phi_0\rangle \\
&= (1 + \hat{T}^S + \frac{1}{2}(\hat{T}^S)^2 + \hat{T}^D + \frac{1}{6}(\hat{T}^S)^3 + \hat{T}^S\hat{T}^D \\
&\quad + \frac{1}{2}(\hat{T}^D)^2 + \frac{1}{2!}(\hat{T}^S)^2\hat{T}^D + ...)|\Phi_0\rangle \\
&= |\Phi_0\rangle + t_a^p\left|\Phi_a^p\right\rangle + t_a^q\left|\Phi_a^q\right\rangle + ... + \left(\frac{1}{2}t_a^p t_b^q + t_{ab}^{pq} + ...\right)\left|\Phi_{ab}^{pq}\right\rangle + ... \\
&\quad + \left(\frac{1}{6}t_a^p t_b^q t_c^r + \frac{1}{2}t_a^p t_{bc}^{qr} + ...\right)\left|\Phi_{abc}^{pqr}\right\rangle + ...
\end{aligned} \tag{1.29}$$

With the untruncated $\hat{C}$ and $\hat{T}$ operators, both configuration interaction and coupled cluster theory approach the FCI solution. While finite order CI simply truncates the Hilbert space $\{\Phi_I\}$, finite order CC constitutes a more sophisticated approximation: By virtue of the ansatz (1.25), each higher order coefficient in C^I is constructed from contributions of different order, since, e.g.,

$$\hat{C}^Q \approx \hat{T}^Q + \hat{T}^S\hat{T}^T + \frac{1}{2!}(\hat{T}^D)^2 + \frac{1}{2!}(\hat{T}^S)^2\hat{T}^D + \frac{1}{4!}(\hat{T}^S)^4, \tag{1.30}$$

such that even with truncated $\hat{T}$, we can account for the contributions of lower order product terms up to infinite order, formally arriving at an approximation for the full, untruncated C^I (e.g., in CCSD we still recover the last three terms of the quadruple expression in eqn. (1.30)). The size of C^I is of no concern (e.g., in terms of storage on a computer), since CC theory never requires its explicit representation. A detailed discussion of the meaning of the coupled cluster ansatz (e.g., from a diagrammatic perspective [25, 26, 37]) is beyond the scope of this introduction. We will however discuss certain implications of this ansatz in Sec. 1.1.7.

Table 1.1: Traditional computational scaling of density functional theory (DFT), Møller-Plesset perturbation theory (MPn), configuration interaction theory (CI), and coupled cluster theory (CC) of different order with the number of orbitals k.

DFT		MPn		CI		CC	
type	cost	order	cost	order	cost	order	cost
LDA,GGA	$\mathcal{O}\left(k^3\right)$	2	$\mathcal{O}\left(k^5\right)$	SD	$\mathcal{O}\left(k^6\right)$	SD	$\mathcal{O}\left(k^6\right)$
hybrid	$\mathcal{O}\left(k^4\right)$	3	$\mathcal{O}\left(k^6\right)$	SDT	$\mathcal{O}\left(k^8\right)$	SDT	$\mathcal{O}\left(k^8\right)$
double-hybrid	$\mathcal{O}\left(k^5\right)$	4	$\mathcal{O}\left(k^7\right)$	SDTQ	$\mathcal{O}\left(k^{10}\right)$	SDTQ	$\mathcal{O}\left(k^{10}\right)$

Perturbation theory is in principle based on a restricted CI-type expansion, and we formally approximate the nonzero parts of C^I through perturbative arguments. As this is in practice unnecessary for lower order PT, its applicability as a single-reference post-HF method for the dynamic correlation problem is better gauged from a perturbative argument: For PT to work, $|\Phi_0\rangle$ is required to be a good, qualitatively correct zeroth-order approximation to $|\Psi\rangle$ – which is exactly the regime in weakly interacting problems.

Density functional theory (DFT) [40] is a completely different approach to the electron correlation problem. In practice it usually works best in dynamic correlation situations. As our discussion is focussed on wavefunction theories, we will omit a discussion of DFT in this context.

The computational scaling of the presented dynamic correlation methods[12] can be found in Tab. 1.1.

[12]Note, that the actual cost scaling can very much depend on the system, ratio n to k, and employed algorithm.

1.1.6 Strongly interacting systems, static correlation, and multi-reference methods

Static (or '*nondynamic*') *correlation* in contrast refers to the situation in strongly interacting systems where the electronic structure requires multiple reference functions of comparable weight to establish the qualitative features of the chemical bonding situation. This long-range effect is associated with the correlation of electrons in nearly degenerate valence orbitals and occurs regularly in, e.g., bond breaking, transition metal chemistry, low-dimensional conjugated systems, excited states, and (near-) degeneracy problems. Physically, this effect is founded in the delicate balance in the valence degrees of freedom between the kinetic energy, which favours delocalization, and the Coulomb energy, which favours localization. This results in competing electronic configurations and the correct electronic structure contains contributions from multiple determinants with significant coefficients. Single-reference methods are prone to catastrophic failure in these cases, since they cannot recover the correct qualitative structure of the wavefunction (cf. perturbation theory argument from previous section). The excitation hierarchy paradigm cannot be applied in these cases.

At the heart of current static correlation methods is the complete active space (CAS) approach, in which a subspace of strongly correlated orbitals $\{\varphi_i^{act}\}$ is identified $\{\{\varphi^{occ}\};\{\varphi^{unocc}\}\} \longrightarrow \{\{\varphi^{core}\};\{\varphi^{act}\};\{\varphi^{virt}\}\}$ (see Fig. 1.2) and the many-body space it spans $\{\Phi_I^{act}\}$ is solved with brute-force FCI techniques: Complete active space self-consistent-field (CASSCF) theories [41] or the more general multi-configuration self-consistent-field (MCSCF) ansatz correctly describe this type of electronic structure by expanding the wavefunction in the complete space of the optimized valence (or 'active') degrees of freedom, but do so at the cost of

a factorial scaling with the number of active electrons (due to the FCI kernel). In practice, an incomplete set of valence orbitals has to be selected for the active space – usually on the basis of energy considerations or chemical intuition – and it cannot be extended when going to larger systems (e.g., with more polymer units). For many interesting applications the feasible active spaces give an insufficient representation of the static correlation problem. A correct description in large systems is generally very difficult to obtain. Despite the impressive progress in local generalized valence bond and coupled cluster (CC) theories (e.g., [42, 43, 44, 45, 46, 47, 48, 49, 50, 51, 52, 53, 54]) which provide some capacity to break, e.g., single bonds, such approaches do not possess the flexibility of a true multi-reference theory. The fundamental challenge therefore remains to find a multi-reference electronic structure method that is sufficiently flexible to correctly describe static correlation, yet which exhibits a nonfactorial scaling, and can thus be applied to large systems.

Note, that the distinction between dynamic and static electron correlation is a convenient conceptual one, rather than rigorously founded. We find a smooth transition between both regimes in realistic situations[13]. As will become evident in the second part of this thesis, both types of electron correlation – static and dynamic – commonly occur at the same time, and the overlap of these regimes usually leads to challenging problems for computational electronic structure methods. Multi-reference version of the dynamic correlation methods described in the previous section have been devised, e.g., MRPT/CASPTn [55, 56, 57, 58, 59, 60] , MRCI, MRCC, and the canonical transformation theory (CT) [61, 62, 63, 64, 65] . The Hartree-Fock reference $|\Phi_0\rangle$ from the single-

[13]Note for example, that in the CASSCF solution for the static correlation in the active space, most determinants will actually have small coefficients and by definition contribute to the dynamic correlation energy.

reference version is replaced with $\left|\Phi_0^{MR}\right\rangle$, which in practice often corresponds to $\left|\Phi_0^{CAS}\right\rangle$. The dynamic correlation procedure is performed *on-top* of the multi-reference static correlation approach for the active space. Note however, that the application of these methods is both complicated and expensive. In particular the appealing MRCC is still in a prototype stage due to theoretical and technical problems.

1.1.7 Size-consistency, size-extensivity, and variational bounds

At this point we will introduce two important aspects in the treatment of electron correlation, i.e., *size-consistency* and *size-extensivity*. While these terms are often used interchangeably in the literature, they both have distinct definitions, which we will review for clarification [37]. Both are concerned with the issue, in how far a certain wavefunction ansatz (and the method based on it) gives a balanced account of correlation contributions.

The term *size-consistency* (or *strict separability*) was originally introduced by Pople in 1973 [66] and refers to the question, whether a method gives a consistent result for two independent, non-interacting molecules (i.e., the intramolecular interactions are correlated, but there is no intermolecular interaction), when described in one calculation with both molecules *or* two separate calculations for each molecule[14]. Since the molecules are non-interacting, the result of both approaches should clearly be the same. Nonetheless, this is not a given for all wavefunctions. The capability of yielding size-consistent results is obviously a desirable feature and a hallmark of a well designed theory. It can be traced

[14]We omit a discussion of the basis set superposition error (BSSE)– an artifact due to the incompleteness of the one-electron basis – which can interfere with the size-consistency question.

back to *multiplicative separability* of the wavefunction, with respect to the two molecules A and B under consideration, i.e.,

$$\left|\Psi_{A,B}\right\rangle = |\Psi_A\rangle \otimes |\Psi_B\rangle \tag{1.31}$$

and

$$E_{A,B} = E_A + E_B. \tag{1.32}$$

A comparison of the coupled cluster and configuration interaction wavefunctions (eqns. (1.19) and (1.25)) is very instructional in this context:

$$\begin{aligned}
\left|\Psi_A^{CI}\right\rangle &= \left(1 + \hat{C}_A\right)\left|\Phi_A^0\right\rangle, && (1.33)\\
\left|\Psi_B^{CI}\right\rangle &= \left(1 + \hat{C}_B\right)\left|\Phi_B^0\right\rangle, && (1.34)\\
\left|\Psi_A^{CI}\right\rangle \otimes \left|\Psi_B^{CI}\right\rangle &= \left[\left(1 + \hat{C}_A\right)\left|\Phi_A^0\right\rangle\right] \otimes \left[\left(1 + \hat{C}_B\right)\left|\Phi_B^0\right\rangle\right] \\
&= \left(1 + \hat{C}_A\right)\left(1 + \hat{C}_B\right)\left(\left|\Phi_A^0\right\rangle \otimes \left|\Phi_B^0\right\rangle\right) \\
&= \left(1 + \hat{C}_A + \hat{C}_B + \hat{C}_A\hat{C}_B\right)\left|\Phi_{A,B}^0\right\rangle, && (1.35)
\end{aligned}$$

(assuming that the reference function $\left|\Phi_{A,B}^0\right\rangle$ is separable, which is usually (but not always) the case), while

$$\begin{aligned}
\left|\Psi_{A,B}^{CI}\right\rangle &= \left(1 + \hat{C}_{A,B}\right)\left|\Phi_{A,B}^0\right\rangle \\
&= \left(1 + \hat{C}_A + \hat{C}_B\right)\left|\Phi_{A,B}^0\right\rangle \\
&\neq \left|\Psi_A^{CI}\right\rangle \otimes \left|\Psi_B^{CI}\right\rangle, && (1.36)
\end{aligned}$$

i.e., the crossterms $\hat{C}_A\hat{C}_B$ are missing. Hence

$$E_{A,B}^{CI} \neq E_A^{CI} + E_B^{CI}, \tag{1.37}$$

i.e., CI theory is not size-consistent, with the exception of FCI, which exhausts all possible excitations inclusive $\hat{C}_A\hat{C}_B$.

We compare the CI behavior to the coupled cluster ansatz:

$$\begin{aligned}
\left|\Psi_{A,B}^{CC}\right\rangle &= \exp\left[\hat{T}_{A,B}\right]\left|\Phi_{A,B}^{0}\right\rangle \\
&= \exp\left[\hat{T}_{A}+\hat{T}_{B}\right]\left(\left|\Phi_{A}^{0}\right\rangle\otimes\left|\Phi_{B}^{0}\right\rangle\right) \\
&= \exp\left[\hat{T}_{A}\right]\exp\left[\hat{T}_{B}\right]\left(\left|\Phi_{A}^{0}\right\rangle\otimes\left|\Phi_{B}^{0}\right\rangle\right) \\
&= \left(\exp\left[\hat{T}_{A}\right]\left|\Phi_{A}^{0}\right\rangle\right)\otimes\left(\exp\left[\hat{T}_{B}\right]\left|\Phi_{B}^{0}\right\rangle\right) \\
&= \left|\Psi_{A}^{CC}\right\rangle\otimes\left|\Psi_{B}^{CC}\right\rangle
\end{aligned} \tag{1.38}$$

with

$$E_{A,B}^{CC} = E_{A}^{CC} + E_{B}^{CC}, \tag{1.39}$$

i.e., CC theory is size consistent, and has a clear advantage over the CI method.

In 1994, Taylor [67] proposed a more restrictive definition of size-consistency, requiring that a size-consistent method not only give the (qualitatively) correct description in the non-interacting limit (i.e., for long separations), but also along the complete potential energy curve.

Size-extensivity is a thermodynamic term and was popularized in the quantum chemistry context by Bartlett in 1981 [29]. It refers to the requirement that in interacting systems, the amount of correlation energy recovered has to scale proportional to system size (i.e., it is extensive, in the same sense of extensivity of thermodynamic properties in the limit of large systems). That means that the relative amount of correlation energy accounted for is independent of system size

$$\lim_{n\longrightarrow\infty}\frac{E_{corr}}{E_{total}} \longrightarrow const. \tag{1.40}$$

Methods which are not size-extensive account for smaller and smaller fractions of the correlation energy (or they increasingly overestimate it) with increasing

system size, such that

$$\lim_{n \longrightarrow \infty} \frac{E_{corr}}{E_{total}} \longrightarrow 0(, \infty). \tag{1.41}$$

We again omit for simplicity the insightful diagrammatic argument, but note that CC theory is size-extensive due to the cluster structure of C^I, while CI theory is not.

While CASSCF methods are in principle size-extensive due to their FCI kernel, they lose this property once the active space cannot be scaled with system size due to prohibitive cost.

Finally we will mention the *variational nature* of results [68]: quantum chemical methods based on a wavefunction ansatz x, which is solved as an expectation value problem

$$\frac{\left\langle \Psi^x \left| \hat{H} \right| \Psi^x \right\rangle}{\langle \Psi^x | \Psi^x \rangle} = E^x \geqslant E_{exact} \tag{1.42}$$

give energies E^x, which are an upper bound to the exact energy E_{exact}. This is not the case for perturbatively obtained energies. Variational bounds are a useful feature which allows the study of convergence towards completeness with an increase in the set of variational parameters in the wavefunction ansatz.

1.1.8 Electron correlation in quasi-one-dimension and the example of organic electronic materials

Quasi-one-dimensional systems constitute a special regime of electron correlation [69, 70, 71, 72, 73]. Many organic electronic materials [74] (e.g., conjugated organic polymers and carbon nanotubes) belong to this class of systems and exhibit unusual interacting electron effects, arising from the one-dimensional

(1D) nature of their conjugated π-backbone [75, 76]. In quasi-1D structures the physics that is familiar from three dimensions is notably modified, as a result of the coupled quasi-1D motions of many electrons (see Fig. 1.7).

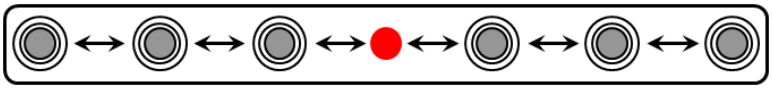

Figure 1.7: Electron correlation in 1D: if the red reference electron moves to the left, it strongly interacts with the neighboring electron, which in turn interacts with all other electrons on the left side in a cascade fashion. The analogue holds true, if the reference electron moves to the right.

As a simple example, in linear polyenes, electron-electron interactions contribute to make the lowest excited singlet state (the 2^1A_g state) one of double-excitation nature, rather than the singly excited highest occupied molecular orbital (HOMO) $\rightarrow$ lowest occupied molecular orbital (LUMO) state as one would expect in a single particle picture [77, 78, 79] (see Fig. 1.8). A more extreme example of this occurs in metallic nanotubes [80, 81] at low temperatures, where the qualitative electronic structure is believed to be of Luttinger liquid form [82, 83, 84]. Luttinger liquids show a low-energy spectrum without singly excited states, but instead, all low-energy excitations are of collective nature. The electronic and optoelectronic properties of these molecules is of great technological interest [85, 86, 87, 88].

As mentioned before quasi-1D systems with strongly interacting electrons as another qualitatively unique electronic structure regime. The inadequacy of the mean-field picture for low-dimensional systems is theoretically well understood by the Ginzburg dimensionality analysis and criterion. The correct description of this unusual electronic situation is challenging, and today's con-

Figure 1.8: Low-energy excitations of the hexatriene molecule: Instead of the 1^1B_u state (corresponding to the HOMO⟶LUMO transition), we find the 2^1A_g state as the lowest excited state.

ventional electronic structure methods face great difficulties, many tend to qualitatively fail. Single-reference ansätze are usually inappropriate and multi-reference methods often cannot cover the relevant active spaces, as the space of interacting orbitals grows with increasing chain length. The conventional FCI solver in CAS approaches hits the wall of factorially scaling cost and there is no progress possible. In practice, calculations on a series of polymers cannot increase the active space, while the valence space grows. Consequently, this leads to an unbalanced description in a series of polymers. While the formal determinantal space is far too large to be treated by conventional methods, we can utilize the compact DMRG ansatz to make progress on the static correlation problem in long molecules.

1.2 Density matrix renormalization group

The density matrix renormalization group (DMRG) is a relatively new method in electronic structure theory. It was introduced by Steven R. White – a former Cornell graduate student – to condensed matter physics in 1992 [89, 90] and together with Richard L. Martin to *ab initio* quantum chemistry in 1999 [91]. The DMRG has enabled the solution of a number of hard electronic structure prob-

lems that were previously intractable with any other technique, in particular complex static correlation problems with active spaces beyond the reach of conventional methods (cf. Sec.1.1.6). The success of DMRG arises from its compact, yet highly flexible wavefunction ansatz, which is uniquely suited and adapted to capture the physics in the static correlation regime [2].

While DMRG has become one of the standard techniques in condensed matter physics, it has not yet – a decade after its introduction – found its way into mainstream computational quantum chemistry. Despite a handful of standalone implementations by development groups (such as the Chan Group), and a number of proof-of-principle applications (some of which will be presented in this thesis), it is not featured in a single program package. This may well be attributed to the complexity of its implementation and its generally unfamiliar theoretical structure, which have led to a number of misconceptions and misunderstandings. Unlike common methods, which introduce electron correlation in the well established excitation order hierarchy (cf. Sec. 1.1.5) or by brute-force (cf. Sec. 1.1.6), DMRG is much closer related to the structured approaches known from tensor networks, entanglement and quantum information theory. DMRG can be seen as the first step of a paradigm shift towards new ways of thinking about and taking on the electron correlation problem.

We will first give an overview over the basic ideas of renormalization group (RG) techniques (Sec. 1.2.1), give a review of Wilson's numerical renormalization group (NRG) ansatz, and analyze its failure for general problems (Sec. 1.2.2). Then we will introduce the DMRG from its original and intuitive algorithmic perspective, and will explicitly go through the steps and linear algebra operations of the renormalization sweeps (Sec. 1.2.3). This part will also address

specific issues arising in the context of its application in quantum chemistry. This is followed by a presentation of the more recent perspective of the matrix product state (MPS) wavefunction ansatz behind the DMRG method (Sec. 1.2.4), which is a valuable addition to the bare algorithmic prescription. It has become apparent that this alternative view on the DMRG can in certain situations be more convenient and powerful than the traditional view. We will emphasize the connection between both – the algorithmic and wavefunction – perspectives for a concise understanding of this method, its features and characteristics. The latter will be summarized in Sec.1.2.5.

1.2.1 Basic ideas of RG techniques

Renormalization group ideas have a long tradition in different areas of physics, in particular in statistical mechanics [92, 93]. Kenneth G. Wilson – at the time a physics professor at Cornell University – used RG ideas as the basis for his theory on critical phenomena and 2nd-order phase transitions, and was awarded the 1982 Nobel Prize in physics for his work [94]. RG approaches are based on the following notion: many physical problems are described by a prohibitively large number of degrees of freedom, which renders them infeasibly complex and intractable (in the quantum chemistry context, this is the number of possible electron configurations in the FCI ansatz, $\dim(\{\Phi_I\})$). In order to make progress, RG techniques successively 'integrate out' degrees of freedom, i.e., the degrees of freedom are 'renormalized'. The renormalization process can be divided into three steps. We start with a focus on a finite set of (in some sense) 'local' degrees of freedom of a subsystem. In the first step (called '*blocking*') we increase the length scale of our focus, i.e., we extend the scope of the subsystem, and the

associated number of degrees of freedom grows quickly. The second step is the '*transformation*' step, in which we transform these original degrees of freedoms into a new representation, which is more compact and problem adapted. In the third step (called '*decimation*') we truncate the number of these new degrees of freedom. Since the problem adapted representation introduces a rapidly converging expansion, the truncation step is well controlled, very efficient, and it averts the excessive growth in complexity. This process can be iterated to longer and longer length scales. Different renormalization group approaches define different transformation and truncation strategies.

We arrive at a description of our original problem within a small number of *effective* degrees of freedom (see Fig. 1.9). The central issue in this coarse graining procedure is that we have to retain an accurate account of all physical properties of interest (e.g., the energy of the system).

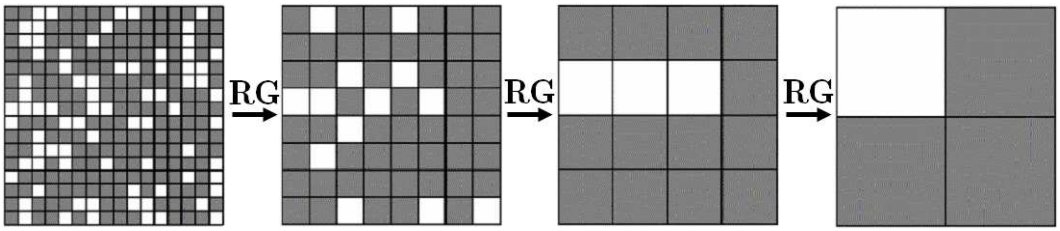

Figure 1.9: Sketch of the successive coarse-graining of the degrees of freedom during the renormalization procedure.

1.2.2 The numerical RG approach

Kenneth Wilson also devised the numerical renormalization group, and he successfully employed it to solve the Kondo problem [95]. The basic idea – and ultimately the fundamental flaw – of the NRG is to use a local energy criterion

in each decimation step, i.e., it uses the assumption that the most important degrees of freedom, i.e., the states not to truncate, are the ones with the lowest energy at each renormalization iteration (we will give a more details in the following section by comparing it to the DMRG). While this idea is intuitively appealing, it has the problem that this truncation is based solely on the energetics of the length scale that is being renormalized. In other words, states which may be energetically important for an isolated, local subsystem, may not be the important ones for the entire system (called 'supersystem'), if the essential couplings are not small, and vice versa. This energetic separation of length scales is given in the Kondo problem, however in many other situations it is not.

1.2.3 The DMRG algorithm

The density matrix renormalization group [96] represents the adaptation of the general RG ideas discussed in Sec. 1.2.1 to electronic structure theory. It is a direct descendant of Wilson's NRG, and its development was based on the analysis of the NRG failure for general systems in the example of the 1D-particle-in-a-box-model [89, 90]. DMRG was originally applied to one-dimensional (1D) spin and lattice problems in condensed matter physics, using simple model Hamiltonians such as the Hubbard Hamiltonian [97], the Heisenberg Hamiltonian, the Ising Hamiltonian and $t - J$ Hamiltonian [69]. The relevant Hamiltonian for *ab initio* quantum chemistry is the full electronic Hamiltonian in eqn. (1.3), and we are (usually) interested in molecular problems[15].

[15]Note, that there are also a number of studies within the semiempirical Pariser-Parr-Pople (PPP) hamiltonian [98, 99], which is a traditional non-*ab-initio* quantum chemical ansatz.

Instead of solving for simple model hamiltonians or the *ab initio* hamiltonian, we could in principle also solve for more complicated effective (dressed) hamiltonians from quasiparticle theories.

An instructive approach to DMRG is to go step-by-step through a semi-technical description of the DMRG algorithm for a very simple example – in the following we chose the diatomic nitrogen molecule N_2 in the $2s,2p_x,2p_y,2p_z$ valence active space, i.e., as a (10e,8o) CAS problem – and explain the method, its physical motivation and implications as we proceed.

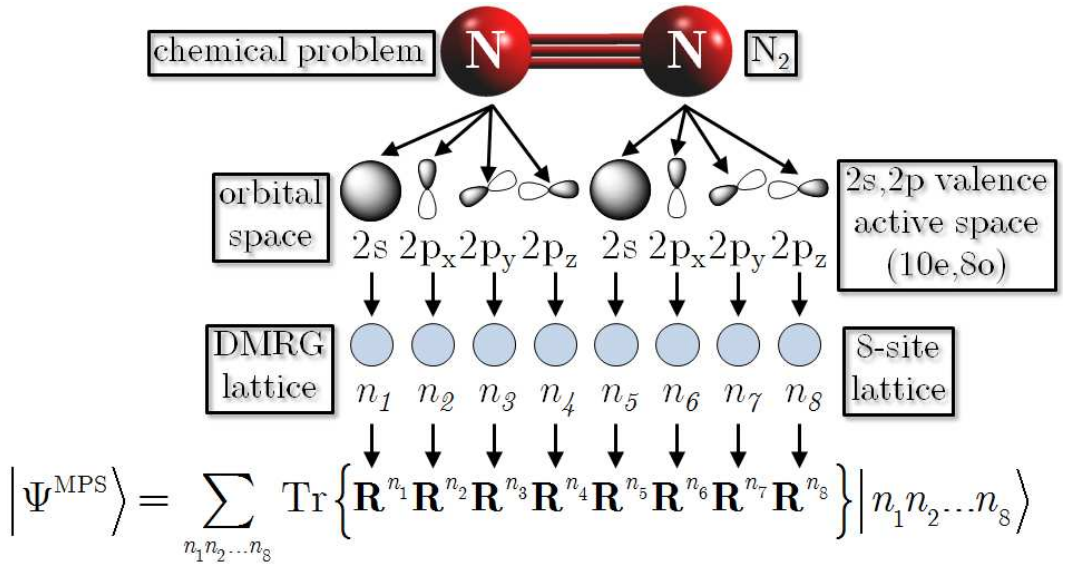

Figure 1.10: DMRG mapping from the chemical problem and its representation in a one-particle space to a 1D DMRG lattice problem with the connection to the MPS wavefunction ansatz.

We begin with the DMRG setup of our molecular problem (Fig. 1.10): We project the eight spatial[16] orbitals $\{\phi_i\}$ of the N_2 onto a one-dimensional array of lattice sites – the 'DMRG lattice' – and by that effectively map the molecular problem onto a 1D lattice problem[17]. For the simplicity of our argument we chose the (orthonormalized) atomic orbital basis (see Sec. 2.3 for a detailed

[16]During this exercise, we will use spatial orbitals for the simplicity of our argument. For the actual implementation, it is beneficial to formally work in a spin orbital basis, so that we will change our description in this respect in the following chapters.

[17]While the motivation for this setup is not apparent at this stage, it will later become apparent from the connection with the MPS wavefunction ansatz.

discussion of the implications of the one-particle representation and its projection/ordering). Each orbital ϕ_i corresponds to one lattice site n_i and is associated with a four-dimensional Fock space $\mathcal{F}(\phi_i) \equiv \mathcal{F}^{n_i} = \{|vac\rangle, |\alpha\rangle, |\beta\rangle, |\alpha\beta\rangle\}^{n_i}$, i.e., with the ith orbital can either be unoccupied, single occupied with spin up, single occupied with spin down, or double occupied. These states are the 'local' degrees of freedom. The Fock space of the total system – the supersystem – is build from the *direct product* of all eight local Fock spaces

$$\mathcal{F}^{sup} \equiv \mathcal{F}(\phi_1\phi_2...\phi_8) = \begin{Bmatrix} |vac\rangle \\ |\alpha\rangle \\ |\beta\rangle \\ |\alpha\beta\rangle \end{Bmatrix}^{n_1} \otimes \begin{Bmatrix} |vac\rangle \\ |\alpha\rangle \\ |\beta\rangle \\ |\alpha\beta\rangle \end{Bmatrix}^{n_2} \otimes ... \otimes \begin{Bmatrix} |vac\rangle \\ |\alpha\rangle \\ |\beta\rangle \\ |\alpha\beta\rangle \end{Bmatrix}^{n_8}, \tag{1.43}$$

and grows exponentially with the number of sites k as $\dim(\mathcal{F}^{sup}) = 4^k$, i.e., in our example $\dim(\mathcal{F}^{sup}) = 4^8 = 65536$. The Hilbert space for the correct number of electrons and spin m_s has only $\dim(\mathcal{H}^{sup}) = 3136$ for this tiny example (cf. eqn. (1.9)), however in a more realistic cc-pVDZ basis [100, 101] (with frozen core), this would grow to $\dim(\mathcal{H}^{sup}) = 4.3 \times 10^9$. For orientation, the mean-fieled reference $\sigma_s^2\sigma_s^{*2}\sigma_{p_z}^2\pi_{p_x}^2\pi_{p_y}^2$ most closely corresponds to states such as $|\alpha\beta\rangle^{n_1} \otimes |\alpha\rangle^{n_2} \otimes |\alpha\rangle^{n_3} \otimes |\alpha\rangle^{n_4} \otimes |\alpha\beta\rangle^{n_5} \otimes |\beta\rangle^{n_6} \otimes |\beta\rangle^{n_7} \otimes |\beta\rangle^{n_8} \equiv 2s_{N1}^2 2p_{z,N1}^{\alpha} 2p_{x,N1}^{\alpha} 2p_{y,N1}^{\alpha} 2s_{N2}^2 2p_{z,N2}^{\beta} 2p_{x,N2}^{\beta} 2p_{y,N2}^{\beta}$ (and its spin-flip permutations) on the DMRG lattice. Again, the goal of the DMRG ansatz is to avoid the unsustainable scaling of the state space.

We now define site 1 as the *system* with space $\mathcal{F}^{sys} \equiv \mathcal{F}^{n_1} = \{|vac\rangle, |\alpha\rangle, |\beta\rangle, |\alpha\beta\rangle\}^{n_1}$, site 2 as the *neighbor* with space $\mathcal{F}^{nei} \equiv \mathcal{F}^{n_2} = \{|vac\rangle, |\alpha\rangle, |\beta\rangle, |\alpha\beta\rangle\}^{n_2}$, and sites 3 to 8 as the *environment* (see Fig. 1.12). *System*, *neighbor* and *environment* together comprise the *supersystem*[18]. We can easily generate the Hamiltonian matrix with the states on site 1, i.e., $\mathbf{H}^{n_1}$, and on site 2, i.e.,

[18] We here describe the 'one-site' algorithm, i.e., we have one neighbour site. The more traditional 'two-site' version has one neighbour site associated with the system and one neighbour

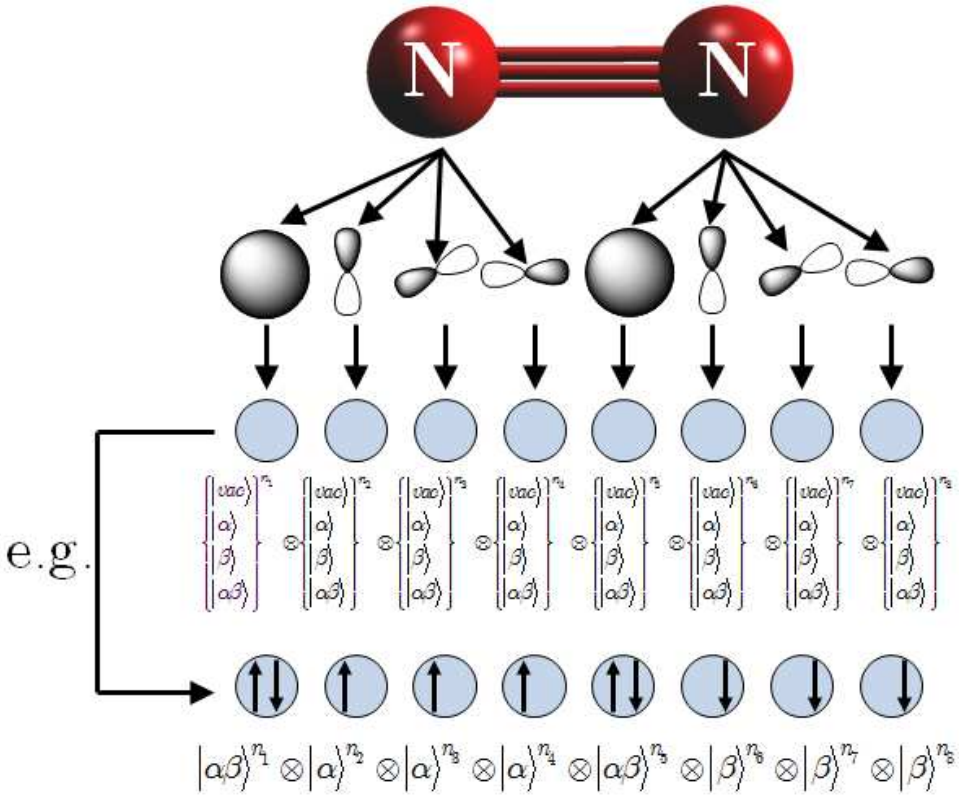

Figure 1.11: Growth of the lattice Fock space and example of low energy state.

$\mathbf{H}^{n_2}$ (again, in the quantum chemistry context we use eqn. 1.24). Now we block the first two sites, i.e., we extend the system to a larger length scale ($sys \otimes n_2 \longrightarrow sys, n_2$), such that $\mathcal{F}^{sys,n_2} = \mathcal{F}^{sys} \otimes \mathcal{F}^{nei} = \mathcal{F}^{n_1} \otimes \mathcal{F}^{n_2}$, $\dim(\mathcal{F}^{sys,n_2}) = 4^2 = 16$, and $\mathbf{H}^{sys,n_2} = \mathbf{H}^{sys} \otimes \mathbf{H}^{nei} = \mathbf{H}^{n_1} \otimes \mathbf{H}^{n_2}$. At this stage, we have still an exact representation of our two-site problem, but we have to introduce a truncation to hold off the growing complexity.

In the NRG approach discussed in the previous section, we proceed ac-

site associated with the environment. The latter approach is more expensive but can be more robust in complicated systems, in which the 'one-site' procedure may fail to converge to the correct minimum. We will remark on this problem towards the end of this section.

Instead of our notation with system, neighbour, environment, and supersystem the corresponding terms *left block*, *site*, *right block* and *superblock* are also frequently used in the literature.

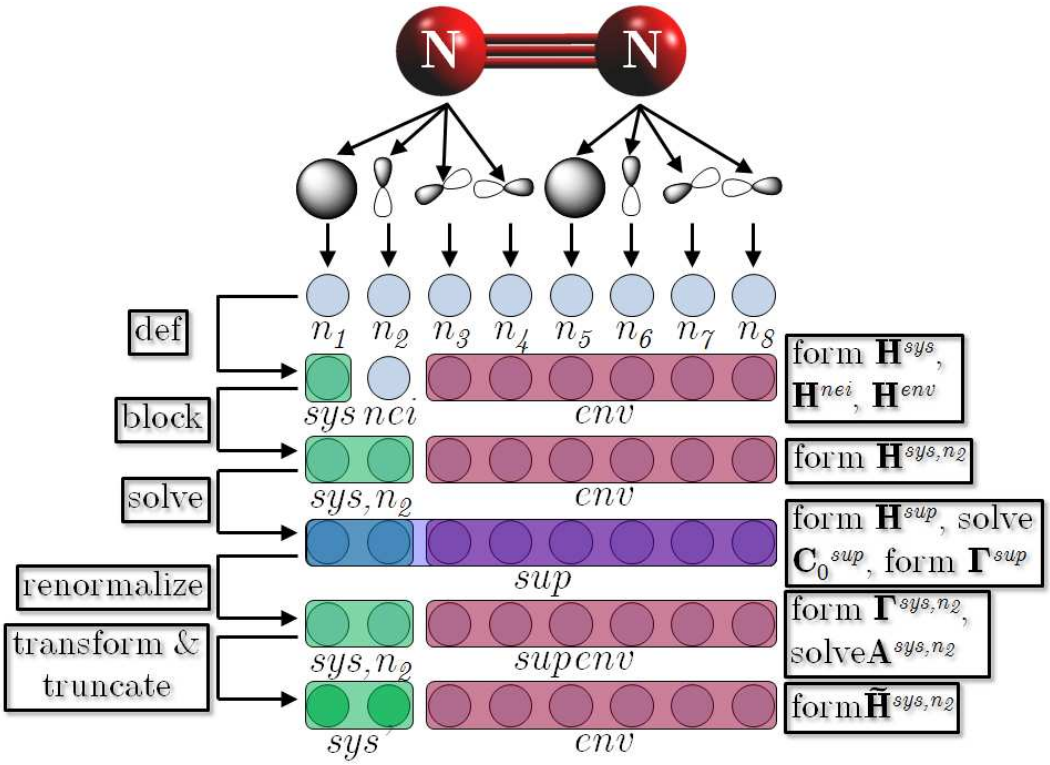

Figure 1.12: The first DMRG iteration, which leads to a renormalization of sites n_1 and n_2.

cording to the following strategy: We diagonalize the extended/blocked system Hamiltonian $\mathbf{H}^{sys'}\mathbf{C}^{sys'} = \mathbf{E}^{sys'}\mathbf{C}^{sys'}$, and obtain its eigenvalues $E_1^{sys,n_2} \leqslant E_2^{sys,n_2} \leqslant ... \leqslant E_M^{sys,n_2} \leqslant ... \leqslant E_{16}^{sys,n_2}$ and eigenstates $\left|\Psi_1^{sys,n_2}\right\rangle, \left|\Psi_2^{sys,n_2}\right\rangle, ..., \left|\Psi_M^{sys,n_2}\right\rangle, ..., \left|\Psi_{16}^{sys,n_2}\right\rangle$. We now retain the M lowest energy eigenvectors (where M is some preset number) of the extended system and discard the higher states $\left|\Psi_{M+1}^{sys,n_2}\right\rangle, ..., \left|\Psi_{16}^{sys,n_2}\right\rangle$[19]. While the lowest eigenstates are obviously the most important states for the isolated extended system itself that is not at all the case once it is embedded in the environment, in particular if system and environment are strongly entangled. Since the truncation does not takes this connection into consideration, it leads

[19]In practice, it is not actually necessary to diagonalize the whole matrix but we can instead utilize a diagonalization scheme like the Davidson [102, 103] or the Lanczos [104] method, which give successively higher roots, and we can stop the procedure after M roots.

to a generally poor performance for the supersystem (see Fig. 1.13).

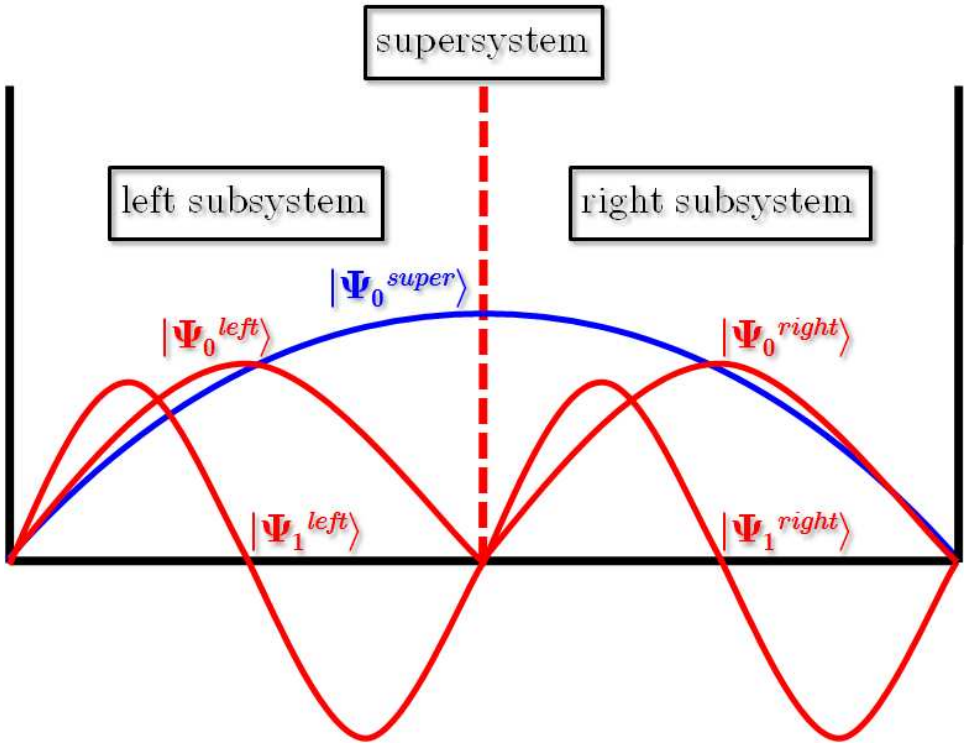

Figure 1.13: A simple particle-in-a-box model shows that the low-energy eigenstates of the left and right subsystem are not a good basis for the expansion of the supersystem ground state (note the boundary condition incompatibility; cf. Ref. [4]).

The DMRG adopts the following approach instead: In addition to $\mathcal{F}^{sys,n_2}$ and $\mathbf{H}^{sys,n_2}$ we generate an approximate representation of the environment, i.e., we pick by some criterion[20] a set of states (say, $\dim(\mathcal{F}^{env}) = 16$ out of the 4096 possible environment states in the example), which are deemed important: $\mathcal{F}^{env} = \{|x\rangle, |y\rangle, |z\rangle, ...\}^{n_3-n_8}$. At this stage in the algorithm, these states are Slater determinants (of variable particle number), and we can build the Hamil-

[20]Criteria for the selection are, e.g., that the environment states can complement the extended system states with respect to the supersystem particle number, spin, and symmetry, and within these constraints may be energetically favorable.

A well design warm–up procedure can substantially improve the DMRG convergence.

tonian matrix $\mathbf{H}^{env}$. We now block the extended system with the environment to get a representation of the entire supersystem[21], i.e., $\mathcal{H}^{sup} = \mathcal{F}^{sys,n_2} \otimes \mathcal{F}^{env}$, $\mathbf{H}^{sup} = \mathbf{H}^{sys,n_2} \otimes \mathbf{H}^{env}$, and $\dim(\mathcal{H}^{sup}) = 16^2 = 256$. Note, that $\mathcal{F}^{sys,n_2}$ was complete and exact, while $\mathcal{F}^{env}$ was incomplete and very approximate, which transfers to $\mathcal{H}^{sup}$. In the blocked $\mathcal{H}^{sup}$ we now perform the DMRG transformation step, i.e., we transform our original degrees of freedom (at this stage still Slater determinants) into a problem adapted representation. For this we first solve for the ground state of $\mathbf{H}^{sup}$ – i.e., we solve the Schrödinger equation for the supersystem in a state space, which is complete in the extended system part, and approximate in the environment part –

$$\begin{aligned} \mathbf{H}^{sup}\mathbf{C}_0^{sup} &= E_0^{sup}\mathbf{C}_0^{sup} \\ \Longleftrightarrow \mathbf{H}^{sup}\left|\Psi^{sup}\right\rangle &= E_0^{sup}\left|\Psi^{sup}\right\rangle, \end{aligned} \tag{1.44}$$

obtain the eigenvector $|\Psi^{sup}\rangle$, and with this build the density matrix

$$\begin{aligned} \mathbf{\Gamma}^{sup} &= \left|\Psi^{sup}\right\rangle\left\langle\Psi^{sup}\right| \\ &= \left(\mathbf{C}_0^{sup}\right)^{\dagger}\mathbf{C}_0^{sup}. \end{aligned} \tag{1.45}$$

We can now obtain the extended system density matrix $\mathbf{\Gamma}^{sys,n_2}$, which is a reduced density matrix of the supersystem, by tracing out the basis states of the environment

$$\begin{aligned} \mathbf{\Gamma}^{sys,n_2} &= \mathrm{Tr}^{env}\mathbf{\Gamma}^{sup} \\ &= \mathrm{Tr}^{env}\left|\Psi^{sup}\right\rangle\left\langle\Psi^{sup}\right|. \end{aligned} \tag{1.46}$$

The physical picture is that of a quantum system embedded in an implicit environment, i.e., the environment information is folded into the system density

[21] Note, that the space for the supersystem has to have the correct particle number and symmetries. For the sake of argument, we assume that $\mathcal{H}^{sup} = \mathcal{F}^{sys,n_2} \otimes \mathcal{F}^{env}$, which is generally not possible. In practice, we choose a larger $\mathcal{F}^{env}$, obain $\mathcal{F}^{sup} = \mathcal{F}^{sys,n_2} \otimes \mathcal{F}^{env}$, and from $\mathcal{F}^{sup}$ we select the appropriate $\mathcal{H}^{sup}$.

matrix $\mathbf{\Gamma}^{sys,n_2}$. We now diagonalize this extended system density matrix $\mathbf{\Gamma}^{sys,n_2}$

$$\mathbf{\Gamma}^{sys,n_2}\mathbf{A}^{sys,n_2} = \mathbf{w}^{sys,n_2}\mathbf{A}^{sys,n_2}, \tag{1.47}$$

and their eigenvectors form the new many-body basis states. Note, that these basis states are not Slater determinants any more, but each basis state is formally an expansion in terms of many Slater determinants, i.e., a more complex object with higher information density. They are associated with a weight corresponding to their importance, i.e., $w_1^{sys,n_2} \geqslant w_2^{sys,n_2} \geqslant ... \geqslant w_M^{sys,n_2} \geqslant ... \geqslant w_{256}^{sys,n_2}$ for $\left|A_1^{sys,n_2}\right\rangle, \left|A_2^{sys,n_2}\right\rangle, ..., \left|A_M^{sys,n_2}\right\rangle, ..., \left|A_{256}^{sys,n_2}\right\rangle$, and we can now introduce a truncation after the M most relevant states of the extended system, which takes its embedding in the environment into account: The retained states represent our renormalized set of degrees of freedoms for the first two sites/orbitals: $\tilde{\mathcal{F}}^{sys,n_2} = \{|A_1\rangle, |A_2\rangle, ..., |A_M\rangle\}^{n_1,n_2}$ with $\dim\left(\tilde{\mathcal{F}}^{sys,n_2}\right) = M$. We point out that this is in a well defined sense the optimal basis for our problem setup (within the approximations introduced by the environment).

There remains an apparent question about the renormalized Hamiltonian matrix $\tilde{\mathbf{H}}^{sys,n_2}$: If each basis state is essentially a complicated FCI-type expansion, then we have not gained anything by truncating the set of transformed states, as we still have to generate and store $\tilde{\mathbf{H}}^{sys,n_2}$ in the full basis of Slater determinants first. The DMRG bypasses this problem by directly rotating the Hamiltonian matrix from its old representation into the renormalized basis by

$$\tilde{\mathbf{H}}^{sys,n_2} = (\mathbf{R}^{n_2})^T \mathbf{H}^{sys,n_2}\mathbf{R}^{n_2}. \tag{1.48}$$

The rotation (or renormalization) matrix $\mathbf{R}$ is rectangular, since it rotates from the larger into the smaller (truncated) basis. It is constructed from the retained M eigenvectors of the extended system density matrix $\mathbf{\Gamma}^{sys,n_2}$, i.e.,

$$\mathbf{R}^{n_2} = \mathbf{A}^{sys,n_2}_{(:,1...n)}. \tag{1.49}$$

The index n_2 shows that this rotation is associated with renormalizing the Fock space at site n_2 in the lattice. We always only keep the numerical representation of the Hamiltonian (and all other operator matrices of interest, e.g., the ones related to certain properties) and keep transforming it in each renormalization iteration. There is neither the need nor generally (due to its size) the possibility to explicitly expand the DMRG basis in terms of the original Slater determinants. This completes the first renormalization iteration.

We now redefine the renormalized extended system (sites 1 and 2) to be the new system, we remove site 3 from the environment, and define it as the new neighbor. It again has $\mathcal{F}^{n_3} \equiv \{|vac\rangle, |\alpha\rangle, |\beta\rangle, |\alpha\beta\rangle\}^{n_3}$ and a simple $\mathbf{H}^{n_3}$. We block and extend the length of our system to site 3, i.e., $\mathcal{F}^{sys,n_3} = \tilde{\mathcal{F}}^{sys,n_2} \otimes \mathcal{F}^{n_3}$, $\dim(\mathcal{F}^{sys,n_3}) = 4M$ (e.g., $M = 4$ for the sake of argument; usually M is chosen substantially larger), and $\mathbf{H}^{sys,n_3} = \tilde{\mathbf{H}}^{sys,n_2} \otimes \mathbf{H}^{n_3}$. We make an approximation for the remaining environment $\mathcal{F}^{env} = \{|x'\rangle, |y'\rangle, |z'\rangle, ...\}^{n_4-n_8}$, and, e.g., $\dim(\mathcal{F}^{env}) = 16$. We then block the extended system with the new environment and obtain $\mathcal{F}^{sup} = \mathcal{F}^{sys,n_3} \otimes \mathcal{F}^{env} = \tilde{\mathcal{F}}^{sys,n_2} \otimes \mathcal{F}^{n_3} \otimes \mathcal{F}^{env}$ and $\mathbf{H}^{sup} = \mathbf{H}^{sys,n_3} \otimes \mathbf{H}^{env}$ (note, that $\mathcal{F}^{n_3}$ is exact, $\tilde{\mathcal{F}}^{sys,n_2}$ contains the approximations and truncation from the first iteration, and $\mathcal{F}^{env}$ is again an *ad hoc* approximation). We renormalize as described above and obtain $\tilde{\mathcal{F}}^{sys,n_3} = \{|B_1\rangle, |B_2\rangle, ..., |B_M\rangle\}^{n_1-n_3}$, and $\tilde{\mathbf{H}}^{sys,n_3} = (\mathbf{R}^{n_3})^T \mathbf{H}^{sys,n_3} \mathbf{R}^{n_3}$ after the second iteration. Note, that $\dim\left(\tilde{\mathcal{F}}^{sys,n_3}\right) = M$, instead of $4^3 = 64$, i.e., we have avoided the exponential scaling of the state space. After the next iteration, we have $\tilde{\mathcal{F}}^{sys,n_4} = \{|C_1\rangle, |C_2\rangle, ..., |C_M\rangle\}^{n_1-n_4}$, $\tilde{\mathbf{H}}^{sys,n_4}$ and we continue in the same fashion, until the entire environment is consumed by the system and we have a completely renormalized representation of the supersystem. We have now finished the first sequence of renormalization iterations – a 'sweep' – through the DMRG lattice.

Let us summarize a couple of key points at this stage: We have successfully restricted $\dim\left(\tilde{\mathcal{H}}\right) = M$, we now work in a new n-electron basis instead of Slater determinants, and we have introduced two sources of error:

1. We have introduces the truncation of $\mathcal{H}$. The associated error ϵ is related to the weight of the truncated reduced density matrix eigenvectors

$$\epsilon = 1 - \sum_{\alpha=1}^{M} w_a. \tag{1.50}$$

   This is a controlled and well defined error due to the physically motivated truncation scheme: We only truncated states beyond M with comparably small weight in the density matrix. We can always decrease this error by increasing M, until we in principle exhaust the complete Hilbert space and obtain FCI results. In practice, this is neither possible (for big systems) nor necessary, as the DMRG basis leads to a rapidly converging wavefunction expansion. Since M is continuously adjustable, we have a direct control over the achieved accuracy (unlike, e.g., in conventional methods, where we have to invoke a complete new class of excitations to improve results, with a dramatic increase of the cost).

2. We had to introduce a rather primitive *ad hoc* approximation for the environment, which obviously inserted an error into the description of our supersystem, and which propagated into our renormalization.

The solution for the second problem is to keep sweeping (see Fig. 1.14): We now start from the other end of the lattice and sweep backwards: We define site 8 as the system with $\mathcal{F}^{sys} = \mathcal{F}^{n_8} = \{|vac\rangle, |\alpha\rangle, |\beta\rangle, |\alpha\beta\rangle\}^{n_8}$ and $\mathbf{H}^{sys} = \mathbf{H}^{n_8}$, block it with site 7 with $\mathcal{F}^{n_7} \equiv \{|vac\rangle, |\alpha\rangle, |\beta\rangle, |\alpha\beta\rangle\}^{n_7}$ and $\mathbf{H}^{n_7}$, and form $\mathcal{F}^{sys,n_7} = \mathcal{F}^{n_7} \otimes \mathcal{F}^{sys}$ and $\mathbf{H}^{sys,n_7} = \mathbf{H}^{n_7} \otimes \mathbf{H}^{sys}$. However, instead of generating the supersystem using

an *ad hoc* guess for the environment, we now use the old system representation from the first sweep, i.e., $\mathcal{F}^{env} = \tilde{\mathcal{F}}^{sys,n_6} = \{|D_1\rangle, |D_2\rangle, ..., |D_M\rangle\}^{n_1-n_6}$, which is a much better approximation to the environment[22]. We proceed in the same fashion during the whole backward sweep and successively improve the description of the environment and supersystem in a series of sweeps. We obtain the energy of the supersystem at each iteration within the sweep (eqn. (1.44)) and have to consider convergence with M and the number of sweeps.

There is one more important technical aspect, which deserves special attention: in particular in the early stages of the algorithm, with crude environment approximations and small M values (which are typically chosen in the beginning), important basis states (e.g., characterized by certain symmetries, etc.) may get truncated, and it may not be possible to recover them in the course of the self-consistent procedure. The consequence is that the algorithm gets stuck in a metastable state. It cannot continue to converge to the true ground state, since important basis states are missing in its expansion. This problem was intensively investigated by Reiher *et al.* in recent years [105, 106]. There is a simple numerical trick to avoid this issue: we add a small amount of a random wavefunction ('noise'), which lives in the complete Fock space without symmetry restrictions, to $|\Psi^{sup}\rangle$ in eqn. (1.45). A more sophisticated alternative is to introduce this noise as system-environment perturbation based on the incompleteness of the environment space [107]. Both lead to a slightly worsened energy, which gets fixed once we fade out the noise after a few sweeps, but most importantly it reconnects these lost states and allows them to be brought back into the expansion. States which entangle the extended system and the environment are particularly important for the convergence, considering a decaying

[22]Note, that according to our notation we should use $\tilde{\mathcal{F}}^{sys,n_6} = \{|E_1\rangle, |E_2\rangle, ..., |E_M\rangle\}^{n_1-n_6}$, but to avoid confusion with the energy, we replaced $|E\rangle \longrightarrow |D\rangle$.

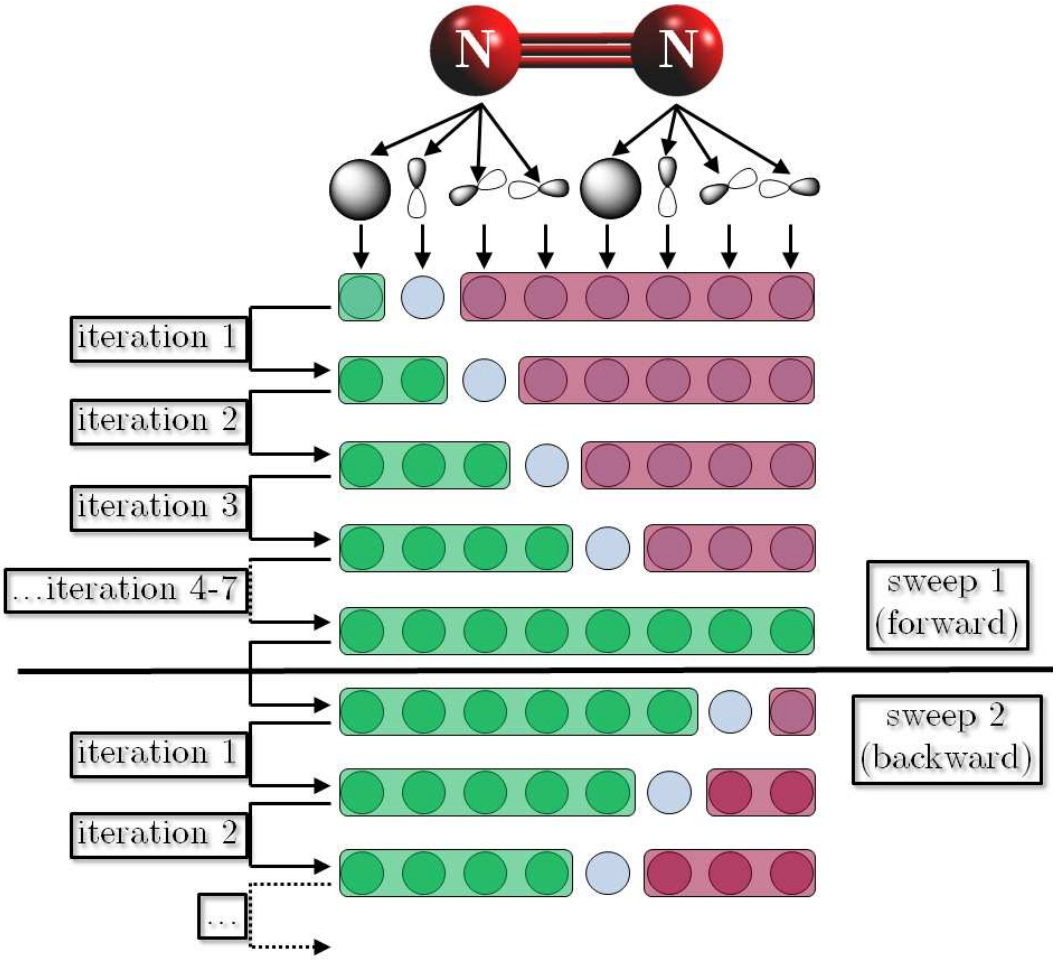

Figure 1.14: The DMRG sweep algorithm introduces the successive renormalization of lattice sites in a series of DMRG iterations. After completion of one sweep, the direction is reversed and we sweep from back ot front (in some expositions, a sweep is defined as the combined forward and backward sweep; due to the change in direction, the *system* and *environment* blocks are often called *left* and *right* blocks to avoid confusion). DMRG sweeps are performed until self-consistency in the DMRG energy is reached.

correlation length. This is the reason for the somewhat more robust behavior of the original 'two-site' version mentioned before, as it allows for a better representation of the boundary states[23].

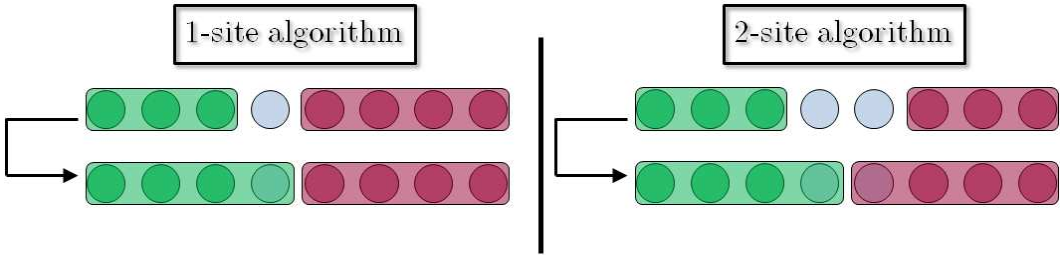

Figure 1.15: Comparison of the one-site and the two-site DMRG algorithm.

This already concludes the prescription for the self-consistent optimization of the DMRG *n*-body basis. While this description of the algorithm appears quite simple, it is worth to note that an efficient and parallel implementation is actually quite challenging, in particular with the full Hamiltonian (i.e., with the entire set of one- and two-electron integrals; cf. eqn. (1.5)). The main technical objective is to organize a suitable decomposition and distribution of the operators and linear algebra.

The work presented in this thesis was based on the BLOCK DMRG-code by Professor Chan, and details of the implementation can be found in Refs. [110, 111, 1]. The other existing quantum chemistry implementations are the very recent one by Yanai – a former post-doctoral researcher in the Chan Group

[23] While the two-site algorithm is more robust, it is also computationally more expensive, since we solve for the supersystem in $16M^2$ instead of $4M^2$ states. The one-site algorithm requires large noise-levels for small M values [107].

Experience however seems to indicate, that after cost-adjustment the one-site algorithm – if applied with caution – shows a superior performance. It in addition has some technical advantages, in particular a well defined wavefunction during all iterations of the sweep, which is, e.g., important when generating reduced density matrices [108, 109].

– and Kurashige at IMS Okazaki (Japan) [112], the code by Zgid – a current post-doctoral researcher in the Chan Group –and Nooijen at the University of Waterloo (Canada) [113, 109, 114], the code by Moritz and Reiher at the ETH Zürich (Switzerland) [105, 115, 106, 116, 117], and older codes by Mitrushenkov *et. al.* [118, 119, 120], Legeza, Röder, Hess [121, 122] and the original code by White *et al*. [91, 123].

The results obtained from the *ab initio* DMRG correspond to the ones we would obtain from standard CASCI/FCI type calculations, which however are infeasible for larger active spaces due to the unfavorable scaling of the FCI engine. As such, DMRG is a static correlation method and can often provide numerically exact or highly accurate results for active spaces of $O(30)$ orbitals. Again, this is made possible by the adapted, optimal many-body basis, which is reference free and hence inherently multi-reference, as well as rapidly convergent. Its complicated, exponential compression of information allows the construction of a polynomially scaling method (for an analysis of the cost scaling of the actual implementation, see Ref. [110, 111, 1] and the following chapter). Corresponding to the ansatz in terms of the 1D DMRG lattice, this method is particularly suited for quasi-one-dimensional problems. Its performance starts to degrade for two- and three-dimensional problems, as well as when dynamic correlation is included. We will more closely investigate this characteristic with respect to these different regimes in Sec. 1.2.4, 1.1.8, and 2.3. There have been attempts to generalize the DMRG idea to higher dimensions, but none has so far been firmly established as a viable route to multi-reference problems in arbitrary dimension.

The moderate number of DMRG studies performed in the quantum chem-

istry context can be found in Refs. [124, 125, 126, 127, 128, 129, 130, 131, 3, 132, 133, 134, 135, 136, 137, 105, 115, 106, 138, 139, 140], and in the following chapters we will describe some of our contributions to the *ab initio* DMRG.

1.2.4 Matrix product state wavefunction ansatz

As related by Östlund and Rommer [141, 142], and subsequently developed by other authors (see e.g., [143, 4]), the DMRG is also fruitfully analyzed from the viewpoint of the underlying wavefunction ansatz, the *matrix product state* (MPS).

We recall the full configuration interaction expansion in eqn. (1.8) for an n-electron system spanned by k orbitals. In occupation number representation, $|\Psi\rangle$ can be expanded as

$$|\Psi\rangle = \sum_{n_1,n_2,\ldots,n_k} C^{n_1 n_2 \ldots n_k} |n_1 n_2 \ldots n_k\rangle \tag{1.51}$$

where $n_i = 0, 1$ (e.g., we switched to a spin-orbital basis) ; $\sum_i n_i = n$. We now decompose the high dimensional coefficient tensor $C^I = C^{n_1 n_2 \ldots n_k}$ into a chained matrix product via repeated singular value decompositions (SVDs). For example, if there are only two orbitals, a singular value decomposition yields

$$C^{n_1 n_2} = \sum_i R_i^{n_1} \sigma_i R_i^{n_2} \tag{1.52}$$

where $\mathbf{R}^{n_1}$ and $\mathbf{R}^{n_2}$ are the singular vectors and $\boldsymbol{\sigma}$ are the singular values. Similarly, for three orbitals, $C^{n_1 n_2 n_3}$ can be decomposed via two singular value decompositions as

$$\begin{aligned} C^{n_1 n_2 n_3} &= \sum_i R_i^{n_1} \sigma_i S_i^{n_2 n_3} \\ &= \sum_{i,j} R_i^{n_1} \sigma_i' R_{ij}^{n_2} R_j^{n_3} \end{aligned} \tag{1.53}$$

where in the SVD of $\mathbf{S}_i$, all singular values have modulus one, since $\mathbf{S}_i$ is an orthogonal matrix. Note that the $R_{ij}^{n_2}$ has two lower indices and is hence a matrix, and that we build up a sum over these auxiliary indices. In this way, through repeated SVDs, the k-dimensional coefficient tensor can be decomposed as a chain of matrix products, as

$$\begin{aligned}
|\Psi\rangle &= \sum_{n_1,n_2,\ldots,n_k} C^{n_1 n_2 \ldots n_k} |n_1 n_2 \ldots n_k\rangle \\
&= \sum_{n_1,n_2,\ldots,n_k} \sum_i R_i^{n_1} \sigma_i S_i^{n_2 \ldots n_k} |n_1 n_2 \ldots n_k\rangle \\
&= \sum_{n_1,n_2,\ldots,n_k} \sum_{i,j} R_i^{n_1} \sigma_i' R_{ij}^{n_2} S_j^{n_3 \ldots n_k} |n_1 n_2 \ldots n_k\rangle \\
&= \ldots \\
&= \sum_{n_1,n_2,\ldots,n_k} \mathrm{Tr}\left\{\mathbf{R}^{n_1}\mathbf{R}^{n_2}\ldots\boldsymbol{\sigma}\ldots\mathbf{R}^{n_k}\right\} |n_1 n_2 \ldots n_k\rangle
\end{aligned} \tag{1.54}$$

with

$$C^{n_1 n_2 \ldots n_k} = \mathrm{Tr}\left\{\mathbf{R}^{n_1}\mathbf{R}^{n_2}\ldots\boldsymbol{\sigma}\ldots\mathbf{R}^{n_k}\right\}. \tag{1.55}$$

So far, we have only reformulated the FCI expansion, since the applied decomposition is exact and the $\mathbf{R}$ matrices have full rank (note that the rank will grow increasing large as the number of orbitals grows).

The matrix product state which underlies the DMRG algorithm, arises by truncating the maximum dimension of the $\mathbf{R}$ matrices to be at most $M \times M$, and thus with this restriction, we write the MPS as

$$|\Psi\rangle = \sum_{n_1,n_2,\ldots,n_k} \mathrm{Tr}\left\{\mathbf{R}^{n_1}\mathbf{R}^{n_2}\ldots\boldsymbol{\sigma}\ldots\mathbf{R}^{n_k}\right\} |n_1 n_2 \ldots n_k\rangle. \tag{1.56}$$

We can now establish the relationship between the MPS and the usual formulation of the DMRG algorithm[24]. Recall that at any point in a DMRG sweep,

[24]We change our notation in the following from system, neighbour, environment, and supersystem to the before mentioned *left block*, *site*, *right block* and *superblock*. While the former best

the orbitals are partitioned into three blocks: the left block (spanning orbitals $1, \ldots, f$, say), the site (orbital $g = f + 1$) and the right block (spanning orbitals $h(= f+2), \ldots, k$). Through successive renormalization transformations we obtain an adaptive many-body basis $\tilde{\mathcal{F}}^{sys,n_f}$ of dimension M to span the orbitals $1, \ldots, f$; let us denote these many-body states by $|l_f\rangle$. First we enlarge the left block by adding the next orbital to give a the extended left bloc with an associated space $\{|l_f\rangle\} \otimes \{|n_g\rangle\}$. Next we renormalize this space to form a new many-body basis $\{|l_g\rangle\}$ for the extended block spanning orbitals $1, \ldots, g$, as

$$|l_g\rangle = \sum_{f,n_g} R^{n_g}_{gf} |l_f n_g\rangle \tag{1.57}$$

where the rows of the matrix $\mathbf{R}^{n_g}$ are the M eigenvectors of the density matrix of the extended block $1, \ldots, g$. After successive renormalizations, we see that the renormalized states take on a matrix product form, e.g.,

$$\begin{aligned} |l_h\rangle &= \sum_{g,n_h} R^{n_h}_{hg} |l_g n_h\rangle \\ &= \sum_{f,g,n_g,n_h} R^{n_h}_{hg} R^{n_g}_{gf} |l_f n_g n_h\rangle \\ &= \ldots \end{aligned} \tag{1.58}$$

where each $\mathbf{R}^{n_i}$ matrix is truncated to have maximum dimension $M \times M$.

To complete the identification of the underlying DMRG wavefunction with the matrix product state, we introduce the corresponding renormalized many-body states $|r_g\rangle$ which span the orbitals $g = f + 1, \ldots, k$. In the tensor-product space of the left and right blocks, we can write the full wavefunction in the form

$$|\Psi\rangle = \sum_{l_f, r_g} C^{l_f r_g} |l_f r_g\rangle. \tag{1.59}$$

reflects the phyical motivation behind the DMRG algorithm, it can be confusing considering the change in direction from forwards to backwards sweeps. The latter notation has a fixed reference frame.

Performing an SVD, we obtain

$$|\Psi\rangle = \sum_f |\bar{l}_f\rangle \sigma_f |\bar{r}_f\rangle. \tag{1.60}$$

Substituting in the matrix product decomposition of the DMRG many-body basis for the left and right block basis states from (1.58) in eqn. (1.60) we identify the DMRG wavefunction with the matrix product state (1.56) as the special case of a one-dimensional tensor network ansatz. Consequently, the DMRG can be viewed as a self-consistent optimization algorithm for the matrix product state where the renormalization matrices $\mathbf{R}^{n_i}$ which parametrize the ansatz are determined one by one from the density matrices of the blocks after each blocking step in a DMRG sweep. The number of retained states in the DMRG M thus coincides with the dimensionality of the matrices that parametrize the MPS. We note that the position of $\boldsymbol{\sigma}$ in the matrix product state corresponds to the point of division between left and right blocks in the DMRG algorithm. In principle, the DMRG wavefunction varies with different block partitionings along a sweep, but in practice, the variation is quite small.

1.2.5 Features of the DMRG

Starting from the introduction above, let us summarize the key features of the DMRG/MPS ansatz.

1. **Multi-reference method for static correlation**: It is clear that the Hartree-Fock reference or any other particular electron configuration has no special significance in the DMRG ansatz. By this DMRG avoids being unphysically biased, e.g., along a potential energy curve. Furthermore, we do not

order or rank excitations relative to a single-reference state (cf. Sec. 1.1.5). Consequently, we also do not truncate the FCI wavefunction expansion after a certain excitation order like in restricted configuration interaction theories (e.g., configuration interaction with single and double substitutions (CISD), which ignores all triple and higher excitations from a HF determinant). That means that none of the coefficients $C^{n_1 n_2 \cdots n_k}$ are restricted to be zero (cf. Fig. 1.6). DMRG is hence an inherently multi-reference method which provides the unique possibility of accurately describing *large* static electron correlation problems. It can be viewed as an avenue to CASCI/FCI results without a brute-force solution of the active space problem. In fact, we propose the use of DMRG as a replacement for FCI as the kernel/solver for the active space part of general multi-reference methods (see Sec. 6.1), as long as no explicit Slater determinant expansion is required for successive dynamic correlation treatment. E.g., 2nd-order complete active space perturbation theory (CASPT2) only requires reduced density matrices of the active space, which DMRG can provide.

2. **Variational**: Since we can associate a wavefunction with any DMRG block configuration, and a DMRG energy is evaluated as an expectation value of such a wavefunction, the energies appearing in the DMRG procedure are strictly variational in the sense of an upper bound to the true energy (see Sec. 1.1.7).

3. **Size-consistency**: Within a physical ordering of the orbitals on the DMRG lattice, the matrix product state for two widely separated systems factorizes into the product of matrix product states for each system separately. To see this, first arrange the orbitals into left and right blocks, with the left block containing orbitals of the first system, and the right block containing

orbitals of the second system. Since there is no coupling, the matrix product state for the total block configuration is a product $|\Psi\rangle = |l\rangle|r\rangle$, where $|l\rangle$ is a matrix product state for the first system considered alone (without changing the orbital ordering) and similarly for $|r\rangle$. Consequently, the DMRG energy is size-consistent (see Sec. 1.1.7).

4. **Compactness**: The number of variational parameters in the matrix product state is $O(M^2k)$,as we have k renormalization matrices of size $M \times M$ in the MPS wavefunction ansatz. Note, that the number of orbitals k is proportional to the number of electrons n). This polynomial complexity replaces the factorial number of degrees of freedom in the FCI wavefunction. The introduced adapted many-body basis features a rapidly converging and naturally truncated multi-reference expansion. Its compact form is the key to the treatment of large active spaces. The correlation length recovered by the DMRG/MPS ansatz is determined by M.

5. **Computational cost and scaling**: The density matrix renormalization group is generally an $O(k^2M^4 + k^3M^3)$ polynomially scaling method. The current active space limit for general systems is $O(30)$. In chapter 2 we will show, how DMRG can be made a quadratically scaling $O(k^2)$ method in quasi-one-dimensional systems.

CHAPTER 2

QUADRATIC SCALING LOCAL DMRG AND ITS APPLICATION TO POLYENES AND HYDROGEN-CHAINS

We have devised a local *ab initio* density matrix renormalization group (LDMRG) algorithm to describe multi-reference correlations in large systems. For long molecules that are extended in one of their spatial dimensions, we can obtain an exact characterization of correlation, in the given basis, with a cost that scales only quadratically with the size of the system. The LDMRG allows us to correlate the full valence space of systems with appreciable chain length and overcome the factorial scaling and inevitably resulting incompleteness of FCI based CAS methods. The reduced scaling is achieved solely through integral screening and without the construction of correlation domains. We demonstrate the scaling, convergence, and robustness of the algorithm in polyenes and hydrogen chains. We converge to exact correlation energies (in the sense of full configuration interaction, with 1-10 μE_{h} precision) in all cases and correlate up to 100 electrons in 100 active orbitals. We further use our algorithm to obtain exact energies for the metal-insulator transition in hydrogen chains and compare and contrast our results with those from conventional quantum chemical methods.

The orbital localization and integral transformation code used in this project was written by Dr. Wim Cardoen and was based on the corresponding modules in the PSI3 program package [144]. Funding by a Kekulé Fellowship of the Fond der Chemischen Industrie (Fund of the German Chemical Industry) is acknowledged. Computations were carried out in part on the Nanolab-Cluster of the Cornell NanoScale Science & Technology Facility (CNF), supported by NSF

ECS 03-05765. The results of this study were published in 'J. Hachmann, W. Cardoen, G. K.-L. Chan, *J. Chem. Phys.* 125 (**2006**), 144101' [1], and this chapter is based on our exposition in this paper.

2.1 Background

The goal of this work is to answer the question of how to describe static electron correlation in systems which are large in only one out of their three spatial extents. As discussed in Sec. 1.1.8, many organic electronic materials are a prime example for this class of problems. We demonstrate that the density matrix renormalization group provides a solution to this question in a flexible and efficient way, and hence opens the possibility of high-quality wavefunction studies of long molecules and polymer chains. Our previous analysis showed that the DMRG behaves as a *local*, *multi-reference*, *size-consistent*, *size-extensive*, and *variational* theory (see Sec. 1.2.5). From the *intrinsic locality* of the DMRG ansatz we formulate a DMRG algorithm, denoted for convenience as LDMRG that scales only *quadratically* with the size of the system, without any need for an artificial imposition of orbital domains. The multi-reference nature of the ansatz also eliminates any need for separately localized occupied and virtual orbitals, which is one of the fundamental problems in other local correlation methods. Using this algorithm, we carry out numerically exact DMRG calculations for long molecules, including polyenes in the π-active space and metallic and insulating hydrogen chains where we correlate up to 100 active electrons in 100 active orbitals. Traditional CAS calculations for active spaces of this order of magnitude are unthinkable due to the astronomical determinantal space.

The structure of our discussion is as follows: We begin with a brief review of

current local correlation methods in Sec. 2.2, in which we focus on their regime of applicability and the analysis of challenges in their local ansatz. For the general introduction of the DMRG algorithm and wavefunction ansatz we refer to our exposition in Sec. 1.2. Building on the previous discussion of its general features (Sec. 1.2.5), we will examine its local properties and their implications for the design of a local DMRG algorithm in Sec. 2.3. The following Sec. 2.4 shows how a simple screening of integral amplitudes results in a robust and naturally quadratic-scaling DMRG algorithm. In Sec. 2.5 we present calculations on hydrogen molecular chains and polyenes in the π-active space and demonstrate the size-extensivity, computational scaling, and convergence of the LDMRG algorithm. As a difficult test of static correlation, we further carry out calculations on the metal-insulator transition in hydrogen chains for both symmetric and asymmetric bond stretching, and compare our results against existing quantum chemical methods (Sec. 2.6). Finally, our conclusions are presented in Sec. 2.7.

2.2 Conventional local correlation methods

The unfavorable scaling of wavefunction based electron correlation methods (see Sec. 1.1.5) such as Møller-Plesset perturbationor coupled cluster theory had limited their applicability to small molecules for a long time. In recent years, low-order scaling, local versions of these methods have been developed. In particular, the groups of Pulay, Werner, Head-Gordon, Ochsenfeld, and Scuseria and the development teams of the MOLPRO [145] and QCHEM [146, 147] program packages have been at the forefront of this development, persistently pushing it from the conceptual stage until its packaged release as black box methods. The current state of these conventional local correlation methods

however only covers the domain of dynamic electron correlation (such as local coupled cluster (LCCn) [148, 149, 150, 151, 152, 153], or local Møller-Plesset perturbation theory (LMPn) [154, 155, 156][1].

At the heart of these local methods is the insight that in a problem with finite correlation length, only excitations into orbitals in the near vicinity are relevant [158]. The amplitudes of excitations into distant orbitals is small and can be discarded. Consequently, the Hilbert space that actually has to be considered decreases drastically.

There are two central problems in these approaches: Firstly, local correlation methods require a localized orbital space. Since these methods are of single-reference nature, there is no invariance with respect to rotations between occupied and virtual orbital space, i.e., both spaces have to be localized separately. The limited rotational freedom in these subspaces can often lead to poor results of the localization scheme, i.e., the localized orbitals can still have a wide spread. We will show in the following section that this is not an issue in the LDMRG.

The second problem is the definition of correlation domains, which artificially cut the real space of the problem at hand into subspaces, in which excitations are considered. Excitations outside a correlation domain are neglected. While this is generally a good physical approximation, it can lead to technical difficulties, e.g., when there are no well defined correlation domains in a system. In addition, the domains can lead to bumps in potential energy surfaces, since their boundaries change in the course of a change in the geometry. Recently,

[1]Note, that the local multi-reference configuration interaction with singles and doubles (MR-CISD) method by Carter *et al.* [157] is formally a linear scaling multi-reference technique. However, only the dynamic correlation CISD part is linear scaling – an important improvement over the original n^6 behaviour – while the multi-reference part is performed by FCI and is hence not scalable. Calculations on systems of different chain length use a fixed CAS size.

schemes were introduced to minimize the occurrence of these unphysical features.

2.3 Locality in the DMRG ansatz

We now extend our discussion of the general properties of the DMRG/MPS ansatz from Sec. 1.2.5 with respect to its particular local features.

As discussed before, the number of variational parameters in the MPS ansatz is $O(M^2k)$ and the correlation length it retrieves is governed by M. Thus in any system with a finite quantum (i.e., off-diagonal) correlation length along the DMRG lattice, we can obtain a given accuracy in the energy per unit site with *constant* M, independent of the size of the system. In such cases, for a given accuracy, the complexity of the DMRG wavefunction only scales linearly with the size of the molecule, i.e., as $O(k)$ (since M does not need to be increased). The restriction to a given M naturally determines the correlation length captured by the ansatz, i.e., there is no need to *a priori* impose any correlation domains (cf. Sec. 2.2). By increasing M we account for increasingly longer ranged correlations until we cover the complete correlation length of the given problem.

We emphasize that the *correlation length* embodied by the MPS ansatz is *measured strictly along the DMRG lattice*, rather than as necessarily exists in the physical space. In the quantum chemistry context its range in turn refers to the chosen orbital representation, and the particular way in which it is projected onto the DMRG lattice. If the orbital space maps geometrically onto the real space then the correlation length clearly also translates to real space. In this case, the DMRG can exploit the locality of correlations in gapped systems. This situation

is ideally realized for quasi-one-dimensional systems in a local, topologically ordered basis (e.g., the p_z orbitals along the backbone of a π_z-conjugated polyene). It then becomes clear that a local framework is the ideal way in which to think about and set up the DMRG for gapped systems with non-diverging real space correlation, which are spatially extended in only one of the three dimensions – i.e., long molecules. Only in a local representation is the finite correlation length in real space efficiently translated to a finite correlation length along the DMRG lattice. The efficiency of the DMRG for this class of problems can be traced back to the underlying MPS wavefunction structure: correlations in the chained product of renormalization matrices are introduced site-by-site (i.e., in a local fashion), in the same way they arise physically (cf. 1.1.8). Note, that the LDMRG description reflects the origin and structure of the given electron correlation problem (cf. Sec. 1.1.2), which makes it a powerful technique.

At this point we want to discuss the consequences of employing the DMRG in regimes, which are less suitable to its structure, i.e., if we use it on higher-dimensional systems, dynamic correlation problems or in a non-local framework. It is clear that there is generally no good projection of a higher-dimensional system onto the one-dimensional DMRG lattice[2]. The same is true for dynamic correlation problems, which are associated with many orbitals per atom center, which again cannot be projected onto the DMRG lattice efficiently. In both cases we face an incompatibility of the dimensionality between the method and the problem. The width in real and orbital space, respectively, is not well represented by the MPS ansatz. The consequence is that artificial long range correlations are introduced in the description of the problem on the

[2]There are exceptions in special cases, e.g., if the correlations are extremely short ranged in the higher dimensions. However, these cases are better described as a collection of independent one-dimensional systems, rather than as a true higher-dimensional one.

DMRG lattice, which are not present in the physical problem itself. While the DMRG is ideal for one-dimensional systems, its performance necessarily degrades for higher dimensions, following the same line of argument as before: the DMRG tries to account for higher-dimensional correlations in a inherently one-dimensional fashion, which is very inefficient. The method cannot exploit the structure of the many-body problem any more, but is in contrast ill equipped for a higher-dimensional correlation structure[3]. In these cases, we have to scale M in order to capture the long-range correlations along the DMRG lattice and maintain accuracy. It turns out that this scaling is exponential with the width of the system, much like full configuration interaction or CASCI/CASSCF theory. In practice, we have shown that with reasonable M we can still obtain highly accurate DMRG energies even in non-one-dimensional molecular systems with up to $O(40)$ active orbitals, which is outside the range of FCI theory. To model much larger extended non-one-dimensional systems of strongly interacting electrons, further progress will be required making use of more general tensor network ideas. Nonetheless even the original DMRG framework offers progress for two- and three-dimensional problems, as a direct consequence of our previous discussion.

We note, that the DMRG as a true multi-reference method is in principle independent of the representation of the initial set of orbitals. In practice – consistent with the previous discussion – the selection of an appropriate basis and its projection onto the DMRG lattice is crucial for a well behaved convergence behavior. In a non-local one-electron basis, e.g., the delocalized canonical MO basis, which may be projected based on an energy criterion, the correlation length

[3]Following the discussion in Sec. 1.2, the profile of the reduced density matrix in the DMRG many-body basis is very flat, i.e., the weights decay slowly and the truncation after a finite M leads to large errors.

accounted for is along this (less intuitive) energy scale. This approach corresponds to the original quantum chemistry DMRG. It can be useful in cases, in which the correlations of a system are not primarily determined spatially (i.e., in dense systems without natural order or gapless systems with long-range real space correlations). However, for gapped systems with finite real space correlations, this basis and projection will also lead to artificially long range correlations on the DMRG lattice, i.e., to a description which is more complicated than the problem. In other cases where a strictly local basis leads to artificial long range correlations, a carefully designed non-local basis can moderate this problem. While the structure of the physical problem and of the DMRG lattice are constants, the orbital representation and projection strategy can be used to accomplish the cardinal goal of minimizing the range of correlations along the DMRG lattice. Note, that the choice of orbital space and projection is generally a hard problem, but for gapped quasi-one-dimensional systems the LDMRG can easily be identified as the ideal strategy.

Note, that a finite correlation length implies only that we are away from a quantum critical point; such wavefunctions need not be close to the Hartree-Fock reference in any sense, as is indeed the case for systems with strong interactions. Thus, the local correlation nature of the DMRG is different from that of other local correlation methods (such as local LCCSD) since these require the *correction* to the mean-field reference to be small *and* to possess finite correlation length. Thus the DMRG is a naturally local scaling ansatz, and so long as the determination of the energy is also performed with an account of locality (e.g., through screening or multipole expansion) a low-order scaling correlation theory arises. Indeed this is the basis of the quadratic scaling algorithm in the next section. Quadratic complexity is the correct physical complexity for strongly

interacting systems with finite correlation length. The DMRG ansatz possesses a further technical advantage. Since no localizable Hartree-Fock reference is required, the favorable scaling of the DMRG is obtained in *any local basis*, and does not in particular need separate localization in the occupied and virtual spaces. This is particularly advantageous when modelling correlated states which possess a shorter quantum correlation length than their parent mean-field reference (e.g., systems with small Hartree-Fock bandgaps), for which orbital localization is often more difficult.

We can summarize that the DMRG ansatz by virtue of its construction is well suited for the design of a local, low-order scaling static correlation method for long molecules – complementing the currently available local dynamic correlation methods described in Sec. 2.2. We again point out the value of identifying and exploiting suitable physical regimes for a method. In case of the LDMRG, this is the regime of static correlation (cf. Sec. 1.1.6) in quasi-one-dimensional problems (cf. Sec. 1.1.8).

2.4 A quadratic scaling parallelized DMRG algorithm

The full computational scaling of a single conventional DMRG sweep is $O(M^2k^4) + O(M^3k^3)$. Here, the leading $O(k^4)$ scaling arises in essence from the number of two-electron integrals v_{ijkl} in the Hamiltonian eqn. (1.24).

Recall that M can be kept fixed, independent of system size in a long molecule. Thus to implement a quadratic scaling DMRG algorithm we need only screen the contributions from the two-electron integrals. This can be achieved by working in a localized basis. (Note we can use any localized or-

thonormal basis and we do not need to separately localize the occupied and virtual spaces as is commonly required in local correlation methods. For example, later in this work, we shall use the basis of overlap symmetrically orthonormalized atomic orbitals). As is well understood, in a large system described in a localized basis, the number of significant two-electron integrals below a given threshold scales only quadratically as non-classical Coulomb integrals, i.e., integrals of the form $v_{ijkl} = \frac{1}{2}(i(1)l(1)|j(2)k(2))$, where $i(1), l(1)$ or $j(2), k(2)$ functions are widely separated, vanish exponentially with the separation between i, l or j, k centers.

In the DMRG, we work with a number of intermediate combinations of operators on each of the blocks of orbitals which are subsequently combined to construct the full H [3, 133]. A DMRG sweep, consisting of $O(k)$ sweep iterations (each comprising a different block configuration), requires $O(M^2k^4) + O(M^3k^3)$ time, $O(M^2k^2)$ memory, and $O(M^2k^3)$ disk storage. These asymptotic costs originate from manipulating the two-index intermediate operators $A_{ij}, B_{ij}, P_{ij}, Q_{ij}$ on the various blocks:

$$A^{\text{blk}}_{ij(\in\text{blk})} = a_i a_j \tag{2.1}$$

$$B^{\text{blk}}_{ij(\in\text{blk})} = a_i^\dagger a_j \tag{2.2}$$

$$P^{\text{blk}}_{ij(\notin\text{blk})} = \sum_{k,l\in\text{blk}} v_{ijkl} a_k a_l \tag{2.3}$$

$$Q^{\text{blk}}_{ij(\notin\text{blk})} = \sum_{k,l\in\text{blk}} x_{ijkl} a_k^\dagger a_l \tag{2.4}$$

$$x_{ijkl} = v_{ijkl} - v_{jikl} - v_{ijlk} + v_{jilk}. \tag{2.5}$$

To begin, we employ screening to determine a set of significant two-index operators that must be considered on each block, according to the following

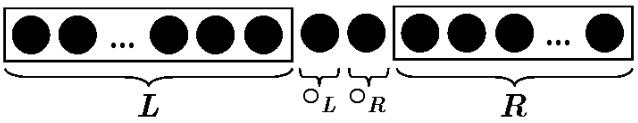

Figure 2.1: Standard two-site block configuration in DMRG. From left to right, L, $\circ_L$, $\circ_R$, R.

criterion:

$$
\begin{aligned}
&A^{\text{blk}}_{ij(\in\text{blk})}\text{discard if } v_{ijkl} < \text{thresh}_1 \text{ for } \textbf{all } kl \in \text{blk} \\
&B^{\text{blk}}_{ij(\in\text{blk})}\text{discard if } x_{ijkl} < \text{thresh}_1 \text{ for } \textbf{all } kl \in \text{blk} \\
&P^{\text{blk}}_{ij(\notin\text{blk})}\text{discard if } v_{ijkl} < \text{thresh}_1 \text{ for } \textbf{all } kl \in \text{blk} \\
&Q^{\text{blk}}_{ij(\notin\text{blk})}\text{discard if } x_{ijkl} < \text{thresh}_1 \text{ for } \textbf{all } kl \in \text{blk}.
\end{aligned} \tag{2.6}
$$

In a DMRG block configuration, there are four kinds of blocks (in the so-called 'two-site' version of the algorithm): the left block L, an orbital to be blocked with the left block $\circ_L$, an orbital to be blocked with the right block $\circ_R$, and the right block R (Fig. 2.1). Without screening, the number of two-index operators that must be considered on each block is $O(k^2)$, but in each case this is reduced to $O(k)$ after screening since eqns. (2.6) require centres i, j to be close in space. Since the number of operators is reduced, we also reduce the memory cost to $O(M^2k)$ per sweep iteration (block configuration). The disk usage is reduced to $O(M^2k^2)$ per sweep.

Next, we consider the computational costs of the different manipulations involving the two-index operators in each of the three stages of a sweep iteration: (1) blocking, (2) solving for the wavefunction, and (3) decimation:

1. *Blocking*: Here we construct representations of the operators in the tensor product space of a large block and an additional orbital; for concreteness,

we take the large block as the left block L, and the additional orbital as $\circ_L$, and we consider the operator P_{ij}. First, we accumulate $P^L_{ij}, P^{\circ_L}_{ij}$ in the new space $\{L\} \otimes \{\circ_L\}$; for each such term, the accumulation requires $O(M^2)$ time. Since there are $O(k)$ screened P_{ij} operators on both blocks L and $\circ_L$, in total this requires $O(M^2k)$ time per blocking step and thus $O(M^2k^2)$ time per sweep. Next, we sum over the new terms appearing in eqns. (2.1), (2.2) that arise from the combinations $k \in L, l \in \circ_L$ and $k \in \circ_L, l \in L$; each such term requires $O(M^2)$ time per blocking step. Without screening the number of new terms becomes $O(k)$, but with screening we discard any contributions where $v_{ijkl} < \text{thresh}_2$ for **all** $kl \in$ blk and this decreases the number of new terms to $O(1)$ for each significant P_{ij} operator per blocking step. Consequently, the time to accumulate the additional contributions is $O(M^2) \times O(1) \times$ no. significant $P_{ij} = O(M^2k)$ per blocking step, or $O(M^2k^2)$ time per sweep. Repeating this analysis for the A_{ij}, B_{ij}, Q_{ij} operators, we observe that these also involve $O(M^2k^2)$ time per sweep.

2. *Solving for the wavefunction*: In an iterative Davidson algorithm [159], the contributions of P_{ij}, Q_{ij} to the Hamiltonian matrix multiply takes the form $\sum_{i,j}(P^{L\circ_L}_{ij} \otimes A^{\dagger\ \circ_R R}_{ij})|\Psi\rangle, \sum_{i,j}(Q^{L\circ_L}_{ij} \otimes B^{\circ_R R}_{ij})|\Psi\rangle$. Each $\otimes$ requires $O(M^3)$ time, and thus the overall cost is determined by the number of ij indices to sum over. From the screening criterion thresh_1, this is $O(k)$ for each block configuration, and thus the total time for a single Hamiltonian multiply takes $O(M^3k)$, or $O(M^3k^2)$ per sweep.

3. *Decimation*: In the decimation for each two-index operator, each transformation takes $O(M^3)$ time. After screening, only $O(k)$ ij indices need be considered per block, and thus the time to transform all $A_{ij}, B_{ij}, P_{ij}, Q_{ij}$ operators is $O(M^3k)$ per renormalization step, or $O(M^3k^2)$ per sweep.

Table 2.1: Time, memory, and disk costs associated with the two-index operators in the original DMRG and screened LDMRG algorithms. The two-index operators determine the asymptotic computational costs of the algorithm.

Operator	Blocking		Solving		Decimation		Memory		Disk	
	DMRG	LDMRG	DMRG	LDMRG	DMRG	LDMRG	DMRG	LDMRG	DMRG	LDMRG
A_{ij}, B_{ij}	M^2k^3	M^2k^2	M^3k^3	M^2k^2	M^3k^3	M^3k^2	M^2k^2	M^2k	M^2k^3	M^2k^2
P_{ij}, Q_{ij}	M^2k^4	M^2k^2	M^3k^3	M^2k^2	M^3k^3	M^3k^2	M^2k^2	M^2k	M^2k^3	M^2k^2

In summary, integral screening in the LDMRG reduces the total computation cost per sweep to $O(M^3k^2) + O(M^2k^2)$ time (i.e., quadratic scaling, since M in long molecules is independent of system size for a chosen accuracy and hence a constant), $O(M^2k)$ memory, and $O(M^2k^2)$ disk. Table 2.1 summarizes the key operations and costs of the screened algorithm.

Finally, we note that the above screening procedure is easily combined with the parallelized algorithm employed in previous calculations with the BLOCK code [133]. Once the list of screened ij indices is determined via eqns. (2.6), the significant operators are distributed over the processors, and all manipulations involving these operators are then carried out in parallel. This screened parallelized algorithm was added to the code base of BLOCK and utilized to perform the calculations described in all of the following work.

2.5 Numerical analysis of the LDMRG in long systems

In the current section, we report our numerical investigations of (i) the accuracy and extensivity of the LDMRG ansatz in long molecules, (ii) computational performance of the quadratic-scaling algorithm and robustness of the screening criteria, (iii) convergence of the LDMRG ansatz, and (iv) errors compared against standard correlation methods. We have chosen two classes of systems as representative 'long' molecules: planar *all-trans*-polyenes C_kH_{k+2} ranging from $k = 4, 8, \ldots, 48$ (modelled in the π_z-active space) and hydrogen molecule chains $(H_2)_{k/2}$ ranging from $k = 10, 20, \ldots, 100$. The geometries of the polyenes (based on [160]) and hydrogen chains are given in Fig. 2.2. We note that although the bond lengths in the hydrogen molecule chains are alternating, the molecules are

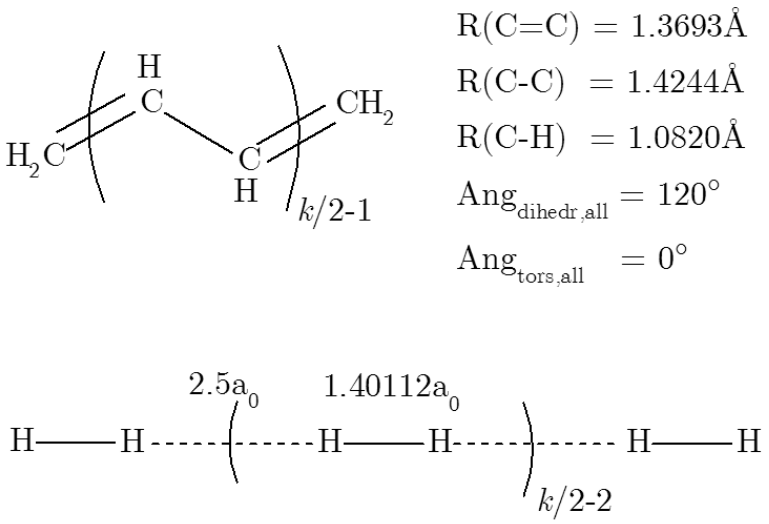

Figure 2.2: Geometries of the chemical systems used in the LDMRG study in Sec. 2.5.

still spaced sufficiently closely to be interacting.

2.5.1 Computational details

All electronic integrals were obtained using the PSI3.2 package [144]. We used an STO-3G minimal basis for the polyene calculations and an STO-6G minimal basis for the hydrogen molecular chains [161, 162]. Polyene calculations were performed in the π_z-active space spanned by one p_z orbital on each carbon center, with each carbon atom contributing one electron; thus in C_kH_{k+2} we used a $(k\text{e}, k\text{o})$ active space. The remaining electrons were placed in doubly occupied restricted Hartree-Fock (RHF) orbitals generated by the PSI3.2 program. Calculations on the hydrogen chains correlated all electrons.

We used a localized orthonormal basis as input to the LDMRG calculations.

In both the polyenes and hydrogen chains this was obtained by symmetrically orthonormalizing ($S^{-1/2}$) the atomic orbital basis. The orthonormalized orbitals were then ordered in their natural topological order, i.e., in the order of their originating atoms along the chain. Since each atom contributes only one basis function, this ordering is unique.

The LDMRG calculations were performed with the parallel BLOCK code [133] with integral screening as described in Sec. 2.4, on 4-18 processors. Except where stated otherwise (see Sec. 2.5.3), we applied screening thresholds of $\text{thresh}_1 = 10^{-7}\ E_\text{h}$ and $\text{thresh}_2 = 10^{-20}\ E_\text{h}$. No spatial symmetry was used. DMRG sweeps were performed with progressively increasing M values (a sweep schedule) and a small amount of random noise (between $10^{-6} - 10^{-9}$ in the matrix norm) was added to the density matrix in the early sweeps ($M \leqslant 100$) to prevent loss of quantum numbers [3, 133]. A typical schedule to obtain $M = 50, 100, 250$ DMRG energies is as follows: sweeps 1-6: $M = 50$ (with noise), sweeps 7-12: $M = 50$, sweeps 13-18: $M = 100$ (with noise), sweeps 19-24: $M = 100$, sweeps 25-30: $M = 250$. We have converged our LDMRG energies to 8 significant figures; unconverged digits are denoted in italics. Because of the complexity of the *ab initio* DMRG method and the nonlinearity of the optimization, there is a small dependence of the DMRG energies on the precise computational setup (e.g., the way in which M is increased in sweeps) which may lead to some variation in the last significant digit.

2.5.2 Accuracy and extensivity of the DMRG ansatz

In Tabs. 2.2 and 2.3 we present the energies obtained with our quadratic scaling LDMRG algorithm for the *all-trans*-polyene series and hydrogen molecular chains. For comparison, we also present 2nd-order Møller-Plesset (MP2) and coupled cluster calculations (CCSD, CCSD(T)) obtained using the PSI3.2 (hydrogen chains) and DALTON 2.0 [163] (active-space polyenes) packages.

In the largest M LDMRG calculations shown, the correlation energies are exact energies for the many-particle Schrödinger equation (in the given one-particle basis) to the digits displayed. For example, in the polyenes, calculations at the LDMRG(500) and LDMRG(1000) level did not change the energy in the μE_h-range. To confirm the exactness of our LDMRG calculations, we also performed explicit active space FCI calculations (using MOLPRO 2002.6 [164]) for C_4H_6 and C_6H_8 and obtained agreement to all displayed digits. Following the discussion in Sec. 2.5.1, the hydrogen molecular chain energies are presented to 10 μE_h precision, corresponding to eight significant figures in the electronic energy of the longer chains. There are only improvements of the order of 1 μE_h when going to LDMRG(100) and thus the LDMRG(50) correlation energies for the hydrogen molecular chains are exact to the digits displayed.

The largest Hilbert space considered (for the $(H_2)_{50}$ system containing 100 electrons in 100 orbitals) has $\dim(\mathcal{H})=10^{58}$. That we are able to obtain a numerically exact correlation energy with the LDMRG illustrates the compactness of the LDMRG description in systems that are still interacting but have finite correlation lengths, which allows us to keep M fixed as the system size grows (see Sec. 1.2.4). A related feature of the LDMRG ansatz is that of size-consistency/extensivity of the energy, which we now discuss.

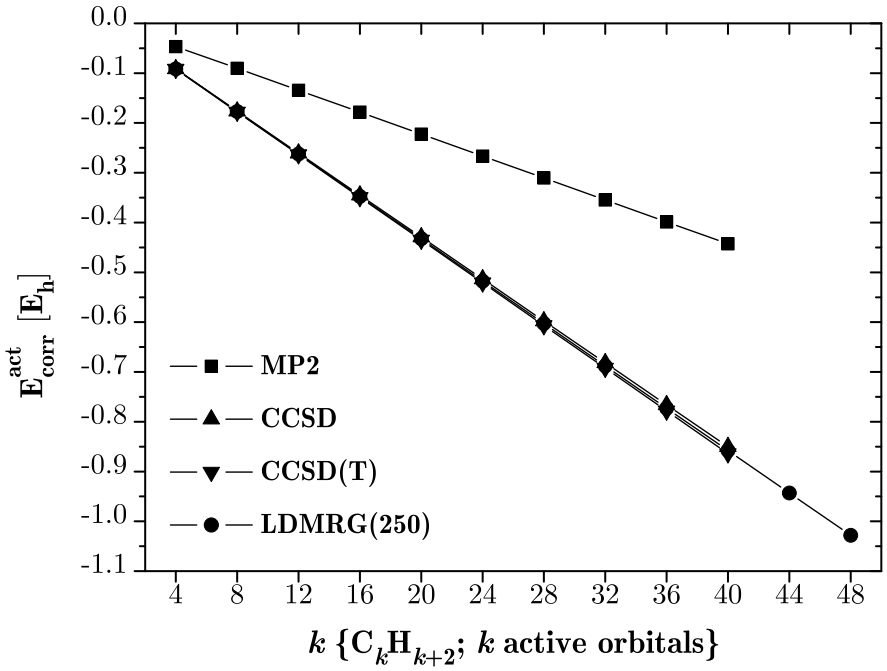

Figure 2.3: *All-trans*-polyenes: Active space correlation energy from MP2, CCSD, CCSD(T) and LDMRG(250) as a function of polyene chain length. On the scale of the graph, the LDMRG and CC results nearly overlap.

In Fig. 2.3, we plot the active space correlation energy E_{corr}^{act} as a function of polyene chain length. A clear linear relationship between chain length and correlation energy is observed. Figure 2.4 shows in detail how the active space correlation energy per additionally introduced C_4H_4-unit converges to a constant in the limit of long polyenes.

We also performed a series of lower accuracy LDMRG calculations for the polyenes, with $M = 5 - 40$ states. Due to the variational nature of the DMRG, these approach the exact energy from above. Figure 2.5 presents the logarithm of the percentage error in the correlation energy relative to the 'exact'

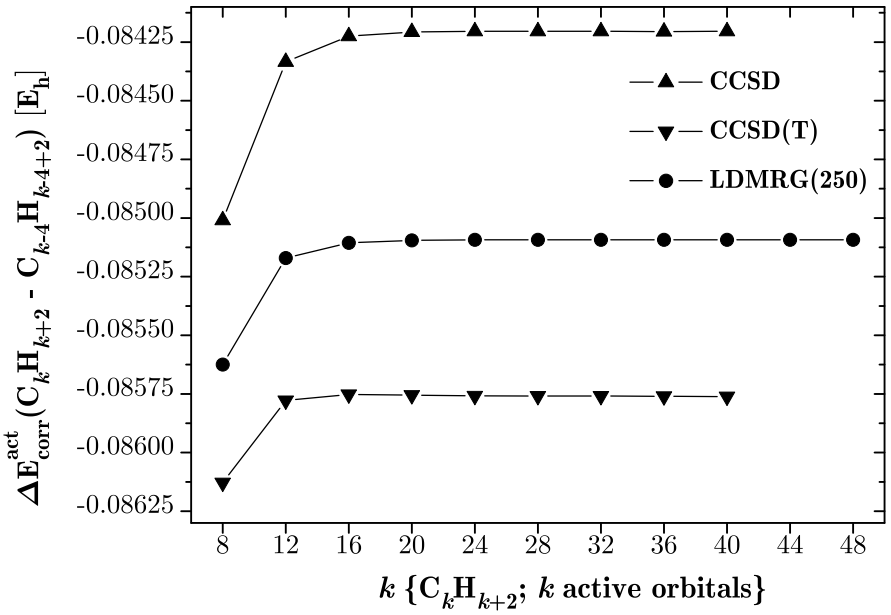

Figure 2.4: *All-trans*-polyenes: Active space correlation energy at CCSD, CCSD(T) and LDMRG(250) level of theory per additionally introduced C_4H_4-unit.

LDMRG(250) energies, as a function of chain length. In small systems the LDMRG calculations are exact, since the DMRG states span the whole *n*-particle space. In the longer polyenes, the percentage errors increase to a saturating value, demonstrating the size-extensivity of the approximate LDMRG calculations. Similar observations can be made for the hydrogen molecular chains.

2.5.3 Computational scaling and screening robustness

In Fig. 2.6 we present the asymptotic computational scaling of the sweep time for the LDMRG calculations as a function of the number of active orbitals for the polyenes and hydrogen molecular chains. Here sweep times were measured

Table 2.2: *All-trans*-polyenes: Dimension of the FCI determinant space, total RHF energy, RHF active space electronic energy; active space correlation energies at MP2, CCSD, CCSD(T) and different LDMRG levels of theory. The active space electronic energy contains the core-active Coulomb and exchange contributions, but no nuclear repulsion. "*conv.*" denotes converged results, where increased M did not change the significant figures in the energy. All LDMRG results with $M \geqslant 250$ converged. $C_{44}H_{46}$ and $C_{48}H_{50}$ could not be computed by DALTON due to an address limitation. All energies are given in hartree.

				E_{corr}^{act}					
Molecule	dim($\mathcal{H}$)	E_{RHF}	E_{corr}^{act}	MP2	CCSD	CCSD(T)	LDMRG(50)	LDMRG(100)	LDMRG(250)
C_4H_6	3.6×10^{1}	-153.006 364	-3.169 490	-0.046 529	-0.091 435	-0.091 668	-0.091 502	*conv.*	*conv.*
C_8H_{10}	4.9×10^{3}	-304.889 389	-8.426 391	-0.090 346	-0.176 445	-0.177 797	-0.177 127	*conv.*	*conv.*
$C_{12}H_{14}$	8.5×10^{5}	-456.773 412	-14.589 838	-0.134 320	-0.260 779	-0.263 575	-0.262 296	-0.262 297	*conv.*
$C_{16}H_{18}$	1.7×10^{8}	-608.657 556	-21.345 452	-0.178 366	-0.345 003	-0.349 327	-0.347 399	-0.347 403	*conv.*
$C_{20}H_{22}$	3.4×10^{10}	-760.541 718	-28.542 181	-0.222 434	-0.429 210	-0.435 082	-0.432 490	-0.432 498	*conv.*
$C_{24}H_{26}$	7.3×10^{12}	-912.425 883	-36.090 721	-0.266 507	-0.513 414	-0.520 840	-0.517 579	-0.517 591	*conv.*
$C_{28}H_{30}$	1.6×10^{15}	-1064.310 048	-43.931 953	-0.310 582	-0.597 618	-0.606 599	-0.602 668	-0.602 684	*conv.*
$C_{32}H_{34}$	3.6×10^{17}	-1216.194 214	-52.023 816	-0.354 658	-0.681 822	-0.692 358	-0.687 757	-0.687 777	*conv.*
$C_{36}H_{38}$	8.2×10^{19}	-1368.078 379	-60.334 842	-0.398 734	-0.766 027	-0.778 118	-0.772 846	-0.772 870	*conv.*
$C_{40}H_{42}$	1.9×10^{22}	-1519.962 544	-68.840 593	-0.442 810	-0.850 231	-0.863 879	-0.857 935	-0.857 962	-0.857 963
$C_{44}H_{46}$	4.4×10^{24}	-1671.846 710	-77.521 543	–	–	–	-0.943 024	-0.943 055	-0.943 056
$C_{48}H_{50}$	1.0×10^{27}	-1823.730 875	-86.361 727	–	–	–	-1.028 113	-1.028 147	-1.028 149

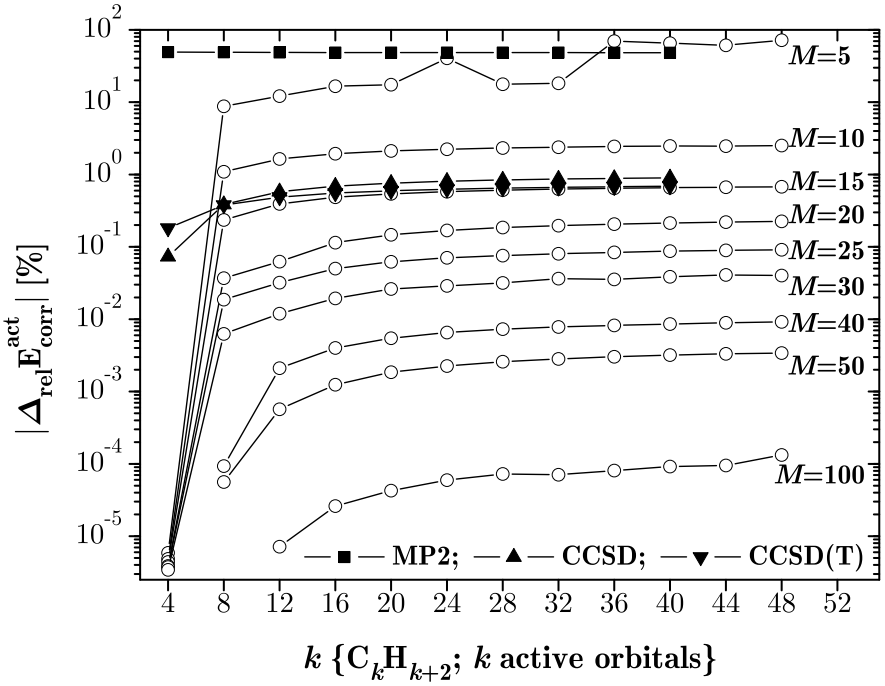

Figure 2.5: *All-trans*-polyenes: Relative errors in the active space correlation energies for LDMRG with various M (compared to the exact LDMRG(250) results). The black marked curves are the errors of MP2, CCSD, and CCSD(T) as reference. The plot shows absolute magnitudes in logarithmic scale.

after several sweeps at a given M level had been performed, to remove the bias that occurs immediately after a transition from a lower M calculation in the sweep schedule.

We fitted the timing data to obtain the computational scaling of LDMRG as a function of the number of active orbitals. The scaling exponents for the polyenes and the $(H_2)_{k/2}$ chains with different M and screening thresholds are given in Table 2.4.

In the polyenes we find a reduced scaling of near-quadratic order, with an

Table 2.3: $(H_2)_{k/2}$-chains: Dimension of the FCI determinant space, total RHF energy, RHF electronic energy; correlation energies at MP2, CCSD, CCSD(T) and LDMRG(50) levels of theory. All LDMRG results with M=50 converged. All energies are given in hartree.

				E_{corr}			
Molecule	dim($\mathcal{H}$)	E_{RHF}	$E_{RHF,el}$	MP2	CCSD	CCSD(T)	LDMRG(50)
$(H_2)_5$	6.4×10^4	-5.553 26	-16.036 48	-0.068 34	-0.101 93	-0.102 04	-0.102 09
$(H_2)_{10}$	3.4×10^{10}	-11.088 22	-38.784 11	-0.137 53	-0.203 77	-0.204 04	-0.204 15
$(H_2)_{15}$	2.4×10^{16}	-16.623 18	-64.210 83	-0.206 72	-0.305 61	-0.306 03	-0.306 21
$(H_2)_{20}$	1.9×10^{22}	-22.158 14	-91.378 72	-0.275 91	-0.407 44	-0.408 02	-0.408 26
$(H_2)_{25}$	1.6×10^{28}	-27.693 11	-119.841 65	-0.345 10	-0.509 28	-0.510 01	-0.510 32
$(H_2)_{30}$	1.4×10^{34}	-33.228 07	-149.336 70	-0.414 29	-0.611 12	-0.612 01	-0.612 38
$(H_2)_{35}$	1.3×10^{40}	-38.763 03	-179.690 11	-0.483 48	-0.712 95	-0.714 00	-0.714 44
$(H_2)_{40}$	1.2×10^{46}	-44.297 99	-210.778 35	-0.552 67	-0.814 79	-0.815 99	-0.816 49
$(H_2)_{45}$	1.1×10^{52}	-49.832 95	-242.509 08	-0.621 87	-0.916 63	-0.917 98	-0.918 55
$(H_2)_{50}$	1.0×10^{58}	-55.367 92	-274.810 58	-0.691 06	-1.018 47	-1.019 98	-1.020 61

exponent between 2.1 – 2.2. For reasonable screening thresholds (i.e., thresh_1 10^{-6} E_h–10^{-8} E_h) no significant differences in the scaling is observed. We also do not see a significant scaling dependence on M. In the hydrogen chains a similar reduced scaling was found, in this case with exponents ranging from 2.2 – 2.4. In both cases, it is clear that the screened LDMRG algorithm has reduced the computational scaling of the DMRG to quadratic order. As an example of absolute times per sweep, for the largest system $(H_2)_{50}$ using 18 2.0 GHz Opteron processors, we required 27 min for $M = 50$, 37 min for $M = 100$, and 73 min for $M = 250$.

Since the LDMRG employs screening, we should assess the robustness of the criterion that is used. To this end, we studied the polyene correlation energies computed with screening thresholds (thresh_1) of 10^{-6} E_h, 10^{-7} E_h, 10^{-8} E_h and 10^{-20} E_h (the energy of the latter can be considered unscreened). A se-

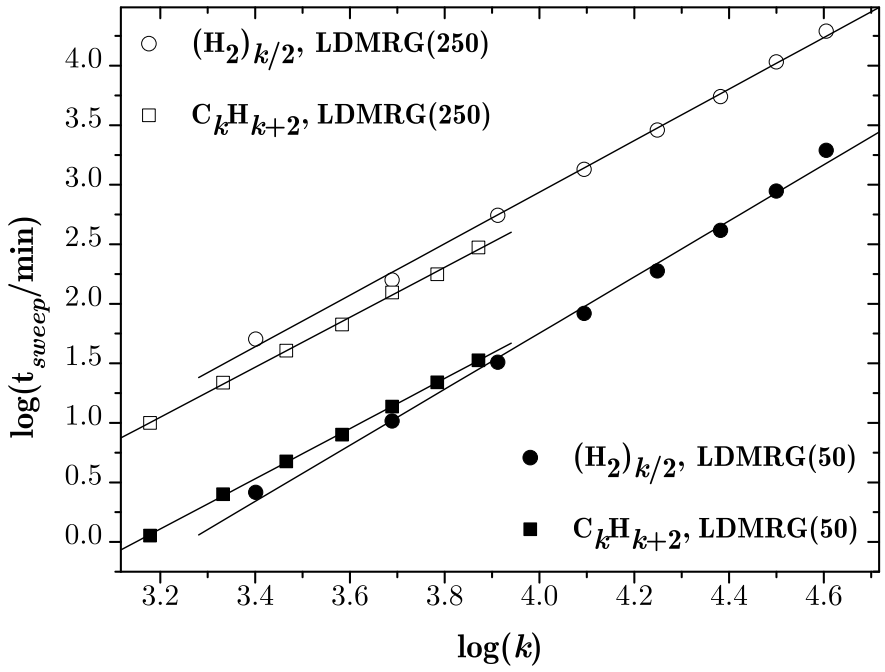

Figure 2.6: $(H_2)_{k/2}$ chains (circles) and *all-trans*-polyenes (squares): Asymptotic timing data (i.e., total time per sweep) of LDMRG with $M = 50$ (filled marks) and $M = 250$ (unfilled marks) for 10^{-7} E_h-screening in log-log-representation with linear fit.

lection of results is presented in Table 2.5. We observe the correlation energy to be converged at the μE_h level with respect to the screening threshold when $\text{thresh}_1 = 10^{-7}$ E_h, which is the reason for using this setting during this study. In practice, this threshold could be relaxed for lower accuracy calculations.

2.5.4 Sweep and error convergence

As discussed in the introduction, there are two types of convergence in DMRG calculations. The first is the convergence of the energy as a function of the num-

Table 2.4: Asymptotic scaling exponents (with standard error) of LDMRG depending on M and the screening threshold.

	Scaling exponent		
System (thresh$_1$ [E_h])	LDMRG(50)	LDMRG(100)	LDMRG(250)
C_kH_{k+2} (10^{-6})	2.12±0.02	2.11±0.01	2.07±0.09
C_kH_{k+2} (10^{-7})	2.11±0.02	2.11±0.01	2.10±0.03
C_kH_{k+2} (10^{-8})	2.12±0.01	2.07±0.02	2.09±0.03
C_kH_{k+2} (10^{-20})	3.27±0.08	3.33±0.10	3.53±0.06
$(H_2)_{k/2}$ (10^{-7})	2.36±0.06	2.18±0.05	2.16±0.04

Table 2.5: *All-trans*-polyenes: Active space correlation energies from LDMRG(250) with screening thresholds 10^{-6} E_h and 10^{-7} E_h; absolute and relative errors of 10^{-6} E_h-screening (compared to the exact results from 10^{-7} E_h-screening). All energies are given in hartree.

	E_{corr}^{act}			
Molecule	(10^{-6} E_h)	(10^{-7} E_h)	Δ_{abs}	Δ_{rel} [%]
C_8H_{10}	-0.177 127	*conv.*	0	0
$C_{16}H_{18}$	-0.347 405	-0.347 404	-0.000 001	-0.46×10^{-5}
$C_{32}H_{34}$	-0.687 765	-0.687 777	0.000 008	1.52×10^{-5}
$C_{40}H_{42}$	-0.857 942	-0.857 963	0.000 021	3.01×10^{-5}
$C_{48}H_{50}$	-1.028 093	-1.028 149	0.000 056	6.41×10^{-5}

ber of sweeps, holding the number of DMRG states M fixed. We observed that on average, convergence was achieved in only 4 – 6 sweeps for small M and 2 – 4 sweeps for large M values (not inclusive of the noise sweeps and the preceding sweeps in the schedule).

The second type of convergence relates to the approach of the DMRG energy

to the exact energy as the number of retained states M is increased. Here, we analyze our data for the DMRG calculations on polyenes with different M values. The precise analytic form of the DMRG energy convergence as a function of M has been a matter of debate in the literature [129, 3, 165, 166, 105]. We have previously found good agreement with the proposed form of Okunishi et al. [165, 166],

$$\Delta E(M) \sim \exp\left[-\kappa \left(\log M\right)^{\alpha}\right], \; \alpha = 2 \tag{2.7}$$

which is slower than exponential but still faster than algebraic. In Fig. 2.7 we plot the logarithm of the percentage error in the correlation energy against $(\log M)^2$, which shows a clear linear fit. By contrast, the inlay plots the logarithm of the percentage error against M, which demonstrates that the error indeed does not decay exponentially. Fitting our data (omitting $M = 5$) to the general form of eqn. (2.7) we obtained an exponent of $\alpha \sim 1.6 - 1.8$. Fixing $\alpha = 2$, we obtain values between $\kappa = 1.80 \pm 0.03$ (for $C_{12}H_{14}$) and $\kappa = 1.45 \pm 0.03$ (for $C_{48}H_{50}$).

Corresponding to the rapid energy convergence we also observed a rapid decrease of the truncated weight of the density matrix as M is increased. This shows that the local representation is well suited to the chemical system and physical problem at hand [167, 137, 4].

2.5.5 Comparison with perturbation and coupled cluster theories

In the polyene calculations (Table 2.2) the largest DMRG absolute error is 35 μE_{h} for the $C_{48}H_{50}$ molecule at the $M = 50$ level. This corresponds to $\sim 10^{-3}$% of the exact active space correlation energy, and $\sim 10^{-5}$% of the exact total active

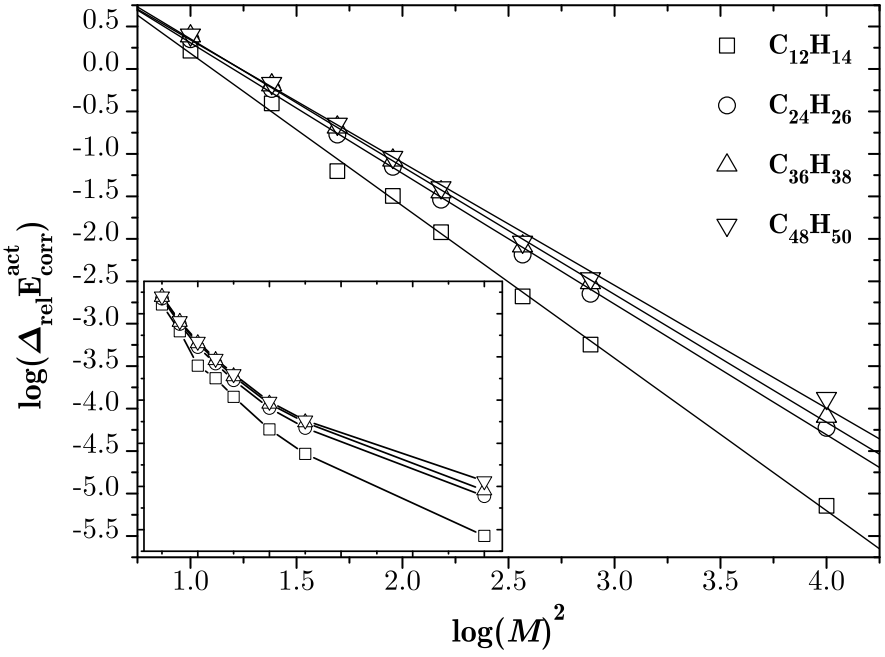

Figure 2.7: *All-trans*-polyenes: Convergence of the relative errors in the active space correlation energies for LDMRG as a function of M (compared to the exact LDMRG(250) results). The main plot shows magnitudes in logarithmic scale over $\log(M)^2$ (with linear fit), the inlay shows them over $\log(M)$.

space electronic energy. Compared to the coupled cluster errors, LDMRG(50) is already better by 2-3 orders of magnitude. The LDMRG(100) gives a further order of magnitude improvement, and is essentially exact. In our more approximate calculations (Fig. 2.5) we find that LDMRG with $M = 10$ performs better than MP2, and with $M = 15$ better than CCSD and CCSD(T). The results for $M = 5$ are not reliable due to loss of important quantum numbers.

Surprisingly we observe that the CCSD(T) results lie below the exact energies computed with LDMRG. This may be related to the small size of the basis

and in general the triples correction performed relatively badly for the polyenes.

In case of the hydrogen chains, the convergence of the LDMRG with M was more rapid and results were already exact with $M = 50$. CCSD(T) also performed better in this system, the triples correction improved on CCSD by 1/2 order of magnitude, and the resulting energies were consistently above the exact energies.

2.6 The metal-insulator transition in linear hydrogen

As an example of a challenging electronic problem, we studied the symmetric and asymmetric bond stretching in a linear H_{50} chain. In both these cases, the system transitions from a state with metallic correlations at compressed geometries to an insulating state with strong multi-reference correlation in the dissociation region. This bond breaking process hence exhibits a varying nature of chemical bonding and electron correlation.

In case of the symmetric dissociation we begin with a uniform bond distance between all H-atoms of R=1.0a_0, and stretch all 49 bonds symmetrically and simultaneously to R=1.2, 1.4, ..., 4.2a_0. The final structure consists of 50 equidistant, nearly-independent H-atoms on a line.

In case of the asymmetric dissociation we distinguish alternating bonds as intermolecular and intramolecular with R_{inter} and R_{intra}. The first geometry is R_{intra}=R_{inter} =1.4a_0. In the following geometries R_{intra} is kept fixed at 1.4a_0 while R_{inter} grows to R_{inter}=1.6, 1.8, ..., 4.2a_0. The final structure consists of 25 equidistant, nearly-independent H_2 molecules at equilibrium bond distance on a line.

We computed the electronic energy using the LDMRG (with up to 1000 states) in the minimal STO-6G basis, where we correlated all 50 electrons in 50 orbitals.

All calculations were carried out in the STO-6G basis correlating all electrons (50 electrons in 50 orbitals). The LDMRG calculations again used the $S^{-1/2}$ basis.

2.6.1 Symmetric dissociation

The calculated energies for the symmetric dissociation are summarized in Table 2.6. The potential energy curves at RHF, MP2, and exact LDMRG level of theory are plotted in Fig. 2.8. It can immediately be seen how the contribution of correlation increases along the dissociation coordinate: In the dissociation limit the share of the correlation energy in the total energy grows to ~20% and in the electronic energy to ~7%, which emphasizes the importance of nondynamic correlation in this problem.

As is expected, RHF and MP2 behave poorly as the chain dissociates. The coupled cluster energies cannot even be converged for bond lengths R>2.0a_0. This is a fundamental problem in CC theory that is well documented e.g. in the work of Takahashi, Paldus and coworkers [168, 169, 170] where in one-dimensional systems, even for physically relevant coupling parameters, the coupled cluster doubles equations may have no real solutions. The correlation energy errors for different methods relative to the exact LDMRG results are shown in Fig. 2.9.

It is understood that we need to retain more states in the LDMRG in the

Table 2.6: Symmetric dissociation of H_{50}: Total RHF energy, RHF electronic energy; correlation energies at MP2, CCSD, CCSD(T) and various LDMRG levels of theory. All LDMRG results with $M \geqslant 500$ converged. The coupled cluster calculations for larger R could not be converged (see text). All energies are given in hartree.

			E_{corr}						
R [a_0]	E_{RHF}	$E_{RHF,el}$	MP2	CCSD	CCSD(T)	LDMRG(50)	LDMRG(100)	LDMRG(250)	LDMRG(500)
1.0	-16.864 88	-191.825 14	-0.361 45	-0.407 29	-0.417 39	-0.402 *72*	-0.417 27	-0.419 14	-0.419 19
1.2	-22.461 27	-168.261 49	-0.401 83	-0.470 11	-0.483 30	-0.475 *90*	-0.485 21	-0.486 35	-0.486 38
1.4	-25.029 76	-150.001 38	-0.444 73	-0.543 03	-0.559 36	-0.557 *16*	-0.563 30	-0.564 00	-0.564 02
1.6	-26.062 25	-135.412 42	-0.491 88	-0.631 18	-0.650 89	-0.652 *72*	-0.656 74	-0.657 18	-0.657 19
1.8	-26.265 98	-123.466 13	-0.545 50	-0.741 67	-0.765 47	-0.769 *82*	-0.772 42	-0.772 66	-0.772 67
2.0	-26.008 20	-113.488 34	-0.607 89	-0.883 29	-0.912 70	-0.916 *11*	-0.917 76	-0.917 89	*conv.*
2.4	-24.835 76	-97.735 87	-0.768 83	–	–	-1.324 16	-1.324 77	-1.324 81	*conv.*
2.8	-23.360 81	-85.846 62	-0.995 30	–	–	-1.913 81	-1.913 98	-1.913 99	*conv.*
3.2	-21.896 33	-76.571 41	-1.307 78	–	–	-2.671 *90*	-2.671 95	*conv.*	*conv.*
3.6	-20.574 29	-69.174 36	-1.723 32	–	–	-3.528 46	-3.528 48	*conv.*	*conv.*
4.2	-18.955 95	-60.613 15	-2.558 99	–	–	-4.793 76	*conv.*	*conv.*	*conv.*

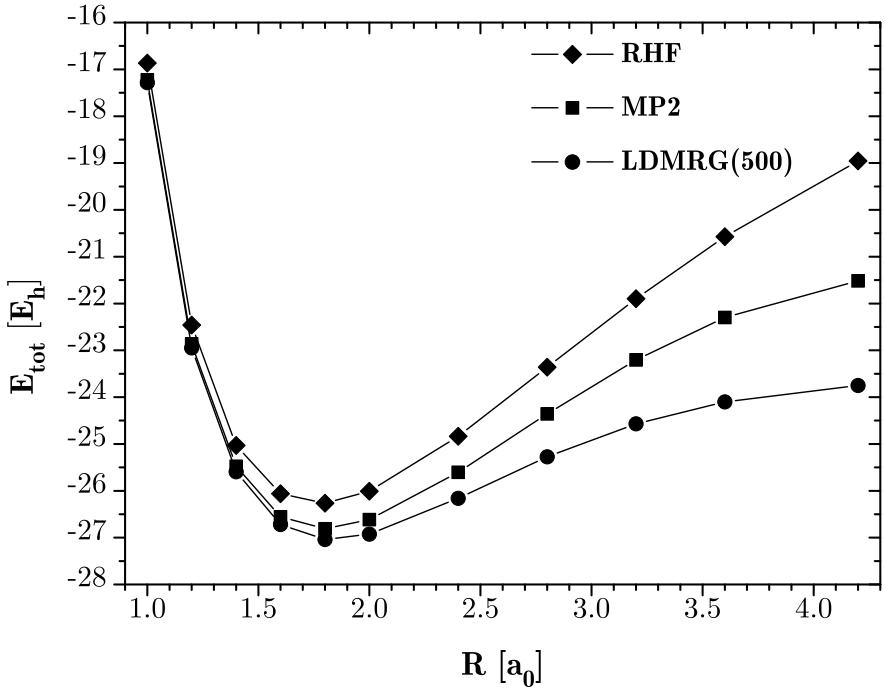

Figure 2.8: Symmetric dissociation of H_{50}: Potential energy curves from RHF, MP2, and exact LDMRG. On the scale of the graph, the few available CCSD and CCSD(T) datapoints were indistinguishable from the LDMRG data.

metallic regime if we start from a local atomic orbital basis, since we need to capture the delocalization and long-range off-diagonal correlations [4]. We find that both the convergence with the number of sweeps as well as with M is slower as compared to calculations in the nonmetallic regime. At R=1.0a_0 LDMRG(50) is worse than CCSD, LDMRG(100) slightly worse than CCSD(T), and for R<1.6a_0 LDMRG(50) is still worse than CCSD(T). In the metallic region LDMRG required M = 500 to converge to the numerically exact result. In essence, by using orthonormalized atomic orbitals, we are starting from a particularly unfavorable one-particle basis to describe metallic behavior. By performing the DMRG

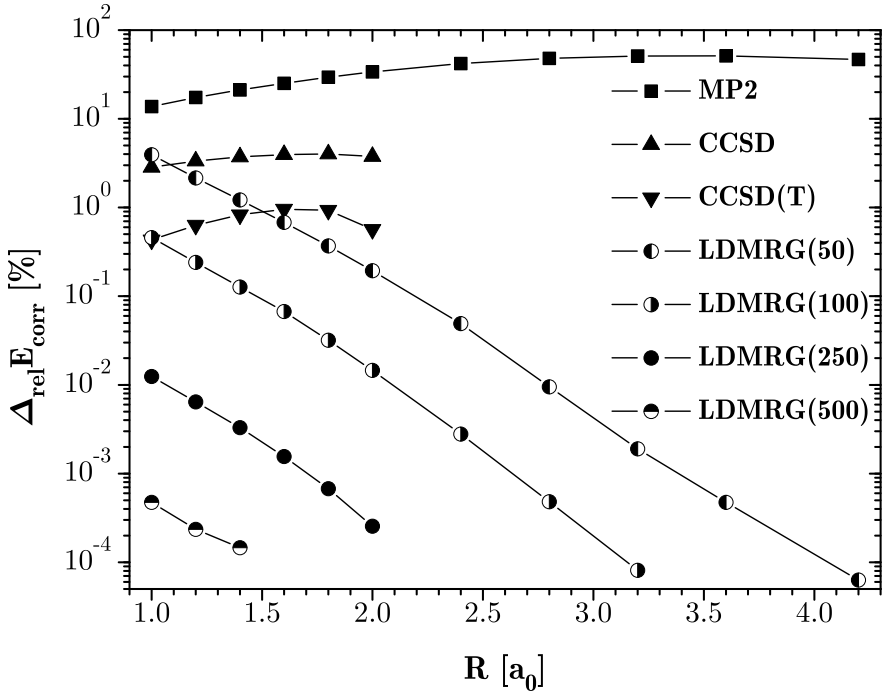

Figure 2.9: Symmetric dissociation of H_{50}: Relative errors in the correlation energies at MP2, CCSD, CCSD(T), and different LDMRG levels of theory (compared to the exact LDMRG results) in logarithmic scale.

in a set of separately localized occupied and virtual orbitals such as Boys orbitals [171], we expect that the degradation in efficiency of the DMRG would be avoided.

2.6.2 Asymmetric dissociation

The calculated energies for the asymmetric dissociation are summarized in Table 2.7. In this system, the restricted Hartree-Fock reference dissociates correctly (to a set of non-interacting hydrogen molecules), which can be understood by

Table 2.7: Asymmetric dissociation of H_{50}: Total RHF energy, RHF electronic energy; correlation energies at MP2, CCSD, CCSD(T) and various LDMRG levels of theory. All results with $M \geqslant 500$ converged. Energies are given in hartree.

			E_{corr}						
R_{inter} [a_0]	E_{RHF}	$E_{RHF,el}$	MP2	CCSD	CCSD(T)	LDMRG(50)	LDMRG(100)	LDMRG(250)	LDMRG(500)
1.4	-25.029 76	-150.001 38	-0.444 73	-0.543 03	-0.559 36	-0.557 16	-0.563 30	-0.564 00	-0.564 02
1.6	-25.963 71	-142.811 31	-0.392 61	-0.516 01	-0.522 30	-0.523 02	-0.523 64	-0.523 67	*conv.*
1.8	-26.617 68	-136.573 91	-0.369 20	-0.505 47	-0.508 73	-0.509 38	-0.509 48	*conv.*	*conv.*
2.0	-27.071 82	-131.089 88	-0.357 01	-0.503 04	-0.504 97	-0.505 48	-0.505 50	*conv.*	*conv.*
2.4	-27.609 24	-121.878 99	-0.346 20	-0.507 17	-0.508 03	-0.508 37	*conv.*	*conv.*	*conv.*
2.8	-27.873 62	-114.445 23	-0.341 62	-0.512 77	-0.513 22	-0.513 45	*conv.*	*conv.*	*conv.*
3.2	-28.004 68	-108.324 99	-0.338 67	-0.516 18	-0.516 42	-0.516 56	*conv.*	*conv.*	*conv.*
3.6	-28.069 65	-103.203 54	-0.336 34	-0.517 50	-0.517 63	-0.517 71	*conv.*	*conv.*	*conv.*
4.2	-28.111 00	-96.924 54	-0.333 73	-0.517 49	-0.517 54	-0.517 58	*conv.*	*conv.*	*conv.*

changing to a localized basis in the space of restricted occupied orbitals. For this reason, the restricted MP2 and CC theories are also qualitatively correct and we see that their energies (Fig. 2.10) lie parallel to the exact LDMRG values along the dissociation curve. Unlike in the symmetric dissociation, the correlation energy saturates rapidly to $\sim$ 1.8% of the total energy as the bonds are stretched. Fig. 2.11 shows how the percentage errors in the correlation energy for the different methods decrease along the dissociation coordinate. Again, we see reduced performance of the DMRG in the metallic regime due to the unsuitability of the underlying orbital basis, but still a systematic convergence with M. For large R_{inter} we observed very rapid convergence with M and number of sweeps, and in fact for R_{inter}=4.2a_0 the LDMRG energy was already exact after 4 noise sweeps with $M = 50$. In the limit of complete dissociation, the CCSD theory becomes exact for this system and this is confirmed by convergence to the LDMRG results.

In order to demonstrate the metal-insulator transition more explicitly we computed the one-particle reduced density matrix γ during our LDMRG calculations. In Fig. 2.12 we have plotted the off-diagonal decay of the α one-particle density matrix from element $\gamma_{25,25} \rightarrow \gamma_{25,50}$. In the metallic regime (short R_{inter}) we see the long-ranged oscillations in the off-diagonal elements, while in the insulating regime (long R_{inter}) the off-diagonal elements decay much more rapidly. A similar picture is obtained from the density matrix during symmetric dissociation.

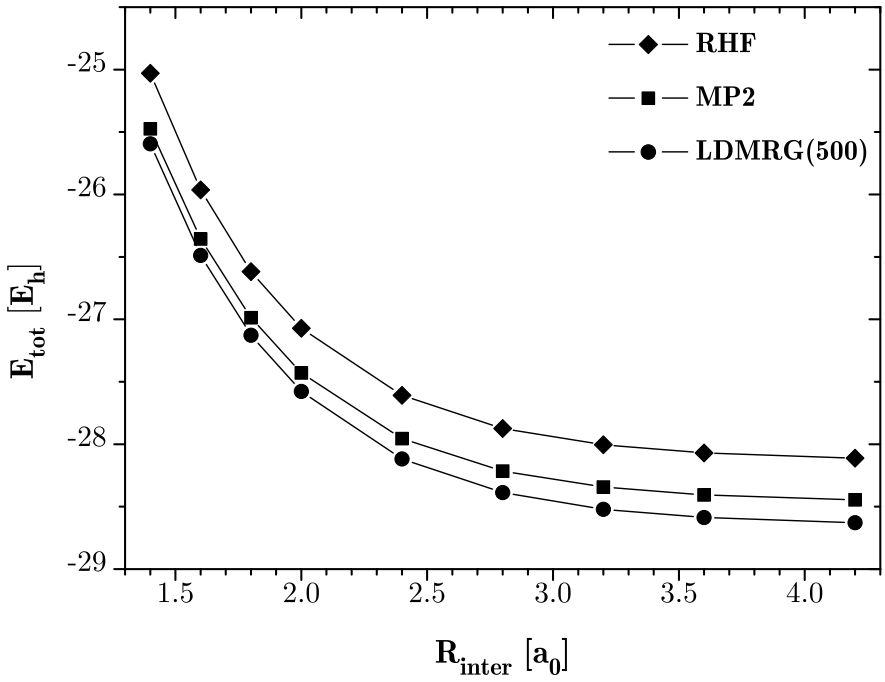

Figure 2.10: Asymmetric dissociation of H_{50}: Potential energy curves from RHF, MP2, and exact LDMRG. On the scale of the graph, the LDMRG, CCSD, and CCSD(T) curves are indistinguishable.

2.7 Conclusions

We began this work with the question of how to describe static correlation in large systems with the restriction that such systems are large in only one dimension. In our investigations, we have shown how the density matrix renormalization group provides a natural answer to this problem. The matrix product state that underlies the DMRG is a local, variational, size-consistent, size-extensive, and inherently multi-reference ansatz that can efficiently exploit the special structure of quasi-one-dimensional correlation. Using the intrinsic locality of the ansatz, we have formulated a *quadratic* scaling DMRG algorithm,

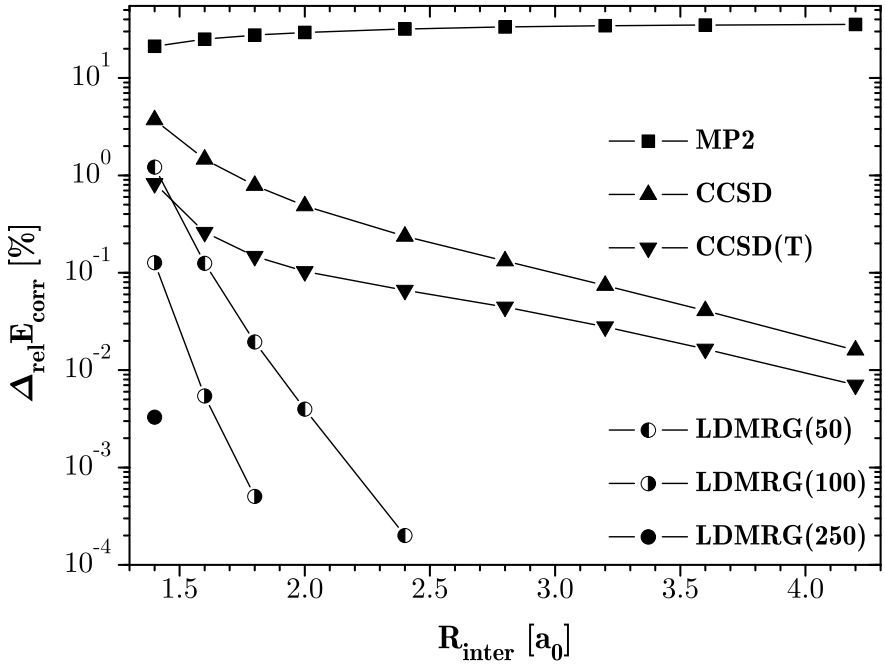

Figure 2.11: Asymmetric dissociation of H_{50}: Relative errors in the correlation energies at MP2, CCSD, CCSD(T), and different LDMRG levels of theory (compared to the exact LDMRG results) in logarithmic scale.

using only a straightforward screening framework without the imposition of correlation domains. Due to its multi-reference nature, the LDMRG also bypasses the problems associated with localization of separated or restricted orbital subspaces. With this CAS method, we could then obtain numerically exact solutions of the many-particle Schrödinger equation for *all-trans*-polyenes up to $C_{48}H_{50}$ (correlating the π_z-electrons) and hydrogen molecular chains up to $(H_2)_{50}$ (correlating 100 electrons in 100 orbitals). To date, the latter is still the largest numerically exact solution of the Schrödinger equation with the full nonrelativistic, electronic Hamiltonian.

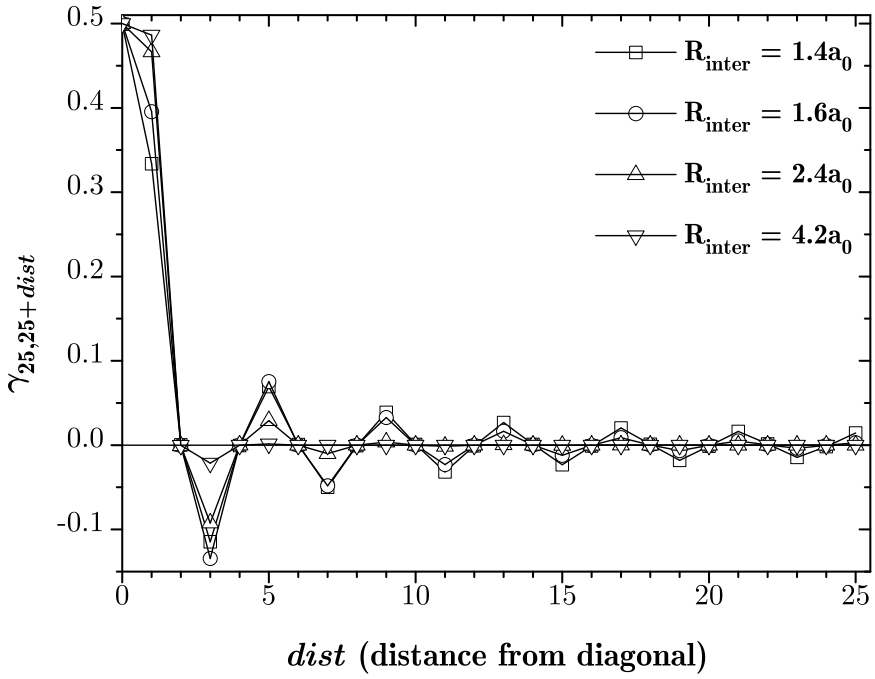

Figure 2.12: Asymmetric dissociation of H_{50}: Half-cross-section of the LDMRG α-one-particle density matrix at α-orbital no. 25.

By construction, a unique advantage of the LDMRG as compared to other local correlation methods is its ability to capture static correlation. We can take advantage of locality in multi-reference problems so long as the correlation length is finite. We have demonstrated the capability and efficiency of the LDMRG in these situations by obtaining numerically exact correlation energies in the metal-to-insulator transition of linear H_{50} chains, where we correlate 50 electrons in 50 orbitals.

With the possibility of accurately capturing nondynamic correlation in long molecules, we can now begin to address the quantitative description of strongly interacting states as found in the spectrum of materials such as the conjugated

organic polymers. Here, the natural next step would be to combine an LDMRG description of the static correlation in the active π-space with recent developments in perturbationand canonical transformation theory [61, 62, 63, 64, 65] in the Chan Group, to incorporate the dynamic correlation that arises in larger basis sets.

CHAPTER 3

THE RADICAL CHARACTER OF THE ACENES

We present a detailed investigation of the acene series using high-level wavefunction theory. Our local *ab initio* density matrix renormalization group algorithm has enabled us to carry out complete active space calculations on the acenes from napthalene to dodecacene correlating the full π-valence space. While we find that the ground-state is a singlet for all chain-lengths, examination of several measures of radical character, including the natural orbitals, effective number of unpaired electrons, and various correlation functions, suggests that the longer acene ground-states are *polyradical* in nature.

Some of the early initial DMRG calculations on acenes in model geometries were set up by Jonathan J. Dorando and Michael Avilés. Funding by a Kekulé Fellowship of the Fond der Chemischen Industrie (Fund of the German Chemical Industry) is acknowledged. The results of this study were published in 'J. Hachmann, J. J. Dorando, M. Avilés, G. K.-L. Chan, *J. Chem. Phys.* 127 (**2007**), 134309' [172], and this chapter is based on our exposition in this paper.

3.1 Background

The acenes are the series of ladder-like compounds consisting of linearly-fused benzene rings (Fig. 3.1) [173, 174]. Due to their technological potential as organic electronic materials [175, 176, 177] and their intrinsic value as models for more complex conjugated molecules, they have been the subject of many theoretical and experimental investigations [178, 179, 180, 181, 182, 183, 184, 185, 186]. In a number of recent studies, it has been proposed that longer acenes

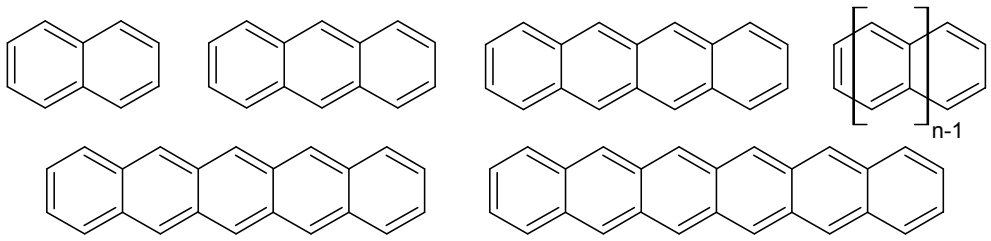

Figure 3.1: The first few members and the unit cell of the acene series.

may possess an unusual electronic ground-state that is not the simple closed-shell singlet suggested by molecular orbital arguments. Based on extrapolating the experimental singlet-triplet gap of the acenes up to pentacene, Angliker *et al.* [179] predicted that the ground state of higher acenes from nonacene upwards would be a triplet. Density functional calculations by Houk *et al.* [183] also predicted a singlet-triplet cross-over. However, Bendikov *et al.* [184] noted that the restricted singlet density functional ground-state would become unstable to an open-shell singlet, or *singlet diradical*, configuration for acenes longer than hexacene. The open-shell singlet-triplet gap for the longest acene studied (decacene) was estimated as ranging from 1.5 (BLYP/6-31G(d)) to 5.7 (B3LYP/6-31G(d)) kcal/mol.

Despite these intriguing findings, the density functional results leave many interesting questions unanswered. For example, how diradicaloid are the acenes really compared to conventional diradical systems? As we go to longer acenes, might we expect to find tri- and even higher polyradical ground states? And if so, how do we understand the electronic structure and bonding in these states? Such questions, which probe the essential *many-electron* character of di- (and indeed poly-) radicalism, are not easily answered through density func-

tional theory based on a single Kohn-Sham determinant.

For this reason we have decided to explore the nature of the acene ground-state using high-level wavefunction-based electronic structure theory. The many-electron correlations in radical wavefunctions tell us about the coupled simultaneous motions of the electrons. Conceptually, singlet states with unpaired electrons require multi-configurational wavefunctions [187, 188, 189, 190, 191, 192, 193, 194, 195] as used, for example, in the complete active space family of methods [196]. In the acenes, the ideal choice of active space would be the complete π-valence space, i.e., the set of all conjugated p_z orbitals. However, the exponential cost of traditional CAS methods as a function of the number of correlated orbitals and electrons renders calculations with the complete π-valence space impossible for acenes much longer than anthracene, which already has 14 conjugated orbitals and electrons (cf. Sec. 1.1.8). Consequently, earlier CAS calculations could only use an incomplete π-valence space [197, 184].

As discussed before, the density matrix renormalization group provides a way to overcome the traditional exponential complexity of CAS methods in long molecules such as the acenes [198, 199]. We will employ the local *ab initio* DMRG method introduced in the previous chapter to compute an essentially exact CAS wavefunction with an effort that scales only quadratically with the length of the molecule[1]. Consequently, we can now extend the range of traditional CAS calculations in the acene series to significantly longer oligomers of relevant size. In the current work we apply our *ab initio* DMRG algorithm to the acene series from napthalene (2-acene) to dodecacene (12-acene), in all cases correlating exactly the complete π-valence space. First we revisit the question of

[1] All calculations in this chapter are performed using our LDMRG algorithm, but for simplicity we will use the general term DMRG.

the relative stabilities of the singlet and triplet states. Then, using our correlated wavefunctions, we embark on a detailed study of the radical nature of these systems. We find intriguingly that the higher acenes are not only diradicals, but possess increasing polyradical character. By explicit visualization of the electron correlation, we uncover a coupled motion of the electrons that gives a new picture of bonding in molecules with extended conjugation, showing that even systems such as the acenes can continue to provide fertile sources of surprising electronic structure.

3.2 Computational methodology

In the present context, we can regard the DMRG as an efficient way to exactly correlate, in the sense of full configuration interaction, the electrons in the active space. Active space full configuration interaction theory is sometimes referred to as CASCI. Recall that CASCI is the same as the more common CASSCF (complete active space self-consistent field) method [196] but lacks the step of orbital optimization. Orbital optimization is possible within the DMRG and was implemented after completion of this study within the Chan Group [108], as well as by Zgid and Nooijen [114], but has not been used here. For the molecules in this work, the DMRG energies are converged to better than 0.1 kcal/mol and would be identical to the so-called CASCI energies if it were possible to compute these in the traditional manner.

DMRG calculations on the acenes were performed at the UB3LYP/6-31G(d) [200, 201] optimized singlet and triplet geometries which were essentially the same as those used by Bendikov *et al.* [184]. These structures have D_{2h} point-

group symmetry. The rung C-C bonds are somewhat longer than the ladder C-C bonds and the ladder C-C bonds display increasing bond alternation towards the ends of the chain. For example in singlet decacene, the rung and ladder C-C bonds were 1.464 Å and 1.405 Å respectively at the middle of the chain, while the difference in successive ladder C-C bonds lengths was 0.058 Å at the end of the chain as compared to 0.010 Å at the middle. We point out that the geometry – in particular symmetry, bond-length alternancy and Peierls distortion– can potentially have an important effect on the spin gap and electronic structure of the acenes [180], and it is an open question, whether the DFT geometries are a good representation of the actual geometries in the long chain length limit.

The active space was chosen to be the complete π-valence space, consisting of all conjugated carbon p_z orbitals, and all π-electrons were correlated. The σ-electrons were treated within a frozen-core approximation using the restricted Hartree-Fock orbitals. The calculations used either the minimal STO-3G basis [202] (up to dodecacene) or Dunning's double-ζ DZ [203, 204] basis (up to hexacene) as indicated. In the case of the DZ basis, two p_z orbitals per carbon were used to make a 'double' complete π-valence space. Thus whereas e.g. the DMRG/STO-3G calculations for pentacene correspond to a (22e,22o) CASCI, the DMRG/DZ calculations would correspond to a (22e,44o) CASCI.

3.3 The singlet-triplet gap

In Fig. 3.2 we present the computed DMRG singlet-triplet energy gaps as a function of the acene length. The calculations on dodecacene correspond to a (50e, 50o) CASCI and are only made possible through the DMRG algorithm. In-

cluded for comparison are the UB3LYP/6-31G(d) and UBLYP/6-31G(d) singlet-triplet gaps (using open-shell wavefunctions where stable) as first reported by Bendikov *et al.* [184], which we have recomputed and extended to the complete set of acenes studied here [205]. While experimental triplet energies are somewhat difficult to compare directly with theoretical gas phase calculations, we have also included current experimental estimates where available[2] [206, 207, 208, 209].

Our DMRG calculations clearly confirm that the acenes maintain a singlet ground-state configuration and that there is a finite singlet-triplet gap for all chain-lengths. Going from the minimal STO-3G to the DZ basis and the corresponding larger double-active space, the singlet-triplet gap decreases by a few kcal/mol. With the DZ basis the hexacene DMRG gap is 17.5 kcal/mol. The remaining error in the DMRG calculations arises from the neglect of dynamical and σ-π-correlations, which would generally further decrease the gap size. However, we estimate the effect of dynamical correlation on the gap to be very small when using the complete (and the double complete) π-valence space, on the order of a few kcal/mol. In Table 3.2 we present additional CASSCF and CASPT2 results (including the CASSCF and MRMP calculations of Kawashima *et al.* [197]) for the smaller acenes to estimate the effects of dynamical correlation. CASPT2 [210] and MRMP [211] both incorporate dynamical correlation on top of the CASSCF reference through 2nd-order perturbation theory. We observe in naphthalene that when using a complete π-valence space the CASSCF singlet-triplet gap is very close (within 1-2 kcal/mol) to the CASPT2 singlet-triplet gap. It is only when incomplete active spaces are used that the CASPT2/MRMP gap is significantly different from the CASSCF gap. In all cases, the DMRG complete

[2]The hexacene 'experimental' number reported in Houk *et al.* [183] is in fact the theoretical extrapolation given in [179] and is too low.

Table 3.1: Singlet-triplet gap ($E_t - E_s$) energies in kcal/mol for the acene series.

[n]acene	DMRG/STO-3G	DMRG/DZ	UB3LYP/6-31G(d)	UBLYP/6-31G(d)	Experiment
2	61.5	61.0	62.6	60.4	61.0 [206]
3	45.9	44.0	41.8	40.2	43.1 [207]
4	34.7	31.9	27.7	26.7	29.3 [208]
5	26.7	23.4	17.9	17.4	19.8 [209]
6	21.0	17.5	10.9	10.9	–
8	14.2	–	5.8	3.0	–
10	11.6	–	5.6	1.7	–
12	10.7	–	7.3	2.5	–

and double π-valence space gaps are closer to the experimental result than the MRMP gap in an incomplete active space. This highlights the importance of the complete π-valence space for π-electron excitations.

Comparison of the UBLYP and UB3LYP gaps with the experimental data suggests that the DFT results are an underestimate. This is particularly true for UBLYP which substantially underestimates the gap. Surprisingly, the DFT gaps appear to *increase* between 10-acene and 12-acene, which clearly points to a failure of the single-reference picture.

Using our DMRG data we can extrapolate to the infinite polyacene limit. Empirically, we find that the singlet-triplet gap is well fitted by an exponential form $a + be^{-c}$, giving a gap for the infinite chain of 8.69 ± 0.95 (STO-3G) and 3.33 ± 0.39 (DZ) kcal/mol respectively, somewhat lower than the previous estimate of 12.2 kcal/mol obtained by Raghu *et al.* [199] using the semi-empirical Pariser-Parr-Pople (PPP) Hamiltonian [98, 99].

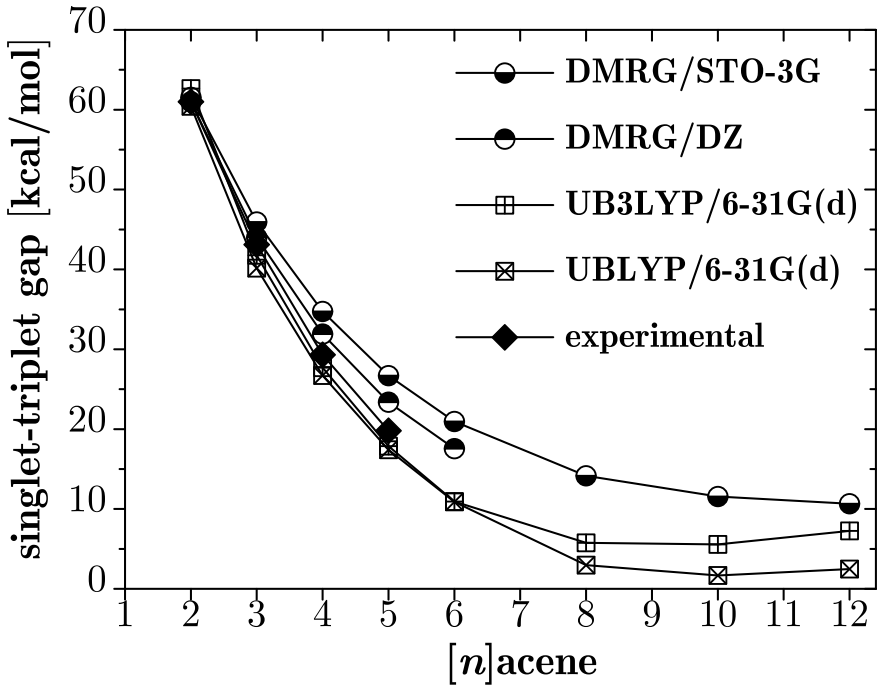

Figure 3.2: Singlet-triplet energy gap as a function of the acene length.

3.4 Polyradical character of the ground-state

Having established that the acene ground-states are singlets, are they then singlet diradicals as argued by Bendikov *et al.* [184]? A simple way to establish whether there are unpaired electrons in a correlated wavefunction is to examine the occupation numbers of the (spinless) natural orbitals – in a closed shell configuration, these are always 2 (doubly occupied) or 0 (unoccupied), while values close to 1 indicate single occupancy and unpaired electrons [212]. In Fig. 3.3 we plot the occupancies of the natural orbitals for the acene series. We have designated the two orbitals with occupancies closest to 1 the HONO ('highest occupied natural orbital' with occupancy greater than 1) and LUNO ('lowest

Table 3.2: Effect of active-space size and dynamic correlation on the singlet-triplet gap in smaller acenes. Complete = complete π-valence space, double = double π-valence space, partial = incomplete active space: 2-acene (8,8), 3- and 4-acenes (12,12). DZP = Dunning DZ basis with polarization functions [203, 204] except for results of Kawashima *et al.* [197]. All energies in kcal/mol.

[1]CASSCF/MRMP calculations of Kawashima *et al.* [197]; vertical singlet-triplet gap in a cc-pVDZ basis without polarization functions on H.

[*n*]acene	2	3	4
complete/DZ			
CASSCF	61.1	–	–
CASPT2	60.5	–	–
complete/DZP			
CASSCF	61.1	–	–
CASPT2	59.7	–	–
partial/DZP			
CASSCF	67.1	60.0[1]	47.3[1]
CASPT2/MRMP	56.9	46.1[1]	34.8[1]
complete/STO-3G			
DMRG	61.5	45.9	34.7
double/DZ			
DMRG	61.0	44.0	31.9
experiment	61.0	43.1	29.3

unoccupied natural orbital' with occupancy less than 1) respectively. These natural orbitals together with usual HOMO and LUMO are shown in Fig. 3.4.

As can be seen, as we proceed to longer acenes the occupancy of the HONO and LUNO indeed approach 1, which is consistent with Bendikov *et al.*'s prediction of diradical character. The DZ basis, while yielding less radical character (e.g., the occupancy of the HONO in pentacene is 1.66 and 1.73 using the STO-

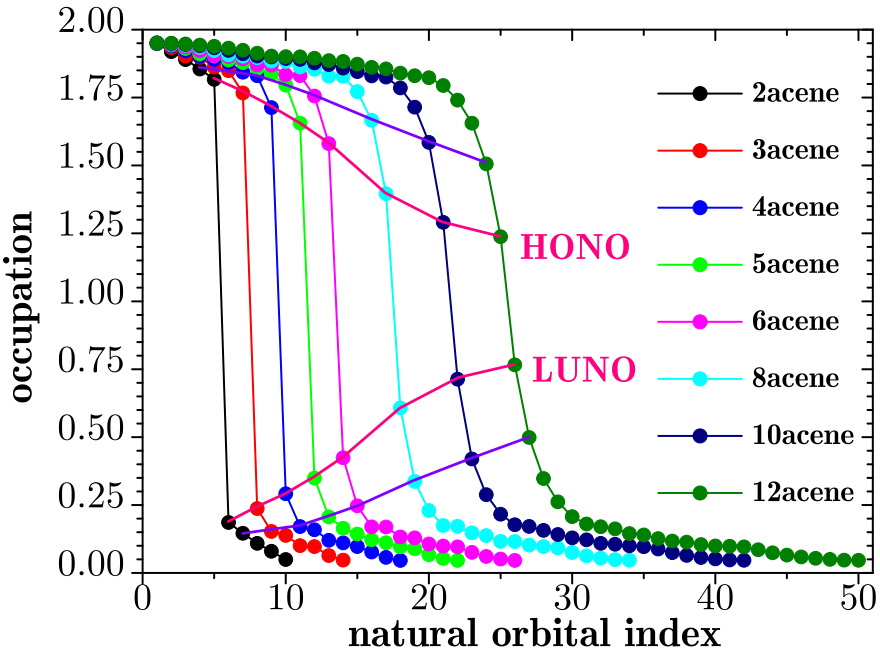

Figure 3.3: Natural orbital occupation numbers for the acene series in the STO-3G basis. The lines are guides for the eye to show the evolution of the occupation numbers for the near-singly occupied orbitals as a function of chain length.

3G and DZ bases, respectively) shows the same general behavior. The decreased radical character in the DZ basis is consistent with the general observation that radical character is reduced by dynamic correlation. However, what is surprising is that if we follow the *trend* for the next nearest single occupancy orbitals (the HONO-1 and the LUNO+1), the rate at which they approach single occupancy is comparable to that of the HONO and LUNO. This suggests that if we were to proceed to acenes longer than the 12-acene, *we would eventually find not a diradical ground-state, but a polyradical ground-state*.

Several different measures of the number of 'effectively unpaired' electrons

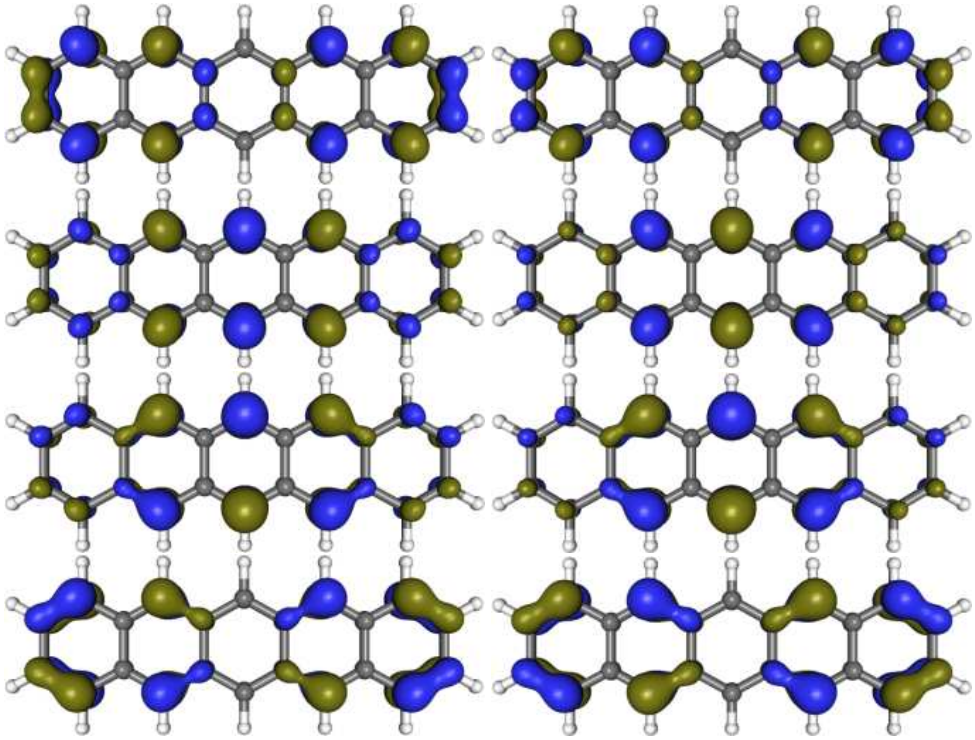

Figure 3.4: Plots of the pentacene molecular orbitals (left: LUMO+1, LUMO, HOMO, HOMO-1) and natural orbitals (right: LUNO+1, LUNO, HONO, HONO-1).

in a molecule have previously been proposed. While such integrated measures must contain less information than the underlying distribution of natural orbital occupations examined above, we include them here for completeness. We have investigated two measures, due to Takatsuka [213, 214, 215, 216, 217] and Head-Gordon respectively, [218, 219, 220], defined via

$$n_{\text{unpaired}}^{\text{Takatsuka}} = \sum_i 2n_i - n_i^2 \tag{3.1}$$

$$n_{\text{unpaired}}^{\text{Head-Gordon}} = \sum_i \min(n_i, 2 - n_i) \tag{3.2}$$

Here n_i is the occupation number of the ith natural orbital, which ranges from 0 to 2. The contribution from each orbital is a maximum when $n_i = 1$, whence each orbital contributes 1 electron to the effective number of unpaired electrons.

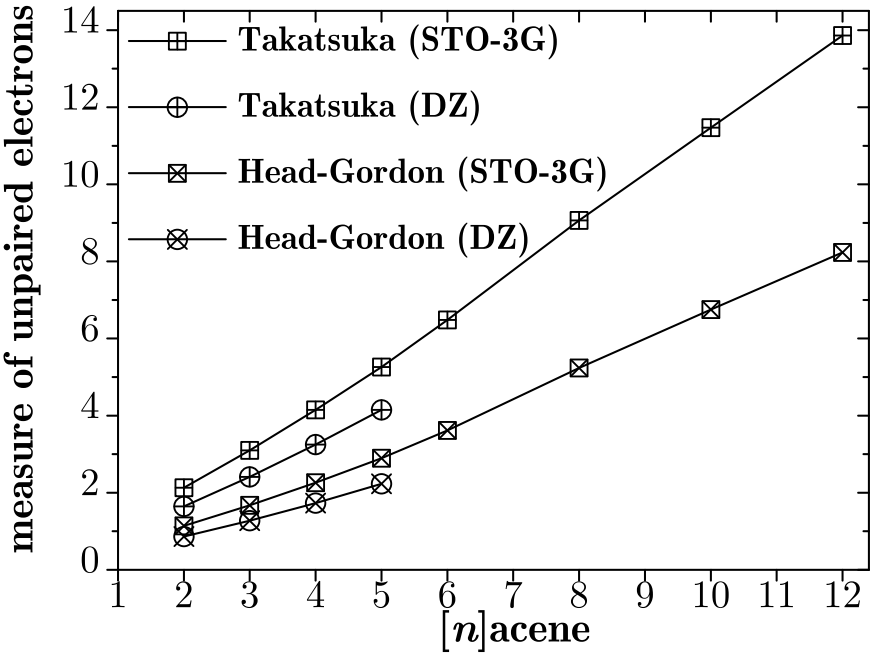

Figure 3.5: Measures of the number of unpaired electrons in the acene series. See comment in text.

These measures are plotted for the acenes in Fig. 3.5.

Some care must be taken when interpreting Fig. 3.5. Certainly, the values must not be taken literally; 12-acene does not contain 14 unpaired electrons! Both measures are extensive, meaning that they increase with the size of the molecule. (This also means that a large enough assembly of nearly closed-shell molecules would appear to have a substantial number of unpaired electrons using these measures. In such a case, however, the HONO and LUNO occupation numbers would *not* change and would stay near 2 and 0 as the number of molecules is increased, unlike what we see in the acenes). However, extensive scaling should only be observed for system sizes larger than the typical size of

an unpaired electron. Examination of the gradients of the plots in Fig. 3.5 shows an onset of extensive scaling around hexacene, which is consistent with the observation of Bendikov *et al.* that the first symmetry breaking of the density functional calculations occurs also at this chain-length. This further suggests that we can roughly associate *one unpaired spin with every five to six rings*.

3.5 Visualizing electron correlations

3.5.1 Theoretical background

We have now shown that the longer acenes are not only singlet diradicals but exhibit increasingly polyradical character.How are we to understand its electronic structure? We can visualize the simultaneous behavior of the multiple electrons involved in the polyradical behavior through their correlation functions. Correlation functions have long been used to understand bond-alternation and electron correlation in conjugated systems [221, 198]. We have evaluated three correlation functions, the particle-particle, spin-spin, and singlet diradical correlation functions which we now describe. In this section we shall be concerned with the correlations of the electrons in real-space. Thus in the following, indices i and j always refer to the (orthogonalized) p_z *atomic* orbitals on atoms i and atom j respectively. $\langle n_i^\sigma \rangle$ and $\langle S_i^z \rangle$ refer to the average σ occupancy and z-component of the spin in these orbitals.

Particle-particle:

$$C_{\text{particle}}(i,j) = 4\left(\langle n_i^\alpha n_j^\beta \rangle - \langle n_i^\alpha \rangle \langle n_j^\beta \rangle\right) \tag{3.3}$$

This measures the correlation between the α population of orbital i and β pop-

ulation of orbital j. In a single-determinant wavefunction (such as the Kohn-Sham wavefunction) there are no $\alpha\beta$ correlations and this quantity is identically zero.

Spin-spin:

$$C_{\text{spin}}(i,j) = 4\left(\langle S_i^z S_j^z\rangle - \langle S_i^z\rangle\langle S_j^z\rangle\right) \tag{3.4}$$

This measures the correlation between the spin in orbital i and the spin in orbital j. Note that in wavefunctions that preserve the correct singlet-spin symmetry as used in this work, $\langle S_i^z\rangle = \langle S_j^z\rangle = 0$. Because there are $\alpha\alpha$ and $\beta\beta$ correlations from the Pauli principle even in single determinant wavefunctions, this quantity does not fully vanish in non-interacting systems.

Singlet diradical:

$$\begin{aligned} C_{\text{diradical}}(i,j) &= 2\left(\langle d_i^\alpha d_j^\beta\rangle - \langle d_i^\alpha\rangle\langle d_j^\beta\rangle + \langle d_i^\beta d_j^\alpha\rangle - \langle d_i^\beta\rangle\langle d_j^\alpha\rangle\right) \\ d_i^\alpha &= n_i^\alpha(1-n_i^\beta) \end{aligned} \tag{3.5}$$

The single occupancy operator d_i^α measures the probability that an orbital i is occupied with α spin without any simultaneous β occupancy. This and the joint diradical probability density $\langle d_i^\alpha d_j^\beta\rangle$ were introduced by Dutoi *et al.* [222]. The function $C_{\text{diradical}}$ above is obtained by removing the independent probabilities of single occupation (e.g. $\langle d_i^\alpha\rangle\langle d_j^\beta\rangle$) from the probability density of Dutoi *et al.*, to give the correlation between single occupancies of orbitals i and orbital j with opposite spin. Again, because of Pauli type correlations in single determinant wavefunctions, this quantity does not fully vanish in non-interacting systems.

To make the meanings of these correlation functions explicit, we can examine the following limiting cases for 2-electron wavefunctions Ψ. (Here ϕ_1 and ϕ_2 are

disjoint orthogonal atomic orbitals).

1. Singlet diradical $\Psi = \frac{1}{2}(\phi_1\phi_2 + \phi_2\phi_1)(\alpha\beta - \beta\alpha)$. In this case, the above correlation functions assume their extremum values of 1 or -1. Thus we would find $C_{\text{particle}}(1,1) = C_{\text{particle}}(2,2) = -1$, $C_{\text{spin}}(1,1) = C_{\text{spin}}(2,2) = 1$, $C_{\text{diradical}}(1,1) = C_{\text{diradical}}(2,2) = -1$, and $C_{\text{particle}}(1,2) = 1$, $C_{\text{spin}}(1,2) = -1$, and $C_{\text{diradical}}(1,2) = 1$.
2. Closed-shell singlet $\Psi = \frac{1}{2\sqrt{2}}(\phi_1 + \phi_2)(\phi_1 + \phi_2)(\alpha\beta - \beta\alpha)$. In this case all correlation functions are identically 0, reflecting the absence of $\alpha\beta$ correlation.
3. Triplet $m_s = 0$ diradical $\Psi = \frac{1}{2}(\phi_1\phi_2 - \phi_2\phi_1)(\alpha\beta + \beta\alpha)$. Here all correlation function values are identical to those for the singlet diradical wavefunction. (One observes that the $m_s = 0$ triplet wavefunction differs from that of the singlet diradical only in the phase relationship between orbital products such as $\phi_1^\alpha\phi_2^\beta$ and $\phi_1^\beta\phi_2^\alpha$, thus to distinguish the two one should examine averages such as $\langle S_i^+ S_j^- \rangle$. Note that $m_s = 1$ triplet states were used in this study).

3.5.2 Correlation functions

Figs. 3.6 and 3.7 show plots of the different correlation functions evaluated for the singlet ground states of napthalene, pentacene and dodecacene. Since the correlation functions are functions of two positions, we have plotted them as a function of the second position with the first (reference) position fixed (indicated by the boxed value in the figures).

In Fig. 3.6 all plots have the reference position fixed at the centre of the lower

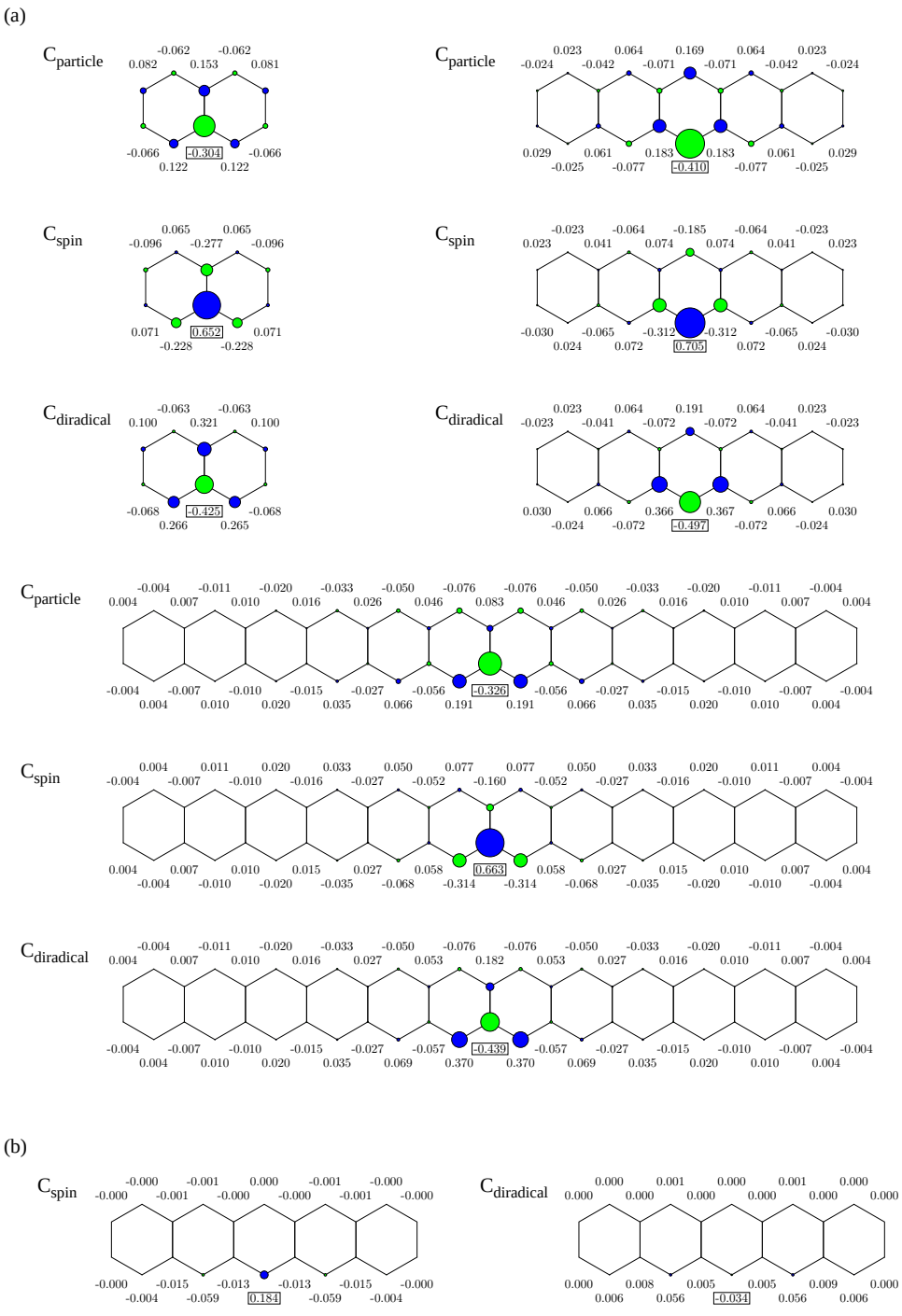

Figure 3.6: (a) Particle-particle, spin-spin, and singlet diradical correlation functions evaluated for napthalene, pentacene, and dodecacene in the STO-3G basis (reference point indicated by the boxed value). The value of the correlation function is indicated by the numbers; the size and color of the circles give the magnitude and sign. (b) A non-interacting model.

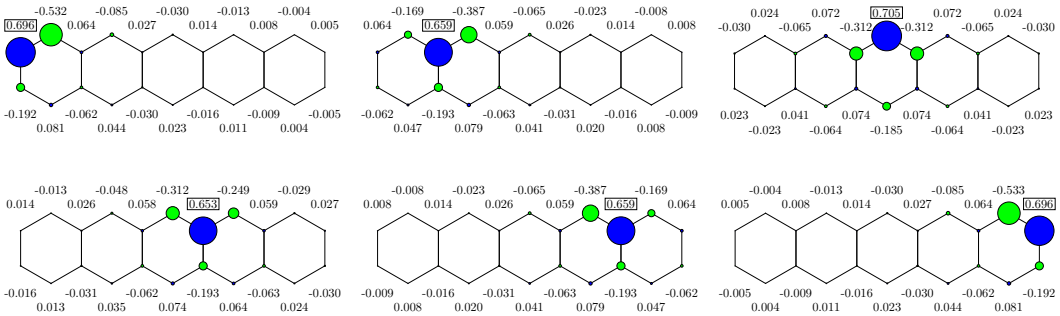

Figure 3.7: Spin-spin correlation functions for pentacene as we move the reference point of the correlation function (indicated by the boxed value) around the ring.

acene strand. Examining C_{particle} we see that it is large and negative at the reference position. Thus given an α electron in this orbital, there is a significantly *decreased* chance of finding a simultaneous β occupation of the orbital, or more simply, double occupancy of the atomic orbital is disfavored. Moving one atom away, C_{particle} is large and positive reflecting an *increased* chance of finding the orbital to be occupied with opposite spin to that at the reference position. This antiferromagnetic correlation continues further away from the reference position in a pattern of positive and negative values of C_{particle}, though the rapidly decreasing amplitudes indicate that the correlations are short-ranged.

Examining the spin-spin C_{spin} and singlet diradical $C_{\text{diradical}}$ correlation functions yields a similarly consistent picture. C_{spin} is large and positive at the reference position while $C_{\text{diradical}}$ is large and negative, which both indicate that the orbital has a strong tendency towards single occupation. The neighboring atoms further show strong single-occupancy, antiferromagnetic correlation with large negative (positive) values of C_{spin} ($C_{\text{diradical}}$), and this correlation decreases rapidly further away from the reference position. While C_{spin} and $C_{\text{diradical}}$ do not identically vanish for a single determinant uncorrelated wavefunction, their cor-

responding plots for pentacene in Fig. 3.6 show that aside from a small reduced propensity for double occupancy at the reference position which results from electron delocalization, there are no significant antiferromagnetic correlations along the chains. (Recall that C_{particle} is identically zero in the single determinantal wavefunction).

Comparing the correlation functions of napthalene and dodecacene shown in Fig. 3.6, for which the reference atom is in both cases at an 'inner' position on the strand, we see that there is a (slight) increase in the antiferromagnetic correlations as the length of the acene increases. In napthalene the correlation between the reference atom and the atom on the neighboring strand is stronger than the correlation to its neighbors on the same strand, a situation which is reversed in the longer acenes. This is consistent with the increasing difference between the ladder and rung C-C bond-lengths, which leads to the view of the longer acenes as a pair of coupled polyacetylene strands [183, 184].

Fig. 3.7 shows the spin-spin correlation plots where we move the reference position around the ring. As expected the antiferromagnetic correlations persist as the reference position is moved. Bond alternation is stronger near the edges of the pentacene ring and this leads to asymmetrical correlations between the reference position and its neighbors; stronger correlations are observed across the shorter bonds.

3.6 The nature of bonding in the acene polyradical state

The correlation functions evaluated above present a dynamic picture of the electronic motion in the acenes. Tracking a single electron as it makes its way

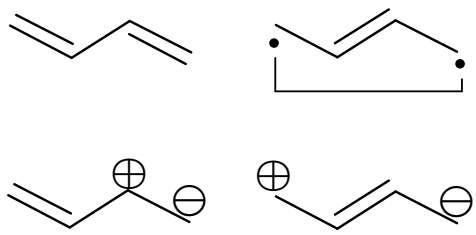

Figure 3.8: Covalent (top) and ionic (bottom) resonance structures for a conjugated system. Note that electron delocalisation requires a combination of both covalent and ionic resonance structures with roughly equal weights.

around the ring, a second electron is pulled along, antiferromagnetically coupled to the first and distributed over the nearest neighbor atoms.

Short-range antiferromagnetic correlations naturally bring to mind resonating valence bonds [223, 224, 225, 226, 227, 228]. Recall that we can expand any wavefunction in terms of resonance structures, which may be classified as covalent, singly ionic, doubly ionic and so on (see Fig. 3.8). (In this language, the resonance structures are viewed only as a many-body basis for expanding the wavefunction; the molecular geometry is fixed across the different structures). From our correlation functions we see that the acene ground state is dominated by *covalent* resonance structures (no double occupancy of the p_z orbitals) with short-range spin-couplings (i.e. short-ranged antiferromagnetic correlations).

We should note that the use of the word resonance here is different from the colloquial usage where resonance structures are a simple metaphor for delocalization. In terms of the resonance structures as a physical basis, electron delocalization requires superposition of covalent *and* ionic structures with roughly

equal weights. In the limit where the wavefunction is comprised only of covalent structures, we instead have an extreme *localization*: the electrons are fixed and unpaired on each of the atomic sites with only a spin degree of freedom, which fluctuates between different kinds of spin-couplings. Wavefunctions which are predominantly covalent in nature can therefore be viewed as polyradicals as every electron is unpaired in a localized, isoenergetic atomic orbital. The covalent nature of the acene ground-state revealed by the correlation functions argues for this polyradical interpretation, which is consistent with the picture given earlier by the natural orbital occupations.

Valence bond language in conjugated π-systems has long been appreciated in the context of their low-lying states, which are conventionally classified as covalent or ionic depending on the main resonance structures. Typically, covalent states appear more naturally described in the valence bond language. For example, in the polyenes, which may be thought of as making the two legs of the acene ladder, the lowest excitation is a covalent $2A_g$ state which appears to have large *double* excitation character from a molecular orbital viewpoint. However, this low-lying double excitation is easily understood in the valence bond language as arising from the singlet-recoupling of two singlet→triplet excitations on adjacent double bonds [229, 230, 231, 232, 233, 234]. Valence bond descriptions and analyses have also been examined in the context of radical electronic structure [190, 235]. In traditional CAS calculations, to extract a valence bond picture one usually re-parametrizes the wavefunction through a valence bond expansion (sometimes known as CASVB [236, 237, 238, 239, 240]). Such studies also find that the benzene ground-state should be viewed as a covalent state with antiferromagnetic spin-couplings, in accordance with what we have found for the acenes. The exponential size of the valence bond basis limits the CASVB

analysis to small molecules, but as we have demonstrated, correlation functions provide an alternative mechanism to infer the resonance nature of a state.

In a simple view of bonding, such as that afforded by the Hubbard [97, 241] or Pariser-Parr-Pople models there are two scales of energy, the resonance or hopping energy t associated with delocalization and the Coulomb repulsion energy U associated with double occupancy of an atomic orbital. When $U/t \gg 1$, we may be said to be in the strongly interacting regime. Under such circumstances, the molecular orbital picture begins to break down and instead the appropriate qualitative wavefunction is the superposition of covalent resonance structures as described above. A standard choice of parameters for conjugated polymers in the Ohno parametrization of the PPP Hamiltonian is $U = 11.26$ eV and $t = 2.4$ eV [242, 243, 198], placing systems such as the acenes in the moderately strongly interacting spectrum of Hamiltonians and therein lies an understanding of the polyradical character and covalent ground-state that we have observed.

3.7 Conclusions

In summary, motivated by predictions of unusual ground-states in the longer acene molecules, we investigated acene electronic structure with high-level wavefunction theory. Using a new *ab initio* density matrix renormalization group algorithm we could carry out complete active space calculations on the acenes from napthalene to dodecacene that correlated the full π-valence space. We find that the ground-state remains a singlet as the chain-length increases, with a finite singlet-triplet gap in the infinite chain limit. Detailed examination

of the wavefunctions, natural orbitals, and effective number of unpaired electrons further reveals that the longer acenes exhibit singlet *polyradical* character in their ground-state. Through a series of correlation functions we observe that electrons are antiferromagnetically coupled in pairs on neighboring atoms as they move around the acene chains. These results are consistent with a view of the longer acenes as moderately strongly interacting electronic systems, for which the appropriate reference description is a polyradical wavefunction arising from a resonance of predominantly covalent valence bond structures. We note that such a viewpoint is essential to understand the excitations of these systems. Finally, our study illustrates that even simple systems such as the acenes can provide unusual surprises in their electronic structure.

CHAPTER 4

INTRODUCTION II: COMPUTATIONAL TRANSITION METAL CHEMISTRY

The performance and availability of computers as well as user-friendly quantum chemistry program packages and methods – in particular modern density functional theory (DFT) [40, 244] – has in recent years reached a point that enables experimental research groups in all parts of chemistry to augment their work by computational studies. Especially transition metal chemistry with its wealth of unusual electronic and magnetic phenomena invites theoretical investigations [245, 246].
Single-core coordination compounds pose a complex set of problems, but they are generally still well covered by modern electronic structure techniques (in contrast to coupled multi-core systems, which are generally problematic). Key to the success of a computational study in this field is a sound theoretical and technical background, even for standard black-box techniques.

In this chapter we present a selection of computational approaches for transition metal complexes. We focus on the identification of pitfalls in designing and performing these calculations, as well as analyzing their outcomes. We advocate the use of computational tools beyond DFT, in particular – whenever necessary – multi-reference methods (such as the complete active space self-consistent field (CASSCF) approach [247] or the complete active space 2nd-order perturbation theory (CASPT2) [57]) which are still less commonly employed. In this context and in the context of experimental evidence we discuss the limitations and reliability of results at various levels of theory.

We begin this chapter with a discussion of the electron correlation problem in the specific situation of transition metal compounds (Sec. 4.1), which is one of the hard problems in contemporary computational quantum chemistry. In Secs. 4.2 to 4.4 we review a number of viable computational options, Sec. 4.5 discusses corrections for relativistic, thermodynamic, and solvation effects, and the final section is concerned with techniques to analyze the obtained electronic states.

4.1 Electron correlation in transition metal compounds

The partially filled d-shell of the transition metal block, poor overlap of the atomic orbitals, the resulting low-energy excited states and (near-)degeneracies are at the heart of both the interesting electronic structure properties as well as their complicated theoretical description [248, 249]. The 3d-elements are particularly challenging because of the small separation of energy-scales between the d-orbitals and the 4s/4p-shell (compared to the higher periods). The ensuing electronic structure is strongly affected by electron correlation, and the conceptual distinction between dynamic and static correlation effects (cf. 1.1) is particular beneficial. As argued in Sec. 1.1.5, the former is concerned with the effect of instantaneous, short-ranged electron-electron repulsions, which can be accounted for by correcting the predominant electron configuration with many *small* contributions of other configurations. It hence only requires a quantitative correction to a single-reference wavefunction and can be described by methods such as Kohn-Sham (KS) DFT [250], perturbation theory, or coupled cluster theory, which are designed accordingly. Static correlation refers to the situation, where the wavefunction of a system is complicated and requires an expansion

in terms of multiple electron configurations of *comparable* weight for a qualitatively correct description (cf. 1.1.6). Single-reference methods are consequently prone to dramatic failure when applied to static correlation problems. Low-spin states are usually more effected by static correlation, since already the construction of the correct spin-function requires multiple configurations.

Transition metal complexes are demanding because they often exhibit large contributions from both static and dynamic correlation (i.e., their wavefunction is comprised of a number of leading configurations and many others with smaller weights), which are subject to subtle tuning according to the metal and ligand characteristics. This is reflected by the capability of the d-block complexes to feature energetically competing states with distinct bonding situations, oxidation numbers, spin states and coordination structures[1]. Their (relative) magnitude can differ significantly between different states, which makes the computation of gaps a difficult task. The goal of chemical accuracy (i.e., $\leqslant 1$ kcal/mol error) or even spectroscopic accuracy (i.e., $\leqslant 1$ cm^{-1} error) remains out of reach for most problems.

4.2 Density functional theory studies

Density functional theory has become the workhorse of computational chemistry due to its generally favorable trade-off of efficiency and accuracy, and because it is an easy-to-use black-box method[2]. An excellent review by Neese [246] discusses in detail the machinery and performance of DFT for calculating

[1] These very features enable them to act as diverse catalysts in biochemistry and technical applications.

[2] See Sec. 6.2 for a more detailed discussion of this aspect.

molecular and spectroscopic properties of transition metal complexes. As DFT is based on a single Kohn-Sham determinant it has to be applied with particular caution to this branch of chemistry, since it may give an inadequate description for complex bonding situations. The broken-symmetry (BS) [251, 252, 253] solutions[3] mimic to some degree multi-reference behavior within the single-reference ansatz and give reasonable energies and electron densities for problems with less pronounced static correlation. The BS wavefunction is often severely spin-contaminated and not an eigenfunction of the spin-squared operator $\hat{S}^2$ – which is formally not required of a KS model system[4] – but in a variational sense it is a better approximation to the eigenfunction of the Hamiltonian $\hat{H}$ than its restricted counterpart. The resulting spin densities however are unphysical and have to be interpreted with caution (see Sec. 4.6).

The quality of DFT results for different properties can vary significantly, and is also dependent on the flavor of the employed functional. An important weakness in this context is the dependence of DFT spin gaps on the amount of exact exchange in hybrid functionals [246, 254, 255]: Hartree-Fock theory exactly accounts for exchange interactions (i.e., Fermi or Pauli antisymmetry correlation), but by definition does not describe Coulomb correlation. It is hence significantly biased towards stabilizing high-spin states. Pure and gradient corrected DFT behaves in the opposite way as the exchange term is subject to the self-interaction error (SIE) [256], while correlation contributions are effectively accounted for. Consequently, low-spin states are systematically favored [257]. The popular hybrid functionals benefit from a cancellation of these effects by adding

[3] The term 'broken-symmetry DFT' is used in different contexts. We use it for freely spin-polarized solutions, in which α- and β-spin density break symmetry. We do not refer to the parametrization of Heisenberg spin Hamiltonians.

[4] A good wavefunction has to be an eigenfunction of $\hat{S}^2$, a Kohn-Sham determinant does not necessarily have to be one.

exact HF exchange to the exchange-correlation functional. However, by adjusting the amount of HF exchange, the computed spin state ordering and gaps can be tuned [258, 259], which renders DFT results to some degree arbitrary. The comparison of hybrid and GGA functional results can be used to gauge the likely range of a spin gap, as the former is biased towards the high-spin, the latter towards the low-spin state.

DFT is known to generally yield good geometries for transition metal compounds with a slight tendency towards overestimating weaker metal-ligand (M-L) bond distances [260, 261, 262]. They are usually at least competitive with lower level wavefunction based methods such as 2nd-order Møller-Plesset perturbation theory [263, 264]. Although higher level wavefunction methods can give more accurate results (at considerably or prohibitively higher cost) [265, 266], the accuracy provided by the DFT approach is sufficient for most properties of interest. Electronic effects are usually not too sensitive with respect to the exact geometry, so consequently, corrections for minor zero-point rovibrational and anharmonicity effects to the equilibrium structures can be omitted. The PBE0 hybrid functional [267, 268, 269, 270, 271] demonstrated an edge over other standard functionals for systems containing 3d-metals in recent systematic benchmark studies by Bühl *et al.* [260, 261, 262].

Infrared (IR) spectra of the vibrational modes and their thermochemical contributions are generally well reproduced by DFT in the harmonic approximation [244]. Hybrid functionals show sometimes larger errors due to missing anharmonic corrections, while errors in the harmonic frequencies and missing anharmonicity often compensate fortuitously in GGAs.

The application of time-dependent density functional theory (TDDFT) [272]

to vertical excitations is often the only practical first principle route to obtaining complete spectra in the ultraviolet/visible (UV/vis) frequency range for complexes of appreciable size. Unfortunately, TDDFT suffers from a number of quantitative and qualitative deficiencies, which are particularly relevant for theoretical transition metal spectroscopy [246]. There are three main sources of bias, which lead to quantitative shifts of TDDFT transition energies: 1) Orbital relaxations for excited states are only accounted for to first order in the underlying linear response framework, which leads to an overestimate of the excitation energies. 2) The self-interaction error of DFT promotes orbital delocalization and consequently introduces a global red-shift of the spectrum. 3) HF exchange in hybrid functionals has the opposite effect and causes an overall blue-shift. The resulting error remains acceptable due to the cancellation of these shifts.

However, in addition to these quantitative errors, TDDFT also shows qualitative failures. The SIE has a particular impact on charge-transfer (CT) transitions, resulting in gross underestimates for their excitation energies, which can shift them into entirely unphysical regions of the spectrum (HF exchange can to some extent balance out this effect). Double and other multiple excitations common in transition metal compounds are missing from the TDDFT spectra due to the underlying adiabatic approximation. This also significantly affects the quality of single excitations which would otherwise interact with them. Finally, the defective long-range form of common functionals leads to unphysical Rydberg states, which are shifted to unreasonably high energies.

The biggest deficit of UV/vis spectra predicted by TDDFT is thus the frequent occurrence of artifacts, i.e., additional spurious states (e.g., when high-energy CT states erroneously slip into the UV/vis region) or missing ones (e.g., multi-excitation states). In summary, the TDDFT description lacks a uniform quality

for states of different nature, which leads to a limited reliability of the computed spectra.

Electron paramagnetic resonance (EPR) parameters, such as zero-field splitting (ZFS) and the g-tensor, are valuable spectroscopic quantities for the characterization of open-shell species. The calculation of g-tensors in DFT is well established. Experience has shown that basis set demand is not too high and the use of hybrid functionals is recommended, although spin contamination can become an issue [246]. The g-tensors computed by DFT tend to be too small. ZFS in a modern coupled-perturbed SCF ansatz with all relevant terms was only recently introduced in DFT [273, 274, 275, 276]. Although there is still little experience it appears to be a promising development.

4.3 CASSCF/CASPT2 studies

High-level wavefunction based *ab initio* studies are still rare in transition metal chemistry [277, 278, 279, 280, 281] due to their high computational cost and relatively complicated setup (compared to DFT). While DFT is sufficiently accurate for many systems and properties, it is, as discussed above, not reliable for others.

The complete active space self-consistent field (CASSCF) method [247] is the conventional choice to generate multi-reference wavefunctions which capture the static electron correlation. Complete active space 2nd-order perturbation theory (CASPT2) has emerged as a feasible and (almost) size-consistent [282] method to account for dynamic correlation on top of a multi-reference wavefunction [283]. The caveat of all wavefunction based methods is that extensive

basis sets are necessary to recover the dynamic correlation. Inadequate basis sets lead to an unbalanced description of exchange and correlation [256, 284], which results in overstabilization of high-spin states.

4.4 Basis sets

Custom basis sets are a common tool in quantum chemical studies of transition metal compounds, usually providing the metal with a more sophisticated basis than the ligands. DFT generally only shows a relatively small basis set dependence [244, 285, 244] and has the advantage of fast convergence to the complete basis set limit. We can already expect semi-quantitative results within a double-ζ polarized basis. Wavefunction based methods however require large basis sets with high angular momentum functions to quantitatively account for electron correlation [277, 278]. Atomic natural orbitals (ANOs) [286, 287, 288, 289, 290] are a popular choice for CASSCF/CASPT2 studies. Basis set extension as ideally provided by ANO basis functions can be used to gauge the degree of convergence with respect to the one-particle space.

4.5 Corrections for relativistic, solvation, and thermodynamic effects

The 3d transition metals exhibit only moderate relativistic effects, and a scalar relativistic correction, e.g., by means of the 2nd-order Douglas-Kroll-Hess approximation (DKH2) [291, 292, 293, 294, 295, 296], usually accounts for them

sufficiently. The corrections often lead to notable shifts in the total energy without significantly changing the relative energies or electronic structure. Relativistic contraction leads to slightly shortened M-L bonds.

While experimental setups commonly involve a solvation medium, computational studies are by default conducted *in vacuo*. There are a number of possibilities [297, 298] to account for environment and external field effects (e.g., on different states and charge distributions) by solvents. Explicit solvent models are quite expensive and so implicit continuum uniform dielectric [299, 300, 301, 302] approaches such as the self-consistent reaction field (SCRF) [303, 304] polarized continuum models (PCM) are commonly used. The self-consistent isodensity polarized continuum model (SCI-PCM) [305] for example defines the solvent cavity based on a surface of constant ρ around the solute, which corresponds to its physically accessible shape. The self-consistent optimization integrates the solvation effects into the electronic problem, as they are coupled via the cavity definition. This allows for a responsive solvation model, which can account for qualitative changes to the gas phase results. Vertical transitions in excited state calculations occur on a shorter time scale than the reorientation of a solvent in its response, and hence a non-equilibrium treatment is appropriate for this problem.

For comparison with experimental data, it is beneficial to compute thermodynamic corrections for vibrational and finite-temperature effects to the total energies E (i.e., the sum of electronic and nuclear energy; cf. eqn. 1.5). The standard Gibbs free energies $G^{\ominus}$ (energy differences $\Delta G^{\ominus}$, respectively) at $T = 298.15$ K and $p = 1$ atm computed by most quantum chemistry packages (e.g., GAUSSIAN 03 [205]) are based on some very basic approximations (ideal gas transla-

tional, rigid rotor rotational, and harmonic oscillator vibrational contributions; single accessible electronic state [304]). We point out the limitations of these simple models in the context of transition metal chemistry (e.g., considering the multiple competing states with sometimes tiny energetic differences).

4.6 Analysis of electronic states

In the following we will describe a selection of techniques employed in the analysis of computed wavefunctions (i.e., Kohn-Sham-determinants in the case of DFT) [306, 307, 308, 309, 310, 311]. Note that these approaches to characterize states are not based on rigorous quantum mechanical operators and observables, but are rather physically motivated (however ultimately arbitrary) attempts of mapping out conceptual quantities.

4.6.1 Population analysis

Mulliken's population analysis (MPA) [312] is one of the traditional methods for the analysis of electronic wavefunctions with respect to atomic charge (q_{MPA}) and spin distributions (n^s_{MPA}), which it extracts from the density matrix with an equal partitioning of the overlap population. It has long been known [312, 308] that it suffers from serious flaws and artifacts, in particular due to the arbitrary and indiscriminate overlap partitioning (which neglects polarization effects in heteronuclear atom pairs), and due to the formal assumption of a balanced basis set for all atom centers. Even in balanced basis sets, diffuse functions feature large overlap populations, which are treated unphysically in the MPA frame-

work, and lead to erroneous results and strong basis set dependence[5]. Despite these shortcomings the Mulliken population analysis is still regularly used in computational studies since it is essentially obtained without additional cost.

The natural population analysis (NPA) [313] is a more modern alternative for the determination of intramolecular partial charges. Further popular alternatives are, e.g., the Löwdin population analysis [314], Becke analysis [315], atomic polar tensor (APT) charge analysis [316], electron localization function (ELF) method [317], and the CHelp [318] and CHelpG [319] schemes.

4.6.2 Bader's Atoms-in-Molecules analysis

Bader's Atoms-in-Molecules (AIM) method [320, 321, 322] derives atomic electron counts (n_{AIM}) and charges ($q_{AIM} = n_{atom} - n_{AIM}$), as well as the number of unpaired electrons on the atomic centers (n^s_{AIM}) by analyzing the real space topology of the numerical electron density $\rho = \rho^\alpha + \rho^\beta$ and differential spin density $\rho^s = \rho^\alpha - \rho^\beta$, respectively. We obtain n_{AIM} and n^s_{AIM} on the atom center A as

$$n_{AIM}(A) = \int_{\tau_A^{AIM}} \rho(\mathbf{x}) d\mathbf{x}, \tag{4.1}$$

$$n^s_{AIM}(A) = \int_{\tau_A^{s,AIM}} \rho^s(\mathbf{x}) d\mathbf{x}, \tag{4.2}$$

where the AIM analysis determines the critical surfaces τ_A^{AIM} and $\tau_A^{s,AIM}$ of zero-flux in the gradient vector field of ρ and ρ^s, respectively, around atom A

$$\nabla\rho(\mathbf{x}_A^{AIM}) \cdot \mathbf{n}(\mathbf{x}_A^{AIM}) = 0, \tag{4.3}$$

$$\nabla\rho(\mathbf{x}_A^{s,AIM}) \cdot \mathbf{n}(\mathbf{x}_A^{s,AIM}) = 0, \tag{4.4}$$

[5] We note, that the differential spin populations n^s_{MPA} obtained in the following study appear to be more robust due to cancellation of errors.

which are the bounding surfaces for the integrations in eqns. (4.1) and (4.2) (see Fig. 4.1; $\mathbf{x}_A^{AIM}$ and $\mathbf{x}_A^{s,AIM}$ are the points that define the surfaces τ_A^{AIM} and $\tau_A^{s,AIM}$; $\mathbf{n}(\mathbf{x}_A^{AIM})$ is the unit vector normal to τ_A^{AIM} at $\mathbf{x}_A^{AIM}$, and $\mathbf{n}(\mathbf{x}_A^{s,AIM})$ to $\tau_A^{s,AIM}$ at $\mathbf{x}_A^{s,AIM}$). Note, that there is an alternative route to n_{AIM}^s by computing n_{AIM}^α and n_{AIM}^β from ρ^α and ρ^β separately, i.e., as $n_{AIM}^s = n_{AIM}^\alpha - n_{AIM}^\beta$ instead of by the integration over ρ^s in eqn. (4.2). Both approaches have theoretical deficiencies, since on the one side ρ^s can not necessarily be associated to atom centers, and n_{AIM}^α and n_{AIM}^β on the other side are based on different atomic domains.

AIM is not based on orbital populations and hence not prone to its partitioning issues. It is known to give reliable results with little basis set dependence, and is established for the use in transition metal chemistry [323, 324].

4.6.3 Frontier orbitals, active space natural orbitals, electron and spin densities

The interpretation of frontier orbitals is a common approach to describing the bonding situation in a chemical compound. We point out that the physical significance of molecular orbitals (MOs) – in particular if generated from DFT – is limited and inferences have to be treated with prudence, especially in the presence of multi-reference correlations[6]. The KS-DFT orbitals in particular are based on an artificial noninteracting model system, which may in a static correlation situation be very different from the true physical system.

[6] As discussed in Sec. 1.1.3, the Hartree-Fock and Kohn-Sham single-determinant ansatz only defines the occupied one-electron space, but it is invariant with respect to particular representations. The different orbital sets are associated with different physical interpretations. The canonical MOs are the eigenfunctions of the Fock operator (i.e., the energy eigenfunctions in the independent particle model), while local orbitals reflect, e.g., the extent of atom- or bond-centered localizability.

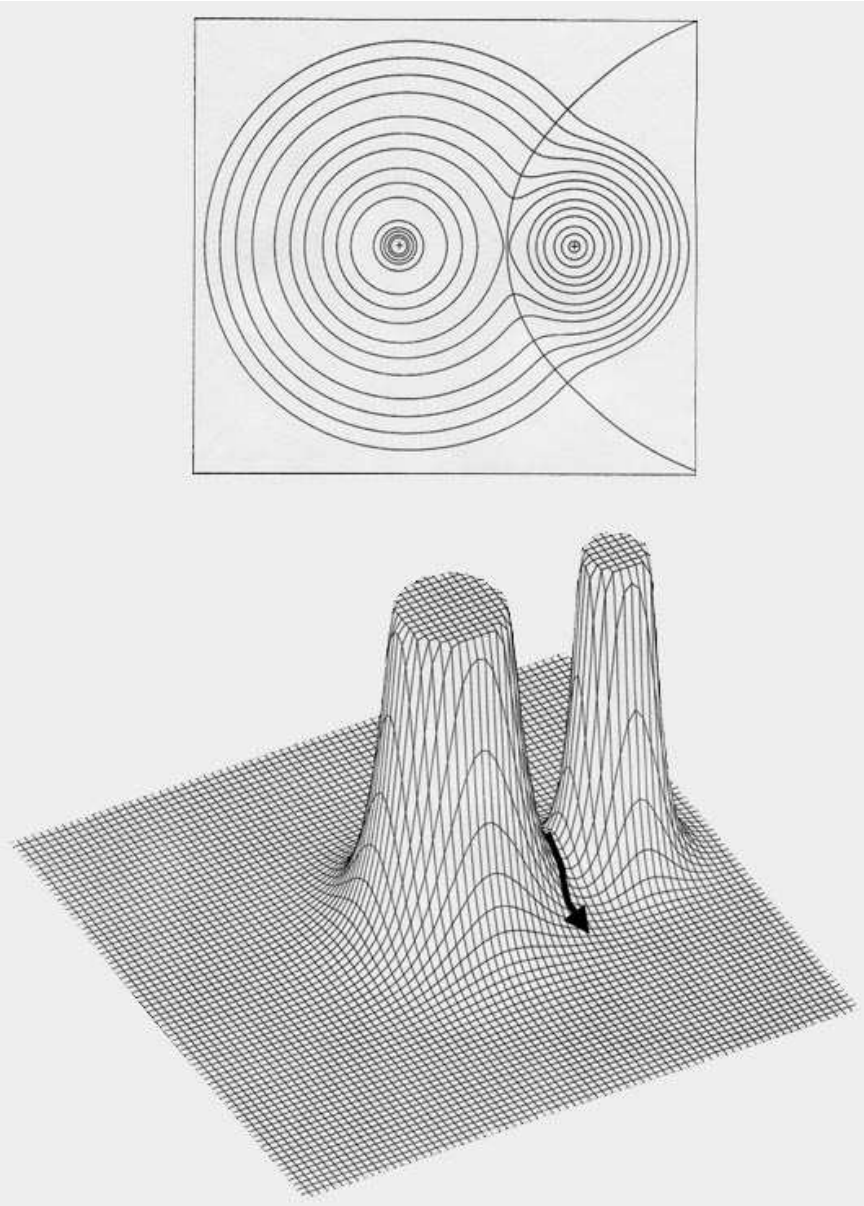

Figure 4.1: Contour map of the electron density for the example of a LiF molecule. The boundary separating the basin of the F atom on the left, from the Li atom on the right, is also indicated. It is defined by the path of steepest descent from the point of minimum density along the Li-F internuclear axis indicated in the relief map of the density shown in the lower diagram. (Figure and caption reproduced from Ref. [321]).

Natural orbitals (NOs) contain more information, as they are the eigenfunctions of the (correlated) reduced one-electron density matrix, and provide a way to interpret multi-reference results. They can be very useful for a bonding analysis, e.g., in combination with the leading CI coefficients or their fractional occupation. While canonical DFT-MOs tend to be delocalized from lack of self-interaction and generally mix metal and ligand orbitals (which complicates their interpretation), CASSCF-NOs are often more localized, and correlation between orbital regions can easily be identified.

Electron- and spin-densities are easily analyzed and correspond to actual physical quantities/observables. They are usually more reliable and robust with respect to the employed method compared to the underlying orbital space, however, their information content is obviously reduced. We again point out that antiferromagnetic (AFM) spin density distributions of broken-symmetry DFT solutions are not physical – the true wavefunction has no regions of excess α- and β-spin – but an artifact of the single-reference ansatz. BS-DFT spin densities can be viewed as the superposition of unrestricted natural orbital (UNO) or projected restricted open-shell orbital (RO) densities, which give an indication of the leading configuration in more complicated states. Complex and exotic configurations with large spin contamination and problematic convergence behavior point to multi-reference situation.

CHAPTER 5

THE ELECTRONIC STRUCTURE OF 3D-M(SMIF)$_2$

Recently, 3d-metal complexes with the *'smif'*-ligand (1,3-di(2-pyridyl)-2-azapropenide) from vanadium to nickel were synthesized by Wolczanski *et al.* [325]. Most of the M(smif)$_2$ complexes are paramagnetic open-shell systems with small spin gaps. Spectroscopic data of these complexes and their ions indicate a number of interesting electronic and magnetic properties including low-temperature spin crossovers, unusual oxidation states, and non-innocent ligand behavior.

We approached these issues in the present theoretical investigation employing a range of first principle methods from density functional to multi-reference wavefunction based theory. Single-metal coordination complexes are usually considered complicated but tractable systems for modern electronic structure methods. However, even standard black-box techniques still need to be applied with care to obtain meaningful and robust results for these problems. Using the M(smif)$_2$ complexes as a showcase, we highlight some of the technical and methodological pitfalls that can arise in these calculations and the interpretation of their results. We also discuss the limitations and reliability of results at various levels of theory within the context of the experimental evidence.

This chapter is structured in the following way: We begin with an introduction of the 3d-M(smif)$_2$ series of complexes. In Sec. 5.2 we present the computational methods and analytical tools used in this investigation. In Sec. 5.3 we report and analyze the results for the M(smif)$_2$ series and a number of specific examples in the context of the experimental questions and summarize our key findings in Sec. 5.4. The details of the experimental work will be presented

elsewhere [325].

The experimental work associated with this project was performed by Brenda A. Frazier and Peter T. Wolczanski, and we acknowledge the following contributors for experimental data: Emil B. Lobkovsky (XRD geometries), and Serena DeBeer George (XAS data). We also thank Thomas R. Cundari for providing his preliminary DFT results on some of the studied complexes (none of this data was actually used in the presented work), and Troy Van Voorhis, Roald Hoffmann, and Emily A. Carter for helpful discussions on oxidation states, as well as Christopher J. Cramer and Frank Neese for discussions on DFT and CASSCF performance. This work is in preparation for publication.

5.1 The 3d-M(smif)$_2$ series of complexes

The novel class of hexa-coordinated, pseudo-octahedral M(smif)$_2$-complexes ($MN_6C_{24}H_{20}$; '*smif*'=(1,3-di(2-pyridyl)-2-azapropenide); M=Ti,V,Cr,Mn,Fe,Co,Ni; see Figs. 5.1 and 5.2) is at the center of the present study. Zn(smif)$_2$ was somewhat accidentally synthesized by Westerhausen and Kneifel in 2004 [326]. Wolczanski *et al.* [325] recently synthesized and characterized the 3d-M(smif)$_2$ series from vanadium to nickel including some of their cations. Most of the M(smif)$_2$ complexes are paramagnetic open-shell systems with small spin gaps. Spectroscopic data of these complexes and their ions indicate a number of interesting electronic properties, including low-temperature spin crossovers [327, 328], unusual oxidation states, and non-innocent ligand behavior [329], which motivated this study. The organic, tridentate *smif*-ligand coordinates with its negatively charged aza-nitrogen and the two lone-pairs of its pyridyl-nitrogens. It features a conjugated π-electron system capable of delocalizing charges and fa-

Figure 5.1: Structures and colors of the $M(smif)_2$ series (courtesy of P. T. Wolczanski).

cilitating backbonding. The formal oxidation state of the metal-center is +2, however redox activity of the ligand could potentially lead to behavior corresponding to M(III), i.e., the effective oxidation state (EOS) does not match the formal one. The coordination situation ranges – depending on the metal – from strong-field to weak-field environments with metal-aza bond distances between 1.90 and 2.22 Å.

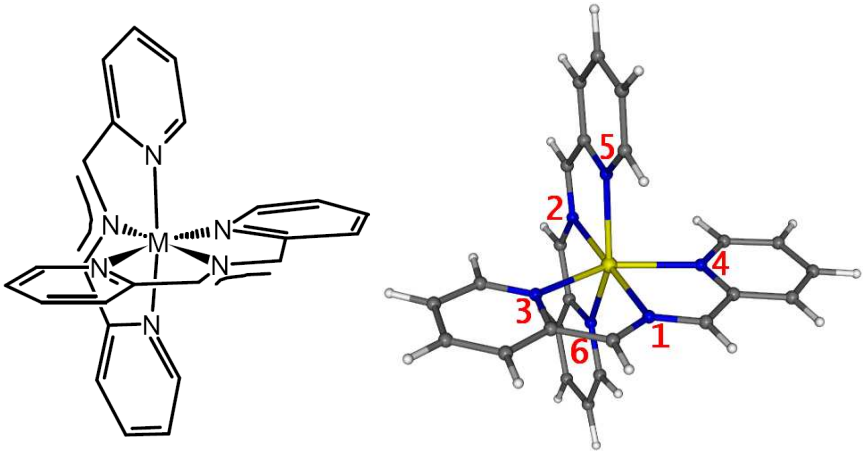

Figure 5.2: Stereo-structure of the M(smif)$_2$ complexes in ideal D_{2d} symmetry. The numbering indicates the metal-ligand bond labels used below.

5.2 Computational details

Our investigation of the M(smif)$_2$-complexes builds on experience of previous work by, e.g., Neese and coworkers using DFT (e.g., [330, 331, 332, 333, 334, 335]) and Pierloot (e.g., [277, 278]), Gagliari (e.g., [336, 337, 338, 339]), Taylor *et al.* (e.g., [279, 280]) employing CASSCF/CASPT2 methods.

5.2.1 DFT and TDDFT calculations

The DFT and TDDFT calculations in this study were performed with the GAUSSIAN 03 program package [205], except for EPR data, which we computed with the ORCA code [276]. We utilized an all-electron, unrestricted, open-shell approach with the generalized gradient approximation (GGA) functional BLYP [340, 341, 342], the meta-GGA TPSS [270] (in GAUSSIAN named TPSSTPSS), and

the hybrid functionals B3LYP [340, 341, 343] and PBE0 [267, 268, 269, 270, 271] (in GAUSSIAN named PBE1PBE). B3LYP (containing 20% exact exchange) is probably the most commonly deployed functional and 'de facto standard' [246], while PBE0 (containing 25% exact exchange) has demonstrated one of the best general performances for coordination compounds amongst standard functionals in recent years (see, e.g., the benchmark studies in Refs. [262, 344]). TPSS has a similar record amongst non-hybrid functionals. Based on our previous review of the merits and drawbacks of the broken-symmetry DFT solutions, we consistently followed open-shell instabilities of restricted solutions, but stress the implications of this approach.

Basic calculations utilized the common split valence 6-31G* Pople basis [345, 346, 347] with all spherical harmonics (5d,7f), i.e., 494 basis functions, and for higher accuracy we reoptimized states in the Dunning-style cc-pVTZ basis [100, 101] (1248 functions) obtained from the EMSL database [162, 348, 349] (see Tab. 5.1). The comparison of results from both basis sets allows us an assessment of the extent of basis set incompleteness.

The $M(smif)_2$ series requires tight numerical integration, and all DFT calculations used an Euler-Maclaurin-Lebedev (99,590) quadrature grid [350]. We started from unrestricted BS guess wavefunctions without symmetry constraints and employed both the common self-consistent field (SCF) as well as a quadratically convergent solver [351, 352] for difficult cases. Situations with close-lying and strongly interacting states, particularly common for low-spin, exhibit vibronic coupling and are often exceedingly hard to converge. All results were tested for electronic stability [353, 354].

We optimized the geometries of all $M(smif)_2$ in every spin state at UPBE0/6-

Table 5.1: Employed basis set contractions and number of basis functions (bf).

	6-31G*	cc-pVTZ
M	[5s,4p,2d,1f]⟶34 bf	[7s,6p,4d,2f,1g]⟶68 bf
C,N	[3s,2p,1d]⟶14 bf	[4s,3p,2d,1f]⟶30 bf
H	[2s]⟶2 bf	[3s,2p,1d]⟶14 bf
total	494 bf	1248 bf

	'ANO0'	'ANO1'	ANO-augDZP
M	[5s,4p,2d]⟶27 bf	[7s,6p,5d,2f,1g]⟶73 bf	[6s,5p,4d,2f]⟶55 bf
C,N	[3s,2p]⟶9 bf	[3s,2p,1d]⟶14 bf	[4s,3p,2d]⟶23 bf
H	[1s]⟶1 bf	[2s]⟶2 bf	[3s,2p]⟶9 bf
total	317 bf	533 bf	925 bf

31G* level of theory and compared the results in a number of cases with the ones obtained with the BLYP and/or B3LYP functionals. We started each optimization without symmetry restriction, refined the results using point group symmetry, and tested all stationary points for structural stability on the basis of frequency calculations. In selected cases with competitive energetics we reoptimized the geometries at the cc-pVTZ level[1]. The M(smif)$_2$ require very tight optimization criteria and Farkas' modified direct inversion in the iterative subspace (GDIIS) [355, 356] algorithm substantially improved the convergence behavior. From the frequency checks we also obtained IR spectra and thermochemical data[2].

At the stationary points we computed vertical gaps at UPBE0/6-31G* level

[1] GAUSSIAN unfortunately does not allow an efficient optimization of geometries within the DKH2 approximation due to missing analytic derivatives, and we can hence not account for relativistic M-L bond contraction.

[2] Note, that vibrational contributions to $G^{\ominus}$ are not well defined for geometries other than the minima for the employed model chemistry.

and for selected cases with UTPSS/6-31G* and/or UPBE0/cc-pVTZ (DKH2) as well. The adiabatic gaps refer to the energetic differences of the global minima on the different state surfaces. For the cases, in which we did not compute thermodynamic corrections at the triple-ζ level (e.g., for single-point UPBE0/cc-pVTZ (DKH2) on UPBE0/6-31G* geometries), we utilized the best available double-ζ values. We computed both EPR parameters (g-tensors, zero-field splitting (ZFS)) and UV/vis spectra (with excited states up to at least 3.25 eV) at UPBE0/cc-pVTZ (DKH2) level. The TDDFT excitations incorporated SCI-PCM solvation (standard isodensity of $\rho = 0.0004$ [357]) with the experimental solvents, i.e., the relatively unpolar benzene and the moderately polar tetrahydrofuran (THF) with dielectric constants of $\varepsilon = 2.2706$ and 7.58 *a.u.*, respectively. We also tested the influence of synthesis relevant solvents (i.e., THF and polar acetonitrile with $\varepsilon = 36.64$ *a.u.*) on the ground state electron density distribution.

5.2.2 CASSCF/CASPT2 calculations

Our CASSCF/CASPT2 single point calculations on the DFT geometries were performed in MOLPRO 2006.1 [358, 359, 360, 361, 362, 363, 364]. We utilized Werner's internally contracted RS2C version of CASPT2 [364] in combination with the standard projected, non-diagonal zeroth-order Fock Hamiltonian, moderate level shifts to bypass convergence problems due to intruder states [55], and the frozen-core approximation (i.e., fixed double occupation) for the inner (1s for N,C; 1s,2s,2p for M) orbitals in this part. Note that a number of different contraction schemes and zeroth-order Hamiltonians are used in different CASPT2 implementations [56, 57, 58, 59, 60], which can lead to slightly different results.

Roos' atomic natural orbitals (ANOs) [287, 289] are a popular choice for CASSCF/CASPT2 studies. We used a small 'ANO0' contraction to establish active spaces, a more extended 'ANO1' contraction for most production calculations and Roos' original ANO-augDZP contraction for a more balanced treatment of the ligands (see Tab. 5.1).

The challenging aspect of every multi-reference calculation (besides the computational demand) is the design and realization of an adequate active space, in which the static correlation problem is covered. We will hence describe this aspect in some detail: we generally aimed for the biggest computationally affordable active space to avoid numerical and physical problems due to insufficiencies in this area (remember that the factorially scaling cost prohibits a further increase in active space size). We identified 18 orbitals that can provide a satisfactory description of the important interactions in the 3d-M(smif)$_2$ complexes, and could in practice correlate between 16 and 18 of them, depending on electron count and use of symmetry. The CASSCF orbital space has usually many minima, and it is thus laborious (and sometimes impossible) to realize a desired active space[3]. We employed the following two strategies for the suc-

[3]Initial guess orbitals from HF or DFT can differ substantially from the intended orbitals. Large basis sets introduce further complications. In particular the unoccupied space is often diffuse and hard to interpret. After deciding for and initial orbital set and generating it, we have to essentially go through the list of all MO coefficients and MO plots to select the ones that most closely resemble the targeted active orbitals. The orbital energies are an additional factor of consideration.

Once an undesired orbital accidentally enters the active space, the other orbitals are adjusted to it in a sense of a local minimum. When we try to exchange the undesired orbital against a more suitable one, this bias of the remaining orbitals often leads to the situation, that the first orbital is rotated back. It is hence important to avoid intrusion of these orbitals in the first place.

Very high and very low energy orbitals can get rotated into the active space, because already modest fractional occupations of these orbitals lead to significant energetic contributions. This effect however should be recovered by a successive dynamic correlation treatment, and only orbitals with a substantial fractional occupation should span the exactly correlated subspace.

In some cases, the desired active space does not actually constitute a minimum, and the CASSCF optimization will replace orbitals in favor of others which minimize the energy. In this situation it is impossible and not sensible to realize the targeted active space.

cessive active space build-up for electron poor (1) and electron rich (2) systems (irreducible representations for an idealized O_h symmetry are given in the explanation):

1. (a) start with the metal 3d orbitals: (*n*e,5o)-CAS; 't_{2g}' are d_{xy}, d_{xz}, d_{yz}, 'e_g^*' are d_{z^2}, $d_{x^2-y^2}$; the number of d-electrons *n* depends on the specific element and charge

   (b) add a metal 4d: (*n*e,10o)-CAS; these orbitals are generally unoccupied

   (c) add one π_L and π_L^* (L stands for ligand based, i.e., centered on one of the nitrogens) for each 't_{2g}'-d-orbital: ([n + 6]e,16o)-CAS; the three π_L are generally doubly occupied and π_L^* unoccupied

   (d) if feasible: add one or both σ_{M-L} 'e_g' orbitals, i.e., d_{z^2} and/or $d_{x^2-y^2}$: ([n + 8]e,17o)-CAS or ([n + 10]e,18o)-CAS; these orbitals are generally doubly occupied

2. (a) start with the metal 3d orbitals: (*n*e,5o)-CAS.

   (b) add a metal 4d for each of the three 't_{2g}' and the σ_{M-L} 'e_g' corresponding to each 'e_g^*': ([n + 4]e,10o)-CAS; the former are generally unoccupied, the latter occupied

   (c) add one π_L and π_L^* for each 't_{2g}'-d-orbital: ([n + 10]e,16o)-CAS

   (d) if feasible: add one or both 4d orbitals for the two 'e_g^*' d-orbitals: ([n + 10]e,17o)-CAS or ([n + 10]e,18o)-CAS

The 3d orbitals account for the essential physics and chemistry of the transition metal complexes. Including a 4d set is important for the overall d-space

If the orbital set we aim for is not feasible in terms of size, it is sensible evaluate and compare the results for the possible subsets.

All these practical issues require some effort and experience, which makes CAS studies more complicated and less attractive then black-box DFT.

representation, called double-shell-effect [365]. The ligand based π_L and π_L^* orbitals overlap with the 't_{2g}' set of 3d orbitals and facilitate π-bonding and back-bonding. The σ_{M-L} 'e_g' orbitals heavily involve the 3d orbitals of appropriate symmetry and improve their description.

It is beneficial to distinguish between occupation patterns, in which the 'e_g^*'-3d orbitals are occupied or partially occupied (i.e., electron rich and/or high-spin systems), and those where they are not (i.e., few electron and/or low-spin systems). In the former case the first strategy is most appropriate, in order to account for the double shell effect of all occupied or partially occupied 3d-orbitals. In the letter case, in which the 'e_g^*'-3d orbitals are already unoccupied, the double shell effect for these orbitals is deemed less important. We always include the full set of six π_L and π_L^* orbitals to allow for a description of metal to ligand coupling.[4]

We start our active space construction from UBLYP orbitals, which are suitable due to their only moderate delocalization. To bypass the issue of multiple local minima, we always employed several approaches and guesses in the generation of an active space, hereby also generating various smaller active spaces which we shall use for the discussion of active space effects in the following sections. Cross-projection of active spaces from different symmetries was used as an additional tool to obtain the desired active spaces.

The CASPT2 calculations are only possible with a reduced active space, and we explore the use of reoptimized and non-reoptimized orbitals from the larger active space CASSCF calculations.

[4]The comparison of results from each strategy in the two cases confirms, that this approach is sensible.

In addition to the ground state CASSCF/CASPT2 energies, we studied the natural orbitals and resulting electron and spin densities, as well as excited states by means of state averaged CASSCF (SA-CASSCF) in selected cases.

We introduce the following measure of multi-reference character of a configuration interaction (CI) type wavefunction based on the CI eigenvalues C^i:

$$m_{MR} = \sum_{i=0} \left(C^i - \delta_{i0} \right)^2 \tag{5.1}$$

(where δ_{i0} represents the HF single-reference with coefficient 1).We truncated the sum for convenience at $C^i < |0.05|$. Large values of m_{MR} indicate large multi-reference character and the ideal single-reference limit is given by $m_{MR} = 0$.

5.2.3 Oxidation states and partial charges

The classical oxidation state concept is still one of the most popular ways to classify and categorize coordination compounds in inorganic chemistry. Instead of concentrating on the notion of quantized oxidation states associated with absolute integer charges, we examine the obtained electronic wavefunctions with respect to electron and spin density distributions. By applying the partitioning schemes introduced in Sec. 4.6 we arrive at partial charges on the atomic centers. Such partial charges do not correspond to the oxidation states, except in purely ionic compounds. Rather than by contemplating their absolute values, we obtain effective oxidation states by comparing the obtained partial charges to the ones from simple reference systems (at the same level of theory) of well established oxidation states and a chemical structure comparable to our system of interest (for a detailed discussion of this approach see App. A). In the

$M(smif)_2$ series, the core is formally a M(II), but due to potentially non-innocent ligands could also behave as a M(III). We chose the *trans*-$MCl_2(H_2O)_4$ and *trans*-$[MCl_2(H_2O)_4]^+$ as reference systems for M(II) and M(III), for which in some cases experimental XAS data was also available. Note, that the two axial Cl^- ions correspond to the anionic aza-nitrogens, and the neutral, equatorially coordinated water molecules represent the pyridyl-nitrogens.

We performed AIM analysis of the obtained wavefunctions using the GRID BASED AIM BADER CHARGE ANALYSIS PROGRAM (V0.25C) [366, 367, 368]. We generally made use of the frozen core approximation, which we validated for selected cases, and watched for convergence of the charges and the correct number of electrons with respect to the FFT grid. We also list the results of the Mulliken analysis for the $M(smif)_2$ complexes for comparison, which as seen yield an unphysical interpretation.

5.3 Results and discussion

5.3.1 3d-$M(smif)_2$ series

The 3d-$M(smif)_2$ series reveals a number of overarching attributes, whose understanding also proved crucial to the adequate choice and setup of computational tools.

Preliminary multi-reference calculations on some of the $M(smif)_2$ indicated only moderate static correlation, which justified the use of DFT as our primary computational approach.

Many of the M(smif)$_2$ exhibit an extremely flat potential energy surface (PES) with respect to internal degrees of freedom. Motions and distortions involving the coordinative bonds can occur with only very small energy penalties (with the exception of dissociation or decomplexation, indicating a reasonably stable coordination of the tridentate smifs). This finding is supported by experimental evidence, since X-ray diffraction (XRD) results for the V, Cr, Mn, Co, and Ni complexes show each two separate specimen per unit cell, which in some cases display striking dissimilarities. The floppy nature and lack of distinct minima in combination with standard convergence thresholds can easily lead to substantial discrepancies to the fully converged geometries, such that very tight optimization criteria had to be enforced to resolve all structural details.

Not only are the PESs flat, they are also structured, i.e., they often feature a host of stationary points – both minima and saddle points (or higher order transition states (TS)). This structure introduces complicated catch regions for the computational optimization, and a single guess (e.g., from XRD) can easily lead to a local minimum. We hence employed between 15 and 25 guesses for each complex and spin state (covering a range of symmetries and M-L bond distances) to thoroughly sample the PES for all relevant structural features.

The different minima constitute distinct isomers, i.e., there are several geometries in which a M(smif)$_2$ can be stable. These are associated with different electronic states with sometimes fundamentally different properties. The overall ground state PES is hence subdivided into patches of different state surfaces (of like or unlike spin)[5]. In Co(smif)$_2$ for example, short M-L bonds favor a doublet state with EOS +3, for intermediate M-L bonds we find a classical doublet ground state, and for loose coordination a classical quartet is most sta-

[5]Note, that these domains not necessarily contain minima.

Table 5.2: Metal-ligand bond distance relations in the $M(smif)_2$ complexes of different symmetry. Bond distances with the same letter within a colums are equal.

bond	d(M-N)				
	D_{2d}	D_2	C_{2v}	C_s	C_2
M-N^1	a	a	a	a	a
M-N^2	a	a	b	b	a
M-N^3	b	b	c	c	b
M-N^4	b	b	c	d	c
M-N^5	b	b	d	e	b
M-N^6	b	b	d	e	c

ble. We also find examples of isomers with very similar geometry (e.g., the two $[Cr(smif)_2]^+$ doublet minima). Currently synthetic work attempts to introduce steric modifications (e.g., spacers) to the smif ligand, which would force the complex into a different region of the PES with a different state. The crossing regions of different surfaces as well as their close vicinity are numerically challenging and plagued by electronic instabilities. Inversely, we can deduce such an electronic situation from the displayed convergence behavior. The $\langle S^2 \rangle$ is a sensitive index to keep track of different states.

The ideal high-symmetry structure of the $M(smif)_2$ is a D_{2d}. The computed geometries (see Fig. 5.3) also show a number of Jahn-Teller (JT) [369] like distortions which break degeneracies and lead to lower symmetry solutions. These structures can be derived from D_{2d} by pulling outwards, twisting, or canting the ligand(s): we can arrive at a D_2 structure by *propeller twisting* both smif-ligands, and at a C_{2v} structure by *pulling* one smif outwards (relative to the other), which is usually accompanied by a decrease of the NNN-angle of the smif-'pincer' (i.e.,

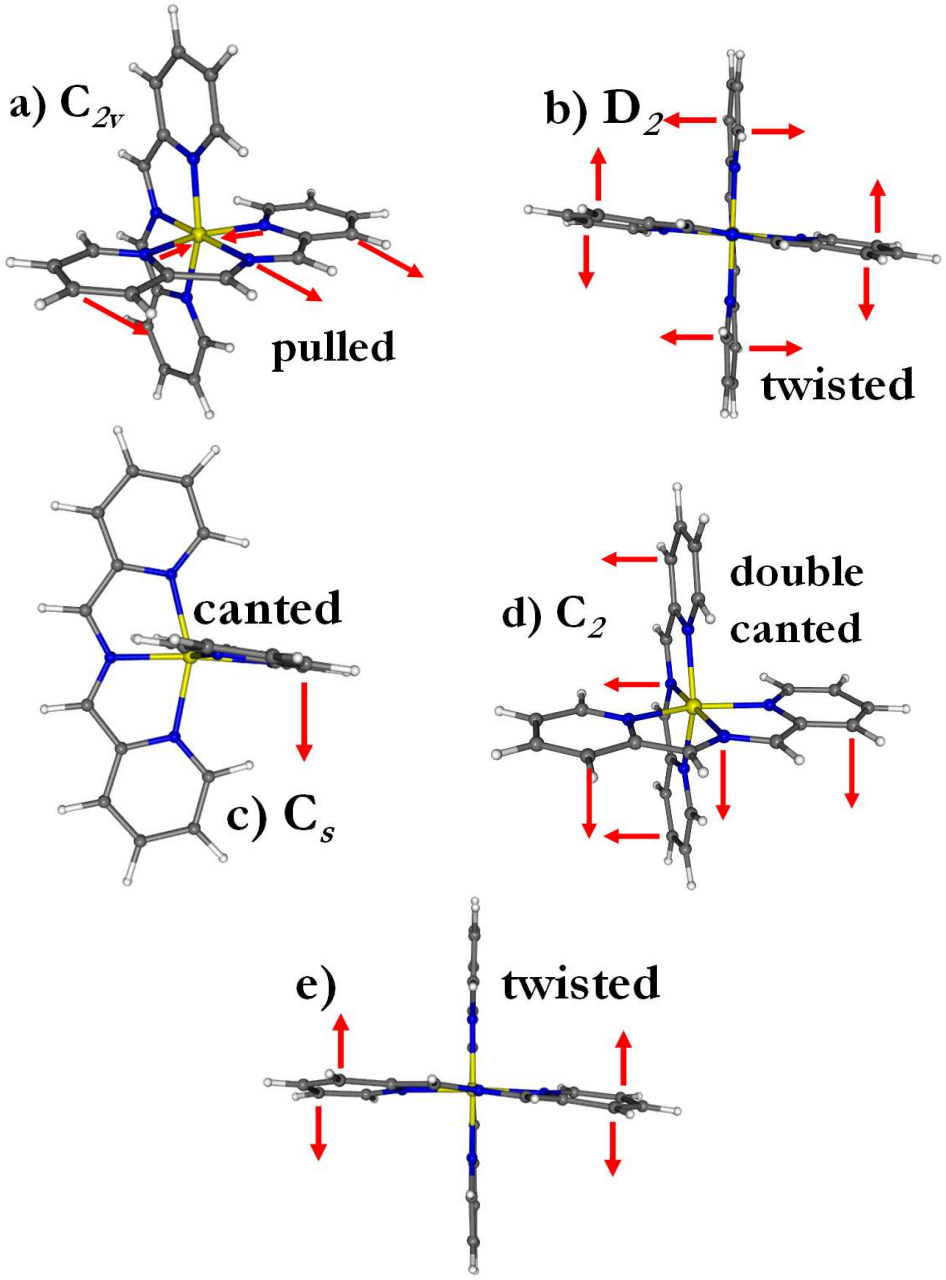

Figure 5.3: Examples of characteristic features (compared to the ideal D_{2d} symmetry) of experimental and computed $M(smif)_2$ geometries: a) C_{2v} geometry: one smif pulled away from the metal; b) D_2 geometry: both smifs are propeller-twisted, and do not stand orthogonal to each other; c) C_s geometry: one smif canted; d) C_2 geometry: both smifs canted; e) $Cr(smif)_2$ X-ray 2: one strongly propeller-twisted smif.

while the aza-nitrogen moves away, the pyridyl-nitrogens move closer). *Canting* of one of the smifs leads to a C_s geometry, and canting of both results in a C_2 (see Tab. 5.2 for M-L bond relations). Note, that the D_2 and C_2 structures are chiral, as they are lacking an axis of improper rotation (rotary reflection). The overlap and interactions with the π-system are apparently an important factor for these distortions.

In addition to these ideal geometries we find additional deformations in the XRD structures. The computed saddle points correspond to these distortions, e.g., in Ti(smif)$_2$ we find a C_2 minimum and transition states for the interconversion of the enantiomers, i.e., $C_2 \longrightarrow C_s$ [TS]$\longrightarrow D_{2d}$ [TS^2]$\longrightarrow C_s^*$ [TS]$\longrightarrow C_2^*$. They hence belong to the same state surface. The associated barriers are usually very small ($\sim$ 1 kcal/mol) and thermally accessible, although the structural distortions can be significant. It becomes clear, that all computational thresholds/grids have to be very tight, as their errors are otherwise bigger than the present energetic differences.

The optimized geometries from B3LYP and BLYP with standard thresholds generally overestimate the M-L bond distances by 1.5–2.5%, which is improved using PBE0 and tight convergence by a factor of 2 to 4.

5.3.2 Ti(smif)$_2$

The Ti(smif)$_2$ complex is formally a d^2-system (possible spin states $S = 0, 1$), which could so far not be synthesized. We make theoretical predictions about its geometric and electronic structure. The results of our DFT investigation are summarized in Tabs. 5.3 and 5.4.

Table 5.3: Computationally optimized M-L bond-distances in Ti(smif)$_2$ (in Å), average metal-aza and M-L bond-distances as well as JT distortions of the different stationary points. Percentage differences between the triplet and singlet stationary points are shown in brackets. We also give the average deviation ($|\Delta d|^{av}$), largest deviation (Δd^{max}), and spread of deviations ($|\Delta\Delta d|^{max}$).

bond	C_2 ^{1}X	C_s ^{1}A" [TS]	D_{2d} ^{1}X [TS^2]	C_2 ^{3}B	C_s ^{3}A" [TS]	D_{2d} ^{3}A$_1$ [TS^2]
Ti-N^1	2.105	2.099	2.105	2.124 (+0.9%)	2.110 (+0.5%)	2.113 (+0.4%)
Ti-N^2	2.105	2.111	2.105	2.124 (+0.9%)	2.136 (+1.2%)	2.113 (+0.4%)
Ti-N^3	2.123	2.125	2.127	2.135 (+0.6%)	2.142 (+0.8%)	2.147 (+0.9%)
Ti-N^4	2.131	2.125	2.127	2.166 (+1.6%)	2.142 (+0.8%)	2.147 (+0.9%)
Ti-N^5	2.123	2.122	2.127	2.135 (+0.6%)	2.138 (+0.8%)	2.147 (+0.9%)
Ti-N^6	2.131	2.137	2.127	2.166 (+1.6%)	2.180 (+2.0%)	2.147 (+0.9%)
Ti-N^{1,2av}	2.105	2.105	2.105	2.124	2.123	2.113
Ti-N^{av}	2.120	2.120	2.120	2.142	2.141	2.136
distortion	4.5°	5.0°	NA	11.1°	9.3°	NA
$\|\Delta d\|^{av}$	NA	NA	NA	1.0%	1.0%	0.8%
Δd^{max}	NA	NA	NA	+1.6%	+2.0%	+0.9%
$\|\Delta\Delta d\|^{max}$	NA	NA	NA	1.1%	1.5%	0.6%

For this complex, we found only one singlet and one triplet isomer (see Tabs. 5.3, 5.4 and Fig. 5.4). At the UPBE0/6-31G* level we obtain a triplet ground state with an adiabatic gap of just 3.6 kcal/mol ($\Delta G^{\ominus}_{t-s}$ = 2.5 kcal/mol). Both spin-states feature an unexpected electronic structure.

[^{1}Ti(III)-FM:] The singlet state minimum has C_2 symmetry and a non-classical electronic structure with EOS +3 and a $(t_{2g})^{.5\alpha,.5\beta}(e_g^*)^0(\pi_L^{nb})^{.5\alpha,.5\beta}$ configuration: it can be derived from a metal-based EOS +2 $(t_{2g})^{\alpha,\beta}(e_g^*)^0$ configuration (i.e., $d_{xz}^{\alpha}d_{yz}^{\beta}$) by partially transferring the unpaired electrons onto the symmetry-adapted, noninnocent ligand-π-systems, leading to the EOS +3 (note that the actual charge transfer is somewhat smaller, but consistent with the EOS +3 ref-

Table 5.4: Adiabatic total energy (ΔE) and standard Gibbs free energy gaps ($\Delta G^{\ominus}$ (in kcal/mol) between the different stationary states of Ti(smif)$_2$; spin-squared expectation values ($\langle S^2 \rangle$) before and after annihilation of the first spin contaminant; AIM charges (q_{AIM}(Ti)), effective oxidation states (EOS), and integrated spin densities (n^s_{AIM}(Ti)) on the titanium ; leading configurations, coupling type, and state label. All calculations on UPBE0/6-31G* level.

	C_2 ^{1}X	C_s ^{1}A" [TS]	D_{2d} ^{1}X [TS^2]	C_2 ^{3}B	C_s ^{3}A" [TS]	D_{2d} ^{3}A$_1$ [TS^2]
ΔE	3.626	3.628	3.632	0	0.05	0.2
$\Delta G^{\ominus}$	2.5	4.6	7.0	0	1.2	3.3
$\langle S^2 \rangle$	1.0083/0.0669	1.0088/0.0709	1.0073/0.0585	2.0258/2.0004	2.0244/2.0003	2.0111/2.0001
q_{AIM}(Ti)	2.33	2.33	2.35	2.22	2.23	2.27
EOS		(III)			(III)	
n^s_{AIM}(Ti)	0.09	0.06	0.08	1.37	1.37	1.36
config	$(t_{2g})^{.5\alpha,.5\beta}(e^*_g)^0(\pi^{nb}_L)^{.5\alpha,.5\beta}$			$(t_{2g})^{.5\alpha,.5\alpha}(e^*_g)^0(\pi^{nb}_L)^{.5\alpha,.5\alpha}$		
coupling	FM (M-M-AFM, L-L-AFM)			FM		
label	^{1}Ti(III)-FM			^{3}Ti(III)-FM		

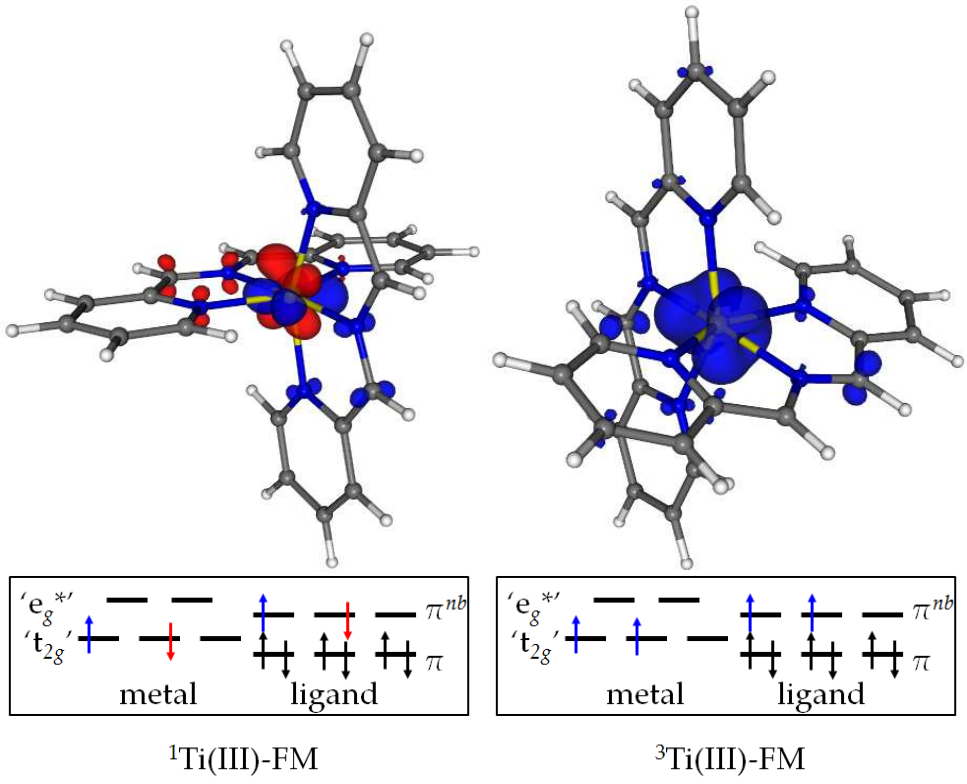

^{1}Ti(III)-FM ^{3}Ti(III)-FM

Figure 5.4: Spin density isosurfaces and configurations of the differerent Ti(smif)$_2$ isomers.

erence). This state interacts with other close-by singlets (e.g., with a ^{1}Ti(III)-FM variation 3 kcal/mol above and a classical closed-shell $(t_{2g})^2(e_g^*)^0$ state 5 kcal/mol higher), however none of them constitutes a local minimum. The fact that we do not find a competitive AFM state (i.e., $(t_{2g})^\alpha(e_g^*)^0(\pi_L^{nb})^\beta$) indicates the significance of covalent π-backbonding despite relatively long M-L bonds. The M-M-AFM is favoured over the closed-shell configuration in this weak-field coordination. While the spin density in each smif is shifted towards one of the pyridyl rings in the canted C_2 minimum, it is evenly delocalized in the corresponding higher-symmetry saddle points.

[^{3}Ti(III)-FM:] The triplet C_2 ^{3}B isomer is largely analogous to the ^{1}Ti(III)-FM – re-

Table 5.5: Adiabatic total energy gaps (in kcal/mol) at UPBE0/6-31G* (top), UTPSS/6-31G* (middle), and UPBE0/ccpVTZ (DKH2) level (bottom) between the singlet and triplet states for the different stationary points on the Ti(smif)$_2$-PES. The vertical gaps for each geometry are given in brackets.

label	C_2 ^{3}B	C_2 ^{1}X	C_s ^{3}A" [TS]	C_s ^{1}A" [TS]	D_{2d} $^3A_1$ [TS^2]	D_{2d} ^{1}X [TS^2]
^{1}Ti(III)-FM	4.2 (4.2)	3.6 (3.3)	4.0 (4.0)	3.6 (3.3)	3.9 (3.7)	3.6 (3.2)
^{3}Ti(III)-FM	0	0.4	0.0	0.4	0.2	0.4
^{1}Ti(III)-FM	3.4 (2.8)	2.2 (2.2)	3.4 (2.8)	2.2 (2.2)	2.9 (2.5)	2.2 (2.2)
^{3}Ti(III)-FM	0.5	0	0.6	0.0	0.4	0.0
^{1}Ti(III)-FM	4.0 (3.5)	2.7 (2.7)	3.7 (3.3)	2.8 (2.7)	3.1 (3.1)	2.7 (2.7)
^{3}Ti(III)-FM	0.5	0.1	0.4	0.1	0.1	0

lated by a spin-flip of the distributed β-electron – except for a notable difference between the singlet and triplet state partial charge on the metal, which indicates a certain dependence of the EOS on the spin state.

The analogy between the states is also found in their PESs: Both curves feature a chiral C_2 minimum with an extremely flat $C_2 \longrightarrow C_s$ [TS]$\longrightarrow D_{2d}$ [TS^2]$\longrightarrow C_s^*$ [TS]$\longrightarrow C_2^*$ interconversion, with transition state barriers of only 0.002 kcal/mol ($\Delta G^{\ominus}_{s-s}$ = 2.1 kcal/mol) and 0.006 kcal/mol ($\Delta G^{\ominus}_{s-s}$ = 4.5 kcal/mol) for the singlet as well as 0.05 kcal/mol ($\Delta G^{\ominus}_{t-t}$ = 1.2 kcal/mol) and 0.17 kcal/mol ($\Delta G^{\ominus}_{t-t}$ = 3.3 kcal/mol) for the triplet. Despite the quasi-degeneracy of the stationary points in each PES, the overall appearance of their minimum and saddle points differs notably due to tilted ligands. The M-L bond distances and the electron and spin density distribution is however barely effected. Consequently, we do not expect an effect on the spectroscopic signature like in a $D_{2d}/D_2 \longrightarrow C_{2v}$ JT distortion. In addition to having the same PES structure, the corresponding stationary points on both curves have also very similar M-L bonds, with the triplet geometries

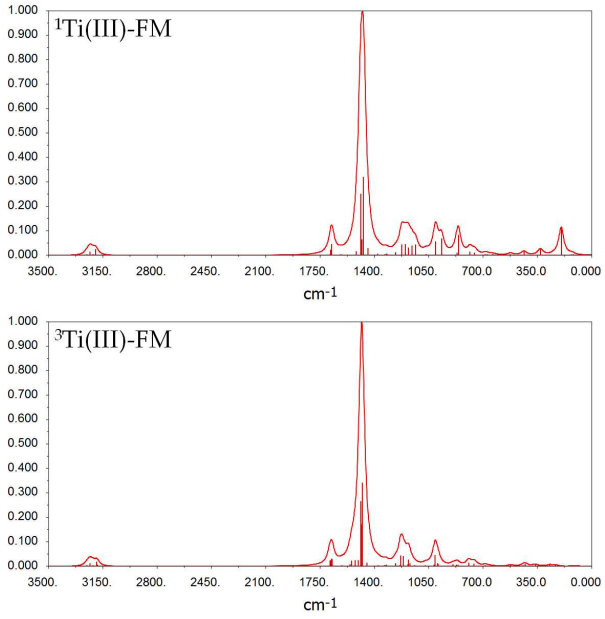

Figure 5.5: IR-spectra of the Ti(smif)$_2$ singlet and triplet states.

slightly more canted and d(Ti-N^{av}) longer by $\sim$ 1%. Apart from these small deviations, both curves are essentially parallel, separated by a 3-4 kcal/mol gap (see Tab. 5.5). This is confirmed at the UTPSS/6-31G* and UPBE0/cc-pVTZ (DKH2) level, which give slightly smaller vertical gaps of 2-3 and 2.5-3.5 kcal/mol, respectively, and an adiabatic gap of 1.7 and 2.2 kcal/mol, respectively. The IR spectra of both states are essentially identical, which is consistent with their similar geometry and related electronic structure (see Fig. 5.5).

We summarize that both singlet and triplet surface are very flat with near-zero barriers and they are parallel to each other with very small gaps, with the triplet being the ground state. We propose temperature dependent magnetization measurements to verify our prediction once the titanium complex can be produced.

5.3.3 Co(smif)$_2$

The Co(smif)$_2$ compound is formally a d^7-system with $S = \frac{1}{2}, \frac{3}{2}$ as possible spin states. Only relatively low-resolution XRD-data could be obtained and it shows two complexes per unit cell (see Tab. 5.6). Both XRD structures have approximate C_{2v} symmetry, however they differ substantially: XRD2 exhibits much stronger $D_{2d} \longrightarrow C_{2v}$ symmetry breaking and shorter d(Co-N^{av}) than XRD1. All ligands feature slight deformations: both smifs of XRD1 are bent, while XRD2 has one twisted and one bent smif.

Experimentally, a spin of S = '1' was determined in solution at RT (by Evan's method, Guoy balance measurement, and SQUID), indicating a ~50:50 mixture of doublet and quartet, which requires a very small spin gap between these states. SQUID measurements show a characteristic transition from $S = \frac{1}{2}$ at $T = 10K$ to a mixture of doublet and quartet at higher temperature. This supports the notion of a doublet ground state with a thermally accessible quartet. The low-temperature spin-crossover is a direct consequence of the near degeneracy of these two spin states.
A mixture of doublet and quartet states was considered as a possible source for the stark differences between the two experimental geometries.

The UPBE0/6-31G* geometry optimization found two doublet and three quartet isomers (see Tabs. 5.6, 5.7 and Fig. 5.6). At this level, a quartet was obtained as the overall ground state with an adiabatic gap of 6.5 kcal/mol ($\Delta G^{\ominus}_{q-d}$ = 7.6 kcal/mol) to the next doublet. None of the optimized structures is in close agreement with either of the XRD geometries, but there is reasonable correspondence between XRD2 and the C_{2v} $^2A_1$ isomer (i.e., the lowest doublet), as well as XRD1 and the corresponding D_{2d} $^2B_2$ transition state.

Table 5.6: XRD and computed M-L bonds in $Co(smif)_2$ (in Å), average metal-aza and M-L bonds as well as JT distortions. Percentage differences between theory and experiment shown in brackets (values for the XRDs are with respect to their average). The Δ XRD column contains the experimental errors. We give average deviations ($|\Delta d|^{av}$), largest deviations (Δd^{max}), and spread of deviations ($|\Delta\Delta d|^{max}$).

bond	XRD1	XRD2	Δ XRD1	Δ XRD2
Co-N^1	1.962 (+1.5%)	1.904 (–1.5%)	±0.005 (±0.3%)	±0.005 (±0.3%)
Co-N^2	1.971 (+0.3%)	1.961 (–0.3%)	±0.005 (±0.3%)	±0.004 (±0.2%)
Co-N^3	2.054 (+1.9%)	1.979 (–1.9%)	±0.005 (±0.2%)	±0.005 (±0.3%)
Co-N^4	2.059 (+1.6%)	1.993 (–1.6%)	±0.005 (±0.2%)	±0.005 (±0.3%)
Co-N^5	2.091 (–1.1%)	2.138 (+1.1%)	±0.005 (±0.2%)	±0.005 (±0.2%)
Co-N^6	2.092 (–1.2%)	2.143 (+1.2%)	±0.005 (±0.2%)	±0.005 (±0.2%)
Co-$N^{1,2av}$	1.967	1.932	NA	NA
Co-N^{av}	2.038	2.020	NA	NA
distortion	–	–	NA	NA
$\|\Delta d\|^{av}$	1.3%	1.3%	0.2%	0.2%
Δd^{max}	+1.9%	–1.9%	±0.3%	±0.3%
$\|\Delta\Delta d\|^{max}$	3.1%	3.1%	0.6%	0.6%

bond	C_{2v} $^2A_1$	D_{2d} $^2B_2$ [TS]	D_2 $^2B_3$
Co-N^1	1.891 (–3.6/–0.7%)	1.896 (–3.3/–0.4%)	1.884 (–4.0/–1.1%)
Co-N^2	1.948 (–1.2/–0.6%)	1.896 (–3.8/–3.3%)	1.884 (–4.5/–3.9%)
Co-N^3	1.958 (–4.6/–1.0%)	2.077 (+1.1/+4.9%)	1.927 (–6.2/–2.6%)
Co-N^4	1.958 (–4.9/–1.8%)	2.077 (+0.8/+4.2%)	1.927 (–6.4/–3.3%)
Co-N^5	2.195 (+4.9/+2.6%)	2.077 (–0.7/–2.9%)	1.927 (–7.9/–9.9%)
Co-N^6	2.195 (+4.9/+2.4%)	2.077 (–0.7/–3.1%)	1.927 (–7.9/–10.1%)
Co-$N^{1,2av}$	1.919	1.896	1.884
Co-N^{av}	2.024	2.016	1.913
distortion	0.058 (3.0%)	NA	88.6°/0.6°
$\|\Delta d\|^{av}$	4.0/1.5%	1.8/3.1%	6.1/5.1%
Δd^{max}	±4.9/+2.6%	–3.8/+4.9%	–7.9/–10.1%
$\|\Delta\Delta d\|^{max}$	9.8/4.4%	4.9/8.2%	3.9/9.0%

bond	C_2 ^4X	C_s ^4A" [TS]	C_{2v} $^4B_1$	D_{2d} $^4A_2$	D_{2d} $^4B_1$ [TS]
Co-N^1	2.090 (+6.5/+9.8%)	2.086 (+6.4/+9.6%)	1.877 (–4.3/–1.4%)	1.879 (–4.2/–1.3%)	1.876 (–4.4/–1.5%)
Co-N^2	2.090 (+6.0/+6.6%)	2.094 (+6.2/+6.8%)	1.947 (–1.2/–0.7%)	1.879 (–4.7/–4.2%)	1.876 (–4.9/–4.3%)
Co-N^3	2.126 (+3.5/+7.4%)	2.134 (+3.9/+7.9%)	1.928 (–6.1/–2.6%)	1.929 (–6.1/–2.5%)	1.930 (–6.0/–2.4%)
Co-N^4	2.157 (+4.7/+8.2%)	2.169 (+5.3/+8.8%)	1.928 (–6.4/–3.3%)	1.929 (–6.3/–3.2%)	1.930 (–6.3/–3.1%)
Co-N^5	2.126 (+1.6/–0.6%)	2.129 (+1.8/–0.4%)	2.210 (+5.7/+3.4%)	1.929 (–7.7/–9.8%)	1.930 (–7.7/–9.7%)
Co-N^6	2.157 (+3.1/+0.6%)	2.129 (+1.8/–0.6%)	2.210 (+5.7/+3.1%)	1.929 (–7.8/–10.0%)	1.930 (–7.7/–9.9%)
Co-$N^{1,2av}$	2.090	2.090	1.912	1.879	1.876
Co-N^{av}	2.124	2.124	2.017	1.913	1.912
distortion	10.7°	10.2°	0.071 (3.7%)	NA	NA
$\|\Delta d\|^{av}$	4.3/5.5%	4.2/5.7%	4.9/2.4%	6.1/5.1%	6.2/5.2%
Δd^{max}	+6.5/+9.8%	+6.4/+9.6%	–6.4/+3.4%	–7.8/–10.0%	–7.7/–9.9%
$\|\Delta\Delta d\|^{max}$	4.9/10.4%	4.6/10.2%	12.1/6.6%	3.6/8.7%	3.3/8.4%

Table 5.7: Adiabatic total energy (ΔE) and standard Gibbs free energy gaps ($\Delta G^{\ominus}$ (in kcal/mol) between the different stationary states of Co(smif)$_2$; spin-squared expectation values ($\langle S^2 \rangle$) before and after annihilation of the first spin contaminant; AIM charges (q_{AIM}(Co)), effective oxidation states (EOS), and integrated spin densities (n^s_{AIM}(Co)) on the cobalt ; leading configurations, coupling type, and state label. All calculations on UPBE0/6-31G* level.

	C_{2v} $^2A_1$	D_{2d} $^2B_2$ [TS]	D_2 $^2B_3$	C_2 ^4X	C_s ^4A" [TS]	C_{2v} $^4B_1$	D_{2d} $^4A_2$	D_{2d} $^4B_1$ [TS]
ΔE	6.5	7.9	21.2	0	0.02	35.7	51.8	54.2
$\Delta G^{\ominus}$	7.7	9.7	23.3	0	0.04	34.8	53.0	53.9
$\langle S^2 \rangle$	0.7576/0.7501	0.7573/0.7500	0.7632/0.7502	3.7642/3.7501	3.7635/3.7501	3.7983/3.7511	3.7818/3.7505	3.7793/3.7504
q_{AIM}(Co)	1.34	1.36	1.59	1.38	1.40	1.42	1.62	1.62
EOS	(II)		(III)	(II)		(II)	(III)	(III)
n^s_{AIM}(Co)	0.94	0.92	0.00	2.73	2.72	1.15	0.00	0.04
config	$(t_{2g})^6(e^*_g)^{\alpha}$		$(t_{2g})^6(e^*_g)^0(\pi_L)^6(\pi^{nb}_L)^{\alpha}$	$(t_{2g})^{4,\alpha}(e^*_g)^{\alpha,\alpha}$		$(t_{2g})^6(e^*_g)^{\alpha}(\pi_L)^{4,\alpha}(\pi^{nb}_L)^{\alpha}$	$(t_{2g})^6(e^*_g)^0(\pi_L)^{4,\alpha}(\pi^{nb}_L)^{\alpha,\alpha}$	$(t_{2g})^6(e^*_g)^0(\pi_L)^{4,\alpha}(\pi^{nb}_L)^{\alpha,\alpha}$
coupling	no		(L-L-FM)	no/(σ-FM)		FM/(AFM)	L-L-FM	L-L-FM
label	^{2}Co(II)		^{2}Co(III)	^{4}Co(II)		^{4}Co(II)-FM	^{4}Co(III)	[^{4}Co(II)-FM]*

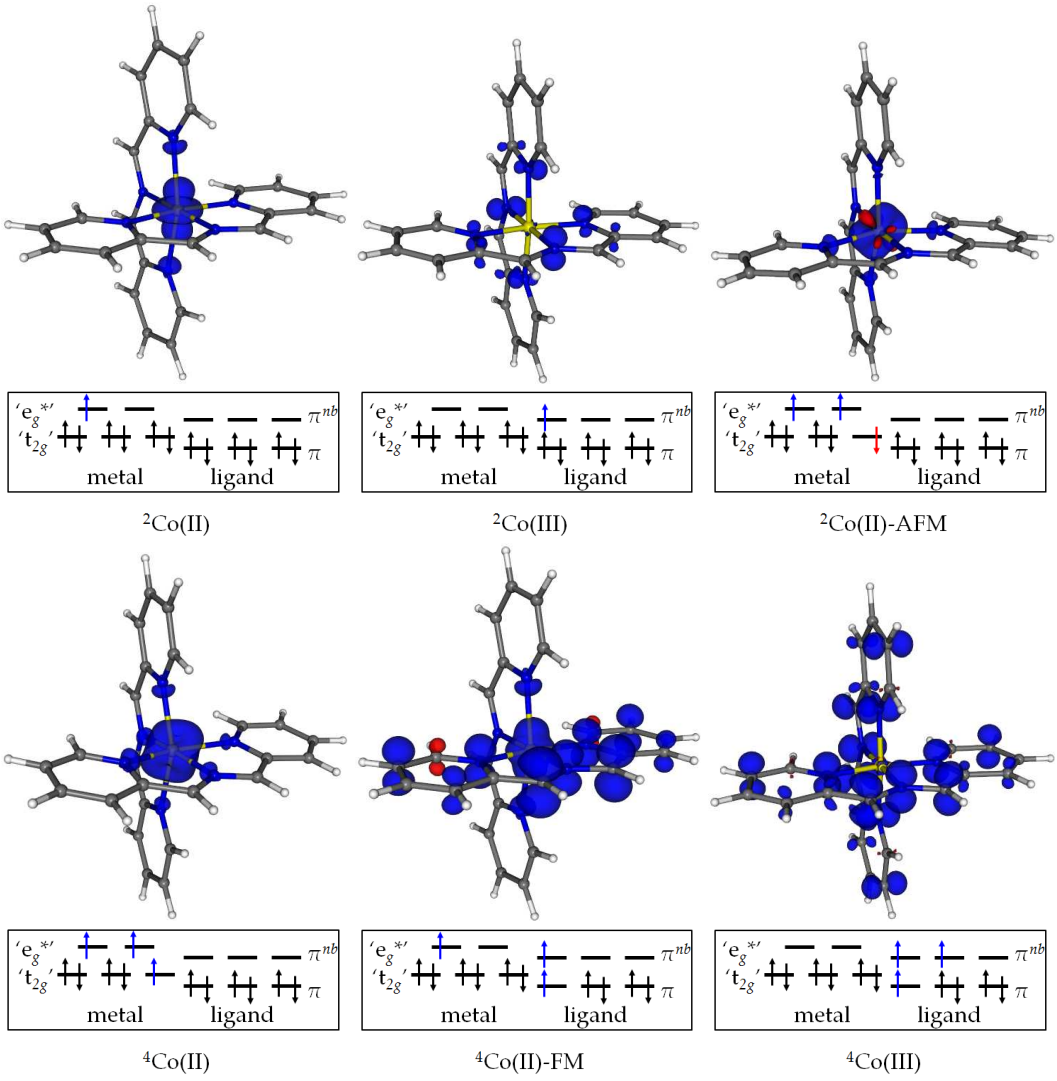

Figure 5.6: Spin density isosurfaces and configurations of the differerent Co(smif)$_2$ isomers.

[^{2}Co(II):] The lowest doublet isomer (C_{2v} $^2A_1$) has a classical electronic structure with EOS +2 and $(t_{2g})^6(e_g^*)^\alpha$ configuration. It shows short metal-aza bonds with moderate $D_{2d} \longrightarrow C_{2v}$ symmetry breaking, whereas the second set of metal-pyridyl bonds is quite long (i.e., the pincer of the second smif is significantly opened). The corresponding D_{2d} $^2B_2$ transition state lies 1.4 kcal/mol ($\Delta G^{\ominus}_{d-d}$ = 2.0 kcal/mol) above this minimum. It shows a somewhat different distribution

of the unpaired electron, changing from a 'd_{x^2}' in C_{2v} to a $d_{x^2-y^2}$ in D_{2d} in accordance with the restored x,y symmetry.

[^{2}Co(III):] The second doublet isomer is a D_2 $^2B_3$ with noninnocent EOS +3 and $(t_{2g})^6(e_g^*)^0(\pi_L)^6(\pi_L^{nb})^\alpha$ configuration, located 14.7 kcal/mol ($\Delta G^{\ominus}_{d-d}$ = 15.6 kcal/mol) above the C_{2v} $^2A_1$ minimum. The D_{2d} $\longrightarrow$$D_2$ JT distortion is small and the metal is tightly coordinated. The resulting strong-field pushes the 'e_g^*' set high in energy, such that an $(e_g^*)^\alpha(\pi_L^{nb})^0$ $\longrightarrow$$(\pi_L^{nb})^\alpha(e_g^*)^0$ transfer of the lone electron to the ligand-π-systems is beneficial (supported by their close vicinity). The unpaired electron is primarily distributed over the nitrogens of both smifs, such that one could argue FM coupling between them – alas there is only one unpaired electron.

[^{4}Co(II):] A quartet C_2 with undetermined state symmetry was found as the global minimum. It shows an EOS +2 and a classical $(t_{2g})^{4,\alpha}(e_g^*)^{\alpha,\alpha}$ configuration (although 0.3 α-electrons are shifted onto the nitrogens along the σ-bonds). The JT D_{2d} $\longrightarrow$$C_2$ canting is moderate, d(Co-N^{av}) is quite long, and the metal-ligand bond-distances are relatively homogenous. A corresponding C_s ^{4}A" transition state with similar canting angle and d(Co-N^{av}) was found just 0.02 kcal/mol ($\Delta G^{\ominus}_{q-q}$ = 0.04 kcal/mol) above. Note, that these structures are essentially degenerate despite the fact that in the C_2 both smifs are canted by ~10°, while in the C_s only one of them is.

[^{4}Co(II)-FM:] The second quartet isomer is a C_{2v} $^4B_1$, 35.7 kcal/mol ($\Delta G^{\ominus}_{q-q}$ = 34.8 kcal/mol) higher in energy than the first minimum. While it also has a classical EOS +2, it features a nonclassical $(t_{2g})^6(e_g^*)^\alpha(\pi_L)^{4,\alpha}(\pi_L^{nb})^\alpha$ configuration, i.e., the metal is FM coupled to the closer smif (there is also some minor AFM spin-density in the periphery of that smif and some σ-FM coupling to the other smif). This state can be derived from a classical doublet by a ligand based

$(\pi_L)^2(\pi_L^{nb})^0 \longrightarrow(\pi_L)^\alpha(\pi_L^{nb})^\alpha$ spin-flip. The corresponding C_{2v} $^2A_1$ state incidentally has a similar geometry: both isomers have comparable *d*(Co-N), moderate JT distortion in the metal-aza bonds, and a rather widely opened second smif. The electronic structure of the corresponding D_{2d} $^4B_1$ transition state, located 18.5 kcal/mol ($\Delta G^{\ominus}_{q-q}$ = 19.1 kcal/mol) above its minimum, exhibits uncommonly pronounced differences: as both smifs are now equally closely coordinated, and due to the increased d-splitting, the remaining α-spin density is relocated from Co to the second smif during the $C_{2v} \longrightarrow D_{2d}$ transition, i.e., $(e_g^*)^\alpha(\pi_L^{nb})^0 \longrightarrow(\pi_L^{nb})^\alpha(e_g^*)^0$ (in addition, there is also some equilibration between the ligands). While there is FM coupling between the two smifs in this $(t_{2g})^6(e_g^*)^0(\pi_L)^{4,\alpha}(\pi_L^{nb})^{\alpha,\alpha}$ configuration, there is none with the metal, as it has no unpaired electrons left. All three α-electrons reside on the smifs, and the EOS +2 of the minimum has changed to an EOS +3. The substantial change in electronic structure along the $C_{2v} \longleftrightarrow D_{2d} \longleftrightarrow C_{2v}^*$ inversion curve is a result of the higher symmetry, which explains the large geometry and energy response.
[^{4}Co(III):] The third quartet isomer is a D_{2d} $^4A_2$ minimum with essentially identical geometry and configuration to the previously discussed TS, but corresponding to a state of different symmetry. It is 2.3 kcal/mol ($\Delta G^{\ominus}_{q-q}$ = 0.9 kcal/mol) more stable than the D_{2d} $^4B_1$ [TS], but is still 16.2 kcal/mol ($\Delta G^{\ominus}_{q-q}$ = 18.2 kcal/mol) above the C_{2v} $^4B_1$ isomer.

Some of the five different isomers have characteristically different IR spectra (see Fig. 5.7): while all EOS +2 systems give similar vibrational signals, they can easily be distinguished from the EOS +3 isomers. This observation may be useful for the exclusion of candidates based on the experimental data.

We computed the adiabatic and vertical gaps for these states at the obtained

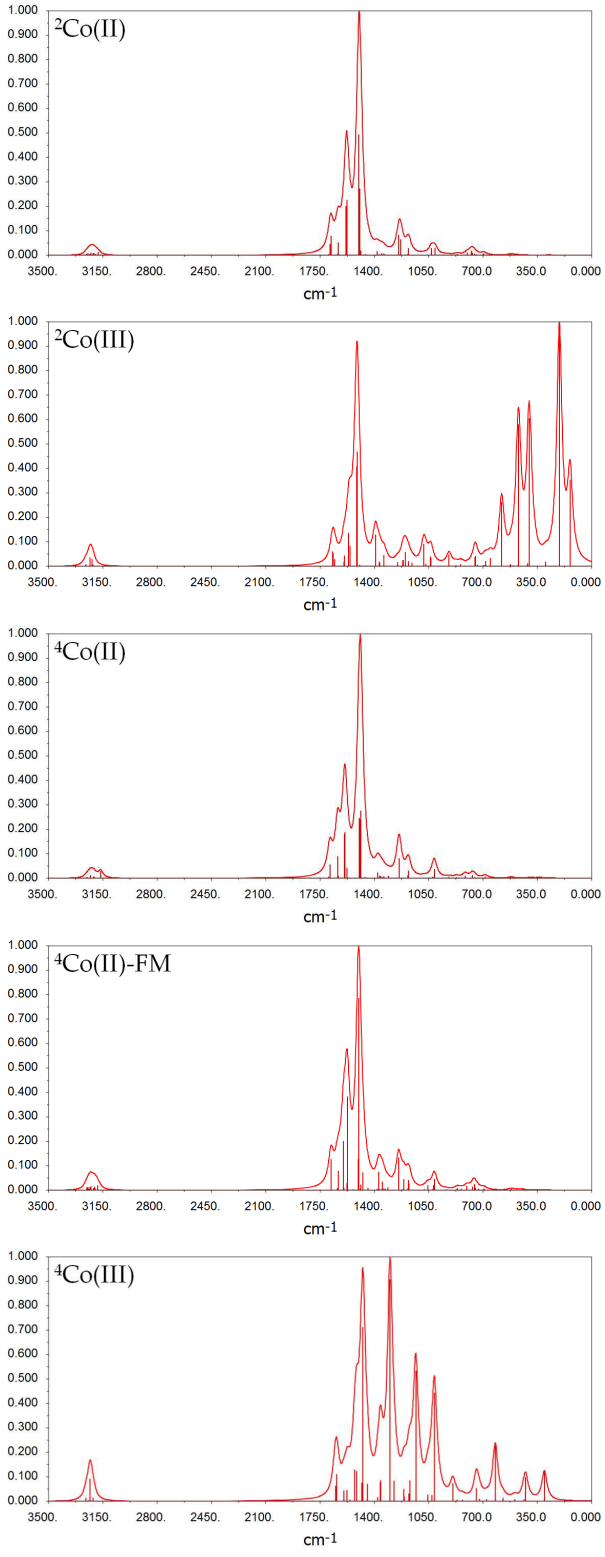

Figure 5.7: IR-spectra of the different Co(smif)$_2$ isomers.

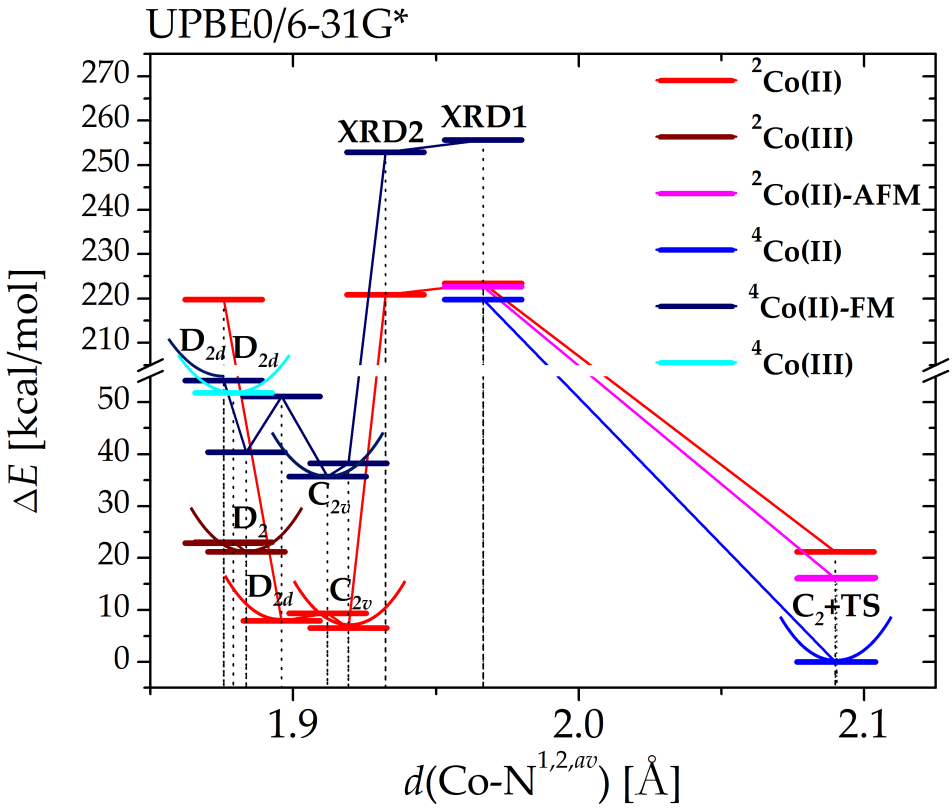

Figure 5.8: PES-projection of $Co(smif)_2$.

stationary point as well as on the XRD structures. In the course of this, we found another qualitatively different doublet state [^{2}Co(II)-AFM] as the lowest doublet for the longer d(Co-N^{1,2av}). It has an EOS +2 with a $(t_{2g})^{4,\beta}(e_g^*)^{\alpha,\alpha}$ configuration, i.e., an AFM occupation of the metal electrons, which can be realized by a metal-based $(t_{2g})^{4,\alpha}(e_g^*)^{\alpha,\alpha} \longrightarrow (t_{2g})^{4,\beta}(e_g^*)^{\alpha,\alpha}$ spin-flip from a classical quartet (being the lowest spin state in this region of the PES). Its preference over the ^{2}Co(II) can be linked to the small weak-field splitting of the d-levels.

The obtained PES profile – projected onto d(Co-N^{1,2av}) – is shown in Tab. 5.8 and Fig. 5.8:

For short d(Co-N^{1,2av}) (including the D_{2d} quartet minimum geometry), the

Table 5.8: Adiabatic total energy gaps (in kcal/mol) at UPBE0/6-31G* level between the different states for the stationary points on the $Co(smif)_2$-PES. The vertical gaps for each geometry are given in brackets.

d(Co-$N^{1,2av}$)	1.876	1.879	1.884	1.896	1.912	1.919	1.932	1.967	2.090	2.090
label	D_{2d} $^4B_1$ [TS]	D_{2d} $^4A_2$	D_2 $^2B_3$	D_{2d} $^2B_2$ [TS]	C_{2v} $^4B_1$	C_{2v} $^2A_1$	XRD2	XRD1	C_2 ^4X	C_s $^4A''$ [TS]
^{2}Co(II)	–	–	–	7.9	9.3	6.5	220.9	223.4 (3.7)	21.2 (21.2)	–
^{2}Co(III)	22.8	23.0	21.2	–	–	–	–	–	–	–
^{2}Co(II)-AFM	–	–	–	–	–	–	–	222.6 (2.9)	16.1 (16.1)	16.2 (16.2)
^{4}Co(II)	–	–	–	–	–	–	–	219.7	0	0.02
^{4}Co(II)-FM	54.2 (31.3)	–	40.4 (19.2)	51.1 (43.3)	35.7 (26.3)	38.2 (31.7)	252.9 (32.0)	255.6 (35.9)	–	–
^{4}Co(III)	–	51.8 (28.8)	–	–	–	–	–	–	–	–

noninnocent ^{2}Co(III) curve is lowest in energy due to the strong-field coordination, which gives it an advantage over the ^{2}Co(II) and quartet states. The equally nonclassical ^{4}Co(III) quartet as well as the turning point of the ^{4}Co(II)-FM curve (see discussion above) are 20-30 kcal/mol higher in energy. Note, that the ^{2}Co(III)$\longrightarrow$ ^{4}Co(III) transition is based on a $(\pi_L)^2(\pi_L^{nb})^0 \longrightarrow (\pi_L)^{\alpha}(\pi_L^{nb})^{\alpha}$ spin-flip on the ligand. The intermediate d(Co-N^{1,2av}) region (including the C_{2v} quartet minimum geometry) is dominated by the ^{2}Co(II) curve, which is 25-45 kcal/mol more stable than the competing ^{4}Co(II)-FM. The vertical transition is also constituted by a ligand-based spin-flip.

XRD2 still belongs to this range, but XRD1 with its longer M-L bonds shows a more complicated and qualitatively different picture: although it still has the ^{2}Co(II) and ^{4}Co(II)-FM states available with a gap comparable to XRD2, it also has low-energy ^{2}Co(II)-AFM and ^{4}Co(II) states, which are the respective doublet and quartet ground states. The latter is the overall lowest state in contrast to the ^{2}Co(II) for XRD2. XRD1 is hence similar to the two long-d(Co-N^{1,2av}) structures. This situation confirms the initial hypothesis that the differences between the XRD structures in the unit cell are related to their spin states. For XRD1, the ^{4}Co(II), ^{2}Co(II)-AFM, and ^{2}Co(II) curves lie within 4 kcal/mol, while the metal-based $(t_{2g})^{4,\alpha}(e_g^*)^{\alpha,\alpha} \longrightarrow (t_{2g})^{4,\beta}(e_g^*)^{\alpha,\alpha}$ spin-flip to the ^{2}Co(II)-AFM curve takes 16 kcal/mol for the C_2 ^{4}X isomer and its TS.

We note that although the XRD structures are more than 200 kcal/mol higher in energy than the optimized geometries, this does not contradict the proposed flat internal PES: the XRD errors are in *all* parts of the complex, and the energetic contributions of the steep PES regions can easily accumulate to this order of magnitude.

In summary, for all short and medium d(Co-N^{1,2av}) values the doublet is the ground state with robust vertical gaps of 20 to 40 kcal/mol, and only very loose coordination leads to a high-spin quartet ground state with a vertical gap of 16 kcal/mol to the next doublet. XRD1 lies on the boundary between these regions.

In light of the experimental data, we assume that the use of the PBE0 hybrid functional leads to overstabilization of the ^{4}Co(II) curve relative to the ^{2}Co(II) for intermediate M-L bonds (the computed gaps are within the margin of the DFT error), which results in an incorrect spin-state ordering. We note, that this is the only qualitatively incorrect result at UPBE0/6-31G* level in our study. Based on the similarity between the XRD2 and the optimized C_{2v} $^2A_1$ structures (a more detailed comparison follows below), we assume that the ^{2}Co(II) isomer is the true ground state. The PES profile and the large vertical gaps suggest that the experimentally observed spin-crossover is based on temperature induced vibrational bond-stretching, which adiabatically drives the Co(smif)$_2$ into the quartet basin. XRD1 can be viewed as a superposition of these isomers. The adiabatic gap is certainly small enough to explain the temperature dependent change in the SQUID susceptibilities. Both competing isomers (i.e., ^{2}Co(II) and ^{4}Co(II)) have a classical electronic structure.

We recomputed the gaps at the UPBE0/cc-pVTZ (DKH2) level to account for basis set and relativistic effects, as well as on the UTPSS/6-31G* level to obtain a lower bracket for ΔE_{q-d} through the use of a meta-GGA functional (all calculations were performed on the previously obtained geometries).

The UTPSS/6-31G* ansatz (see Tab. 5.9) recovers the proposed ^{2}Co(II) isomer as the global minimum, with an adiabatic gap of 10.7 kcal/mol to the

Table 5.9: Adiabatic total energy gaps (in kcal/mol) at UTPSS/6-31G* level (top) and UPBE0-ccpVTZ (DKH2) level (bottom) between the lowest doublet and quartet states for the different stationary points on the $Co(smif)_2$-PES. The vertical gaps for each geometry are given in brackets.

d(Co-$N^{1,2av}$)	1.876	1.879	1.884	1.896	1.912	1.919	1.932	1.967	2.090	2.090
label	D_{2d} $^4B_1$ [TS]	D_{2d} $^4A_2$	D_2 $^2B_3$	D_{2d} $^2B_2$ [TS]	C_{2v} $^4B_1$	C_{2v} $^2A_1$	XRD2	XRD1	C_2 ^4X	C_s $^4A''$ [TS]
S = 1/2	3.7	3.8	3.7	1.4	0	0.1	220.7	222.4	16.6 (5.8)	16.7 (5.9)
S = 3/2	34.4 (30.7)	34.4 (30.6)	38.1 (34.4)	20.5 (19.0)	24.7 (24.7)	23.6 (23.5)	241.9 (21.2)	234.1 (11.7)	10.8	10.8
S = 1/2	17.5	17.8	15.3	2.3	3.7	0.6	197.5	200.8	13.8 (13.7)	13.8 (13.8)
S = 3/2	–	45.7 (27.9)	46.8 (31.5)	34.3 (31.9)	30.1 (26.4)	32.0 (31.4)	229.3 (31.7)	201.0 (0.2)	0.1	0

Table 5.10: Linear interpolation coefficients f between the computed geometries and resulting quality of the XRD representation.

	XRD1			XRD2	
$f(C_{2v})$	1.0	0.266	0.196	1.0	0.603
$f(D_{2d})$	0	0.734	0.639	0	0.397
$f(C_2)$	0	0	0.166	0	0
$\|\Delta d\|^{av}$	4.0%	1.5%	1.0%	1.5%	0.8%
Δd^{max}	±4.9%	–3.4%	–1.8%	+2.6%	–1.7%
$\|\Delta\Delta d\|^{max}$	9.8%	4.2%	2.8%	4.4%	3.0%

^{4}Co(II). Compared to the PBE0 level, the doublet PES is much more shallow towards shorter d(Co-N^{1,2av}), and the vertical doublet-quartet gaps are smaller with 20-35 kcal/mol. The ^{4}Co(II) remains a local minimum for long d(Co-N^{1,2av}) with a small vertical gap of 6 kcal/mol. The Co(smif)$_2$ results show a large functional dependence, underlining its challenging electronic structure.

The UPBE0/cc-pVTZ (DKH2) results (Tab. 5.9) feature overall smaller adiabatic gaps but comparable vertical gaps to UPBE0/6-31G*. The ^{2}Co(II) and ^{4}Co(II) isomers are near degenerate with the quartet winning out by only 0.5 kcal/mol (unchanged by solvation in benzene). We also note that the C_s ^{4}A" transition state geometry gives a lower energy than the C_2 ^{4}X minimum. The two possible reasons are that a) the double-ζ geometry for the TS is slightly closer to the triple-ζ solution than for the minimum, such that the latter will slip below the TS upon reoptimization of the geometry, or b) the JT symmetry breaking is an artifact of the smaller basis.

We now return the issue of the two different XRD structures in more detail. From our analysis of the PES, we interpret XRD2 as derived from the C_{2v}

$^2A_1$ isomer through deformation along the soft $C_{2v} \longrightarrow D_{2d} (\longrightarrow C^*_{2v})$ inversion. The barrier of only 1.1 kcal/mol is in reach of the forces of the crystal packing. A simple linear interpolation of minimum and transition state gives a significantly improved representation of XRD2 (see Tab. 5.10). We interpret XRD1 as a superposition of such a distorted doublet and the near-degenerate C_2 ^4X isomer (for simplicity we omitted the quartet TS in this discussion). The linear interpolation of these three structures produces a good match to XRD1, as the TS evens the two metal-aza-bonds and the quartet isomer increases the overall M-L-bond distances. Note however, that XRD1 does not show the characteristic canting of the quartet C_2. The weights of these interpolations indicate that XRD2 is still close to the minimum along the inversion curve, while XRD1 is much closer to the TS and the two isomers have roughly equal contribution.
We remark on the fact that despite their structural and electronic differences, both XRD geometries are quasi-degenerate.

An EPR study of the $Co(smif)_2$ revealed an anisotropic g-tensor. This spatial directionality is consistent with the C_{2v} symmetry distortion and the resulting 'd_{x^2}' α-density of the ^{2}Co(II) state. For the C_{2v} minimum we obtained g_x=2.001, g_y=2.102, g_z=2.127, and g_{iso}=2.076, and for the D_{2d} transition state g_x=2.029, g_y=2.029, g_z=2.152, and g_{iso}=2.070. The experimental values g_x=2.01, g_y=2.135, and g_z=2.21 correspond well with the C_{2v} isomer.

The experimental UV/vis spectrum (above 410 nm) is dominated by bands at 639.0 nm (molar absorptivity 14,000 $mol^{-1}cm^{-1}$) and 489.5 nm (15,000 $mol^{-1}cm^{-1}$). The TDDFT spectrum for the C_{2v} isomer shows two main peaks at 534.2 nm (oscillator strength f=0.1565) and 464.90 nm (f=0.4012) which is notably blue-shifted. The spectrum on the D_{2d} transition state geometry is in con-

trast only slightly red-shifted with degenerate peaks at 655.52 nm (f=0.0001) and 495.45 nm (f=0.2422), with the former being symmetry-forbidden. The proposed mixture of both structures improves the correspondence with experiment, as the opposed shifts cancel and the symmetry breaking lifts the D_{2d} restrictions on the first peak.

5.3.4 Cr(smif)$_2$-cation

The [Cr(smif)$_2$]$^+$-cation is formally a Cr(III) d^3-system with possible $S = \frac{1}{2}, \frac{3}{2}$ states. Initial Guoy balance measurementsindicated a doublet ground state in violation of Hund's rule. K-edge data from X-ray absorption spectroscopy (XAS) confirmed the +3 oxidation state on the metal (with *trans*-[$CrCl_2(H_2O)_4$]Cl as reference; see Fig. 5.9). The XRD of the Cr(smif)$_2$OTf salt (i.e., with triflate counterion) shows the [Cr(smif)$_2$]$^+$ in approximate D_{2d} symmetry with minor irregular distortions. The metal-ligand bond distances are given in Table 5.11.

We performed DFT geometry optimizations of the cation (without the counterion) in the doublet and quartet state employing the PBE0, B3LYP (for quartet only), and BLYP functionals in the 6-31G* basis. The results are summarized in Tables 5.11 and 5.12.

The optimizations of the doublet state geometry were hard to converge and found *two minima* – one C_{2v} and one C_s – for both, the PBE0 and the BLYP, functionals. The separation between the two *coordination symmetry* and *bond-length isomers* is small in energy with 3.2 kcal/mol for PBE0 and 0.7 kcal/mol for BLYP (see Tab. 5.12 and 5.13) and within the error margin of DFT. The BLYP minima and the lower PBE0 minimum are not in good agreement with

Table 5.11: XRD and computed M-L bond distances in the $[Cr(smif)_2]^+$-cation (in Å). Percentage differences between theory and experiment are shown in brackets. Non-significant figures in the XRD data are given in italics.

bond	XRD	UPBE0/6-31G*		UBLYP/6-31G*	
	~D_{2d}	C_{2v}, $^2B_2$	C_s, $^2A'$	C_s, $^2A'$	C_{2v}, $^2B_1$
Cr-N^1	1.99*05*	1.9384 (–2.6%)	2.0038 (+0.7%)	2.0149 (+1.2%)	1.9643 (–1.3%)
Cr-N^2	1.99*61*	2.0374 (+2.1%)	2.0126 (+0.8%)	2.0410 (+2.2%)	2.0566 (+3.0%)
Cr-N^3	2.03*20*	2.0529 (+1.0%)	2.0284 (–0.2%)	2.0374 (+0.3%)	2.0492 (+0.8%)
Cr-N^4	2.03*59*	2.0529 (+0.8%)	2.0322 (–0.2%)	2.0629 (+1.3%)	2.0492 (+0.7%)
Cr-N^5	2.03*18*	2.0554 (+1.2%)	2.0353 (+0.2%)	2.0612 (+1.4%)	2.0722 (+2.0%)
Cr-N^6	2.03*28*	2.0554 (+1.1%)	2.0353 (+0.1%)	2.0612 (+1.4%)	2.0722 (+1.9%)

bond	UPBE0/6-31G*	UB3LYP/6-31G*	UBLYP/6-31G*
	D_{2d}, $^4B_1$	D_{2d}, $^4B_1$	D_{2d}, $^4B_1$
Cr-N^1	2.0155 (+1.3%)	2.0325 (+2.1%)	2.0419 (+2.6%)
Cr-N^2	2.0155 (+1.0%)	2.0325 (+1.8%)	2.0419 (+2.3%)
Cr-N^3	2.0469 (+0.7%)	2.0681 (+1.8%)	2.0777 (+2.2%)
Cr-N^4	2.0469 (+0.5%)	2.0681 (+1.6%)	2.0777 (+2.1%)
Cr-N^5	2.0469 (+0.7%)	2.0681 (+1.8%)	2.0777 (+2.3%)
Cr-N^6	2.0469 (+0.7%)	2.0681 (+1.7%)	2.0777 (+2.2%)

bond	UPBE0/cc-pVTZ		
	C_{2v}, $^2B_2$	C_s, $^2A'$	D_{2d}, $^4B_1$
Cr-N^1	1.9431 (–2.4%)	2.0088 (+0.9%)	2.0186 (+1.4%)
Cr-N^2	2.0402 (+2.2%)	2.0164 (+1.0%)	2.0186 (+1.1%)
Cr-N^3	2.0607 (+1.4%)	2.0374 (+0.3%)	2.0542 (+1.1%)
Cr-N^4	2.0607 (+1.2%)	2.0402 (+0.2%)	2.0542 (+0.9%)
Cr-N^5	2.0639 (+1.6%)	2.0444 (+0.6%)	2.0542 (+1.1%)
Cr-N^6	2.0639 (+1.5%)	2.0444 (+0.6%)	2.0542 (+1.1%)

Table 5.12: Total energy (ΔE) and standard Gibbs free energy gaps ($\Delta G^{\ominus}$) between the quartet and doublet ground states ($q - d$) and different doublet minima ($d - d$), respectively, in kcal/mol; $\langle S^2 \rangle$ before and after annihilation; MPA and AIM charges (q_{MPA}(Cr), q_{AIM}(Cr)) and spin densities (n^s_{MPA}(Cr), n^s_{AIM}(Cr)) in the $[Cr(smif)_2]^+$-cation. For additional data see Tab. B.1.

	UPBE0/6-31G*		UBLYP/6-31G*		UPBE0/6-31G*	UB3LYP/6-31G*	UBLYP/6-31G*
	C_{2v}, $^2B_2$	C_s, $^2A'$	C_s, $^2A'$	C_{2v}, $^2B_1$	D_{2d}, $^4B_1$	D_{2d}, $^4B_1$	D_{2d}, $^4B_1$
$\Delta E_{q-d}/\Delta E_{d-d}$	20.69	3.25	15.67	0.68	–	–	–
$\Delta G^{\ominus}_{q-d}/\Delta G^{\ominus}_{d-d}$	19.36	4.04	14.77	0.85	–	–	–
$\langle S^2 \rangle$	2.5290	1.7800	1.6123	1.6761	3.7803	3.7769	3.7754
$\langle S^2 \rangle_{ann}$	3.3753	0.9502	0.7932	1.3253	3.7504	3.7503	3.7503
q_{MPA}(Cr)	1.2	1.24	0.94	0.94	1.27	1.14	0.97
q_{AIM}(Cr)	2.0	2.09	1.90	1.89	2.11	2.05	1.94
n^s_{MPA}(Cr)	2.96	1.09	1.22	2.22	3.15	3.08	2.94
n^s_{AIM}(Cr)	2.57	1.02	1.14	1.99	2.92	2.89	2.78

	UPBE0/6-31G*//cc-pVTZ (DKH2)			UPBE0/cc-pVTZ		
	C_{2v}, $^2B_2$	C_s, $^2A'$	D_{2d}, $^4B_1$	C_{2v}, $^2B_2$	C_s, $^2A'$	D_{2d}, $^4B_1$
$\Delta E_{q-d}/\Delta E_{d-d}$	20.78	2.23	–	20.82	2.69	–
$\Delta G^{\ominus}_{q-d}/\Delta G^{\ominus}_{d-d}$	19.45*	3.02*	–	19.03	3.91	–
$\langle S^2 \rangle$	2.5390	1.7864	3.7790	2.5340	1.7846	3.7799
$\langle S^2 \rangle_{ann}$	3.3990	0.9462	3.7504	3.3781	0.9331	3.7504
q_{MPA}(Cr)	0.37	0.33	0.41	0.45	0.41	0.47
q_{AIM}(Cr)	–	–	–	–	–	2.15
n^s_{MPA}(Cr)	2.98	1.11	3.18	2.98	1.12	3.19
n^s_{AIM}(Cr)	–	–	–	–	–	2.92

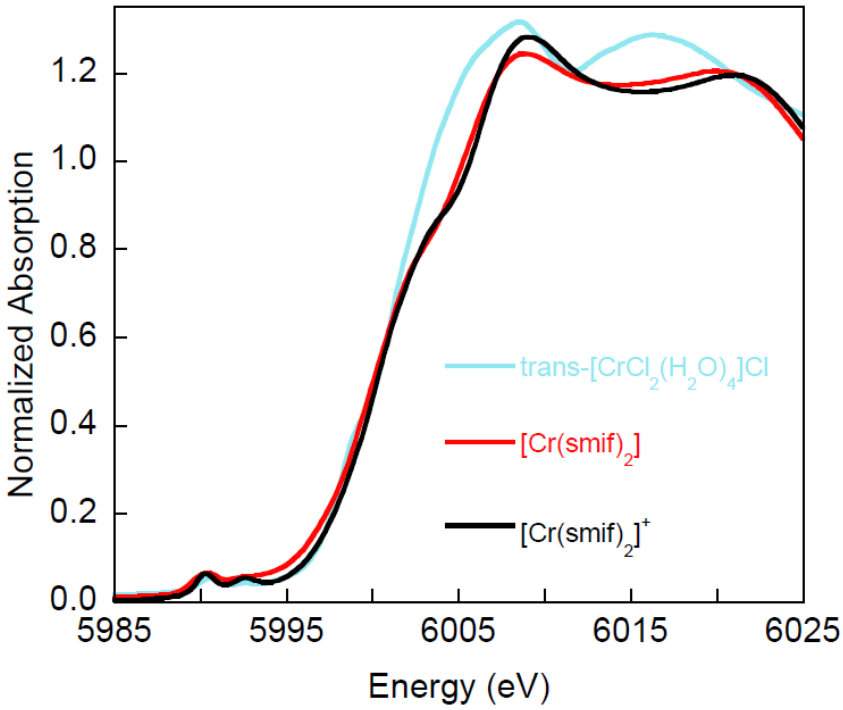

Figure 5.9: XAS spectrum of $Cr(smif)_2$, its cation and the *trans*-$[CrCl_2(H_2O)_4]Cl$ reference (courtesy of S. DeBeer George).

the XRD geometries, and further show notable deviations amongst each other (see Tab. 5.11). The C_{2v} structures exhibit a considerable difference in coordination between the two smifs (i.e., $d_{Cr\text{-}N^1} \neq d_{Cr\text{-}N^2}$), while there is less heterogeneity in the metal-ligand bond distances of the C_s structures. In addition, the C_{2v} minima from PBE0 and BLYP display a different relaxation of the smifs ($d_{Cr\text{-}N^3} = d_{Cr\text{-}N^4} \approx d_{Cr\text{-}N^5} = d_{Cr\text{-}N^6}$ vs. $d_{Cr\text{-}N^3} = d_{Cr\text{-}N^4} \nsim d_{Cr\text{-}N^5} = d_{Cr\text{-}N^6}$) and a different ground state symmetry ($^2B_2$ vs. $^2B_1$). The smif-canting in the C_s geometry is more pronounced in the BLYP result than in PBE0. The higher PBE0 minimum (C_s $^2A'$) is close to the experimental geometry and would from this perspective be a reasonable candidate. It shows only a small Jahn-Teller distortion from D_{2d} symmetry while at the same time displaying a very flat PES around the

minimum. The $[Cr(smif)_2]^+$ doublet optimization is a persuasive example for the importance of a careful PES sampling, as one of the minima may well have stayed undetected, or the subtle Jahn-Teller distortion may have been missed.

All Kohn-Sham determinants for the doublet states exhibit large spin-contamination up to $\langle S^2 \rangle = 2.53$ (ideal doublet $\langle S^2 \rangle = 0.75$), and annihilation of the first spin contaminant does not substantially improve this situation. The obtained doublet wavefunctions differ substantially in character, e.g., when comparing $\langle S^2 \rangle$ values, population and AIM analysis of the spin densities, or frontier orbitals, despite being close in energy. We find the electronic structure in each case to be involved: the C_{2v} $^2B_2$ for example is a broken-symmetry state (within the DFT description), in which 2.57 unpaired α-electrons on chromium are antiferromagnetically (AFM) coupled to 1.57 unpaired β-electrons on *one* of the ligands (see Fig. 5.10), resulting in the overall single excess α-electron of the doublet wavefunction. Note the alternating spin density pattern on the ligand. The nonequivalence of the two smifs is reflected in both the different coordination (due to the symmetry breaking in C_{2v}) and the electronic structure. The AFM is somewhat smaller in the corresponding BLYP wavefunction, and the order of the two doublet states is inverted. The second minimum (C_s $^2A'$) is also a broken-symmetry solution, but as Fig. 5.10 shows of entirely different nature. These observations suggest that the low-spin state is of multi-reference character and may not be well represented by the single-reference DFT approach.

The geometry optimizations of the quartet state were in contrast straightforward and all approaches led to high-symmetry D_{2d} structures and $^4B_1$ states. The PBE0 quartet structure is a good match to the experimental geometry[6]

[6]When we assess the deviations from the X-ray results, it is not sufficient to only consider the average magnitude of deviation, but also its spread. The doublet C_s $^2A'$ geometry has an average percentage deviation of only 0.4%, but the spread of values is 1.0%, while the quartet

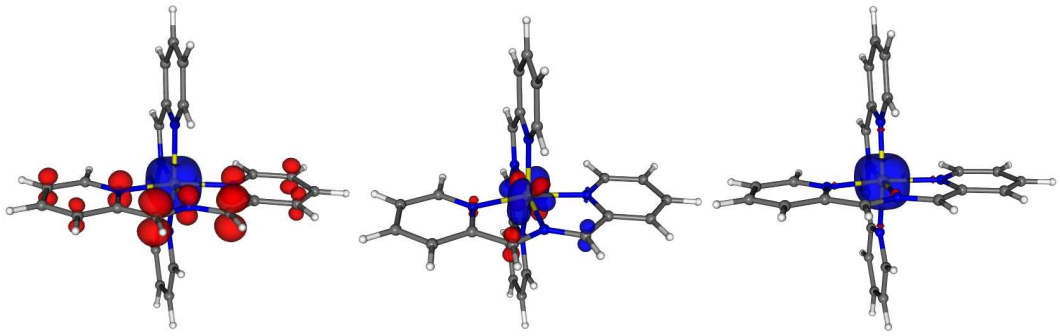

Figure 5.10: Spin density isosurfaces in the $[Cr(smif)_2]^+$-cation: UPBE0 C_{2v} $^2B_2$ BS-AFM state (left), spin-contaminated C_s $^2A'$ state (center), and D_{2d} $^4B_1$ state (right) (blue: $\rho^s = 0.015$; red: $\rho^s = -0.015$). Note the complicated symmetry breaking and spin coupling in the two doublet states, compared to the conventional quartet.

with a small systematic overestimate of the metal-ligand bond lengths by ~1%. B3LYP and even more so BLYP show the same trend with significantly larger overestimates (see Tab. 5.11). The superior performance of the PBE0 functional is consistent with the benchmark study by Brühl et al. [260, 262] (if not otherwise stated, the further discussions refer to the PBE0 results, and higher level calculations are based on the UPBE0/6-31G* geometry).

The comparison of (lower) doublet (C_{2v} $^2B_2$) and quartet minima shows a significant gap of 20.7 kcal/mol (PBE0) and 15.7 kcal/mol (BLYP), respectively, with the high-spin state being energetically favored. Thermal free energy corrections reduce this gap somewhat to 19.4 and 14.8 kcal/mol however without changing the overall order of magnitude (see Tab. 5.13), which again points

shows an average of 0.8% deviation with only a 0.8% spread. In the triple-zeta basis, we find 1.1% deviation but the spread is only 0.5% (all values refer to the PBE0 results). Although the deviations are increased, they refer to a *systematic* overestimate of the bond lengths.

Note, that the experimantal data has also limited accuracy, and refers to the crystal phase (which introduces additional packing effects) compared to the isolated molecule calculation.

towards the quartet as the ground state.

The quartet wavefunctions have only minor spin-contamination of up to $\langle S^2 \rangle = 3.78$ (ideal quartet $\langle S^2 \rangle = 3.75$), and annihilation was successful. This indicates a wavefunction of essentially single-reference nature. We find a chromium charge of q_{AIM}(Cr)=2.11 and have the counterintuitive situation of four remaining electrons on the chromium, while the integrated spin density n^s_{AIM}(Cr)=2.92 finds three *unpaired* electrons. The frontier orbitals and gross orbital populations of the PBE0 quartet state show the degenerate d_{xz} and d_{yz}, as well as the d_{xy} (i.e., the 't_{2g}'-set) α-occupied, while d_{z^2} and $d_{x^2-y^2}$ (and to a smaller degree 4s and 4p) are each partially occupied (accounting for the fourth electron) with roughly equal amount of α and β spin-density[7]. The frontier orbitals are quite delocalized and the mixing of metal and ligand based AOs complicates conclusions with respect to the bonding situation. The computed spin density ρ^s corresponds well to the overlap of the d_{xz}-, d_{yz}-, and d_{xy}-orbitals (see Fig. 5.10).

To gauge the basis set dependence of these results we reoptimized the two doublet and one quartet PBE0 minima in the cc-pVTZ basis. For comparison we also computed the cc-pVTZ gaps (with DKH2 relativistic correction) on the previous double-ζ geometry[8]. We only find an insignificant dependence on the geometry, the KS-wavefunction characteristics essentially do not change (see Tab. 5.11 and 5.12), and the comparison of the gaps is shown in Tab. 5.13. We can state that the double-ζ basis is sufficient for geometries and intramolecular charge distributions, but that a triple-ζ basis should probably be considered for

[7]The four α-HOMOs and two α-LUMOs are ligand-based π-MOs, with some d-character mixed in (as far as allowed by symmetry). The α-HOMO-4,5,6 are the d_{xz}, d_{yz} and d_{xy} with some ligand-π contribution, while α-LUMO+2,3 are the unoccupied d_{z^2}, $d_{x^2-y^2}$. All β-HOMOs are of ligand-π-character with only minimal d-mixing. The β-LUMO, LUMO+1,2 correspond to the d_{xz}-, d_{yz}-, and d_{xy}-orbitals with ligand-π contribution, followed by further MOs of that composition and the d_{z^2}, $d_{x^2-y^2}$ as β-LUMO+10,12.

[8]The Gibbs free energy correction also stems from the smaller basis.

Table 5.13: Total energy and standard Gibbs free energy gaps (ΔE and $\Delta G^{\ominus}$, respectively) between the optimized doublet minima ($d-d$) and the quartet and doublet minima ($q-d$) of the $[Cr(smif)_2]^+$-cation at different levels of theory in kcal/mol.

level of theory	ΔE_{d-d}	$\Delta G^{\ominus}_{d-d}$	ΔE_{q-d}	$\Delta G^{\ominus}_{q-d}$
UPBE0/6-31G*	3.2	4.0	20.7	19.4
UPBE0/cc-pVTZ	2.7	3.9	20.8	19.0
UPBE0/6-31G*//cc-pVTZ (DKH2)	2.2	3.0	20.8	19.5
UBLYP/6-31G*	–0.7	–0.9	15.7	14.8

the spin-gaps. We also note that the prudent choice of the utilized functional has a larger impact than the size of the basis set. Finally, we mention the unsatisfactory behavior of the Mulliken charges, in particular comparing the double-ζ and triple-ζ results. The AIM charges show little basis set dependence.

For the doublet state to slip below the quartet – as predicted by the Guoy balance measurements – would require a Jahn-Teller symmetry breaking of its D_{2d} geometry, specifically of the 't_{2g}'-levels. Possible $D_{2d} \longrightarrow C_{2v}$ distortions were explored by a) displacement of one smif (with Cr-N^1 distances between 1.75 and 2.35 Å) and b) opening of one smif-pincer (with angles ϕ_{NNN} between 80° and 118°). The former can only reduce the total energy gap to 12.6 kcal/mol at UPBE0/6-31G* and 10.0 kcal/mol at UBLYP/6-31G* level , the latter to 20.2 kcal/mol and 12.3 kcal/mol, respectively. Consequently, such a splitting is not sufficient to reverse the state ordering. Since even BLYP with its low-spin bias solidly favors the quartet as the ground state, the experimentally proposed state ordering had to be rejected from the theoretical perspective. At this point in our investigation new superconducting quantum interference device (SQUID)

data became available which now placed the quartet state below the doublet, confirming the DFT state ordering[9].

The experimentally proposed chromium oxidation state +3 remained in apparent disagreement with the computationally determined charge of q_{AIM}(Cr)$\simeq$ 2 for all doublet and quartet wavefunctions. We computed the electron distribution in the Cr(III) XAS reference complex *trans*-$[CrCl_2(H_2O)_4]^+$, as well as the neutral *trans*-$CrCl_2(H_2O)_4$ with Cr(II). As mentioned before, the reference shares the same pseudooctahedral, trans-dianionic ligand structure. For the cation (quartet) ground state we found q_{AIM}(Cr)=2.12 and for the neutral complex (quintet) q_{AIM}(Cr)=1.60 (all at UPBE0/6-31G* level of theory), which confirmed the Cr(III) assignment. While it is well known that the formal concept of oxidation states does not exactly reflect the actual intramolecular charge distribution, the magnitude of the discrepancy for this moderate oxidation state was somewhat unexpected. A closer analysis of the relation between oxidation state and atomic charges, in particular with respect to the implications on the bonding situation, will be described in App. A.

We investigated the influence of relativistic and external field effects by solvents on the intramolecular charge distribution (see Tab. 5.14), and find the electronic structure to be robust with respect to these factors. We computed further quartet states on the $^4B_1$ geometry and found a wide variety of electronic structures with the atomic charges in the range from 1.76 to 2.17.

In summary, the computational results for the $[Cr(smif)_2]^+$-cation ground state are – after careful analysis – in good agreement with the experimental data. Since the quartet state is established as the ground state with a substantial

[9]The original measurement was tainted due to a contamination.

Table 5.14: Comparison of vertical relativistic correction and solvation effects to the UPBE0/6-31G* solution: Solvation energy (ΔE^{sol} in kcal/mol), spin-squared expectation value ($\langle S^2 \rangle$) before and after annihilation of the first spin contaminant, as well as Mulliken and AIM charges (q_{MPA}(Cr), q_{AIM}(Cr)) and spin densities (n^s_{MPA}(Cr), n^s_{AIM}(Cr)) on the chromium for the quartet ground state. For additional data see Tab. B.3.

	UPBE0/6-31G*			
		(DKH2)	(DKH2) (SCI-PCM=THF)	(DKH2) (SCI-PCM=AcN)
ΔE^{sol}	–	–	–27.03	–30.45
$\langle S^2 \rangle$	3.7803/3.7504	3.7800/3.7504	3.7802/3.7504	3.7802/3.7504
q_{MPA}(Cr)	1.27	1.26	1.26	1.26
q_{AIM}(Cr)	2.11	2.12	2.12	2.12
n^s_{MPA}(Cr)	3.15	3.15	3.15	3.15
n^s_{AIM}(Cr)	2.92	2.92	2.92	2.92

gap to the doublet, and since it appears to be well represented within the DFT framework, we can forego a higher level wavefunction treatment.

5.3.5 Cr(smif)$_2$

The electron paramagnetic spin resonance (EPR) analysis of the chromium complex (formally d^4 with possible $S = 0, 1, 2$) suggests that this system features a near-degenerate triplet ground state with essentially zero-gap ($\Delta E_{t-t} \sim 0.01$ kcal/mol). The two states in question feature a qualitatively different electronic structure: One of the signals is isotropic ($g = 1.9825$) without hyperfine structure, indicating a spherical distribution of the unpaired electron density around

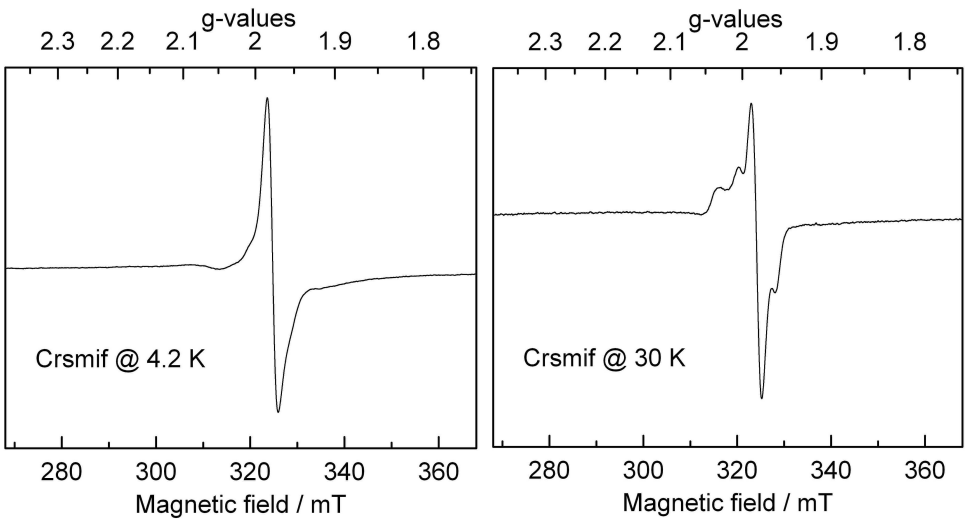

Figure 5.11: EPR spectra of $Cr(smif)_2$ at 4.2 K and 30 K temperature (courtesy of P. T. Wolczanski).

the metal. The other one is anisotropic (g_x = 1.959, g_y = 1.998, g_z = 2.031) with a spatial directionality of the spin density and hyperfine structure due to coupling on the ligand. From this information, states with '$(t_{2g})^4$' and '$(t_{2g})^3(\pi^*)^1$' character were proposed. The relative signal intensity is temperature dependent and a population change can be observed: At T = 4.2 K the EPR shows a ~4:1 signal ratio, which changes to ~1:1 at T = 30 K (see Fig. 5.11). The experiments were performed in highly diluted solution, so that aggregation and polymerization could be discarded. The intermediate S = 1 for these states was confirmed by SQUID and Evan's method measurements.

The comparison of the normalized XAS Cr K-edge spectra of $[Cr(smif)_2]^+$ and $Cr(smif)_2$ to the Cr(III) reference complex *trans*-$[CrCl_2(H_2O)_4]Cl$ indicates that the effective nuclear charge on the metal has not changed upon oxidation (see Fig. 5.9). Hence, a Cr(III) assignment is most appropriate for both cases, instead of the formal Cr(II) in the neutral complex. This points to a domi-

nantly ligand-based redox chemistry, i.e., the smif behaves as a redox-active, non-innocent ligand in $Cr(smif)_2$. The peak separation in the expanded Cr K-pre-edge region implies a very similar ligand-field splitting in the neutral and cationic complex, which can be related to a similar coordination.

The XRD shows a unit cell with two $Cr(smif)_2$ complexes, both resembling a distorted C_{2v} symmetry but with some differences. The first $Cr(smif)_2$ features one ligand with both pyridyl-rings bent, the other smif has a slight propeller-twist. The second $Cr(smif)_2$ in the unit cell shows one flat and one propeller-twisted smif group and resembles at least in part a D_2. Furthermore, the metal is off-center between each pyridyl-nitrogen pair (Fig. 5.3e). The metal-ligand bond distances are given in Tab. 5.15.

The PBE0 and B3LYP geometry optimizations of $Cr(smif)_2$ in the triplet state were a simple case again and converged for both functionals to a $^3B_2$ state in a D_2 symmetry (see Tab. 5.15 and 5.16 for a summary of the results). The obtained geometries are *not* in particularly good agreement with experiment: the obtained D_2 structures have the typical propeller-twist in *both* ligands (which break the higher D_{2d} symmetry; cf. Fig. 5.3). But they do not capture the C_{2v}-like nonequivalence between the two smif ligands in the XRD. Both functionals predict too long metal-ligand bonds (PBE0 less severe than B3LYP). The D_2 structure is chiral, and there naturally exist two distinct but degenerate enantiomers.

The spin density distribution and large spin-contamination of $\langle S^2 \rangle = 2.69$ (ideal triplet $\langle S^2 \rangle = 2$; see Tab. 5.16) reveal that the $Cr(smif)_2$ features a broken-symmetry ground state with antiferromagnetic coupling between metal and coordinating nitrogens (Fig. 5.12): instead of two unpaired electrons forming the

Table 5.15: The two XRD M-L bond distances in the $Cr(smif)_2$ complex (in Å, non-significant figures are given in italics), and the computationally optimized values (both minima and transition states (TS) for PBE0 and B3LYP; triplet states only) with average percentage differences between theory and experiment. For comparison, the values for the doublet cation were added.

bond	XRD 1	XRD 2	UPBE0/6-31G*			UB3LYP/6-31G*	
	bent	twisted	D_2, $^3B_2$	C_{2v}, $^3B_2$ [TS]	C_{2v}, $^2B_2$ [cation]	D_2, $^3B_2$	C_{2v}, $^3B_2$ [TS]
Cr-N^1	1.93*24*	1.94*81*	1.9924 (+2.7%)	1.9427 (+0.1%)	1.9384 (–0.1%)	2.0086 (+3.5%)	1.9578 (+0.9%)
Cr-N^2	2.02*63*	1.99*17*	1.9924 (–0.8%)	2.0527 (+2.2%)	2.0374 (+1.4%)	2.0086 (+0.0%)	2.0702 (+3.0%)
Cr-N^3	2.02*01*	2.02*95*	2.0474 (+1.1%)	2.0377 (+0.6%)	2.0529 (+1.4%)	2.0724 (+2.4%)	2.0620 (+1.8%)
Cr-N^4	2.02*00*	2.04*02*	2.0474 (+0.9%)	2.0377 (+0.4%)	2.0529 (+1.1%)	2.0724 (+2.1%)	2.0620 (+1.6%)
Cr-N^5	2.04*60*	2.02*43*	2.0474 (+0.6%)	2.0608 (+1.3%)	2.0554 (+1.0%)	2.0724 (+1.8%)	2.0865 (+2.5%)
Cr-N^6	2.04*89*	2.04*13*	2.0474 (+0.1%)	2.0608 (+0.8%)	2.0554 (+0.5%)	2.0724 (+1.3%)	2.0865 (+2.0%)

Table 5.16: Total energy (ΔE) and standard Gibbs free energy gaps ($\Delta G^{\ominus}$) between the triplet minimum and transition state ($t - t$) in kcal/mol; spin-squared expectation values ($\langle S^2 \rangle$) before and after annihilation of the first spin contaminant; Mulliken and AIM charges (q_{MPA}(Cr), q_{AIM}(Cr)) and integrated spin densities (n^s_{MPA}(Cr), n^s_{AIM}(Cr)) on the chromium in the Cr(smif)$_2$ (triplet states only; the C_{2v} doublet cation data is added for comparison). Data sets at different levels of theory are presented. For additional data see Tab. B.4.

	UPBE0/6-31G*			UB3LYP/6-31G*	
	D_2, $^3B_2$	C_{2v}, $^3B_2$[TS]	C_{2v}, $^2B_2$ [cation]	D_2, $^3B_2$	C_{2v}, $^3B_2$ [TS]
ΔE_{t-t}	–	0.18	–	–	0.62
$\Delta G^{\ominus}_{t-t}$	–	(1.94)	–	–	(1.57)
$\langle S^2 \rangle$	2.6929	2.7346	2.5290	2.5858	2.6135
$\langle S^2 \rangle_{ann}$	2.0461	2.0546	3.3753	2.0279	2.0316
q_{MPA}(Cr)	1.22	1.22	1.25	1.09	1.08
q_{AIM}(Cr)	2.03	2.03	2.04	1.95	1.96
n^s_{MPA}(Cr)	2.89	2.91	2.96	2.75	2.75
n^s_{AIM}(Cr)	2.56	2.59	2.57	2.49	2.50

triplet state on the metal, we find n^s_{AIM}(Cr)=2.56. The additional 0.56 unpaired α-electrons on the metal are coupled with an equal amount of β-electrons on both ligands.

We now searched for low-lying triplet excited states which might be the source for the complicated EPR signal. Note, that quantitative statements about gaps between near-degeneracy states are outside the accuracy limits of the employed theoretical methods. Nevertheless we can map out potential candidates for the experimentally proposed near-degeneracy triplet states.

We computed the triplet ground states of different symmetry on the $^3B_2$

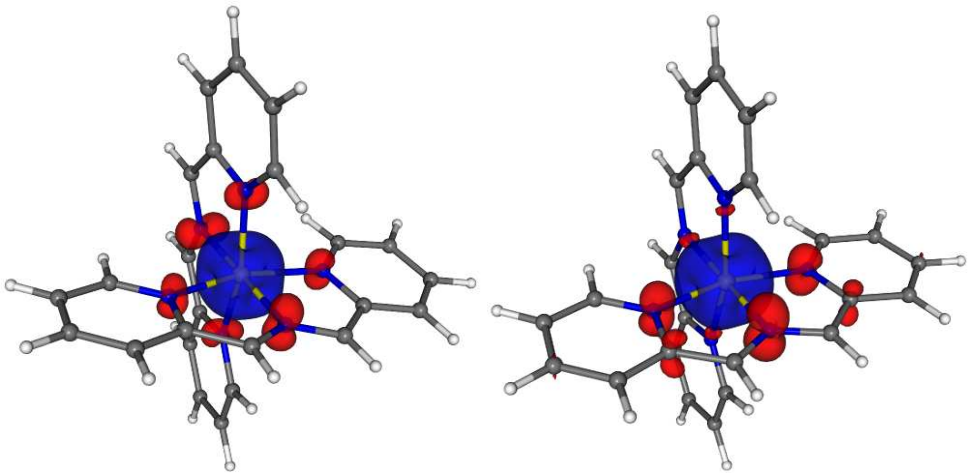

Figure 5.12: Spin density isosurfaces in the Cr(smif)$_2$ UPBE0 D_2 $^3B_2$ BS-AFM state (left), C_{2v} $^3B_2$ transition state (right) (blue: $\rho^s = 0.01$; red: $\rho^s = -0.01$). Note the difference in the symmetry of the spin density distribution of the minimum and the transition state.

UB3LYP/6-31G* geometry[10]. The obtained vertical gaps can be found in Tab. 5.17. These states are too high in energy for potential near-degeneracy, except for the $^3B_3$ state, which may upon geometric relaxation become sufficiently close in energy to the $^3B_2$. However, the spin density distribution of the $^3B_3$ and $^3B_2$ state is essentially identical, so we cannot derive an explanation for the different EPR signals.

In addition to these ground state results we elucidated the low-energy triplet spectrum of Cr(smif)$_2$ my means of TDDFT. We compare the results from B3LYP and BLYP, computed on the B3LYP optimized geometry in Tab. 5.18.

No additional candidates for near-degeneracy emerge[11]. It becomes clear

[10]The PBE0 geometry is of better quality, but was not used because it only became available later.

[11]The TDDFT results are more approximate than the ground state calculations.

Table 5.17: Total energy gaps (ΔE in kcal/mol) between the Cr(smif)$_2$ triplet ground states of different symmetry with respect to the $^3B_2$ state, as well as AIM charges (q_{AIM}(Cr) and spin densities (n^s_{AIM}(Cr)) on the metal. For additional data see Tab. B.5.

UB3LYP/6-31G*	^3A	$^3B_1$	$^3B_2$	$^3B_3$
ΔE_{t-t}	39.7	16.2	–	4.6
q_{AIM}(Cr)	–	–	1.95	1.97
n^s_{AIM}(Cr)	–	–	2.49	2.53

Table 5.18: Selected triplet excited states of Cr(smif)$_2$ from TDDFT with B3LYP and BLYP functionals (covering the lowest state in each symmetry and the lowest bright state): excited states number, state symmetry, vertical excitation energy (ΔE_{t-t} in kcal/mol), and oscillator strength (f). Note, that the unrestricted DFT all results exhibit spin contamination and are hence no pure triplet states.

TD-UB3LYP/6-31G*				TD-UBLYP/6-31G*			
state #	sym	ΔE_{t-t}	f	state #	sym	ΔE_{t-t}	f
1	$^3B_1$	7.6	0.0052	1	$^3B_1$	9.1	0.0034
2	$^3B_3$	17.3	0.0026	2	$^3B_3$	14.0	0.0012
4	$^3B_2$	32.6	0.0000	4	^3A	28.2	0.0000
5	^3A	32.8	0.0000	6	$^3B_2$	31.4	0.0002
12	$^3B_3$	50.9	0.1602	14	$^3B_3$	42.8	0.0420

that all states computed on the D_2 geometry, which has an essentially symmetric immediate coordination shell, will feature a correspondingly symmetric spin density, which seems to exclude possible candidates responsible for the anisotropic EPR signal.

In addition to the D_2 minima we located a close-by C_{2v} symmetry transition state during the geometry optimization with a very low barrier height of 0.2 kcal/mol in PBE0 and 0.6 kcal/mol in B3LYP (see Tab. 5.16). The imaginary displacement vector nicely describes the cumulative twist motion towards the D_2 symmetry. The C_{2v} transition state is identified as the saddle point which connects the two D_2 optical isomers[12]. Some of the structural features of the saddle point are in notable agreement with the experimental findings (e.g., the C_{2v} distortion and the relative metal-ligand bond distances), while others are better represented by the minimum geometry (e.g., the ligand-twist). The small barrier indicates that crystal packing effects or thermal fluctuations are well capable of and may hence be the reason for the observed discrepancies between the two XRD structures. We can now understand the distortions from ideal symmetries as deformations between minimum and saddle point along the flat transition coordinate, which explains the mixture of geometric properties.

Following this explanation for the structural observations, we discuss the related change in the electron distribution, which may be connected to the temperature dependent change in the EPR signal. Despite the tiny energetic difference, the structural difference between minimum and saddle point are substantial: in C_{2v} the two smifs coordinate in a distinct fashion to the chromium, one much closer to the metal than the other ($d_{\text{Cr-N}^2} - d_{\text{Cr-N}^1} = 0.11$ Å), while the

[12]Note, that C_{2v} is a surprising symmetry for a transition state connecting two D_2 geometries; a D_{2d} pathway, in which only the smifs are untwisted and then retwisted would have seemed more likely, as it preserves the smif symmetry of the D_2 minima.

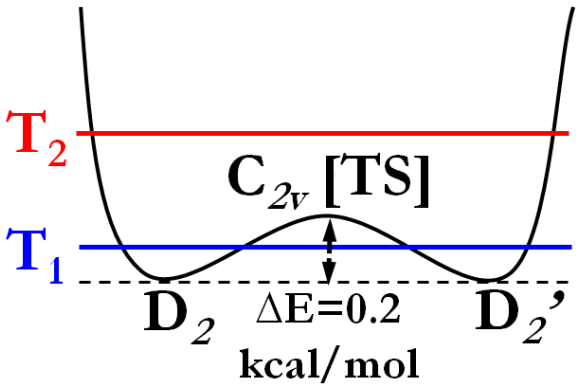

Figure 5.13: Double-well potential in the $Cr(smif)_2$.

smifs are equivalent in D_2. Consistent with its geometric change the transition state spin density is shifted towards the closer smif (Fig. 5.12), spreads further into the periphery of the conjugated π-system, and ultimately introduces spatial directionality and anisotropy (remember that the D_2 spin density does not show a spatial preference). We can now consider a double minimum potential (see Fig. 5.13) which may be linked to the characteristic EPR signal (instead of an explanation based purely one a near-degenerate vertical excited state). At very low temperatures, the $Cr(smif)_2$ predominantly populates the two degenerate D_2 enantiomer minima with spherical electron density, which would lead to the isotropic EPR signal. Beyond a certain temperature, the barrier is easily overcome and we can have a fast inversion of the enantiomers through the C_{2v} transition state with its unbalanced spin density. The increase in temperature also leads to the increase of the anisotropic EPR signal. The thermally accessible barrier also renders a separation of the enantiomers impossible and formally we always find a racemic mixture.

Finally we note that the optimized C_{2v} geometry of the $[Cr(smif)_2]^+$-cation is also similar to the transition state geometry (see Tab. 5.15), which could explain

the XAS prediction of a similar coordination environment. This is not given if we only consider the D_2 minimum.

We determine the metal oxidation state by means of the reference compounds introduced in the previous section, which gave AIM charges of q_{AIM}(Cr)= 1.60 and q_{AIM}(Cr)= 2.12 for Cr(II) and Cr(III), respectively. With q_{AIM}(Cr)= 2.03, the Cr(smif)$_2$ is best represented by a Cr(III) oxidation state, as was predicted by XAS. The claim of a non-innocent smif ligand in combination with chromium is thus confirmed.

Let us now study the change of the electron and spin density distribution in the course of the oxidation towards the cationic complex. We obtain the following picture of the non-classical oxidation process from the triplet Cr(smif)$_2$ to the doublet and quartet [Cr(smif)$_2$]$^+$ within the DFT description:

- Oxidation to the doublet ($S = 1 \longrightarrow S = \frac{1}{2}$):

$$\begin{aligned} \mathrm{Cr(smif)_2} &\longrightarrow [\mathrm{Cr(smif)_2}]^+ + \mathrm{e}^\ominus \\ (n_{AIM}(\mathrm{Cr}) = 4.0;\, n^s_{AIM}(\mathrm{Cr}) = 2.6) &\longrightarrow (n_{AIM}(\mathrm{Cr}) = 4.0;\, n^s_{AIM}(\mathrm{Cr}) = 2.6) + \mathrm{e}^\ominus \end{aligned}$$

  This oxidation process is entirely ligand based, the electron distribution of the metal essentially does not change. An electron with α-spin is removed from one of the ligands (primarily on the aza-nitrogen, carbons *and* hydrogens, which are separated by carbons without spin density), generating the large AFM coupling.

- Oxidation to the quartet ($S = 1 \longrightarrow S = \frac{3}{2}$):

$$\begin{aligned} \mathrm{Cr(smif)_2} &\longrightarrow [\mathrm{Cr(smif)_2}]^+ + \mathrm{e}^\ominus \\ (n_{AIM}(\mathrm{Cr}) = 4.0;\, n^s_{AIM}(\mathrm{Cr}) = 2.6) &\longrightarrow (n_{AIM}(\mathrm{Cr}) = 3.9;\, n^s_{AIM}(\mathrm{Cr}) = 2.9) + \mathrm{e}^\ominus \end{aligned}$$

The β-electron removed during the oxidation to the quartet state originates primarily from the ligands but the charge of the metal also increases (however not as much as the spin density). Approximately 35% of the β-electron was removed from the chromium, but this electron loss was compensated by the closed-shell electron density of 0.27 electrons relocated from the ligand to the metal to balance the intramolecular chemical potential, so that the charge on the metal only increased by 0.08. This results in a decoupled rearrangement of electron and spin density during the oxidation (within the limits of the DFT account).

In addition to this detailed investigation of the triplet states, we computed the minima on the singlet and quintet state PES to obtain the relaxed spin gaps and electronic structure of the high- and low-spin configurations (at UPBE0/6-31G* level only; gaps and barriers were refined through single point UPBE0/cc-pVTZ (DKH2) calculations on these geometries). The results are summarized in Tables 5.19 and 5.20.

The singlet optimization was a particularly hard case. We observed a significant impact of small geometric changes on the $\langle S^2 \rangle$ value, which underlines the strong coupling of the molecular and electronic structure. The singlet wavefunctions exhibit sizable spin contamination.

The optimization of the quintet state was an intermediate case, harder than most other high-spin optimizations but ultimately not too complicated: while the calculations converged quickly and did not encounter electronic instabilities, we found multiple stationary points, i.e., the PES is divided into distinct catch regions. The global minimum has a C_{2v} $^5A_1$ symmetry with very long metal-ligand bonds (in particular compared to the experimental geometry, see

Table 5.19: The two XRD M-L bond distances in the $Cr(smif)_2$ complex (in Å), and the computationally optimized values for singlet and quintet states (both minima and transition states (TS) from PBE0; the triplet data is added for comparison) with average percentage difference to the experimental data.

bond	XRD 1	XRD 2	UPBE0/6-31G*		
	bent	twisted	C_2, ^1A	D_2, $^3B_2$	C_{2v}, $^3B_2$ [TS]
Cr-N^1	1.93*24*	1.94*81*	1.9819 (+2.1%)	1.9924 (+2.7%)	1.9427 (+0.1%)
Cr-N^2	2.02*63*	1.99*17*	1.9819 (–1.3%)	1.9924 (–0.8%)	2.0527 (+2.2%)
Cr-N^3	2.02*01*	2.02*95*	2.0494 (+1.2%)	2.0474 (+1.1%)	2.0377 (+0.6%)
Cr-N^4	2.02*00*	2.04*02*	2.0506 (+1.0%)	2.0474 (+0.9%)	2.0377 (+0.4%)
Cr-N^5	2.04*60*	2.02*43*	2.0494 (+0.7%)	2.0474 (+0.6%)	2.0608 (+1.3%)
Cr-N^6	2.04*89*	2.04*13*	2.0506 (+0.3%)	2.0474 (+0.1%)	2.0608 (+0.8%)

bond	UPBE0/6-31G*			
	C_{2v}, $^5A_1$	D_2, $^5B_2$	D_{2d}, $^5A_2$[TS^3]	C_{2v}, $^5B_1$[TS]
Cr-N^1	2.0528 (+5.8)	2.0142 (+3.8)	2.0879 (+7.6)	1.9924 (+2.7)
Cr-N^2	2.1837 (+8.7)	2.0142 (+0.3)	2.0879 (+3.9)	2.0375 (+1.4)
Cr-N^3	2.1137 (+4.4)	2.0469 (+1.1)	2.2633 (+11.8)	2.0329 (+0.4)
Cr-N^4	2.1137 (+4.1)	2.0469 (+0.8)	2.2633 (+11.5)	2.0329 (+0.1)
Cr-N^5	2.3942 (+17.6)	2.0469 (+0.6)	2.2633 (+11.2)	2.0609 (+1.3)
Cr-N^6	2.3942 (+17.1)	2.0469 (+0.1)	2.2633 (+10.7)	2.0609 (+0.8)

Tab. 5.19), and is hence a weak-field example. The latter is necessary to facilitate the high-spin occupation. The electronic structure of this state is essentially as expected from a crystal field picture, with essentially all four unpaired electrons localized on the metal (see Tab. 5.20 and Fig. 5.14). The unpaired electrons are admittedly augmented by 0.5 electrons worth of closed shell density. Note, that this charge relocation occurs despite the very stretched metal-ligand bonds, and the consequently reduced covalent contribution. The partial charge on the

Table 5.20: Total energy (ΔE) and standard Gibbs free energy gaps ($\Delta G^{\ominus}$) between the triplet and the singlet/quintet ground state ($t-x$) as well as between the stationary points of the same spin ($x-x$) in kcal/mol; spin-squared expectation values ($\langle S^2 \rangle$) before and after annihilation of the first spin contaminant; Mulliken and AIM charges (q_{MPA}(Cr), q_{AIM}(Cr)) and integrated spin densities (n^s_{MPA}(Cr), n^s_{AIM}(Cr)) on the chromium in the Cr(smif)$_2$-series. For additional data see Tab. B.6.

	UPBE0/6-31G*						
	C_2, ^1A	D_2, $^3B_2$	C_{2v}, $^3B_2$[TS]	C_{2v}, $^5A_1$	D_2, $^5B_2$	D_{2d}, $^5A_2$[TS^3]	C_{2v}, $^5B_1$[TS]
$\Delta E_{t-x}/\Delta E_{t-x}$	19.44	–	0.18	7.31	1.69	1.75	1.78
$\Delta G^{\ominus}_{t-x}/\Delta G^{\ominus}_{x-x}$	20.88	–	(1.94)	3.42	4.25	(5.38)	(6.23)
$\langle S^2 \rangle$	1.0809	2.6929	2.7346	6.0160	6.0279	6.0142	6.0344
$\langle S^2 \rangle_{ann}$	0.6974	2.0461	2.0546	6.0001	6.0003	6.0001	6.0004
q_{MPA}(Cr)	1.15	1.22	1.22	1.10	1.25	1.11	1.25
q_{AIM}(Cr)	1.87	2.03	2.03	1.68	2.09	1.67	2.09
n^s_{MPA}(Cr)	–0.20	2.89	2.91	3.95	3.14	3.95	3.13
n^s_{AIM}(Cr)	–0.09	2.56	2.59	3.81	3.01	3.84	2.97

chromium corresponds to an oxidation state +2. Note, that we find a spin state dependent oxidation state, when comparing the triplet and quintet state.

Just 1.7 kcal/mol ($\Delta G^{\ominus}$ = 4.3 kcal/mol) above the C_{2v} minimum – again within the DFT error margin – we find another (optically active) D_2 $^5B_2$ minimum, which features a much closer coordination, and is hence a bond-stretch and symmetry isomer. In the UPBE0/6-31G*//cc-pVTZ (DKH2) single point calculation, the gap is actually inverted and the D_2 minimum is more stable by 3.0 kcal/mol. We point out the striking similarity between the previously discussed D_2 $^3B_2$ and the $^5B_2$ minimum at hand, i.e., we find minima on the essentially identical position of the triplet and quintet PES, whose states even have the same symmetry, and which are energetically separated by a modest

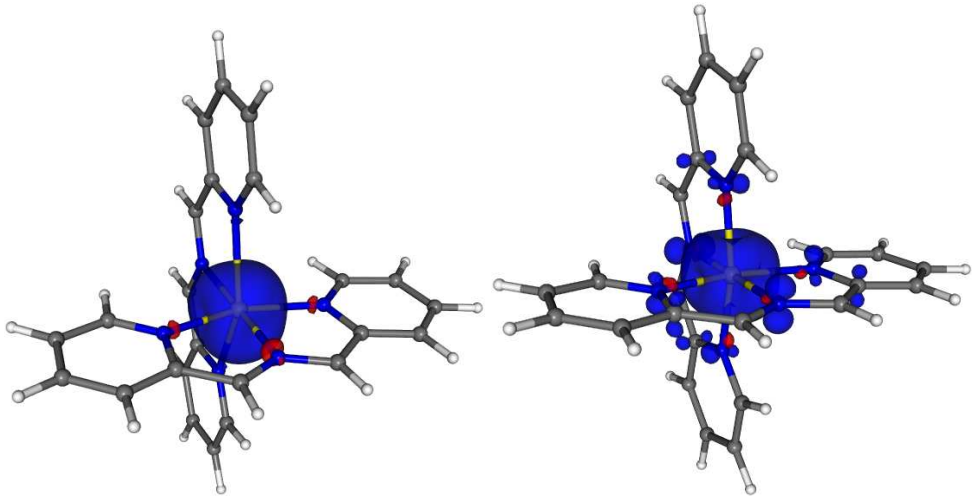

Figure 5.14: Spin density isosurfaces in the $Cr(smif)_2$ UPBE0 C_{2v} $^5A_1$ state (*left*), D_2 $^5B_2$ state (*right*) (blue: $\rho^s = 0.01$; red: $\rho^s = -0.01$). Note the conventional spin distribution in the C_{2v} $^5A_1$, and the noninnocent, FM coupled D_2 $^5B_2$.

9.0 kcal/mol ($\Delta G^{\ominus}$ = 7.7 kcal/mol). The second minimum exposes a completely different electronic structure than the C_{2v} $^5A_1$ minimum (see Fig. 5.14): the oxidation state can clearly be identified as a Cr(III), we find a distinct ferromagnetic coupling between metal and ligand (one of the unpaired electrons is transferred onto both ligands, although not into the outer periphery), and in addition to the three unpaired electrons we find an additional closed shell spin density corresponding to a fourth electron. Note, that the two minima in the cationic doublet state discussed in the previous chapter had a different spin density distribution, but the oxidation state was the same.

Complementing the two minima, we found associated transition states. The two smifs in a C_{2v} are nonequivalent, and we found a D_{2d} $^5A_2$ transition state, which describes the inversion $C_{2v} \longrightarrow D_{2d} \longrightarrow C'_{2v}$ with a barrier height of just 1.8 kcal/mol (*[...]* kcal/mol in cc-pVTZ (DKH2)), which is essentially the same

Table 5.21: Total energy (E) and standard Gibbs free energy ($G^{\ominus}$) spin gaps between the optimized states ($t-s$=triplet-singlet, $t-q$=triplet-quintet) of the $Cr(smif)_2$ in kcal/mol.

level of theory	ΔE_{t-s}	$\Delta G^{\ominus}_{t-s}$	ΔE_{t-q}	$\Delta G^{\ominus}_{t-q}$
UPBE0/6-31G*	19.4	20.9	7.3	3.4
UPBE0/6-31G*//cc-pVTZ (DKH2)			8.7	4.8

as the gap towards the second minimum[13]. The two D_2 $^5B_2$ enantiomers are connected through a C_{2v} $^5B_1$ transition state with 0.1 kcal/mol (*[...]* kcal/mol in cc-pVTZ (DKH2)) barrier (again very similar to the corresponding triplet case, although with a less pronounced symmetry breaking $d_{\text{Cr-N}^2} - d_{\text{Cr-N}^1} = 0.045$ Å). For both isomers the electronic structure does not change significantly in the course of these inversions.

All optimized states display only modest spin-contamination (at most $\langle S^2 \rangle = 6.03$ instead of $\langle S^2 \rangle = 6$) with successful annihilation, which was to be expected for the high-spin state.

In Tab. 5.21 we summarize the acquired spin gaps with respect to the triplet ground state. Note, that the gaps between the spin states are quite small and of the same magnitude as the triplet-triplet excitations contemplated in the beginning.

The complex bonding exhibited in DFT, in particular for the triplet state warranted a further multi-reference investigation. We performed single point CASSCF/CASPT2 calculations on the triplet states of different symmetry on the B3LYP D_2 structure[14].

[13]We note, that the D_{2d} $^5A_2$ transition state features an additional degenerate pair of imaginary canting frequencies, and is hence of third order (symbolized by [TS^3]).

[14]The higher quality PBE0 geometry was not available at this point, but the vertical gaps

In D_2 we find the following orbital symmetry relations: the 't_{2g}' are $d_{xy}(a)$, $d_{xz}(b_2)$, $d_{yz}(b_3)$, and the 'e_g^*' are $d_{z^2}(a)$, $d_{x^2-y^2}(b_1)$. From this we obtain the following idealized target (14e,16o) active space configuration, corresponding to our discussion in Sec. 5.2.2: $\sigma_{d_{z^2}-L}(a)^2$, $\sigma_{d_{x^2-y^2}-L}(b_1)^2$, $\pi_L(a)^2$, $\pi_L(b_2)^2$, $\pi_L(b_3)^2$, $3d_{xy}(a)^1$, $3d_{xz}(b_2)^1$, $3d_{yz}(b_3)^2$, $\pi_L^*(a)^0$, $\pi_L^*(b_2)^0$, $\pi_L^*(b_3)^0$, $3d_{z^2}(a)^0$, $3d_{x^2-y^2}(b_1)^0$, $4d_{xy}(a)^0$, $4d_{xz}(b_2)^0$, $4d_{yz}(b_3)^0$ (the displayed occupation is for the $^3B_2$ ground state). It turned out that this target active space is in part unstable and the optimizations produced the following modifications:

- the $\sigma_{d_{x^2-y^2}-L}(b_1)^2$ is replaced by a $\sigma_{p_z-L}(b_1)^2$ which has strong density overlap with the $\sigma_{d_{z^2}-L}(a)^2$
- the $3d_{x^2-y^2}(b_1)^0$ is replaced by a $\sigma^*_{p_z-L}(b_1)^0$ which has strong density overlap with the $\sigma_{d_{z^2}-L}(a)^2$ and $\sigma_{d_{x^2-y^2}-L}(b_1)^2$
- the $\pi_L^*(a)^0$ is replaced by $\sigma^*_{d_{z^2}-L}(a)^0$, some $\pi_L^*(a)$ character gets mixed into $4d_{xy}(a)$

  The replacement of $\sigma_{d_{x^2-y^2}-L}(b_1)^2$ and $3d_{x^2-y^2}(b_1)^0$ indicates that it is more important to correlate the electrons in the aza-Cr-N σ-bond with additional p orbitals compared to correlating the pyridyl-Cr-N σ-bond with the $d_{x^2-y^2}$ based orbitals, which is sensible. Consequently, the $d_{x^2-y^2}$ orbitals are not treated on a correlated level. This correlation is supported by the extra $\sigma^*_{d_{z^2}-L}(a)$.

Generally the active space is quite compact and localized around the metal. The ligand is mainly involved with orbital from the aza-bridge. Smaller contributions come from the pyridyl-nitrogens, except for the $\pi_L(a)$ type orbitals,

between the states are unlikely to be significantly effected by this.

which are predominantly localized on the ring-N and the bridge-C and to a small degree leak electron density into the ring-π-system. We find some mixing between the π or σ orbitals, respectively, and the d-orbital of like symmetry, usually more so for the more diffuse 4d orbitals but also for 3d.

We now describe noteworthy features of the computed natural orbitals

- ^{3}A: significant mixing of $3d_{xy}$(a) and π_L^*(a), of $3d_{yz}$(b_3) and π_L^*(b_3), as well as of $3d_{xz}$(b_2), π_L^*(b_2)
- $^3B_1$: $4d_{xy}$(a) with some contribution on the aromatic rings
- $^3B_2$: significant mixing of $3d_{yz}$(b_3), π_L^*(b_3) and $4d_{yz}$(b_3)
- $^3B_3$: significant mixing of $3d_{xz}$(b_2), π_L^*(b_2) and $4d_{yz}$(b_2)

The resulting CASSCF energies with a comparison of basis set and active space effects are summarized in Tab. B.7 and 5.22. In this instance we compare the (10e,16o) active space according to strategy 1 and the (14e,16o) active space according to strategy 2. The latter provides significantly lower energies, which supports our conjecture about the active space design. We also tested a (14e,17o)-CASSCF, which shows minor improvement over the (14e,16o), but the additional computational cost is not justified. Note, that the gaps in the pure CASSCF ansatz are very dependent on the active space, since correlation is either completely accounted for in the active space or completely ignored in the external space. While this impacts the reliability of the computed gaps, the electron and spin density distribution are generally well accounted for. For the most relevant cases we determined the multi-reference character according to eqn. (5.1). Tab. 5.23 shows that m_{MR} decreases with larger active space and basis set, which indicates that the static correlation can be described

Table 5.22: Total CASSCF energy gaps of the different symmetry triplet states of $Cr(smif)_2$ with respect to the $^3B_2$ ground state computed within different active spaces (constructed according to previous discussion) and basis sets. The results on the top result from a strategy 1 built-up, the results on the bottom from strategy 2. In case of active space ambiguities, only the best results are given, The (14e,14o) active spaces are the ones reduced for the CASPT2 calculations, the starred examples feature a non-reoptimized reference space. The calculations incoorporate DKH2 relativistic correction but no frozen core approximation. All gaps are given in kcal/mol ('*n.c.*' = not converged). For additional data see Tab. B.7.

CASSCF	^3A	$^3B_1$	$^3B_3$
(4e,5o)/STO-6G	–13.2	*n.c.*	6.0
(4e,5o)/ANO0	45.0	2.6	1.6
(4e,10o)/ANO0	52.9	10.6	4.6
(10e,16o)/ANO0	52.6	21.8	6.1
(12e,17o)/ANO0	60.7	16.7	6.8
(8e,10o)/ANO0	69.8	17.0	7.2
(14e,14o)/ANO0	34.3	22.4	5.7
(14e,14o)/ANO1	33.5	17.7	5.9
(14e,14o)*/ANO0	33.3	20.7	6.3
(14e,14o)*/ANO1	31.4	14.8	7.0
(14e,16o)/ANO0	39.0	17.8	6.6
(14e,16o)/ANO1	40.0	12.9	6.0

more efficiently (in terms of fewer determinants with large coefficients) in this setup. While the multi-reference character is quite substantial in the (14e,14o)-CASSCF/ANO0 ansatz, it is only moderate in (14e,16o)-CASSCF/ANO1. In addition, we obtained the lowest $^3B_2 \longrightarrow {}^3B_2$ gap using a two-state (14e,16o)-SA-CASSCF/ANO0 ansatz and obtained a value of 56.3 kcal/mol.

We next computed the CASPT2 energies. Since the largest possible reference

Table 5.23: Multi-reference character m_{MR} of the $Cr(smif)_2$ CASSCF wavefunctions as a function of active space and basis set size.

CASSCF	$^3B_2$	$^3B_3$
(14e,14o)/ANO0	0.30	0.41
(14e,14o)/ANO1	0.27	0.38
(14e,16o)/ANO0	0.19	0.23
(14e,16o)/ANO1	0.11	0.04

space for the CASPT2 is of size (14e,14o), we removed the two orbitals with the smallest fractional occupation (we also investigated different sensible options in case of ambiguity). There are two different ways to do the CASPT2: we can either start from the (14e,16o)-CASSCF wavefunction, decrease the active space size, and reoptimize the orbitals in a (14e,14o)-CASSCF. Instead of reoptimizing the orbitals for the (14e,14o) reference function, we can also use the original orbitals, which were optimized with respect to a better ansatz. As it is not clear, which approach is preferable, we tested them both. The CASPT2 did not converge without level shifts, so we also investigated the impact of different level shifts. The ^3A state could not be converged at all. The summary of this study can be found in Fig. B.8 and 5.24.

We see that the large basis set calculation without reoptimized active space show a significant deviation from the other results, which indicated, that a reoptimization of the reference space may be the better approach.

We can summarize that for the best CASSCF and CASPT2 calculations, we obtain a triplet-triplet gap in the order of 5-6 kcal/mol (CASSCF: 6.0 kcal/mol; CASPT2: 5.7 kcal/mol) which confirms the DFT results discussed in the beginning. The good performance of the unrestricted DFT may be attributed to the

Table 5.24: Total energy CASPT2 gaps (for different shifts) of the different symmetry triplet states of $Cr(smif)_2$ with respect to the $^3B_2$ ground state, computed within different active spaces (constructed according to previous discussion) and basis sets. The results on the top correspond to to the reoptimized reference space, the results on the bottom to the unreoptimized ones. In case of active space ambiguities, only the best results are given. The ^3A results could not be converged. The calculations incoorporate DKH2 relativistic correction and frozen core approximation. All results given in kcal/mol ('*n.c.*' = not converged.) For additional data see Tab. B.8.

CASPT2	shift	$^3B_1$	$^3B_3$
(14e,14o)/ANO0	0.2	30.6	5.2
	0.3	30.0	5.6
(14e,14o)/ANO1	0.2	26.9	5.7
	0.3	26.2	6.1
(14e,14o)*/ANO0	0.2	28.9	4.6
	0.3	28.3	4.8
(14e,14o)*/ANO1	0.2	23.0	13.0
	0.3	22.4	13.0

only moderate multi-reference situation in the triplet $Cr(smif)_2$.

5.3.6 V(smif)$_2$

The d^3-complex $V(smif)_2$ ($S = \frac{1}{2}, \frac{3}{2}$) is isoelectronic to the previously discussed $[Cr(smif)_2]^+$-cation and the lower analogue of the non-innocent $Cr(smif)_2$. We will focus on a comparison of these three systems. XRD crystallography again found two structures per unit cell, both essentially D_{2d} with moderate distortions: The smif ligands of the first structure are bent, and we find a slight

Table 5.25: The two sets of XRD M-L bond distances in the V(smif)$_2$ complex (in Å), and the computationally optimized values for doublet and quartet states with average percentage difference to the experimental data.

bond	XRD$_1$ ~D_{2d}	XRD$_2$ ~C_{2v}	UPBE0/6-31G* C_s, ^{2}A′	UB3LYP/6-31G* C_s, ^{2}A′	UPBE0/6-31G* D_{2d}, $^4B_1$	UB3LYP/6-31G* D_{2d}, $^4B_1$
V-N^1	2.06*53*	2.03*23*	2.0131 (–1.7%)	2.0393 (–0.5%)	2.0872 (+1.9%)	2.1028 (+2.6%)
V-N^2	2.07*28*	2.06*22*	2.1083 (+2.0%)	2.1179 (+2.4%)	2.0872 (+1.0%)	2.1028 (+1.7%)
V-N^3	2.11*27*	2.11*10*	2.0626 (–2.3%)	2.1000 (–0.6%)	2.1450 (+1.6%)	2.1675 (+2.6%)
V-N^4	2.12*47*	2.11*24*	2.1245 (+0.3%)	2.1474 (+1.4%)	2.1450 (+1.2%)	2.1675 (+2.3%)
V-N^5	2.11*69*	2.11*69*	2.1064 (–0.5%)	2.1355 (+0.9%)	2.1450 (+1.3%)	2.1675 (+2.4%)
V-N^6	2.12*10*	2.12*94*	2.1064 (–0.9%)	2.1355 (+0.5%)	2.1450 (+0.9%)	2.1675 (+2.0%)

$D_{2d} \longrightarrow C_{2v}$ symmetry breaking in both structures, more pronounced however in the second. Both ligands are also slightly canted, introducing some resemblance to a C_2. The metal-ligand bond distances are shown in Tab. 5.25.

An initial Evan's method measurement found a low-spin doublet ground state.

The quartet geometry optimizations in PBE0 and B3LYP were simple, we only encounter modest spin contamination, and all guesses converged to a high-symmetry D_{2d} $^4B_1$ structure, which for both functionals is in good correspondence with the XRD results (again with somewhat exaggerated metal-ligand bond distances, in particular for B3LYP; see Tab. 5.25).

We assess the partial charge of q_{AIM}(V)= 1.87 with respect to the *trans*-$VCl_2(H_2O)_4$/*trans*-$[VCl_2(H_2O)_4]^+$ reference system for V(II) and V(III), which gave q_{AIM}(V)= 1.62 and q_{AIM}(V)= 2.18, respectively. Unlike the Cr(smif)$_2$, in which the metal clearly corresponds to an oxidation state +3, the vanadium

Table 5.26: Total energy (ΔE) and standard Gibbs free energy gaps ($\Delta G^{\ominus}$) between the quartet and doublet minima ($q - d$) in kcal/mol; spin-squared expectation values ($\langle S^2 \rangle$) before and after annihilation of the first spin contaminant; Mulliken and AIM charges (q_{MPA}(V), q_{AIM}(V)) and integrated spin densities (n^s_{MPA}(V), n^s_{AIM}(V)) on the vanadium in the V(smif)$_2$. Data sets at different levels of theory are presented. For additional data see Tab. B.9.

	UPBE0/6-31G*	UB3LYP/6-31G*	UPBE0/6-31G*	UB3LYP/6-31G*
	C_s, ^{2}A′	C_s, ^{2}A′	D_{2d}, $^4B_1$	D_{2d}, $^4B_1$
ΔE_{q-d}	15.00	14.01	–	–
$\Delta G^{\ominus}_{q-d}$	14.32	13.07	–	–
$\langle S^2 \rangle$	1.7147	1.7134	3.7662	3.7627
$\langle S^2 \rangle_{ann}$	0.8514	0.8288	3.7501	3.7501
q_{MPA}(V)	1.22	1.09	1.17	1.05
q_{AIM}(V)	2.06	1.99	1.87	1.86
n^s_{MPA}(V)	1.48	1.31	2.79	2.73
n^s_{AIM}(V)	1.36	1.24	2.66	2.64

complex features a mixed effective oxidation state between a classical V(II) and V(III). The integrated spin density (see Tab. 5.26) on the metal is notably reduced and is in part relocated onto the azaallyl-bridge carbons (see Fig. 5.15), corresponding to a ferromagnetic coupling situation. This nonclassical behavior is consistent with the reductive activity of V(II). The ferromagnetic coupling is in stark contrast to the conventional electron distribution of the isoelectronic quartet [Cr(smif)$_2$]$^+$ and the moderate antiferromagnetic coupling in the neutral triplet Cr(smif)$_2$.

The doublet state geometry optimizations were a hard case. With both functionals we find a minimum with C_s ^{2}A′ symmetry (i.e., one smif is canted), as

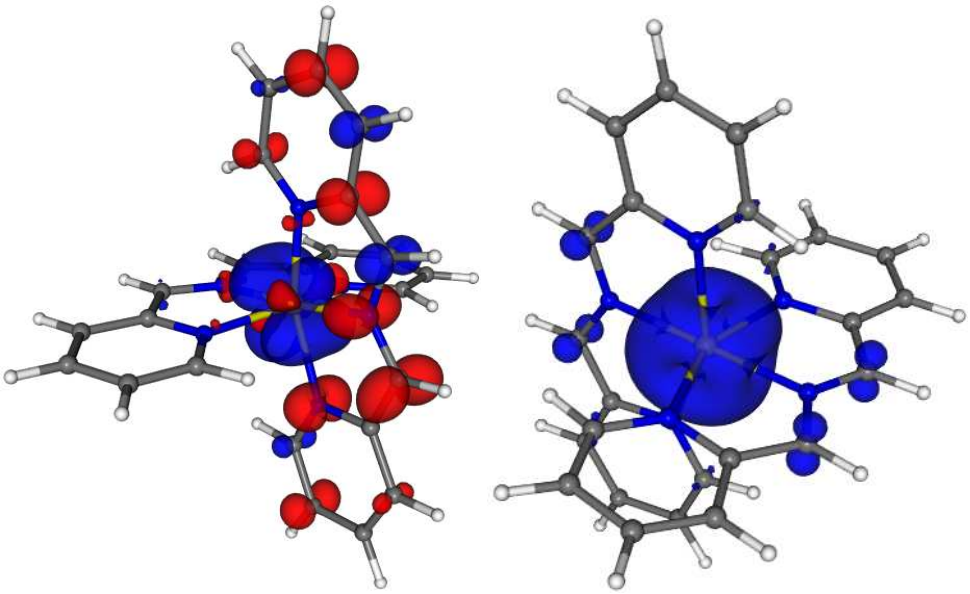

Figure 5.15: Spin density isosurfaces in the V(smif)$_2$ UPBE0 C_s ^{2}A′ (left) and D_{2d} $^4B_1$ state (right) (blue: $\rho^s = 0.005$, red: $\rho^s = -0.005$). Note the complicated symmetry breaking in the doublet and noninnocent behaviour of the smif ligands in the quartet state.

well as some higher symmetry saddle points within 5 kcal/mol. The doublet geometries are also in reasonable agreement with the experimental ones, although the symmetry lowering due to canting is overemphasized (see Tab. 5.25). However, the overall match is still better with the quartet geometry. We note the significantly increased partial charge on the vanadium compared to the quartet state, and in this spin state, the metal leans more towards the V(III) reference value (see Tab. 5.26). This means that we find a notable coupling between spin and effective oxidation state in V(smif)$_2$. The spin density of the doublet state (see Fig. 5.15) reveals a complicated broken symmetry electronic structure of the DFT solution, indicating non-innocent ligand behavior of the closer smif in particular.

In the double-ζ basis we find a total energy quartet-doublet spin-gap of 15.0 kcal/mol and 14.3 kcal/mol in free energy (14.0 kcal/mol and 13.1 kcal/mol, respectively, in B3LYP), and triple-ζ DKH2 single-point calculations give ΔE_{q-d} =14.0 kcal/mol. Based on this solid gap, we could not confirm the experimentally proposed state ordering. At this point in the investigation, the original $S = \frac{1}{2}$ assignment was corrected on the basis of new EPR measurements in favor of the quartet state, which is in accord with Hund's rules[15]. Thus we find the same ground state spin, symmetry and state symmetry (D_{2d} $^4B_1$) as for the isoelectronic $[Cr(smif)_2]^+$-cation, however $V(smif)_2$ displays a notably different electron distribution and longer metal-ligand bonds.

5.4 Conclusions

This work was motivated by the unusual electronic, magnetic, spectroscopic, and geometric properties displayed in Wolczanski's experimental investigation of the 3d-$M(smif)_2$ series [325]. We approached in close collaboration with the experimentalists the open questions surrounding these phenomena with the aim of understanding the underlying electronic situation.

The electronic structure of transition metal compounds is generally a challenging and interesting topic due to the flexible nature of the partially occupied d-orbitals, their interactions with the remaining s and p valence shell on the one side, and the ligands on the other. The structural features of the latter can facilitate intricate interactions and greatly extend the possibilities for electronic phenomena. In the course of the present theoretical study we could demonstrate

[15]The original measurement was tainted due to a contamination.

that the smif-ligand can behave as such a non-innocent ligand by delocalizing and stabilizing charges in its conjugated π-backbone.

The $M(smif)_2$ display the following characteristic features:

- The PESs are extremely flat and have multiple minima and saddle points.
- The overall ground state PES is a patchwork of regions of different intersecting state surfaces. We also find instances of conical intersections (e.g., on the $Mn(smif)_2$ quartet surface).
- The different bond-stretch and symmetry isomers exhibit a wide variety of states associated with different principle configurations, which we deduce from the BS DFT solutions. They include conventional LF-type configurations, AFM and FM coupled states, states with formal EOS +2 (e.g., quintet $Cr(smif)_2$), non-innocent EOS +3 (e.g., triplet $Cr(smif)_2$), or mixed EOS +2/+3 (e.g., $V(smif)_2$). We identify these states by their distinct electron and spin density distribution. The smif can clearly act as a redox-active ligand. Note, that the EOS can be spin dependent (e.g., $Cr(smif)_2$), and for the same spin we can find isomers of different EOS (e.g., quintet $Cr(smif)_2$). The different metals show a distinct EOS preference according to their redox potential, i.e., early metals (Ti, V, Cr) tend to behave as M(III), Mn is flexible and equally shows examples for M(II), M(II/III), and M(III) behavior, while the late metals (Fe, Co, Ni) behave according to the formal M(II).
- We find cases, in which the PESs of different spin states show classical crystal field characteristics, such as long metal-ligand bonds consistent with a weak-field coordination for a high-spin state (e.g., in the hextet

$Mn(smif)_2$) and short metal-ligand bond distances for a strong-field low-spin state (e.g., in the singlet $Fe(smif)_2$).

- In addition to the different configuration domains subdividing the PES, we also find Jahn-Teller like distortions within these domains. We can associate them with intramolecular conversions, e.g., between the enantiomers of chiral D_2 and C_2 complexes. The transition state barriers can be extremely small (< 1 kcal/mol, which is usually associated with rotational barriers and not with bond-stretching modes[16]), although the associated geometric distortions may be significant. The knowledge of these structural features allows an interpretation of dynamic and hence temperature dependent behavior. The $M(smif)_2$ are hence often floppy and it may not be possible to assign a fixed structure. Based on this we could give an explanation for the distortions and deformations in XRD structures (e.g., for the triplet $Cr(smif)_2$) on the basis of crystal packing or thermal effects.
- The spin gaps for the Ti, Cr, Fe, and Co complex are small, and we can support the observation of spin-crossovers from an energetic perspective.

We stress the interplay between the structural arrangements and the electronic situation in each complex. Non-innocent behavior is not a property of a ligand by itself but depends on its context, i.e., the pairing with a compatible metal and also their specific coordination, which play an important role in tuning the relevant energy levels. The nature of states found in different regions of the PES can be explained accordingly. The distinct reciprocal relation between the molecular and electronic structure may be worth further experimental exploration by means of modified smifs, since it should be possible to sterically

[16]We note, that $D_{2d} \longrightarrow C_s \longrightarrow C_2$ transitions associated with the canting of one or both of the smifs can be seen as primarily a rotation of the smif on the sphere of the metal, and we hence expect small gaps.

tune the coordination and by that force the complex into a different state domain on the PES.

In addition to these physical and chemical aspects we will now summarize the technical and practical issues, which were the other focus of this study[17]:

- the uncommonly flat PESs required very tight convergence and accuracy threshold (e.g., by using ultrafine DFT grids) in order to be able to resolve the different structural features displayed in the $M(smif)_2$ series. Less restrictive settings can lead to geometries with substantial deviations from the fully converged results. Our first set of calculations converged to an apparent conglomerate of different structures, which only after more restrictive reoptimization could be identified as a smaller number of actual stationary points.
- it is essential and beneficial to conduct a thorough sampling of the PES, since it can have many stationary points which yield valuable information about the system at hand. The knowledge about the intramolecular saddle points turned out to be crucial for a comprehensive understanding of the PES. Preliminary calculations using only one or a few guess geometries led to a very incomplete picture of the bonding situation of the $M(smif)_2$ complexes (e.g., for $Mn(smif)_2$ an incorrect ordering of the spin states was determined since only a local minimum was found).
- it is important to know the available computational tools and their appropriate employment. In the course of this study we discussed the impact

[17] We reflect on our experience with the $M(smif)_2$ calculations in some detail, as there are very few guidelines on how to practically conduct studies on transition metal compounds. They hold a decidedly different set of potential pitfalls and glitches (e.g., the ubiquitous electronic instabilities) in store compared to most other computational applications, and we encountered a number of difficulties in the beginning of our study.

of different DFT approaches and basis sets, the design and realization of active spaces for CAS methods, the interpretation of different quantities like partial charges and spin densities in the context of their origin (e.g., from MPA, NPA, AIM) and the use of different numerical strategies and algorithms.

We conclude that DFT is a good starting point for computational studies of single center transition metal complexes. It is however important to make a careful selection for the employed functional and not just go with the popular B3LYP. Despite being a black-box method, we have shown that it is important to employ DFT with the due prudence and care and be aware of its limitations, both in terms of accuracy and the physical picture obtained. For truly complicated cases it is recommended to resort to high-level wavefunction methodology such as CASSCF/CASPT2 which can account for the intricate electron correlation effects.

We can summarize that this study is a good example for the fruitful collaboration between experiment and theory. We could successfully connect our computational results with the experimental data and provide a theoretical foundation for a number of them. The computational investigation was able to confirm and elaborate on many of the experimental interpretations (e.g., the redox activity and XAS spectrum of the $Cr(smif)_2$), and contributed to shedding some light on unexplained phenomena (e.g., the deformations found in the XRD geometries, the temperature dependent EPR signal in $Cr(smif)_2$ or the spin state of $Co(smif)_2$). Independent of complementing specific experimental data, we could also successfully illuminate the overall electronic situation of the $M(smif)_2$ series.

CHAPTER 6

SUMMARY AND OUTLOOK

6.1 Density matrix renormalization group in quantum chemistry

We have demonstrated that the density matrix renormalization group can be a valuable tool in quantum chemistry, in particular when employed within our local framework and for the domain of static correlation problems in predominantly one-dimensional molecules. Even if applied outside its ideal regime, the DMRG can serve as a powerful alternative to FCI. We have applied the DMRG in studies previously beyond the reach of *ab initio* quantum chemistry due to the limitations of standard multi-reference wavefunction techniques. By doing so, we could gain new insights into the physics of conjugated π-electron systems.

There has been some progress in the recent years to extend the range of applicability of the DMRG towards properties beyond energies and correlation functions. The basic (local and canonical) DMRG is combined with familiar techniques from the quantum chemical arsenal as well as with new methodological ideas. It is utilized as the solver module for the static correlation aspect and embedded it in the larger algorithmic setup:[1]

- The DMRG was combined with an optimization of the orbital space [108, 114] in the spirit of MCSCF/CASSCF techniques [24, 26, 370, 247] (i.e., corresponding to the transition from CASCI to CASSCF). In the CASCI

[1]The author was involved in a number of these projects, but since he was not the primary contributor, the work will be presented in detail elsewhere.

approach we usually select the active space from canonical Hartree-Fock orbitals (or orbital sets derived from them, e.g., by localization), and they also represent the core space in the frozen-core approximation. These molecular orbitals are optimized based on a single-determinant wavefunction ansatz, which is by definition inadequate in the multi-reference regimes under consideration. Consequently, it is unclear whether they are a good starting point for the task at hand. Instead of employing and relying on these orbitals, we can adapt the one-electron basis to the multi-reference situation by reoptimizing them within the DMRG ansatz.

This orbital space adaptation was not a major concern for the studies presented in the course of this thesis, since they all feature a well defined separation of active and inactive spaces (we always correlated the complete π_z-space, which was orthogonal to the σ-framework of the molecules). Generally however, orbital optimization will be important to ensure the correlation of the best set of active orbitals, in particular in case of non-planar molecules in large basis sets, where a selection of canonical orbitals can be highly suboptimal. We point out that the DMRG-CASSCF approach arrives at a representation in terms of a problem adapted one- *and* many-electron basis.

- One focus of work in the Chan and Yanai Groups has been to combine the DMRG as a static correlation solver with an 'on-top' treatment of dynamic correlation, in the spirit of conventional multi-reference perturbation (MRPT, CASPT), configuration interaction (MRCI), and coupled cluster theory (MRCC). One limitation in this endeavour is that the DMRG does not provide an explicit wavefunction expansion in terms of simple basis states (e.g., Slater determinants), necessary in a straightforward exci-

tation hierarchy treatment of dynamic correlation[2]. Instead, dynamic correlation has to be introduced on the basis of reduced density matrices of a certain rank [371, 372, 373, 374]. The cost of generating (and storing) higher- and higher-body reduced density matrices grows substantially [108, 109]. So far, the DMRG was successfully combined with 2nd-order *n*-electron valence state perturbation theory (NEVPT2 [375]; a variation of MRPT) [376] and the canonical transformation theory [61, 62, 63, 64, 65], which was specifically designed in the Chan Group as a complement to DMRG.

- An algorithm called 'harmonic davidson' was introduced to target excited states in the DMRG (and other multi-reference methods) [377]. The common path to excited states is the 'state-averaging' approach (see e.g., [108]), in which the many-body basis is optimized with respect to the required number of roots of the Hamiltonian at the same time. Since the adaptation of the DMRG basis is less appropriate for each individual state, the quality of their energies degrades, in particular if the states under consideration have a very different electronic structure (and require a different representation). (The *gaps* between the states are usually better, and by increasing M and approaching an FCI quality expansion, all roots eventually converge to their exact value.) Attempts to directly optimize excited state wavefunctions often suffer from the so called '*root-flipping*' (or '*variational collapse*') problem [378], i.e., due to a lack of a variational bound for states other than the ground state, the optimization parameters can leave the optimization basin of the state of interest and converge to a lower energy state. The harmonic davidson method utilizes a shifted and inverted Hamiltonian, which projects out parts of the spectrum and allows the al-

[2]In practice, certain contraction schemes help avoid this route (see, e.g., [363]).

gorithm to converge to the next excited state in the same fashion as if it was the ground state.

- Analytic derivatives and linear response theory were introduced to the DMRG [379] in the spirit of a coupled perturbed ansatz for the first order wavefunction, with the renormalization matrices as the variational parameters [380]. We demonstrated its performance in comparison with more approximate avenues to static and frequency dependent response properties. Methods such as the *correction vector*, *Lanczos-vector*, or *dynamical DMRG* adapt the DMRG many-body basis with respect to both the ground state and its response, instead of solving the coupled-perturbed response equations.

There is still a long list for further developments of DMRG methodology in quantum chemistry. The goal should be to establish it as a standard method in integrated computational chemistry program packages, and to essentially replace the current brute-force FCI part in multi-reference methods with a smarter, more powerful DMRG kernel. A number of development teams, e.g., from NWCHEM [381, 382], MOLPRO [145], MOLCAS [383, 384, 385], QCHEM [146, 147], have shown interest in implementing DMRG into their program packages. The following is an analysis and summary of outstanding tasks:

- At the current stage, the practical application of the DMRG is still challenging and requires expert knowledge as well as experience in order to give correct and reliable results. DMRG has to transition from a complicated expert-only code towards a more black-box software, with an emphasis on user-friendliness. Key aspects for improvements of the current implementations are automation, feedback, and dynamic computa-

tion control. One example is the design of an automated schedule, which controls the choice and progressive increase of M, the number of sweeps and the application and adjustment of noise in the course of the calculation based on the specific progress and convergence behavior. At the current stage, all these parameters have to be adjusted manually and on-the-fly, which is cumbersome, inefficient, error prone, and not sustainable for routine employment. The experience gained in the course of this thesis can be a valuable starting point for the design of a smart driver.

- Instead of choosing M in order to obtain a certain accuracy, we can in principle also choose M in order to optimize the accuracy/cost-ratio (within a given range) by analyzing the profile of the eigenvalue spectrum of the reduced density matrix and truncating in a favorable place. An initial exploration of this idea can be found in Ref. [386].

- As we pointed out earlier, the accuracy of the DMRG results can be adjusted seamlessly by the choice of M (cf. 1.2.3). So far, the DMRG was used to *exactly* correlate active spaces, i.e., the results were typically converged (with respect to the number of DMRG basis states) up to a residual error of $1-10\,\mu E_\mathrm{h}$. Common CAS techniques also arrive at the exact energy (with some numerical/convergence error of comparable order of magnitude), by solving for the space of all possible configurations spanned by an active space. The latter is usually a wasteful approach, since the number of configurations with large contributions in a CAS expansion is usually moderate. Restricted active space (RAS) methods avoid the FCI solution of the active space problem in favor of diagonalizing a lower rank CI space (e.g., only using configurations up to quadruple excitations (CISDTQ) in-

stead of the full configuration space (FCI); cf. Fig. 1.6). This is a cheaper, less accurate approach but it allows the treatment of larger active spaces with a reasonable chance of adequately accounting for the static correlation problem[3]. In the same spirit, we propose a paradigm shift towards cheaper, medium accuracy DMRG calculations (e.g., with a numerical accuracy of up to a few hundred microhartree) of larger active spaces (as compared to expensive, high accuracy calculations of somewhat smaller active spaces, which is current practice). The primary concern of a multi-reference ansatz is to obtain a sufficient representation of the complex electronic structure situation, e.g., as a good zeroth-order wavefunction for an on-top perturbative treatment of the dynamic correlation problem. An insufficient reference function can lead to the infamous '*intruder-state*' problem [24]. An error of a few hundred microhartree in the active space correlation energy should be small compared to errors in an unstable perturbative account of dynamic correlation. Actually, the inherent error in the dynamic correlation treatment is probably of the same order, i.e., it is not really necessary to put in the effort to obtain numerically exact results for the active space problem in the first place. Lower accuracy DMRG calculations are elegantly realized by tuning M without the *ad hoc* assumptions of the RAS ansatz.

- In the context of exploiting information from the DMRG RDM eigenvalue spectrum (see above) and lower accuracy calculations (see previous item) we also propose a more consequent use of extrapolation with respect to

[3]FCI based methods can lead to inadequate descriptions of static correlations in the following sense: While CAS methods exactly account for the static correlation in the active space, the feasable active space may be too small to cover all relevant, strongly interacting orbitals. RAS methods can treat larger active spaces and may overcome that problem, but by restricting the configuration space, it may miss out on a few important terms.
The RAS approach turns out less numerically stable compared to the CAS ansatz.

M, as we know the weight of the truncated RDM eigenvectors (cf. eqn. (1.50)) and the error behavior with M (cf. eqn. (2.7)). Note that while extrapolation schemes are generally popular in quantum chemistry – e.g., the complete basis set extrapolation schemes towards the one-body space limit or the recent extrapolation of the correlation energy with respect to CI excitation order by Bytautas and Ruedenberg [387, 388, 389, 390, 391, 392] (i.e., extrapolation to the n-body limit; cf. Fig. 1.4) – the DMRG is in a unique position due to its physically well defined truncation criterion.

- As discussed above, there has been some progress to establish the DMRG as the static correlation solver in combination with dynamic correlation models. A new tensor contraction engine (TCE) for multi-reference methods is being implemented by the NWCHEM development team, and may become a valuable tool for the rapid development, automated implementation and evaluation of a host of possible dynamic correlation approximations. DMRG could potentially also serve as a starting point for multi-reference density functional (CASDFT/MRDFT) or multi-reference reduced density matrix functional (CASDMFT/MRDMFT) approaches.
- The implementation of periodic boundary conditions for the study of extended periodic systems at highly correlated *ab initio* wavefunction level remains an open task.
- Linear scaling DMRG based on multipole approximations is a further possibility and would make even bigger problems accessible.
- At the current development stage, DMRG is still slower than FCI in most systems which are accessible to the latter[4]. This disadvantage in prefactor

[4]The factorial scaling leads to a very sudden crossover, beyond which FCI becomes impossi-

should clearly be overcome. There is room for many technical and performance improvements which can be harvested from the long experience of conventional, Slater determinant based quantum chemistry algorithm development. Use of symmetries, efficient organizational structures and convergence acceleration are amongst them.

- Last but not least, there is the DMRG ordering problem (cf. Ch. 2.3). The question of the 'ideal' one-particle representation and its projection has to be resolved in a better way than it is now. However, this is a hard problem and despite previous efforts [105, 393, 110, 386] has not reached a satisfactory state.

We have at length discussed the limitations of the DMRG in terms of dimensionality. This particular feature can be traced back to the way, in which correlations are introduced in the wavefunction ansatz, i.e., by means of the two auxiliary indices which connect each site with its left and right neighbor. More general tensor product states (TPS) have been designed with more auxiliary indices, which can connect and correlate sites in more than one dimension (e.g., the projected entangled pair states (PEPS) [394, 395, 396, 397] for 2D and the multi-scale entanglement renormalization ansatz (MERA) [398] for arbitrary dimension). While these approaches have a polynomial parametrization, it unfortunately might not be possible to solve the arising equations in polynomial time.

Nevertheless, we believe that the decomposition of the FCI coefficient tensor, on which the MPS wavefunction is based (see eqn. (1.54)), may be the way of thinking about and constructing the next generation of wavefunction ansätze (in

ble.

a similar way the formulation of an exponential ansatz or of pair theories have triggered a host of new approximations in the past). Instead of directly truncating the FCI coefficient tensor and/or approximating its values, these methods start by approximating the tensor structure itself.

6.2 Transition metal computational chemistry

Computational transition metal chemistry is and will remain a challenging field for the application of electronic structure methodology, as the underlying quantum many-body problem with overlapping static and dynamic correlation regimes is inherently complicated. However, with the availability of more advanced methods and growing experience about the practical issues, computational chemistry is increasingly in the position of making important contributions to the understanding of electronic phenomena in these systems. Furthermore, it will hopefully become an increasingly predictive tool for the development of novel transition metal compounds with interesting properties.

Our work in Ch. 5 has addressed a number of technical problems in computational transition metal chemistry. It requires a great amount of experience and background knowledge to perform the desired calculations in a way which leads to correct and reliable results. All available methods have their limitations in terms of applicability and accuracy, but it turns out that the primary practical concern is to get the correct results within a method in the first place (i.e., the discussion of the intrinsic errors of a DFT result is futile, if a calculation converges unnoticed to an electronic instability). In addition, there are substantial performance differences between methods (e.g., functionals) which are well known

and documented in the literature, but this knowledge appears to be rarely used in the actual application studies, considering the fraction of studies performed with the omnipresent B3LYP approach.

One of the key lessons is that there is significant room for improvements of the available program packages, by which the development community could greatly support the work of applied researchers in this field. Many package development efforts have a focus on providing new variations to the well established electron correlation approximation schemes (e.g., by exploring new functional forms in DFT or new partitioning/projection schemes in coupled cluster theory). While this clearly constitutes important progress, we feel that there should in addition be greater attention to the algorithmic improvements of the basics: elementary features such as quickly and robustly converging SCF algorithms or geometry optimizations, are essential cornerstones of practical computational chemistry – in particular in complicated circumstances such as transition metal chemistry – but have been neglected for some time. In addition, current quantum chemistry codes are often not sufficiently smart in applying the existing algorithms: a major share in the time effort of our transition metal study went into the manual investigation of crashed and/or unconverged or incorrectly converged calculations, reconfiguration of the inputs with respect to employed algorithms and/or settings. While this requires extensive expert knowledge for the individual user, it could easily be automated by simple observations, rules and feedback of the calculation progress, which reflect the problem at hand. What we find however are default settings which more often then not are inappropriate for a specific situation, since they are rarely adjusted to it – and it is obvious that the computational requirements for a saturated organic molecule are decidedly different than for a radical organometallic complex. Fur-

thermore, it would be simple for a code to at least make recommendations for an appropriate model chemistry based on the given molecule, requested properties and required accuracy/available timeframe.

This leads us to revisit the concept of a 'black-box' method: DFT is considered as such a black-box approach, since one only needs to input the problem and model chemistry (i.e., the functional and basis set) and obtains the energy and other properties as output (this is in contrast, e.g., to CAS methods, which require a lot of manipulation and additional input by the user). Our study has demonstrated that current DFT implementations are from a numerical perspective not a black-box methods at all, since they often produce no or incorrect output (in addition to unnecessarily long calculation times), if not manually tweaked in the right direction. A consideration of the big performance differences between methods raises the additional and more general question, to what extent the choice of a model chemistry should be left to the user, and whether it is feasible and beneficial to include this decision (or parts of it) into the black box. We believe that at least the first aspect has to be overcome by more sophisticated, responsive, and intelligent drivers in the program package to justify the claim of a black-box method in a true sense.

APPENDIX A

OXIDATION STATES AND PARTIAL CHARGES

We review the concept of formal oxidation states in transition metal chemistry in the context of computationally determined charge distributions. We address implications of formal and actual electron counts and d-orbital occupations on the classification and understanding of coordination compounds.

A.1 Background

The concept of *oxidation states* is one of the basic tools in chemistry [399] and of particular use for the classification of transition metal compounds: based on the oxidation state of the metal center in a complex, we conclude its number of d-electrons, and in turn possible spin states, electronic d-d transitions between them, resulting coordination geometries, magnetism, reactivity, and other related properties.

It is well known that the assigned integer charges of the oxidation states do not match the 'real partial charges' on the atomic centers (for which we will use the term *charge* for short), and that in particular for large oxidation states such as in Cr(VI) the actual electron distribution will deviate notably from the formal value. Surprisingly, the relation between experimentally or computationally determined charge distributions and the formal oxidation states has not been discussed in much detail, except for Refs. [400, 401, 402, 403, 404, 405, 406, 407, 408, 409]. It has become clear (even though it might not yet be fully appreciated) that the differences between oxidation state and charge can be very substantial, even for low and moderate oxidation states (see e.g., [406]). In this section we

will focus the attention on some of the consequences of the difference in the electron count, such as the implications on the concepts that build upon the oxidation state. We will analyze, how to understand the electronic situation on the metal considering this discrepancy, how the oxidation state concept retains its value, and how the experimental determination of oxidation states fits into this situation.

A.1.1 Concept of oxidation states

The idea of oxidation states developed in close proximity to the theory of valency [410]. In its present form the concept of oxidation states goes back to W. M. Latimer and his 1938 book *The Oxidation States of the Elements and Their Potentials in Aqueous Solution [411]*. IUPAC defines the oxidation state as '*A measure of the degree of oxidation of an atom in a substance. It is defined as the charge an atom might be imagined to have when electrons are counted according to an agreed-upon set of rules* [...]' [8].

Oxidation states are hence based on the partitioning of the valence electrons in a complex towards metal or ligand. The common heterolytic accounting of electrons based on electronenegativity differences readily leads to metals with large positive oxidation states surrounded by ligands with negative ones, corresponding to an idealized ionic bonding. This picture neglects covalency, which usually has a substantial contribution to the overall bonding situation [412]. It is moreover often based on an improper use of electronegativity arguments: The commonly employed electronegativity values χ refer to neutral atoms, while in a compound more sophisticated oxidation state dependent electronegativity

values [413] would have to be applied to account for the concrete electronic situation (since, e.g., the electron distribution between chromium and oxygen in $[CrO_4]^{2-}$ and $[Cr(H_2O)_6]^{3+}$ will be quite different). Note that in the closely related *oxidation number* concept (which is often used synonymously with the oxidation *state*) the electrons in the coordinative bonds are *always* counted towards the ligand, irregardless of the electronegativities [8].

In 1948 L. Pauling introduced his heuristic *electroneutrality principle* [400, 401, 402, 414] and postulated that the charges within a stable complex would only range from -1 to +1 and would arrive there by a suitable combination of ionic and covalent resonance structures (with the weights of classic ionic terms actually small due to the large potential of the charge separation). Pauling argued that the electronegativity differences between metals and ligands never warrant a completely ionic electron distribution, but require substantial covalent bonding contributions with homolytic electron accounting.

C. K. Jørgensen developed in 1969 the concept of *spectroscopic oxidation states* [415], distinguishing between the formal oxidation state and a value corresponding to an experimentally determined metal d-orbital occupation.

A number of more modern (predominantly computational) studies suggest that there is no connection and relation between the oxidation state and the charges [404, 408, 409]. Raebinger *et al.*, e.g., propose a self-regulating feedback mechanism based on the metal orbital hybridization, which upon oxidation/reduction leads to a dispersion of introduced charges.

A.1.2 Defining intramolecular charges

Atomic charges within a compound are not physical observables and hence not directly measurable. The assignment of electrons towards intramolecular centers is consequently not unique, and there is a variety of different approaches, which can be divided into methods based on population analysis in orbital space and methods based on real space partitioning of the electron density (cf. 4.6).

A.1.3 Experimental determination of oxidation states

There is thus also no absolute and unambiguous way to experimentally determine oxidation states. Several methods (predominantly high-energy and spin-resonance spectroscopy such as, e.g., ESCA, Auger, XPS, XANES, NMR, EPR) which are sensitive to local charge distributions are employed in practice are based on a reference compound framework. For details, we refer to a recent review article by Siedel and Kaupp [416] which describes modern spectroscopic techniques used for the assignment of oxidation states.

A.1.4 Related concepts

Despite its simplicity the oxidation state concept has survived because of its great utility in conceptualizing and characterizing transition metal complexes [417, 248]. Using the oxidation state, we obtain the d-electron count on the metal center. Based on crystal or ligand field arguments, these electrons are

distributed over the d-type metal orbitals, resulting in a characteristic occupation pattern, which in turn is best accommodated by a particular coordination geometry. In combination with the electronic characteristics of the ligand, we arrive at low-spin, intermediate-spin, or high-spin states, with the corresponding magnetism, and a ligand field splitting between these spin-states. We systematize ligands according to their capability of splitting the ligand field in the spectrochemical series.

Oxidation states are also useful in the area of electron bookkeeping during redox processes, give an indication of the redox potential towards other compounds, and in consequence the reactivity and corrosiveness.

A.1.5 Comparison of partial charges to reference systems

There is no doubt about the existence of coordination compounds of different oxidation levels (such as the ferrous and ferric ion), which are commonly labeled by certain oxidation states. The resulting electron count has – as discussed – direct consequence on various observable properties. At the same time it is clear that this very electron count does not correspond to the actual charges within the complexes. We try to illuminate the relation between the simple concept and the computational results.

In Ch. 5, we computed the electronic structure and resulting electron density distribution of the series of $M(smif)_2$ complexes (with density functional theory as our primary computational method), as well as reference compounds of the relevant oxidation states to study changes in the charge distributions. While previous studies focussed on results from population analysis schemes, we cen-

tered our study on Bader's Atoms-in-Molecules (AIM) analysis of the charge density topology. Although, as mentioned before, there is no rigorous assignment of partial charges, the AIM approach is a very sensible realization of this quantity. We augmented the AIM results by population analysis to assess, how the real space charges are realized in orbital space.

As discussed in Sec. 5.2.3 we focussed on the computed partial charges instead of absolute integer charges associated with oxidation states, and we concentrated on the relative magnitude of these partial charges with respect to reference systems of well established oxidation state instead of their absolute value.

One key finding in our transition metal study with respect to the question of oxidation states is that despite the discrepancy between the computed charge and the formal oxidation state, the d-orbital occupation pattern deduced on the basis of the oxidation state seem to holds up remarkably well. The Atoms-in-Molecules (AIM) results of the $[Cr(smif)_2]^+$-cation in the quartet state with an effective Cr(III) shows a charge of q_{AIM}(Cr)=2.12, i.e., ~4 electrons reside on the metal center. At the same time the AIM analysis of the spin density finds three *unpaired* electrons on the chromium. A population analysis shows that the $3d_{xy}$, $3d_{xz}$, and $3d_{yz}$ are singly α-occupied, while the fourth electron (which we shall call *residual* electron) is closed-shell (i.e., with roughly same amount of α- and β-spin) distributed over the remaining 3d as well as 4s and 4p orbitals. This resembles a classical d^3 occupation embedded in an electron density dispersed from the ligands to balance out an ionic charge distribution. The residual charges are introduced by an excess of metal atomic orbitals mixed into the ligand based occupied frontier orbitals (as far as possible by symmetry considerations). One contribution for the residual electron density will certainly be the electron den-

sity of the covalent contributions to the dative bond. Our calculations actually show that, e.g., for the *trans*-$[CrCl_2(H_2O)_4]^+$-cation the formal charge on the chlorides is redistributed towards the metal – rather than the lone pairs on the water-oxygens. This suggests that actually the M–Cl^- bond is more covalent than the M–OH_2.

The +3 oxidation state in $[Cr(smif)_2]^+$ was experimentally determined by XAS comparison with the reference compound *trans*-$[CrCl_2(H_2O)_4]^+$, which is considered a classical Cr(III) complex. Their computed AIM charges of q_{AIM}(Cr)=2.12 match exactly (probably somewhat fortuitously). For *trans*-$CrCl_2(H_2O)_4$ we computed q_{AIM}(Cr)=1.60. We see that the discrepancy between oxidation state and charge increases with increased oxidation state, but that the oxidation still predominantly takes place on the metal (i.e., we do not observe non-innocent ligand behavior – as expected for the present ligands). In the homologous fluoride complexes we find for *trans*-$[CrF_2(H_2O)_4]^+$ a value of q_{AIM}(Cr)=2.27 and for *trans*-$CrF_2(H_2O)_4$ q_{AIM}(Cr)=1.71. The higher charges are in good agreement with the difference in electronegativity, comparing Cl and F. Another classic Cr(III) compound, $[Cr(H_2O)_6]^{3+}$ shows q_{AIM}(Cr)=2.27, which can be explained with the lack of an ionic ligand, whose charge could be redistributed. Following the same argument in the opposite case we can rationalize the low charge on the Cr(IV) complex $CrCl_4$ with q_{AIM}(Cr)=1.98. $[CrO_4]^{2-}$, a formal d^0-complex shows q_{AIM}(Cr)=2.64, and the 3.36 residual electrons are distributed more or less evenly over the 3d, 4s and 4p orbitals without an occupation pattern.

We have now verified the magnitude of possible residual charges, discussed their origin, and identified the unconventional way they are attached to the

metal center. One interesting conclusion is that despite the massive residual charges the oxidation state derived d-occupation patterns hold true and the bonding situation is well represented. This might give a fresh view on the traditional oxidation state concept for transition metals. Furthermore, the 'charge bath', in which the d-electrons are embedded, offers an interesting alternative perspective on ligand-field splitting and the spectrochemical series.

We propose a more concise and comprehensive study of the charges in simple 3d-metal-complexes with well established formal oxidation states, covering all 3d metals as well as their known oxidation states, to verify and establish our preliminary findings. In addition, calculations on a series of $[MX_a]^b$ systems (e.g., with M=Cr, X=Cl), with a and b covering all sensible coordination numbers and oxidation states might give a systematic insight. Finally, cases with controversial oxidation states such as the one discussed by Snyder [403, 404, 405] could be of interest for further investigation. Such a study might revitalize the chemical utility of oxidation state concept, if it finds support for the notion that there is no stark contradiction between the concept and the computed values, and that we just have to refine the concept and with that bring it on a more solid foundation.

APPENDIX B

ADDITIONAL M(SMIF)$_2$ DATA

Table B.1: Total energy (E), standard Gibbs free energy ($G^{\ominus}$), nuclear energy (E_{nucl}), spin-squared expectation value ($\langle S^2 \rangle$) before and after annihilation of the first spin contaminant, as well as Mulliken and AIM charges (q_{MPA}(Cr), q_{AIM}(Cr)) and integrated spin densities (n^s_{MPA}(Cr), n^s_{AIM}(Cr)) on the chromium in the $[Cr(smif)_2]^+$-cation at double-ζ level. All energies are given in hartree (E_h).

	UPBE0/6-31G*		UBLYP/6-31G*	
	C_{2v}, $^2B_2$	C_s, $^2A'$	C_s, $^2A'$	C_{2v}, $^2B_1$
E [E_h]	–2297.744919	–2297.739737	–2298.968132	–2298.967053
$G^{\ominus}$ [E_h]	–2297.397676	–2297.391242	–2298.637796	–2298.636435
E_{nucl} [E_h]	3641.688237	3658.702695	3610.425182	3605.868744
$\langle S^2 \rangle$	2.5290/3.3753	1.7800/0.9502	1.6123/0.7932	1.6761/1.3253
q_{MPA}(Cr)	1.2	1.24	0.94	0.94
q_{AIM}(Cr)	2.0	2.09	1.90	1.89
n^s_{MPA}(Cr)	2.96	1.09	1.22	2.22
n^s_{AIM}(Cr)	2.57	1.02	1.14	1.99

	UPBE0/6-31G*	UB3LYP/6-31G*	UBLYP/6-31G*
	D_{2d}, $^4B_1$	D_{2d}, $^4B_1$	D_{2d}, $^4B_1$
E [E_h]	–2297.777896	–2299.447761	–2298.993111
$G^{\ominus}$ [E_h]	–2297.428535	–2299.102155	–2298.661335
E_{nucl} [E_h]	3650.707957	3626.206282	3599.366838
$\langle S^2 \rangle$	3.7803/3.7504	3.7769/3.7503	3.7754/3.7503
q_{MPA}(Cr)	1.27	1.14	0.97
q_{AIM}(Cr)	2.11	2.05	1.94
n^s_{MPA}(Cr)	3.15	3.08	2.94
n^s_{AIM}(Cr)	2.92	2.89	2.78

Table B.2: Total energy (E), standard Gibbs free energy ($G^{\ominus}$), nuclear energy (E_{nucl}), spin-squared expectation value ($\langle S^2 \rangle$) before and after annihilation of the first spin contaminant, as well as Mulliken and AIM charges (q_{MPA}(Cr), q_{AIM}(Cr)) and integrated spin densities (n^s_{MPA}(Cr), n^s_{AIM}(Cr)) on the chromium in the $[Cr(smif)_2]^+$-cation at triple-ζ level. All energies are given in hartree (E_h).

	UPBE0/6-31G*//cc-pVTZ (DKH2)			UPBE0/cc-pVTZ		
	C_{2v}, $^2B_2$	C_s, $^2A'$	D_{2d}, $^4B_1$	C_{2v}, $^2B_2$	C_s, $^2A'$	D_{2d}, $^4B_1$
E [E_h]	–2303.825981	–2303.822420	–2303.859103	–2298.260393	–2298.256107	–2298.293579
$G^{\ominus}$ [E_h]	–	–	–	–2297.915876	–2297.909650	–2297.946201
E_{nucl} [E_h]	3641.688237	3658.999250	3650.707957	3642.755600	3659.429028	3652.480364
$\langle S^2 \rangle$	2.5390/3.3990	1.7864/0.9462	3.7790/3.7504	2.5340/3.3781	1.7846/0.9331	3.7799/3.7504
q_{MPA}(Cr)	0.37	0.33	0.41	0.45	0.41	0.47
q_{AIM}(Cr)	–	–	–	–	–	2.15
n^s_{MPA}(Cr)	2.98	1.11	3.18	2.98	1.12	3.19
n^s_{AIM}(Cr)	–	–	–	–	–	2.92

Table B.3: Comparison of vertical relativistic correction and solvation effects to the UPBE0/6-31G* solutions: Total energy (E in hartree E_h), spin-squared expectation value ($\langle S^2 \rangle$) before and after annihilation of the first spin contaminant, as well as Mulliken and AIM charges (q_{MPA}(Cr), q_{AIM}(Cr)) and spin densities (n^s_{MPA}(Cr), n^s_{AIM}(Cr)) on the chromium for the quartet ground state.

	UPBE0/6-31G*			
		(DKH2)	(DKH2,SCI-PCM=THF)	(DKH2,SCI-PCM=AcN)
E [E_h]	–2297.777896	–2303.378952	–2303.422028	–2303.427472
$\langle S^2 \rangle$	3.7803/3.7504	3.7800/3.7504	3.7802/3.7504	3.7802/3.7504
q_{MPA}(Cr)	1.27	1.26	1.26	1.26
q_{AIM}(Cr)	2.11	2.12	2.12	2.12
n^s_{MPA}(Cr)	3.15	3.15	3.15	3.15
n^s_{AIM}(Cr)	2.92	2.92	2.92	2.92

Table B.4: Total energy (E), standard Gibbs free energy ($G^\ominus$), nuclear energy (E_{nucl}), spin-squared expectation values ($\langle S^2 \rangle$) before and after annihilation of the first spin contaminant, Mulliken and AIM charges (q_{MPA}(Cr), q_{AIM}(Cr)) and integrated spin densities (n^s_{MPA}(Cr), n^s_{AIM}(Cr)) on the chromium in the Cr(smif)$_2$ complex (triplet state only; the C_{2v} doublet cation data is added for comparison). Data sets at different levels of theory are presented. All energies are given in hartree (E_h).

	UPBE0/6-31G*			UB3LYP/6-31G*	
	D_2, $^3B_2$	C_{2v}, $^3B_2$[TS]	C_{2v}, $^2B_2$ [cation]	D_2, $^3B_2$	C_{2v}, $^3B_2$[TS]
E [E_h]	–2297.923791	–2297.923508	–2297.744919	–2299.594907	–2299.593918
$G^\ominus$ [E_h]	–2297.580509	(–2297.577413)	–2297.397676	–2299.254310	(–2299.251803)
E_{nucl} [E_h]	3648.718768	3644.826385	3641.688237	3621.880580	3618.553260
$\langle S^2 \rangle$	2.6929/2.0461	2.7346/2.0546	2.5290/3.3753	2.5858/2.0279	2.6135/2.0316
q_{MPA}(Cr)	1.22	1.22	1.25	1.09	1.08
q_{AIM}(Cr)	2.03	2.03	2.04	1.95	1.96
n^s_{MPA}(Cr)	2.89	2.91	2.96	2.75	2.75
n^s_{AIM}(Cr)	2.56	2.59	2.57	2.49	2.50

Table B.5: Total energy (E in hartree) of the Cr(smif)$_2$ triplet ground states of different symmetry, triplet-triplet gaps (ΔE_{t-t}) with respect to the ^{3}B$_2$ state (in kcal/mol), and AIM charges (q_{AIM}(Cr)) and spin densities (n^s_{AIM}(Cr)) on the metal.

UB3LYP/6-31G*	^{3}A	^{3}B$_1$	^{3}B$_2$	^{3}B$_3$
E [E_h]	–2299.531672	–2299.569200	–2299.594907	–2299.587619
ΔE_{t-t} [kcal/mol]	39.7	16.2	–	4.6
q_{AIM}(Cr)	–	–	1.9503	1.9675
n^s_{AIM}(Cr)	–	–	2.4869	2.5320

Table B.6: Total energy (E), standard Gibbs free energy ($G^{\ominus}$), nuclear energy (E_{nucl}), spin-squared expectation value ($\langle S^2 \rangle$) before and after annihilation of the first spin contaminant, as well as Mulliken and AIM charges (q_M(Cr), q_{AIM}(Cr)) and integrated spin densities (n^s_M(Cr), n^s_{AIM}(Cr)) on the chromium in the singlet and quintet Cr(smif)$_2$ complex (transition states and triplets are added for comparison). All energies are given in hartree (E_h).

	UPBE0/6-31G*						
	C_2, ^1A	D_2, $^3B_2$	C_{2v}, $^3B_2$[TS]	C_{2v}, $^5A_1$	D_2, $^5B_2$	D_{2d}, $^5A_2$[TS^3]	C_{2v}, $^5B_1$[TS]
E [E_h]	–2297.892807	–2297.923791	–2297.923508	–2297.912139	–2297.909450	–2297.909346	–2297.909297
$G^{\ominus}$ [E_h]	–2297.547235	–2297.580509	(–2297.577413)	–2297.575062	–2297.568286	(–2297.566489)	(–2297.565129)
E_{nucl} [E_h]	3647.559353	3648.718768	3644.826385	3510.216160	3645.738116	3507.262162	3644.675187
$\langle S^2 \rangle$	1.0809/0.6974	2.6929/2.0461	2.7346/2.0546	6.0160/6.0001	6.0279/6.0003	6.0142/6.0001	6.0344/6.0004
q_{MPA}(Cr)	1.15	1.22	1.22	1.10	1.25	1.11	1.25
q_{AIM}(Cr)	1.87	2.03	2.03	1.68	2.09	1.67	2.09
n^s_{MPA}(Cr)	–0.20	2.89	2.91	3.95	3.14	3.95	3.13
n^s_{AIM}(Cr)	–0.09	2.56	2.59	3.81	3.01	3.84	2.97

Table B.7: Total CASSCF energies of the different symmetry triplet states of $Cr(smif)_2$ computed within different active spaces (constructed according to previous discussion) and basis sets. The results on the top correspond to to a strategy 1 built-up, the results on the bottom to strategy 2. In case of active space ambiguities, only the best results are given, The calculations incoorporate DKH2 relativistic correction but no frozen core approximation. All results given in hartree. ('*n.c.*' = not converged.

CASSCF	^3A	$^3B_1$	$^3B_2$	$^3B_3$
(4e,5o)/STO-6G	–2289.075396	*n.c.*	–2289.054369	–2289.044787
(4e,5o)/ANO0	–2295.681013	–2295.748574	–2295.752663	–2295.750186
(4e,10o)/ANO0	–2295.707353	–2295.774716	–2295.791619	–2295.784230
(10e,16o)/ANO0	–2295.776172	–2295.825315	–2295.859985	–2295.850196
(12e,17o)/ANO0	–2295.804061	–2295.874245	–2295.900804	–2295.890038
(8e,10o)/ANO0	–2295.711255	–2295.795528	–2295.822544	–2295.811060
(14e,16o)/ANO0	–2295.836615	–2295.870446	–2295.898807	–2295.888294
(14e,16o)/ANO1	–2296.399730	–2296.442940	–2296.463424	–2296.453911

Table B.8: Total CASPT2 energies (for different shifts) of the different symmetry triplet states of $Cr(smif)_2$ computed within different active spaces (constructed according to previous discussion) and basis sets. The results on the top correspond to to the reoptimized reference space, the results on the bottom to the unreoptimized ones. In case of active space ambiguities, only the best results are given. The ^3A results could not be converged. The calculations incoorporate DKH2 relativistic correction and frozen core approximation. All results given in hartree ('*n.c.*' = not converged.

CASPT2	shift	$^3B_1$	$^3B_2$	$^3B_3$
(14e,14o)/ANO0	0.1	–2298.674023	–2298.725496	*n.c.*
	0.2	–2298.658767	–2298.707524	–2298.699248
	0.3	–2298.637319	–2298.685138	–2298.676174
(14e,14o)/ANO1	0.1	–2300.973013	*n.c.*	*n.c.*
	0.2	–2300.954100	–2300.996971	–2300.987834
	0.3	–2300.927168	–2300.968847	–2300.959082
(14e,14o)*/ANO0	0.1	–2298.684104	–2298.730960	–2298.724307
	0.2	–2298.665739	–2298.711759	–2298.704409
	0.3	–2298.643612	–2298.688679	–2298.681062
(14e,14o)*/ANO1	0.1	–2300.981363	*n.c.*	*n.c.*
	0.2	–2300.960440	–2300.997089	–2300.976374
	0.3	–2300.932936	–2300.968694	–2300.948043

Table B.9: Total energy (E), standard Gibbs free energy ($G^{\ominus}$), nuclear energy (E_{nucl}), spin-squared expectation value ($\langle S^2 \rangle$) before and after annihilation of the first spin contaminant, as well as Mulliken and AIM charges (q_M(V), q_{AIM}(V)) and integrated spin densities (n^s_M(V), n^s_{AIM}(V)) on the vanadium in the doublet and quartet V(smif)$_2$ complex. All energies are given in hartree (E_h).

	UPBE0/6-31G* C_s, ^{2}A′	UB3LYP/6-31G* C_s, ^{2}A′	UPBE0/6-31G* D_{2d}, $^4B_1$	UB3LYP/6-31G* D_{2d}, $^4B_1$
E [E_h]	–2197.474190	–2199.138824	–2197.498092	–2199.161148
$G^{\ominus}$ [E_h]	–2197.132482	–2198.801021	–2197.155303	–2198.821843
E_{nucl} [E_h]	3566.466553	3538.564366	3537.880186	3514.886519
$\langle S^2 \rangle$	1.7147/0.8514	1.7134/0.8288	3.7662/3.7501	3.7627/3.7501
q_{MPA}(V)	1.22	1.09	1.17	1.05
q_{AIM}(V)	2.06	1.99	1.87	1.86
n^s_{MPA}(V)	1.48	1.31	2.79	2.73
n^s_{AIM}(V)	1.36	1.24	2.66	2.64

BIBLIOGRAPHY

[1] J. Hachmann, W. Cardoen, and G. K.-L. Chan, J. Chem. Phys. **125**, 144101 (2006).

[2] G. K.-L. Chan et al., An introduction to the density matrix renormalization group ansatz in quantum chemistry, in *Frontiers in Quantum Systems in Chemistry and Physics*, edited by S. Wilson, P. J. Grout, P. Piecuch, J. Maruani, and G. Delgado-Barrio, Progress in Theoretical Chemistry and Physics, Springer, Heidelberg, 2008.

[3] G. K.-L. Chan and M. Head-Gordon, J. Chem. Phys. **116**, 4462 (2002).

[4] U. Schollwöck, Rev. Mod. Phys. **77**, 259 (2005).

[5] P. A. M. Dirac, Proc. Roy. Soc. Lond., A **123**, 714 (1929).

[6] S. Wilson, *Handbook of Molecular Physics and Quantum Chemistry*, Wiley, Chichester, 2003.

[7] E. Schrödinger, Phys. Rev. **28**, 1049 (1926).

[8] A. D. McNaught and A. Wilkinson, *IUPAC Compendium of Chemical Terminology (the "Gold Book")*, Blackwell Scientific, Oxford, 2nd edition, 1997.

[9] M. Born and R. Oppenheimer, Ann. Phys. **389**, 457 (1927).

[10] B. T. Sutcliffe, Fundamentals of computational quantum chemistry, in *Computational Techniques in Quantum Chemistry and Molecular Physics*, edited by G. H. F. Diercksen, B. T. Sutcliffe, and A. Veillard, pages 1–106, Reidel, Dordrecht, 1975.

[11] R. G. Woolley and B. T. Sutcliffe, P.-o. löwdin and the quantum mechanics of molecules, in *Fundamental World of Quantum Chemistry*, edited by E. J. Brändas and E. S. Kryachko, volume 1, page 21, Kluwer, Dordrecht, 2003.

[12] W. Pauli, Z. Phys. **31**, 765 (1925).

[13] R. S. Mulliken, Phys. Rev. **41**, 49 (1932).

[14] W. Heisenberg, Z. Phys. A **38**, 411 (1926).

[15] J. C. Slater, Phys. Rev. **34**, 1293 (1929).

[16] A. Weiße and H. Fehske, Exact diagonalization techniques, in *Computational Many-Particle Physics*, edited by H. Fehske, R. Schneider, and A. Weiße, pages 529–544, Springer, Heidelberg, 2008.

[17] V. A. Rassolov and S. Garashchuk, Chem. Phys. Lett. **464**, 262 (2008).

[18] J. Olsen, P. Jørgensen, and J. Simons, Chem. Phys. Lett. **169**, 463 (1990).

[19] S. Evangelisti and G. Bendazzoli, Nuovo Cim. D **17**, 289 (1995).

[20] R. Pauncz, *Spin Eigenfunctions – Construction and Use*, Plenum Press, New York, 1979.

[21] R. Pauncz, *The Construction of Spin Eigenfunctions – an Exercise Book*, Kluwer Academic/Plenum, New York, 2000.

[22] A. Aspuru-Guzik, A. D. Dutoi, P. J. Love, and M. Head-Gordon, Science **309**, 1704 (2005).

[23] A. Szabo and N. S. Ostlund, *Modern Quantum Chemistry – Introduction to Advanced Electronic Structure Theory*, Dover, Mineola (NY), 1996.

[24] T. Helgaker, P. Jørgensen, and J. Olsen, *Molecular Electronic-Structure Theory*, Wiley, Chichester, 2000.

[25] F. E. Harris, H. J. Monkhorst, and D. L. Freeman, *Algebraic and Diagrammatic Methods in Many-Fermion Theory*, Oxford Univ. Press, New York, 1992.

[26] P. Jørgensen and J. Simons, *Second Quantization-based Methods in Quantum Chemistry*, Academic Press, New York, 1981.

[27] S. Wilson, *Electron Correlation in Molecules*, Clarendon Press, Oxford, 1984.

[28] R. J. Buenker and S. D. Peyerimhoff, Theor. Chim. Acta **35**, 33 (1974).

[29] R. J. Bartlett, Ann. Rev. Phys. Chem. **32**, 359 (1981).

[30] E. Werner, Distr. Softw. Agents Appl. , 19 (1996).

[31] C. C. J. Roothaan, Rev. Mod. Phys. **23**, 69 (1951).

[32] G. G. Hall, Proc. Roy. Soc. Lond., A **205**, 541 (1951).

[33] P.-O. Löwdin, Phys. Rev. **97**, 1509 (1955).

[34] R. J. Jastrow, Phys. Rev. **98**, 1484 (1955).

[35] W. M. C. Foulkes, L. Mitas, R. J. Needs, and G. Rajagopal, Rev. Mod. Phys. **73**, 33 (2001).

[36] E. A. G. Armour, J. Franz, and J. Tennyson, *Explicitly Correlated Wavefunctions*, Collaborative Computational Project on Molecular Quantum Dynamics (CCP6), Warrington, 2006.

[37] T. D. Crawford and H. F. Schaefer III., Rev. Comp. Chem. **14**, 33 (2000).

[38] C. Møller and M. S. Plesset, Phys. Rev. **46**, 618 (1934).

[39] E. U. Condon, Phys. Rev. **36**, 1121 (1930).

[40] R. Parr and W. Yang, *Density-Functional Theory of Atoms and Molecules*, International Series of Monographs on Chemistry, No. 16, Oxford Univ. Press, New York, 1989.

[41] B. O. Roos, Adv. Chem. Phys. **69**, 399 (1987).

[42] T. Van Voorhis and M. Head-Gordon, Chem. Phys. Lett. **317**, 575 (2000).

[43] T. Van Voorhis and M. Head-Gordon, J. Chem. Phys. **112**, 5633 (2000).

[44] T. Van Voorhis and M. Head-Gordon, J. Chem. Phys. **115**, 7814 (2001).

[45] G. J. O. Beran, M. Head-Gordon, and S. R. Gwaltney, J. Chem. Phys. **124**, 114107 (2006).

[46] D. Walter and E. A. Carter, Chem. Phys. Lett. **346**, 177 (2001).

[47] D. Walter, A. Venkatnathan, and E. A. Carter, J. Chem. Phys. **118**, 8127 (2003).

[48] A. Venkatnathan, A. B. Szilva, D. Walter, R. J. Gdanitz, and E. A. Carter, J. Chem. Phys. **120**, 1693 (2004).

[49] B. D. Dunietz and R. A. Friesner, J. Chem. Phys. **115**, 11052 (2001).

[50] G. E. Scuseria and P. Y. Ayala, J. Chem. Phys. **111**, 8330 (1999).

[51] M. Schütz and H.-J. Werner, Chem. Phys. Lett. **318**, 370 (2000).

[52] M. Schütz, J. Chem. Phys. **113**, 9986 (2000).

[53] M. Schütz and H.-J. Werner, J. Chem. Phys. **114**, 661 (2001).

[54] J. E. Subotnik and M. Head-Gordon, J. Chem. Phys. **123**, 064108 (2005).

[55] B. O. Roos and K. Andersson, Chem. Phys. Lett. **245**, 215 (1995).

[56] H.-J. Werner, Mol. Phys. **89**, 645 (1996).

[57] K. Andersson, P.-A. Malmqvist, and B. O. Roos, J. Chem. Phys. **96**, 1218 (1992).

[58] J. J. W. McDouall, K. Peasley, and M. A. Robb, Chem. Phys. Lett. **148**, 183 (1988).

[59] K. Andersson, Theor. Chim. Acta **91**, 31 (1995).

[60] J. P. Finley, Chem. Phys. Lett. **283**, 277 (1998).

[61] G. K.-L. Chan and T. Yanai, Adv. Chem. Phys. **134**, 343 (2007).

[62] T. Yanai and G. K.-L. Chan, J. Chem. Phys. **124**, 194106 (2006).

[63] T. Yanai and G. K.-L. Chan, J. Chem. Phys. **127**, 104107 (2007).

[64] E. Neuscamman, T. Yanai, and G. K.-L. Chan, J. Chem. Phys. **130**, 124102 (2009).

[65] E. Neuscamman, T. Yanai, and G. K.-L. Chan, J. Chem. Phys. **130**, 169901 (2009).

[66] J. A. Pople, Theoretical models for chemistry, in *Energy, Structure, and Reactivity*, edited by D. W. Smith and W. B. McRae, pages 51–61, John Wiley, New York, 1973.

[67] P. R. Taylor, Coupled cluster methods in quantum chemistry, in *Lecture Notes in Quantum Chemistry II*, pages 125–202, Springer, Berlin, 1994.

[68] R. K. Nesbet, *Variational Principles and Methods in Theoretical Physics and Chemistry*, Cambridge Univ. Press, Cambridge, 2003.

[69] Z. N. C. Ha, *Quantum Many-Body Systems in One-Dimension*, World Scientific, Singapore, 1996.

[70] T. Giamarchi, Chem. Rev. **104**, 5037 (2004).

[71] T. Giamarchi, *Quantum Physics in One Dimension*, International Series of Monographs on Physics, No. 121, Clarendon, Oxford, 2004.

[72] S. Roth and D. L. Carroll, *One-Dimensional Metals – Conjugated Polymers, Organic Crystals, Carbon Nanotubes*, Wiley-VCH, Weinheim, 2nd edition, 2004.

[73] A. A. Ovchinnikov and I. I. Ukrainskii, *Electron-Electron Correlation Effects in Low-Dimensional Conductors and Superconductor*, Springer, Berlin, 1991.

[74] R. Farchioni and G. Grosso, *Organic Electronic Materials – Conjugated Polymers and low molecular weight Organic Solids*, Springer, Berlin, 2001.

[75] W. Barford, *Electronic and Optical Properties of Conjugated Polymers*, International Series of Monographs on Physics, No. 129, Clarendon Press, Oxford, 2005.

[76] J.-M. André, J. Delhalle, and J. L. Brédas, *Quantum Chemistry Aided Design of Organic Polymers – An Introduction to the Quantum Chemistry of Polymers and its Applications*, volume 2 of *World Scientific Lecture and Course Notes in Chemistry*, World Scientific, Singapore, 1991.

[77] P. Tavan and K. Schulten, Phys. Rev. B **36**, 4337 (1987).

[78] K. Nakayama, H. Nakahano, and K. Hirao, Int. J. Quantum Chem. **66**, 157 (1998).

[79] J. Lappe and R. J. Cave, J. Phys. Chem. A **104**, 2294 (2000).

[80] S. Reich, C. Thomsen, and J. Maultzsch, *Carbon Nanotubes – Basic Concepts and Physical Properties*, Wiley-VCH, Weinheim, 2004.

[81] R. Saito, G. Dresselhaus, and M. S. Dresselhaus, *Physical Properties of Carbon Nanotubes*, Imperial College Press, London, 2005.

[82] M. Bockrath et al., Nature **397**, 598 (1999).

[83] S. Belluci, J. Gonzalez, and P. Onorato, Phys. Rev. Lett. **95**, 186403 (2005).

[84] J. Lee et al., Phys. Rev. Lett. **93**, 166403 (2004).

[85] W. R. Salaneck, D. T. Clark, and E. J. Samuelsen, *Science and Applications of Conducting Polymers*, A. Hilger, Bristol, 1991.

[86] J. L. Brédas, W. R. Salaneck, and G. Wegner, *Organic Materials for Electronics*, volume 49 of *European Materials Research Society Symposia Proceedings*, North-Holland, Amsterdam, 1994.

[87] W. R. Salaneck, S. Stafström, and J. L. Brédas, *Conjugated Polymer Surfaces and Interfaces – Electronic and Chemical Structure of Interfaces for Polymer Light Emitting Devices*, Cambridge Univ. Press, Cambridge, 1996.

[88] J. Shinar, *Organic Light-Emitting Devices – A Survey*, Springer, New York, 2004.

[89] S. R. White, Phys. Rev. Lett. **69**, 2863 (1992).

[90] S. R. White, Phys. Rev. B **48**, 10345 (1993).

[91] S. R. White and R. L. Martin, J. Chem. Phys. **110**, 4127 (1999).

[92] J. J. Binney, *The Theory of Critical Phenomena – An Introduction to the Renormalization Group*, Oxford Univ. Press, Oxford, 2002.

[93] A. Lesne, *Renormalization Methods – Critical Phenomena, Chaos, Fractal Structures*, Wiley, Chichester, 1998.

[94] K. G. Wilson, Rev. Mod. Phys. **55**, 583 (1983).

[95] K. G. Wilson, Rev. Mod. Phys. **47**, 773 (1975).

[96] I. Peschel, X. Wang, M. Kaulke, and K. A. Hallberg, *Density-Matrix Renormalization – A New Numerical Method in Physics*, Lecture Notes in Physics, Springer, Berlin, 1999.

[97] J. Hubbard, Proc. Roy. Soc. Lond., A **276**, 238 (1963).

[98] R. Pariser and R. G. Parr, J. Chem. Phys. **21**, 767 (1953).

[99] J. A. Pople, Trans. Faraday Soc. **49**, 1375 (1953).

[100] T. H. Dunning Jr., J. Chem. Phys. **90**, 1007 (1989).

[101] N. B. Balabanov and K. A. Peterson, J. Chem. Phys. **123**, 064107 (2005).

[102] E. R. Davidson, J. Comp. Phys. **17**, 87 (1975).

[103] G. L. G. Sleijpen and H. A. Van der Vorst, SIAM Rev. **42**, 267 (2000).

[104] Z. Bai, *Templates for the Solution of Algebraic Eigenvalue Problems – a Practical Guide*, SIAM, Philadelphia, PA, 2000.

[105] G. Moritz, B. A. Hess, and M. Reiher, J. Chem. Phys. **122**, 024107 (2005).

[106] G. Moritz and M. Reiher, J. Chem. Phys. **124**, 034103 (2006).

[107] S. R. White, Phys. Rev. B **72**, 180403 (2005).

[108] D. Ghosh, J. Hachmann, T. Yanai, and G. K.-L. Chan, J. Chem. Phys. **128**, 144117 (2008).

[109] D. Zgid and M. Nooijen, J. Chem. Phys. **128**, 144115 (2008).

[110] G. K.-L. Chan and M. Head-Gordon, J. Chem. Phys. **116**, 4462 (2002).

[111] G. K.-L. Chan, J. Chem. Phys. **120**, 3172 (2004).

[112] Y. Kurashige and T. Yanai, J. Chem. Phys. **130**, 234114 (2009).

[113] D. Zgid and M. Nooijen, J. Chem. Phys. **128**, 014107 (2008).

[114] D. Zgid and M. Nooijen, J. Chem. Phys. **128**, 144116 (2008).

[115] G. Moritz, A. Wolf, and M. Reiher, J. Chem. Phys. **123**, 184105 (2005).

[116] G. Moritz and M. Reiher, J. Chem. Phys. **126**, 244109 (2007).

[117] K. H. Marti, I. M. Ondik, G. Moritz, and M. Reiher, J. Chem. Phys. **128**, 014104 (2008).

[118] A. O. Mitrushenkov, G. Fano, F. Ortolani, R. Linguerri, and P. Palmieri, J. Chem. Phys. **115**, 6815 (2001).

[119] A. O. Mitrushenkov, R. Linguerri, P. Palmieri, and G. Fano, J. Chem. Phys. **119**, 4148 (2003).

[120] A. O. Mitrushenkov, G. Fano, R. Linguerri, and P. Palmieri, arXiv:cond-mat **0306058v1** (2003).

[121] Ö. Legeza, J. Röder, and B. A. Hess, Mol. Phys. **101**, 2019 (2003).

[122] Ö. Legeza, J. Röder, and B. A. Hess, Phys. Rev. B **67**, 125114 (2003).

[123] S. Daul, I. Ciofini, C. Daul, and S. R. White, Int. J. Quantum Chem. **79**, 331 (2000).

[124] Z. Shuai, J. L. Brédas, S. K. Pati, and S. Ramasesha, Proc. SPIE **3145**, 293 (1997).

[125] D. Yaron, E. E. Moore, Z. Shuai, and J. L. Brédas, J. Chem. Phys. **108**, 7451 (1998).

[126] G. Fano, F. Ortolani, and L. Ziosi, J. Chem. Phys. **108**, 9246 (1998).

[127] G. L. Bendazzoli, G. F. S. Evangelisti, F. Ortolani, and L. Ziosi, J. Chem. Phys. **110**, 1277 (1999).

[128] A. O. Mitrushenkov, G. Fano, F. Ortolani, R. Linguerri, and P. Palmieri, J. Chem. Phys. **115**, 6815 (2001).

[129] A. O. Mitrushenkov, R. Linguerri, P. Palmieri, and G. Fano, J. Chem. Phys. **119**, 4148 (2003).

[130] S. R. White and R. L. Martin, J. Chem. Phys. **110**, 4127 (1999).

[131] S. Daul, I. Ciofini, C. Daul, and S. R. White, Int. J. Quantum Chem. **79**, 331 (2000).

[132] G. K.-L. Chan and M. Head-Gordon, J. Chem. Phys. **118**, 8551 (2003).

[133] G. K.-L. Chan, J. Chem. Phys. **120**, 3172 (2004).

[134] G. K.-L. Chan, M. Kállay, and J. Gauss, J. Chem. Phys. **121**, 6110 (2004).

[135] G. K.-L. Chan and T. Van Voorhis, J. Chem. Phys. **122**, 204101 (2005).

[136] Ö. Legeza, J. Röder, and B. A. Hess, Mol. Phys. **101**, 2019 (2003).

[137] Ö. Legeza, J. Röder, and B. A. Hess, Phys. Rev. B **67**, 125114 (2003).

[138] H. Ma, C. Liu, and Y. Jiang, J. Chem. Phys. **120**, 9316 (2004).

[139] H. Ma, F. Cai, C. Liu, and Y. Jiang, J. Chem. Phys. **122**, 104909 (2005).

[140] H. Ma, C. Liu, and Y. Jiang, J. Chem. Phys. **123**, 084303 (2005).

[141] S. Östlund and S. Rommer, Phys. Rev. Lett. **75**, 3537 (1995).

[142] S. Rommer and S. Östlund, Phys. Rev. B **55**, 2164 (1997).

[143] F. Verstraete, D. Porras, and J. I. Cirac, Phys. Rev. Lett. **93**, 227204 (2004).

[144] T. D. Crawford et al., PSI 3.2 (2003), see www.psicode.org.

[145] H.-J. Werner et al., Molpro, version 2009.1, a package of ab initio programs, 2009, see www.molpro.net.

[146] Y. Shao et al., Phys. Chem. Chem. Phys. **8**, 3172 (2006).

[147] Y. Shao et al., Q-CHEM, Version 3.0, Q-Chem, Inc., Pittsburgh, PA, 2007.

[148] C. Hampel and H.-J. Werner, J. Chem. Phys. **104**, 6286 (1996).

[149] M. Schütz and H.-J. Werner, J. Chem. Phys. **114**, 661 (2001).

[150] M. Schütz, Phys. Chem. Chem. Phys. **4**, 3941 (2002).

[151] M. Schütz and H.-J. Werner, Chem. Phys. Lett. **318**, 370 (2000).

[152] M. Schütz, J. Chem. Phys. **113**, 9986 (2000).

[153] M. Schütz, J. Chem. Phys. **116**, 8772 (2002).

[154] G. Hetzer, P. Pulay, and H.-J. Werner, Chem. Phys. Lett. **290**, 143 (1998).

[155] M. Schütz, G. Hetzer, and H.-J. Werner, J. Chem. Phys. **111**, 5691 (1999).

[156] G. Hetzer, M. Schütz, H. Stoll, and H.-J. Werner, J. Chem. Phys. **113**, 9443 (2000).

[157] T. S. Chwee, A. B. Szilva, R. Lindh, and E. A. Carter, J. Chem. Phys. **128**, 224106 (2008).

[158] P. R. Surján, *Correlation and Localization*, Springer, Berlin, 1999.

[159] E. R. Davidson, J. Comp. Phys. **17**, 87 (1975).

[160] J. Catalán and J. L. G. de Paz, J. Chem. Phys. **120**, 1864 (2004).

[161] W. J. Hehre, R. F. Stewart, and J. A. Pople, J. Chem. Phys. **51**, 2657 (1969).

[162] Basis sets were obtained from the Extensible Computational Chemistry Environment Basis Set Database, Version 02/02/06, as developed and distributed by the Molecular Science Computing Facility, Environmental and Molecular Sciences Laboratory which is part of the Pacific Northwest Laboratory, P.O. Box 999, Richland, Washington 99352, USA, and funded by the U.S. Department of Energy. The Pacific Northwest Laboratory is a multi-program laboratory operated by Battelle Memorial Institute for the U.S. Department of Energy under contract DE-AC06-76RLO 1830. Contact Karen Schuchardt for further information.

[163] C. Angeli et al., DALTON, a molecular electronic structure program, release 2.0 (2005), see www.kjemi.uio.no/software/dalton/.

[164] H.-J. Werner et al., MOLPRO, version 2002.6 (2002), a package of ab initio programs, see www.molpro.net.

[165] G. K.-L. Chan, P. W. Ayers, and E. S. Croot, J. Stat. Phys. **109**, 289 (2002).

[166] K. Okunishi, Y. Hieida, and Y. Akutsu, Phys. Rev. E **59**, R6227 (1999).

[167] Ö. Legeza and G. Fáth, Phys. Rev. B **53**, 14349 (1996).

[168] M. Takahashi and J. Paldus, Phys. Rev. B **31**, 5121 (1985).

[169] J. Paldus, J. Čížek, and M. Takahashi, Phys. Rev. A **30**, 2193 (1984).

[170] J. Paldus, M. Takahashi, and R. W. H. Cho, Phys. Rev. B **30**, 4267 (1984).

[171] S. F. Boys, in *Quantum Theory of Atoms, Molecules and the Solid State*, edited by P. O. Löwdin, pages 253–262, Academic, New York, 1968.

[172] J. Hachmann, J. J. Dorando, M. Avilés, and G. K.-L. Chan, J. Chem. Phys. **127**, 134309 (2007).

[173] E. Clar, *Polycyclic Hydrocarbons*, Academic Press, London, 1964.

[174] R. G. Havey, *Polycyclic Aromatic Hydrocarbons*, Wiley-VCH, New York, 1997.

[175] Y. Geerts, G. Klärner, and K. Müllen, Hydrocarbon oligomers, in *Electronic Materials: The Oligomer Approach*, edited by K. Müllen and G. Wegner, pages 1–103, Wiley-VCH, Weinheim, 1998.

[176] C. D. Dimitrakopoulos and P. R. L. Malenfant, Adv. Mater. **14**, 99 (2002).

[177] C. Reese, M. Roberts, M.-M. Ling, and Z. Bao, Mater. Today **7**, 20 (2004).

[178] M. Bendikov, F. Wudl, and D. F. Perepichka, Chem. Rev. **104**, 4891 (2004).

[179] H. Angliker, E. Rommel, and J. Wirz, Chem. Phys. Lett. **87**, 208 (1982).

[180] M. Kertesz and R. Hoffmann, Solid State Comm. **47**, 97 (1983).

[181] S. Kivelson and O. L. Chapman, Phys. Rev. B **28**, 7236 (1983).

[182] K. B. Wiberg, J. Org. Chem. **62**, 5720 (1997).

[183] K. N. Houk, P. S. Lee, and M. Nendel, J. Org. Chem. **66**, 5517 (2001).

[184] M. Bendikov et al., J. Am. Chem. Soc. **126**, 7416 (2004).

[185] R. Mondal, B. K. Shah, and D. C. Neckers, J. Am. Chem. Soc. **128**, 9612 (2006).

[186] A. R. Reddy and M. Bendikov, Chem. Comm. , 1179 (2006).

[187] T. Bally and W. T. Borden, Rev. Comp. Chem. **13**, 1 (1999).

[188] J. F. Stanton and J. Gauss, Adv. Chem. Phys. **125**, 101 (2003).

[189] L. V. Slipchenko and A. I. Krylov, J. Chem. Phys. **117**, 4694 (2002).

[190] L. Salem and C. Rowland, Angew. Chem. Int. Ed. **11**, 92 (1972).

[191] W. T. Borden and E. R. Davidson, J. Am. Chem. Soc. **99**, 4587 (1977).

[192] W. T. Borden, *Diradicals*, Wiley, New York, 1982.

[193] A. Rajca, Chem. Rev. **94**, 871 (1994).

[194] Y. Jung and M. Head-Gordon, ChemPhysChem **4**, 522 (2003).

[195] A. I. Krylov, J. Phys. Chem. A **109**, 10638 (2005).

[196] B. O. Roos, Adv. Chem. Phys. **69**, 399 (1987).

[197] Y. Kawashima, T. Hashimoto, H. Nakano, and K. Hirao, Theor. Chem. Acc. **102**, 49 (1999).

[198] C. Raghu, Y. Anusooya Pati, and S. Ramasesha, Phys. Rev. B **65**, 155204 (2002).

[199] C. Raghu, Y. Anusooya Pati, and S. Ramasesha, Phys. Rev. B **66**, 035116 (2002).

[200] C. Lee, W. Yang, and R. G. Parr, Phys. Rev. B **37**, 785 (1988).

[201] A. D. Becke, J. Chem. Phys. **98**, 5648 (1993).

[202] W. J. Hehre, R. F. Stewart, and J. A. Pople, J. Chem. Phys. **51**, 2657 (1969).

[203] T. H. Dunning Jr., J. Chem. Phys. **53**, 2823 (1970).

[204] T. H. Dunning Jr. and P. J. Hay, in *Methods of Electronic Structure Theory*, edited by H. F. S. III, volume 3, pages 1–28, Plenum Press, New York, 1977.

[205] M. J. Frisch et al., Gaussian 03, Revision E.01, Gaussian, Inc., Wallingford, CT, 2004.

[206] J. B. Birks, *Photophysics of Aromatic Molecules*, Wiley Monographs in Chemical Physics, Wiley-Interscience, London, 1970.

[207] J. Schiedt and R. Weinkauf, Chem. Phys. Lett. **266**, 201 (1997).

[208] N. Sabbatini, M. T. Indelli, M. T. Gandolfi, and V. Balzani, J. Phys. Chem. **86**, 3585 (1982).

[209] J. Burgos, M. Pope, C. E. Swenberg, and R. R. Alfano, Phys. Status Solid. B **83**, 249 (1977).

[210] K. Andersson, P.-A. Malmqvist, and B. O. Roos, J. Chem. Phys. **96**, 1218 (1992).

[211] K. Hirao, Chem. Phys. Lett. **190**, 374 (1992).

[212] D. Döhnert and J. Koutecký, J. Am. Chem. Soc. **102**, 1789 (1980).

[213] K. Takatsuka, T. Fueno, and K. Yamaguchi, Theor. Chim. Acta **48**, 175 (1978).

[214] K. Takatsuka and T. Fueno, J. Chem. Phys. **69**, 661 (1978).

[215] R. C. Bochicchio, J. Mol. Struct.: THEOCHEM **429**, 229 (1998).

[216] V. N. Staroverov and E. R. Davidson, J. Am. Chem. Soc. **122**, 186 (2000).

[217] V. N. Staroverov and E. R. Davidson, Chem. Phys. Lett. **330**, 161 (2000).

[218] M. Head-Gordon, Chem. Phys. Lett. **372**, 508 (2003).

[219] R. C. Bochicchio, A. Torre, and L. Lain, Chem. Phys. Lett. **380**, 486 (2003).

[220] M. Head-Gordon, Chem. Phys. Lett. **380**, 488 (2003).

[221] G. Fano, F. Ortolani, and L. Ziosi, J. Chem. Phys. **108**, 9246 (1998).

[222] A. D. Dutoi, Y. Jung, and M. Head-Gordon, J. Phys. Chem. A **108**, 10270 (2004).

[223] D. Cooper, *Valence Bond Theory*, Elsevier, Amsterdam, 2002.

[224] W. A. Goddard III and L. B. Harding, Ann. Rev. Phys. Chem. **29**, 363 (1978).

[225] J. Gerratt, D. L. Cooper, P. B. Karadakov, and M. Raimondi, Chem. Soc. Rev **26**, 87 (1997).

[226] S. Shaik and P. C. Hiberty, Rev. Comp. Chem. **20**, 1 (2004).

[227] M. A. Garcia-Bach, A. Penaranda, and D. J. Klein, Phys. Rev. B **45**, 10891 (1992).

[228] Y. Gao, C. G. Liu, and Y. S. Jiang, J. Phys. Chem. A **106**, 2592 (2002).

[229] K. Schulten and M. Karplus, Chem. Phys. Lett. **14**, 305 (1972).

[230] T. H. Dunning Jr., R. P. Hosteny, and I. Shavitt, J. Am. Chem. Soc. **95**, 5067 (1973).

[231] I. Ohmine, M. Karplus, and K. Schulten, J. Chem. Phys. **68**, 2298 (1978).

[232] B. S. Hudson, B. E. Kohler, and K. Schulten, Linear polyene electronic structure and potential surfaces, in *Excited States*, edited by E. C. Lim, volume 6, pages 1–95, Academic Press, New York, 1982.

[233] M. Said, D. Maynau, and J. P. Malrieu, J. Am. Chem. Soc. **106**, 580 (1984).

[234] W. Wu, D. Danovich, A. Shurki, and S. Shaik, J. Phys. Chem. A **104**, 874 (2000).

[235] T. Wang and A. I. Krylov, J. Chem. Phys. **123**, 104304 (2005).

[236] K. Hirao, H. Nakano, K. Nakayama, and M. Dupuis, J. Chem. Phys. **105**, 9227 (1996).

[237] T. Thorsteinsson, D. L. Cooper, J. Gerratt, P. B. Karadakov, and M. Raimondi, Theor. Chim. Acta **93**, 343 (1996).

[238] T. Thorsteinsson, D. L. Cooper, J. Gerratt, and M. Raimondi, Trends in methods and applications: A new approach to valence bond calculations: Casvb, in *Quantum Systems in Chemistry and Physics*, edited by R. McWeeny, J. Maruani, Y. G. Smeyers, and S. Wilson, volume 93, Kluwer, Dordrecht, 1997.

[239] D. L. Cooper, T. Thorsteinsson, and J. Gerratt, Adv. Quantum Chem. **32**, 51 (1998).

[240] T. Thorsteinsson and D. L. Cooper, Basic problems and models systems: An overview of the casvb approach to modern valence bond calculations, in *Quantum Systems in Chemistry and Physics*, edited by A. Hernández-Laguna, J. Maruani, R. McWeeny, and S. Wilson, volume 1, page 303, Kluwer, Dordrecht, 2000.

[241] E. H. Lieb and F. Y. Wu, Phys. Rev. Lett. **20**, 1445 (1968).

[242] K. Ohno, Theor. Chim. Acta **2**, 219 (1964).

[243] G. Klopman, J. Am. Chem. Soc. **86**, 4550 (1964).

[244] W. Koch and M. C. Holthausen, *A Chemist's Guide to Density Functional Theory*, Wiley-VCH, Weinheim, 2nd edition, 2001.

[245] T. R. Cundari, *Computational Organometallic Chemistry*, Marcel Dekker, New York, 2001.

[246] F. Neese, Coord. Chem. Rev. **253**, 526 (2009).

[247] B. O. Roos, Adv. Chem. Phys. **69**, 399 (1987).

[248] M. Gerloch, *Transition Metal Chemistry – the Valence Shell in d-Block Chemistry*, VCH, Weinheim, 1994.

[249] D. R. Salahub and M. C. Zerner, *The Challenge of d and f Electrons – Theory*

and Computation, volume 394 of *ACS Symposium Series*, American Chemical Society, Washington, DC, 1989.

[250] W. Kohn and L. J. Sham, Phys. Rev. **140**, A1133 (1965).

[251] L. Noodleman, J. Chem. Phys. **74**, 5737 (1981).

[252] G. Jonkers, C. A. de Lange, L. Noodleman, and E. J. Baerends, Mol. Phys. **46**, 609 (1982).

[253] L. Noodleman and E. R. Davidson, Chem. Phys. **109**, 131 (1986).

[254] S. Zein, S. A. Borshch, P. Fleurat-Lessard, M. E. Casida, and H. Chermette, J. Chem. Phys. **126**, 014105 (2007).

[255] J. N. Harvey, Dft computation of relative spin-state energetics of transition metal compounds, in *Principles and Applications of Densitiy Functional Theory in Inorganic Chemistry I*, edited by N. Kaltsoyannis and J. E. McGrady, pages 151–184, Springer, Heidelberg, 2004.

[256] A. Fouqueau et al., J. Chem. Phys. **120**, 9473 (2004).

[257] R. J. Deeth and N. Fey, J. Comp. Chem. **25**, 1840 (2004).

[258] M. Reiher, O. Salomon, and B. A. Hess, Theor. Chem. Acc. **107**, 48 (2001).

[259] M. Reiher, Inorg. Chem. **41**, 6928 (2002).

[260] M. Bühl and H. Kabrede, J. Chem. Theor. Comp. **2**, 1282 (2006).

[261] M. P. Waller, H. Braun, N. Hojdis, and M. Bühl, J. Chem. Theor. Comp. **3**, 2234 (2007).

[262] M. Bühl, C. Reimann, D. A. Pantazis, T. Bredow, and F. Neese, J. Chem. Theor. Comp. **4**, 1449 (2008).

[263] A. Ricca, C. W. Bauschlicher, and M. Rosi, J. Phys. Chem. **98**, 9498 (1994).

[264] M. Diedenhofen, T. Wagener, and G. Frenking, The accuracy of quantum chemical methods for the calculation of transition metal compounds, in *Computational Organometallic Chemistry*, edited by T. R. Cundari, Marcel Dekker, New York, 2001.

[265] T. Helgaker, J. Gauss, P. Jørgensen, and J. Olsen, J. Chem. Phys. **106**, 6430 (1997).

[266] K. L. Bak et al., J. Chem. Phys. **114**, 6548 (2001).

[267] J. P. Perdew, K. Burke, and M. Ernzerhof, Phys. Rev. Lett. **77**, 3865 (1996).

[268] J. P. Perdew, M. Ernzerhof, and K. Burke, J. Chem. Phys. **105**, 9982 (1996).

[269] J. P. Perdew, K. Burke, and M. Ernzerhof, Phys. Rev. Lett. **78**, 1396 (1997).

[270] J. P. Perdew, V. N. Staroverov, and G. E. Scuseria, Phys. Rev. Lett. **91**, 146401 (2003).

[271] J. P. Perdew, J. Tao, V. N. Staroverov, and G. E. Scuseria, J. Chem. Phys. **120**, 6898 (2004).

[272] E. Runge and E. K. U. Gross, Phys. Rev. Lett. **52**, 997 (1984).

[273] F. Neese, J. Chem. Phys. **127**, 164112 (2007).

[274] S. Sinnecker and F. Neese, J. Phys. Chem. A **110**, 12267 (2006).

[275] F. Neese, J. Am. Chem. Soc. **128**, 10213 (2006).

[276] F. Neese, ORCA 2.6.35 (2008), see www.thch.uni-bonn.de/tc/orca/.

[277] K. Pierloot and S. Vancoillie, J. Chem. Phys. **125**, 124303 (2006).

[278] K. Pierloot and S. Vancoillie, J. Chem. Phys. **128**, 034104 (2008).

[279] A. Ghosh and P. R. Taylor, Curr. Opinion Chem. Bio. **7**, 113 (2003).

[280] A. Ghosh, B. J. Persson, and P. R. Taylor, J. Bio. Inorg. Chem. **8**, 507 (2003).

[281] Y.-K. Choe, T. Nakajima, K. Hirao, and R. Lindh, J. Chem. Phys. **111**, 3837 (1999).

[282] J. M. Rintelman, I. Adamovic, S. Varganov, and M. S. Gordon, J. Chem. Phys. **122**, 044105 (2005).

[283] K. Pierloot, Mol. Phys. **101**, 2083 (2003).

[284] A. Fouqueau, M. E. Casida, L. M. L. Daku, A. Hauser, and F. Neese, J. Chem. Phys. **122**, 044110 (2005).

[285] J. M. L. Martin, Some observations and case studies on basis set convergence in density functional theory, in *Density Functional Theory – A Bridge between Chemistry and Physics*, edited by P. Geerlings, F. De Proft, and W. Langenaeker, pages 111–130, VUB Univ. Press, Brussels, 1999.

[286] J. Almlof and P. R. Taylor, J. Chem. Phys. **86**, 4070 (1987).

[287] P.-O. Widmark, P.-A. Malmqvist, and B. O. Roos, Theor. Chim. Acta **77**, 291 (1990).

[288] P.-O. Widmark, B. J. Persson, and B. O. Roos, Theor. Chim. Acta **79**, 419 (1991).

[289] R. Pou-Amérigo, M. Merchin, I. Nebot-Gil, P.-O. Widmark, and B. O. Roos, Theor. Chim. Acta **92**, 149 (1995).

[290] K. Pierloot, B. Dumez, P.-O. Widmark, and B. O. Roos, Theor. Chim. Acta **90**, 87 (1995).

[291] M. Douglas and N. M. Kroll, Ann. Phys. **82**, 89 (1974).

[292] B. A. Hess, Phys. Rev. A **32**, 756 (1985).

[293] B. A. Hess, Phys. Rev. A **33**, 3742 (1986).

[294] G. Jansen and B. A. Hess, Phys. Rev. A **39**, 6016 (1989).

[295] W. A. de Jong, R. J. Harrison, and D. A. Dixon, J. Chem. Phys. **114**, 48 (2001).

[296] M. Barysz and A. J. Sadlej, J. Mol. Struct.: THEOCHEM **573**, 181 (2001).

[297] G. B. Bacskay and J. R. Reimers, Solvation: Modeling, in *Encyclopedia of Computational Chemistry*, edited by P. von Rague Schleyer, volume 4, pages 2620–2632, John Wiley & Sons, Chichester, 1998.

[298] C. J. Cramer and D. G. Truhlar, Chem. Rev. **99**, 2161 (1999).

[299] K. A. Sharp, Continuum solvation, in *Encyclopedia of Computational Chemistry*, edited by P. von Rague Schleyer, volume 1, pages 571–573, John Wiley & Sons, Chichester, 1998.

[300] S. Mierts, E. Scrocco, and J. Tomasi, Chem. Phys. **55**, 117 (1981).

[301] J. Tomasi and M. Persico, Chem. Rev. **94**, 2027 (1994).

[302] J. Tomasi, B. Mennucci, and R. Cammi, Chem. Rev. **105**, 2999 (2005).

[303] J. Tomasi and B. Mennucci, Self-consistent reaction field methods, in *Encyclopedia of Computational Chemistry*, edited by P. von Rague Schleyer, volume 4, pages 2547–2560, John Wiley & Sons, Chichester, 1998.

[304] J. B. Foresman and A. Frisch, *Exploring Chemistry with Electronic Structure Methods*, Gaussian Inc., Pittsburgh (PA), 2nd edition, 1996.

[305] J. B. Foresman, T. A. Keith, K. B. Wiberg, J. Snoonian, and M. J. Frisch, J. Phys. Chem. **100**, 16098 (1996).

[306] J. Cioslowski, Electronic wavefunction analysis, in *Encyclopedia of Computational Chemistry*, edited by P. von Rague Schleyer, volume 2, pages 892–905, John Wiley & Sons, Chichester, 1998.

[307] S. M. Bachrach, Rev. Comp. Chem. , 171 (2007).

[308] K. B. Wiberg and P. R. Rablen, J. Comp. Chem. **14**, 1504 (1993).

[309] F. Martin and H. Zipse, J. Comp. Chem. **26**, 97 (2005).

[310] F. De Proft, J. M. L. Martin, and P. Geerlings, Chem. Phys. Lett. **250**, 393 (1996).

[311] P. Geerlings, F. De Proft, and J. M. L. Martin, Density-functional theory concepts and techniques for studying molecular charge distributions and related properties, in *Recent Developments and Applications of Modern Density Functional Theory*, volume 4 of *Theoretical and Computational Chemistry*, page 773, Elsevier Science, Amsterdam, 1996.

[312] R. S. Mulliken, J. Chem. Phys. **23**, 1833 (1955).

[313] A. E. Reed, R. B. Weinstock, and F. Weinhold, J. Chem. Phys. **83**, 735 (1985).

[314] P.-O. Löwdin, J. Chem. Phys. **18**, 365 (1950).

[315] A. D. Becke, J. Chem. Phys. **88**, 2547 (1988).

[316] J. Cioslowski, J. Am. Chem. Soc. **111**, 8333 (1989).

[317] A. Savin, J. Mol. Struct.: THEOCHEM **727**, 127 (2005).

[318] L. E. Chirlian and M. M. Francl, J. Comp. Chem. **8**, 894 (1987).

[319] C. M. Breneman and K. B. Wiberg, J. Comp. Chem. **11**, 361 (1990).

[320] R. F. W. Bader, Acc. Chem. Res. **18**, 9 (1985).

[321] R. F. W. Bader, *Atoms in Molecules: A Quantum Theory*, International Series of Monographs on Chemistry, No. 22, Clarendon Press, Oxford, 1990.

[322] P. L. A. Popelier, *Atoms in Molecules: An Introduction*, Prentice Hall, Harlow, 2000.

[323] F. Cortés-Guzmán and R. F. W. Bader, Coord. Chem. Rev. **249**, 633 (2005).

[324] R. F. W. Bader, Coord. Chem. Rev. **249**, 3198 (2005).

[325] B. A. Frazier and P. T. Wolczanski et. al., in preparation .

[326] M. Westerhausen and A. N. Kneifel, Inorg. Chem. Comm. **7**, 763 (2004).

[327] H. Paulsen, L. Duelund, H. Winkler, H. Toftlund, and A. X. Trautwein, Inorg. Chem. **40**, 2201 (2001).

[328] H. Paulsen and A. Trautwein, Density functional theory calculations for spin crossover complexes, in *Spin Crossover in Transition Metal Compounds III*, edited by P. Gütlich and H. A. Goodwin, pages 197–219, Springer, Heidelberg, 2004.

[329] K. P. Butin, E. K. Beloglazkina, and N. V. Zyk, Russ. Chem. Rev. **74**, 531 (2005).

[330] S. Kokatam et al., Inorg. Chem. **46**, 1100 (2007).

[331] K. Ray, S. DeBeer George, E. Solomon, K. Wieghardt, and F. Neese, Chem. Euro. J. **13**, 2783 (2007).

[332] K. Ray et al., J. Am. Chem. Soc. **127**, 4403 (2005).

[333] K. Ray, T. Weyhermüller, F. Neese, and K. Wieghardt, Inorg. Chem. **44**, 5345 (2005).

[334] X. Sun et al., Inorg. Chem. **41**, 4295 (2002).

[335] E. Bill et al., Chem. Euro. J. **11**, 204 (2005).

[336] M. Brynda, L. Gagliardi, and B. O. Roos, Chem. Phys. Lett. **471**, 1 (2009).

[337] G. La Macchia, F. Aquilante, V. Veryazov, B. O. Roos, and L. Gagliardi, Inorg. Chem. **47**, 11455 (2008).

[338] P.-A. Malmqvist, K. Pierloot, A. R. Moughal Shahi, C. J. Cramer, and L. Gagliardi, J. Chem. Phys. **128**, 204109 (2008).

[339] C. J. Cramer, M. Włoch, P. Piecuch, C. Puzzarini, and L. Gagliardi, J. Phys. Chem. A **11**, 1991 (2006).

[340] A. D. Becke, Phys. Rev. A **38**, 3098 (1988).

[341] C. Lee, W. Yang, and R. G. Parr, Phys. Rev. B **37**, 785 (1988).

[342] B. Miehlich, A. Savin, H. Stoll, and H. Preuss, Chem. Phys. Lett. **157**, 200 (1989).

[343] A. D. Becke, J. Chem. Phys. **98**, 5648 (1993).

[344] S. Grimme, J. Phys. Chem. A **109**, 3067 (2005).

[345] W. J. Hehre, R. Ditchfield, and J. A. Pople, J. Chem. Phys. **56**, 2257 (1972).

[346] V. A. Rassolov, J. A. Pople, M. A. Ratner, and T. L. Windus, J. Chem. Phys. **109**, 1223 (1998).

[347] P. C. Hariharan and J. A. Pople, Theor. Chim. Acta **28**, 213 (1973).

[348] D. Feller, J. Comp. Chem. **17**, 1571 (1996).

[349] K. L. Schuchardt et al., J. Chem. Info. Model. **47**, 1045 (2007).

[350] V. I. Lebedev, Russ. Acad. Sci. Dokl. Math. **45**, 587 (1992).

[351] G. B. Bacskay, Chem. Phys. **61**, 385 (1981).

[352] G. B. Bacskay, Chem. Phys. **65**, 383 (1982).

[353] R. Seeger and J. A. Pople, J. Chem. Phys. **66**, 3045 (1977).

[354] R. Bauernschmitt and R. Ahlrichs, J. Chem. Phys. **104**, 9047 (1996).

[355] P. Csaszar and P. Pulay, J. Mol. Struct.: THEOCHEM **114**, 31 (1984).

[356] O. Farkas and H. B. Schlegel, J. Chem. Phys. **111**, 10806 (1999).

[357] V. Gogonea, Self-consistent reaction field methods: Cavities, in *Encyclopedia of Computational Chemistry*, edited by P. von Rague Schleyer, volume 4, pages 2560–2574, John Wiley & Sons, Chichester, 1998.

[358] H.-J. Werner et al., Molpro, version 2006.1, a package of ab initio programs, 2006, see www.molpro.net.

[359] H.-J. Werner and P. J. Knowles, J. Chem. Phys. **82**, 5053 (1985).

[360] P. J. Knowles and H.-J. Werner, Chem. Phys. Lett. **115**, 259 (1985).

[361] H.-J. Werner and W. Meyer, J. Chem. Phys. **73**, 2342 (1980).

[362] H.-J. Werner and W. Meyer, J. Chem. Phys. **74**, 5794 (1981).

[363] H.-J. Werner, Adv. Chem. Phys. **69**, 1 (1987).

[364] P. Celani and H.-J. Werner, J. Chem. Phys. **112**, 5546 (2000).

[365] K. Pierloot, Nondynamic correlation effects in transition metal coordination compounds, in *Computational Organometallic Chemistry*, edited by T. R. Cundari, pages 123–158, Dekker, New York, 2001.

[366] G. Henkelman, A. Arnaldsson, and H. Jónsson, Comp. Mater. Sci. **36**, 354 (2006).

[367] E. Sanville, S. D. Kenny, R. Smith, and G. Henkelman, J. Comp. Chem. **28**, 899 (2007).

[368] W. Tang, E. Sanville, and G. Henkelman, J. Phys.: Cond. Mat. **21**, 084204 (2009).

[369] H. A. Jahn and E. Teller, Proc. R. Soc. Lond., A **161**, 220 (1937).

[370] R. Shepard, Adv. Chem. Phys. **69**, 63 (1987).

[371] E. R. Davidson, *Reduced Density Matrices in Quantum Chemistry*, Academic Press, New York, 1976.

[372] D. A. Mazziotti, *Reduced-Density-Matrix Mechanics – With Applications to Many-Electron Atoms and Molecules*, Wiley-Interscience, Hoboken, NJ, 2007.

[373] A. J. Coleman and V. I. Yukalov, *Reduced Density Matrices – Coulson's Challenge*, volume 72 of *Lecture Notes in Chemistry*, Springer, Berlin, 2000.

[374] J. Cioslowski, *Many-Electron Densities and Reduced Density Matrices*, Mathematical and Computational Chemistry, Kluwer Academic/Plenum, New York, 2000.

[375] C. Angeli, R. Cimiraglia, S. Evangelisti, T. Leininger, and J.-P. Malrieu, J. Chem. Phys. **114**, 10252 (2001).

[376] D. Zgid, D. Ghosh, E. Neuscamman, and G. K.-L. Chan, J. Chem. Phys. **130**, 194107 (2009).

[377] J. J. Dorando, J. Hachmann, and G. K.-L. Chan, J. Chem. Phys. **127**, 084109 (2007).

[378] B. O. Roos, The multiconfigurational (mc) self-consistent field (scf) theory, in *Lecture Notes in Quantum Chemistry*, edited by B. O. Roos, Lecture Notes in Chemistry, pages 177–254, Springer, Berlin, 1992.

[379] J. J. Dorando, J. Hachmann, and G. K.-L. Chan, J. Chem. Phys. **130**, 184111 (2009).

[380] Y. Yamaguchi, *A New Dimension to Quantum Chemistry – Analytic Derivative Methods in ab initio Molecular Electronic Structure Theory*, volume 29 of *International Series of Monographs on Chemistry*, Oxford Univ. Press, New York, 1994.

[381] E. J. Bylaska et al., NWCHEM, a computational chemistry package for parallel computers, version 5.1 (2007), pacific northwest national laboratory, richland, washington 99352-0999, usa., see www.emsl.pnl.gov/docs/nwchem/nwchem.html.

[382] R. A. Kendall et al., Comp. Phys. Comm. **128**, 260 (2000).

[383] K. Andersson et al., MOLCAS 7.4 (2009), see www.teokem.lu.se/molcas.

[384] J. A. Duncan, J. Am. Chem. Soc. **131**, 2416 (2009).

[385] G. Karlström et al., Comp. Mater. Sci. **28**, 222 (2003).

[386] Ö. Legeza, J. Röder, and B. A. Hess, Phys. Rev. B **67**, 125114 (2003).

[387] L. Bytautas and K. Ruedenberg, J. Chem. Phys. **121**, 10905 (2004).

[388] L. Bytautas and K. Ruedenberg, J. Chem. Phys. **121**, 10919 (2004).

[389] L. Bytautas and K. Ruedenberg, J. Chem. Phys. **121**, 10852 (2004).

[390] L. Bytautas and K. Ruedenberg, J. Chem. Phys. **122**, 154110 (2005).

[391] L. Bytautas and K. Ruedenberg, J. Chem. Phys. **124**, 174304 (2006).

[392] L. Bytautas, T. Nagata, M. S. Gordon, and K. Ruedenberg, J. Chem. Phys. **127**, 164317 (2007).

[393] J. Rissler, R. M. Noack, and S. R. White, Chem. Phys. **323**, 519 (2006).

[394] F. Verstraete and J. I. Cirac, arXiv:cond-mat **0407066v1** (2004).

[395] D. Pérez-Garciá, F. Verstraete, J. I. Cirac, and M. M. Wolf, arXiv:quant-ph **0707.2260v1** (2007).

[396] N. Schuch, M. M. Wolf, F. Verstraete, and J. I. Cirac, Phys. Rev. Lett. **98**, 140506 (2007).

[397] V. Murg, F. Verstraete, and J. I. Cirac, Phys. Rev. A **75**, 033605 (2007).

[398] G. Vidal, arXiv:quant-ph **0610099v1** (2006).

[399] R. Hoffmann, American Scientist **89**, 311 (2001).

[400] L. Pauling, J. Chem. Soc. , 1461 (1948).

[401] L. Pauling, *The Nature of the Chemical Bond and the Structure of Molecules and Crystals – An Introduction to Modern Structural Chemistry*, volume 18 of *The George Fisher Baker Non-Resident Lectureship in Chemistry at Cornell University*, Cornell Univ. Press, Ithaca, N.Y, 3rd edition, 1960.

[402] T. M. Dunn, J. Chem. Soc. , 623 (1959).

[403] J. P. Snyder, Angew. Chem. Int. Ed. **34**, 80 (1995).

[404] M. Kaupp and H. G. von Schnering, Angew. Chem. Int. Ed. **34**, 986 (1995).

[405] J. P. Snyder, Angew. Chem. Int. Ed. **34**, 986 (1995).

[406] G. Aullón and S. Alvarez, Theor. Chem. Acc. **in print** (2009).

[407] R. Bianchi, G. Gervasio, and D. Marabello, Comptes Rendus Chim. **8**, 1392 (2005).

[408] R. Resta, Nature **453**, 735 (2008).

[409] H. Raebiger, S. Lany, and A. Zunger, Nature **453**, 763 (2008).

[410] W. B. Jensen, J. Chem. Educ. **84**, 1418 (2007).

[411] W. M. Latimer, *The Oxidation States of the Elements and their Potentials in Aqueous Solutions*, Prentice-Hall, New York, 1938.

[412] J. B. Pendry and C. H. Hodges, J. Phys. C: Solid State Phys. **17**, 1269 (1984).

[413] L. C. Allen, Int. J. Quantum Chem. **49**, 253 (1994).

[414] J. Voitländer and R. Longino, Naturwissenschaften **46**, 664 (1959).

[415] C. K. Jørgensen, *Oxidation Numbers and Oxidation States*, Molekülverbindungen und Koordinationsverbindungen in Einzeldarstellungen, Springer, Berlin, 1969.

[416] S. Riedel and M. Kaupp, Coord. Chem. Rev. **253**, 606 (2009).

[417] R. Janes and E. Moore, *Metal-Ligand Bonding*, Royal Society of Chemistry, Cambridge, 2004.